A NEW TWO-SCALE MODEL FOR LARGE EDDY SIMULATION OF WALL-BOUNDED FLOWS

A Thesis
Presented to
The Academic Faculty

by

Ayse Gul Gungor

In Partial Fulfillment
of the Requirements for the Degree
Doctor of Philosophy in the
School of Aerospace Engineering

Georgia Institute of Technology
August 2009

A NEW TWO-SCALE MODEL FOR LARGE EDDY SIMULATION OF WALL-BOUNDED FLOWS

Approved by:

Professor Suresh Menon,
Committee Chair
School of Aerospace Engineering
Georgia Institute of Technology

Professor Stephen Ruffin
School of Aerospace Engineering
Georgia Institute of Technology

Professor Lakshmi Sankar
School of Aerospace Engineering
Georgia Institute of Technology

Assistant Professor Thorsten Stoesser
School of Civil and Environmental
Engineering
Georgia Institute of Technology

Professor Pui-Kuen Yeung
School of Aerospace Engineering
Georgia Institute of Technology

Date Approved: May 8, 2009

To my family,

Sevgili Annem, Babam & Abim'e

ACKNOWLEDGEMENTS

I would like to first express my gratitude toward my advisor, Dr. Suresh Menon for his invaluable support, guidance, and encouragement. He was considerate and supportive all along. I really appreciate all the opportunities he has given for me both professionally and personally. To study under his guidance has been one the most valuable experience in my life.

I would like to thank Dr. Lakshmi Sankar and Dr. Pui-Kuen Yeung, members of the Thesis Advisory Committee, for their time, guidance and enlightening ideas which were important in improving the quality of this research. I would like to extend my sincere thanks to Dr. Stephen Ruffin and Dr. Thorsten Stoesser, members of the Doctoral Examination Committee, for their critical examination of the thesis and useful comments. I would also like to thank Dr. J.-P. Laval (Laboratoire de Mecanique de Lille) for providing numerical data from his simulations of separated channel flow and Dr. Charles Meneveau (John Hopkins University) for access to the homogeneous turbulence data.

I would also like to thank Dr. Ülgen Gülçat (Istanbul Technical University) for guiding me throughout my stay in Georgia Tech and Dr. A. Rüstem Aslan (Istanbul Technical University) for his helpful suggestions and guidance. I am grateful to Department of Aeronautics and Astronautics in Istanbul Technical University for supporting my doctoral studies.

I would like to thank the Office of Naval Research for the continuing financial support of this research. I am very thankful for the opportunity to use high performance computing resources provided by Naval Oceanographic Office, Army Research Laboratory and Engineer Research and Development Center.

I would also like to thank my previous lab mates Dr. Mehmet Kırtaş, Dr. Satish Undapalli, Dr. Kenji Miki, Dr. Martin Sanchez-Rocha, Dr. Franklin Genin, Nathalie Tramecourt, Dr. Hossam El-asrag, Dr. Chris Stone, Dr. Feiz Homayoon, Dr. Nayan Patel, Jason Hackl and my current lab mates Matthieu Masquelet, Miguel T. Walter, Kaushik Balakrishnan, Leandro Gryngarten, Joey Shultz, Satoshi Ukai, Kalyana Gottiparthi, Andy Smith, Dr. Jung Choi and Dr. Srikant Srinivasan for creating a friendly and comforting environment in the lab. I am indebted to my previous lab mate Dr. Konstantin Kemenov from whom I learned a lot through all those years he was in the lab and later with his e-mails. His patiently-written detailed answers, and helpful discussions were much appreciated.

My special thanks goes to my lab mates Barış Ali Şen and Engin Orçun Kozaka for making my life more enjoyable and easier in the lab. I would like to extend my thanks to my friends Göktan Güzel, Bülent Tutkun, Evren Öner, Faik Sümer, Emre Gündüz, Ersel Ölçer, Faruk and Can Çavuşoğlu and Dr. Oğuz Karvan for their friendship.

I thank to my best friends Dr. Nurhak Erbaş Şen, İpek Kışlalı, and Yasemin Ezber with whom I shared many long talks and had many joyful conservations. Without all their support and guidance I believe I would be lost. Thank you for cheering me up and telling me that everything is gonna be fine when I feel hopeless.

I am most grateful to my parents, my mother Gülseren Güngör and my father Mustafa Güngör. Their unconditional love and support made me achieve many things that otherwise would be impossible. I want to extend them my heartfelt thanks for all they have done and gone through for me. I would like to thank my grandmoms Emine Güngör and Emine Işık, and my sister-in-law Gökçe for their love and support. My dear brother Bahadır Murat, without your guidance and constant support I would be lost. Thank you for everything. I wouldn't have come so far without you. My dear nephew, Bahadır Kayra, knowing that you will be with us in a couple of months drived me to finish this study. We are all waiting for you...

TABLE OF CONTENTS

LIST OF TABLES

LIST OF FIGURES

NOMENCLATURE

Roman Symbols

C_ϵ	model coefficient for subgrid dissipation
C_ν	model coefficient for turbulent viscosity
c	speed of sound
i, j, k	computational grid indices
J	Jacobian of the coordinate system transformation
k	turbulent kinetic energy
k^{sgs}	subgrid turbulent kinetic energy
ℓ	integral length scale
P	production of turbulent kinetic energy
p	pressure
$\mathbf{Q}$, $\mathbf{Q}'$	state vector
Re	Reynolds number
r	spatial position
S	rate of strain
t	time
u, v, w, u_i	Cartesian velocity vector components
u'	rms velocity
v'	turbulent intensity
u'_{sgs}	subgrid scale turbulence intensity
V	volume
x, y, z	Cartesian coordinate directions

Greek Symbols

β	artificial compressibility parameter
$\overline{\Delta}$	grid size
δ_{ij}	Kronecker delta
η	Kolmogorov length scale
μ	dynamic viscosity
ν	kinematic viscosity
ρ	density
τ_{ij}	viscous stress tensor
τ_w	wall shear stress
ξ, η, ζ	spatial directions in computational space

Subscripts

i, j, k	Cartesian tensor indices or species indices
L	laminar
n	time step index
t, T	turbulent quantity
∞	quantity at infinity downstream

Superscripts

0	reference quantity
F	filtered quantity
$\mathcal{L}$	additive large scale quantity
L	large scale quantity
S	small scale quantity

$\mathcal{S}$	additive small scale quantity
sgs	subgrid scale
$test$	test filter scale

Other Symbols

∂	partial derivative operator
∇	gradient operator
$\nabla\cdot$	divergence operator
$\sum$	summation operator
Δ	difference operator
$\widehat{}$	test filter
$\bar{}$	space average
$'$, $''$	fluctuating quantity

Abbreviations

CFD	Computational Fluid Dynamics
CFL	Courant-Friedrichs-Lewy number
CPU	Central Processing Unit
DES	Detached Eddy Simulation
DML	Dynamic Multilevel Method
DNS	Direct Numerical Simulation
LDKM	Localized Dynamic k-equation Model
LES	Large Eddy Simulation
LS	Large Scale
MPI	Message Passing Interface

ODT	One-dimensional Turbulence
PDF	Probability Distribution Function
RANS	Reynolds Averaged Navier - Stokes
RDT	Rapid Distortion Theory
RMS	Root Mean Square, variance
SS	Small Scale
sgs	Subgrid Stress
TKE	Turbulent Kinetic Energy
TLM	Two-Layer Model
TLS	Two Level Simulation
VMS	Variational Multiscale Method

SUMMARY

Large Eddy Simulation (LES) is currently the most promising method for studying flows of practical interest. The reason for this is the capability of LES to resolve the large-scale unsteady flow physics. However, LES of wall-bounded high Reynolds number complex flows is still subject to several challenges. Near the wall, the flow is dominated by vortices that are smaller in size compared with ones in the free flow. Therefore, for simulating wall-bounded flows with LES, either all the near-wall structures are resolved (wall-resolved LES) or modeled (wall-modeled LES). Wall-modeled LES is at present the only alternative for LES of practical flows, and therefore specific modeling of the near-wall region is needed.

The Two Level Simulation (TLS) is a multiscale approach that is based on decomposition of the flow field into large-scale (LS) and small-scale (SS) components. From this decomposition, the coupled system of large- and small-scale governing equations can be derived. TLS approach is investigated in detail in terms of the SS model assumptions, LS functions and LS resolutions. Current analyses improve the understanding of the TLS approach. The TLS approach provides a different perspective on turbulence modeling in which SS are calculated using a SS simulation model instead of modeling the effect of the SS on the LS. Therefore, TLS can be considered as an alternative model for LES of complex flows.

In this thesis, a new hybrid model that combines the multiscale approach based on TLS in the inner region with conventional LES away from the wall is demonstrated. This new approach is significantly different from previous near-wall approaches. In the hybrid TLS-LES, a very fine SS mesh is embedded inside the coarse LES mesh in the near-wall region. The SS equations capture fine-scale temporal and spatial

variations in all three cartesian directions for all three velocity components near the wall. The TLS-LES equations are derived based on defining a new scale separating operator. The TLS-LES equations in the transition region are obtained by blending the TLS LS and LES equations. New commutation error terms are identified in the transition region and are shown theoretically to arise if the blending function is not uniform in space. Similar to the most common LES approaches, these commutation error terms are neglected at present.

A new incompressible parallel flow solver is developed that accurately and reliably predict turbulent flows using TLS-LES. The code uses a primitive variable formulation based on an artificial compressibility approach and a dual time stepping method. The advective terms are discretized using fourth-order energy conservative finite differences. The SS equations are also integrated in parallel, which reduces the overall cost of the TLS-LES approach. The code is validated for decaying isotropic turbulence, turbulent re-circulating flows, and turbulent channel flows.

The TLS-LES approach is validated for canonical wall-bounded turbulent flows at Reynolds numbers based on friction velocity ranging from 395 to 2400. Results of the TLS-LES channel flow suggests that near-wall implementation of TLS is a viable alternative approach for LES of wall-bounded flows. Finally TLS-LES approach is further investigated for a channel flow with convergent-divergent section at the bottom wall and flow in a diffuser. Results demonstrate the ability of the TLS-LES approach to complex flows. It is important to note that the TLS-LES is extended to complex flows without making any changes to the model. This is an important property in terms of the numerical approaches, since most of the prevalent turbulence models require special tuning for one flow to another. Overall, the TLS-LES approach yields very reasonable predictions of most of the crucial flow features in spite of using a relatively coarse grids.

CHAPTER I

INTRODUCTION

In nature, laminar flows are rather an exception, and most of the interesting flows in engineering applications are turbulent. Turbulent flow is three-dimensional, time-dependent, has large Reynolds number (Re), includes a wide range of both time and length scales, and it is diffusive and dissipative [113]. From the point of view of numerical simulations, the existence of a wide range of characteristic length and time scales is crucial, since for a successful simulation one should be able to capture all these scales.

A simulation that resolves all flow scales is called direct numerical simulation (DNS) but the high computational cost of DNS makes it impractical for realistic engineering flows. While DNS is not a feasible method for engineering problems, it is, however, a powerful research tool. From DNS results, almost any quantity can be evaluated, and once the numerical simulation succeeded, the problem can be studied more detailed than possible by experiment. With the advent of massively parallel computers, DNS has been successfully applied to the study of the flow physics of turbulence [53, 49, 44], active flow control and validation of the computational models. A thorough review of different applications of DNS is provided by Moin and Mahesh [80].

An alternative approach to DNS is the large eddy simulation (LES) technique. In LES, the computational cost is reduced by applying a low-pass filter to the turbulent flow, thereby eliminating many of the small-scales below the filter width. In LES, the large energy containing scales are computed directly, while the dynamical effects of the smaller scales resulting from the filtering operation are represented by subgrid scale

(sgs) models. Since the smaller dissipative scales of motion are not resolved in LES, the main role of these sgs models is to remove the energy from the resolved scales. This approach is consistent with the well-accepted notion of turbulent energy cascade from the large energy containing (anisotropic) scales to the small (isotropic) dissipative scales. However, it should be noted that backscattering, i.e., the energy flux from the small scales to the large ones can also contribute to the energy distribution. Therefore, the sgs models must represent both the energy transfer to (forward scatter) and from (back scatter) the unresolved scales accurately.

In general, sgs models can capture these effects only partially. Most commonly used LES model is the well-known algebraic (Smagorinsky) eddy viscosity model [109], which is based on the equilibrium assumption at the small scales. A model based on the kinetic energy of the sgs model can relax this equilibrium assumption [60]. Nevertheless, both models and their dynamic counterparts [28, 60] can only account for the forward scatter of energy. To model backscattering two methods have been proposed but rarely used in practice. First one is to introduce a stochastic forcing [77], while the second one is to modify the eddy viscosity models associated with the forward scattering [28, 60]. In the second approach, backscattering is represented by a negative viscosity. In general, most of the dynamic eddy viscosity models can generate negative value of constants and this property is sometimes interpreted as modeling backscattering. However, these approaches are not based on a physical description of the backscattering, but can be classified in the category of statistical deterministic backward cascade models [102]. For a more detailed description of deterministic statistical and stochastic models, the reader may refer to [102].

The eddy viscosity closures assume a one-to-one correlation between the sgs stress and the large-scale strain rate tensor. However, *a priori* analysis of DNS displayed very little correlation between these two tensors [75]. This lack of correlation between two tensors led Bardina *e*t al. [4] to propose an alternative sgs model called a scale

similarity model. *A priori* analysis showed that modeled sgs stress from the scale similarity analysis exhibit a good correlation with the real stress [4, 71]. However, the scale similarity model dissipates very little energy and is numerically unstable [75]. To overcome this problem, scale similarity model has been combined with the Smagorinsky model to produce the mixed models.

Apart from the problem of modeling the sgs stresses, spatial filtering also creates additional difficulties in LES of turbulent flows for cases with complex geometries or with strong variation of turbulence intensities, which requires non-uniform grids and filter widths [26, 30]. These difficulties are associated with the error due to non-commutation of the filtering operation with spatial differentiation if the filter width is not uniform and boundaries are present [31, 30]. When filtering and differentiation do not commute on a bounded domain, it introduces an extra term, the so-called commutation error term [26, 30, 115]. Developing an effective computational model for this term is an important open problem in the LES. Some progress has been made on the estimation of the size of this error, but still many questions remain unanswered [26, 30, 115].

Another problem arises in the LES of high Re-number wall-bounded flows where the inner region of the boundary layer needs to be directly resolved. This requires huge computational cost [2, 49] and sakes LES impractical for most applications of interest.

The main characteristic features of wall-bounded flows are the viscous, buffer and logarithmic layers. These layers are the main difference between the wall-bounded flows, and isotropic and free- shear turbulence. In the latter, the inertial and dissipative scales do not contribute to the turbulence dynamics; they are essentially passive recipients of the energy generated at the larger scales. The energy produced at the large scales cascades to the smaller scales through the non-local triadic interactions in the inertial range and is dissipated in the smaller scales. A sketch can be found in

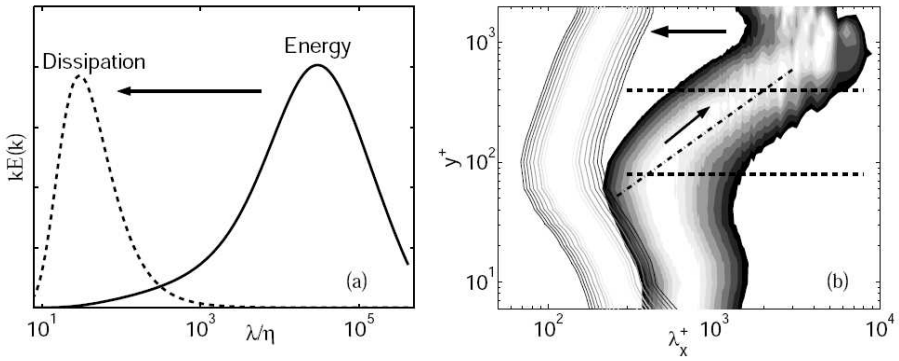

Figure 1: Pre-multiplied spectra, $kE(k)$ of the kinetic energy. (a) In isotropic turbulence, as a function of the isotropic wavelength $\lambda = 2\pi/|k|$. (b) In a numerical turbulent channel [44], plotted as a function of the streamwise wavelength λ_x, and of the wall distance y. The shaded contours are the density of the kinetic energy of the fluctuations. The lines are the spectral density of the surrogate dissipation. The horizontal lines represent the logarithmic layer. The arrows indicate the implied cascades. This figure is obtained from [50].

Fig. 1 (a) for an isotropic turbulence. Model spectrum shows an exact separation of scales for the isotropic flows.

In comparison to isotropic turbulent flows, in wall-bounded flows, the buffer and logarithmic layers are main participants in the turbulence dynamics. Near-wall buffer region, where the effect of viscosity is important, can be equivalent of the dissipative range of isotropic turbulence. However, in the case of the buffer region the dissipative structures are also responsible for turbulent energy production. There is no scale separation in this region, as shown in Fig. 1 (b), since most of the large scales are excluded by the presence of the impermeable wall [50]. The energy and the dissipation scales are of similar sizes.

The near-wall buffer region is dominated by near-wall streaks [59] and quasi-streamwise vortices [100, 51]. The streaks are regions of low and high momentum fluid elongated in the direction of the mean flow. Their average characteristic scales in the longitudinal (L_x^+) and transverse (L_z^+) directions are such that $L_x^+ \approx 200 - 1000$ and $L_z^+ \approx 100$ (given in wall units). The quasi-streamwise vortices are staggered between

these high and low velocity streaks, with a longitudinal spacing about $x^+ = 400$.

Streaks are considered to be of major importance in the regeneration of turbulent energy. The maximum energy production is observed in the near-wall region, at around $y^+ \approx 15$. This energy production in the small-scales introduces backward scattering associated with the sweeping type of events which correspond to jets of high streamwise momentum directed toward the wall. The forward scattering is associated with the ejections which corresponds to jets of low streamwise momentum directed outward. In the outer regions in which the viscous effects no longer dominate the dynamics of the flow, the energy cascade mechanism is associated preferentially with ejection events.

The description of the boundary layer flow structure clearly shows that the LES of this case would be problematic. The turbulence generating mechanism occurs over a wide range of scales, and also turbulence production in the buffer layer is associated with backscatter. Therefore, most commonly used sgs models become invalid for wall-bounded flows. In general, two possible approaches to treat wall-bounded flows are followed. One of them is to resolve directly the near-wall dynamics with sufficiently fine resolution to capture the production mechanism near the wall. However, this approach comes with very high computational cost. The analysis of aerodynamic boundary layers [13] and turbulent channel flows [2, 49] show that the number of grid points required for a proper LES resolution in the near-wall region scales approximately as the square of the Re, which limits the near-wall resolved LES to moderate Reynolds numbers ($Re \approx 10^4$). The second approach is to model the near-wall dynamics. The main advantage of this method is that the resolution requirement can be reduced significantly; but with an additional source of errors due to the models used in the near-wall region [92]. To further discuss the motivation of the current study, some limitations of LES near-wall models are highlighted first in the following section.

1.1 Near-wall Models for Large Eddy Simulations

Near-wall modeling approaches are classified into following groups [91, 92, 102]: those using a wall function near the wall (Equilibrium stress models), those simulating the wall layer in a Reynolds averaged sense (Zonal approaches), and those merging LES with RANS to model the near-wall region (Hybrid approaches). All these approaches rely on theoretical models. Hence, they don't provide enough information about the turbulent structures occurring in this region. Examples of many near-wall models can be found in reviews [92, 11, 91].

Equilibrium Stress Models

The first group of near-wall modeling approaches are equilibrium stress models or wall-function models. The wall function model replaces no-slip velocity boundary conditions at the walls with approximate conditions. These conditions account for the effects of the near-wall turbulence on the outer flow. Such effects enable the LES to accurately capture the large-scale features away from the wall without resolving the inner layer.

Wall stress models, on the other hand, provide an algebraic relationship between local wall stresses and tangential velocities at the first off-wall velocity nodes. This approach was first introduced by Deardorff [21], who considered a coarse LES of plane channel flow at an infinite Re by restricting the second derivatives of the velocity at the first off-wall grid point. This condition forces the plane-averaged profile at this point to satisfy a logarithmic law in the mean. However, the results of the plane channel flow did not compare well with data, as pointed out in [92]. The mismatch was probably caused by the very coarse resolution in the outer layer as well as problems inherent in the model.

Schumann [106] assumed a linear relationship between instantaneous streamwise

velocity at the first grid point of the wall and instantaneous wall shear stress:

$$\tau_{12}(x,z) = \frac{\langle \tau_w \rangle}{\langle \overline{u}(x,y_1,z) \rangle} \overline{u}(x,y_1,z) \quad (1)$$

$$\tau_{23}(x,z) = \nu \frac{\overline{w}(x,y_1,z)}{\langle \overline{w}(x,y_1,z) \rangle} \quad (2)$$

where y_1 denotes the distance between the wall and the first point off the wall, $\overline{u}$ and $\overline{w}$ represent the LES resolved streamwise and spanwise velocities, respectively, and $\langle . \rangle$ represents the time average.

A number of modifications to Schumann's model have been made by Groetzbach [34] and Werner and Wengle [119], who wanted to eliminate the need for *a priori* prescription of the mean wall shear stress, and by Piomelli *et al.* [94], who wanted to account for the effect of sweep and ejection events on the wall shear stress. Even though these relatively simple LES wall stress models work well for attached flows and reduce the computation time by a factor of 10 or more, they have not been well established in separated flow regions because they cannot capture the effects of near-wall structures. This prompted the development of hybrid models in which simpler transport equations are solved in the inner layer.

Zonal Approaches

An alternative, more sophisticated wall-function, or stress model was suggested by Balaras *et al.* [3] and Cabot [10, 11]. In the two-layer model (TLM) proposed by these authors, three-dimensional turbulent boundary layer equations were solved numerically on an embedded near-wall mesh between the wall and the first grid point located at the edge of the inner layer. Here, the inner layer is defined as the viscous sublayer, the buffer region, and part of the logarithmic layer. The model equations for the two tangential velocities can be written as

$$\frac{\partial \overline{u}_i}{\partial t} + \frac{\partial}{\partial x_j} \overline{u}_i \overline{u}_j = \frac{\partial P_e}{\partial x_i} + \frac{\partial}{\partial x_j} \left[(\nu + \nu_t) \frac{\partial \overline{u}_i}{\partial x_j} \right], \quad i = 1, 3, \quad (3)$$

where continuity is used to determine the wall-normal velocity

$$\overline{u}_2 = -\int_0^y (\frac{\partial u_1}{\partial x_1} + \frac{\partial u_3}{\partial x_3}) dy \tag{4}$$

Here, P_e is the near-wall pressure at the first point in the outer layer, and ν_t is the eddy viscosity, which can be defined based on the mixing length theory [3, 11]. The inner layer is calculated by integrating Eq. (3) using the no-slip condition at the wall and the velocity at the first point in the outer layer LES as a free stream condition. The shear stress at the wall is explicitly calculated and then used as a boundary condition for the outer layer LES calculations.

The main features of the TLM approach were further explored by [10, 11], and used also in the simulation of a trailing-edge flow [117]. In the dynamic wall model of Wang and Moin [117], the main idea is to use the Reynolds averaged Navier-Stokes (RANS) model based on turbulent boundary layer equations near the wall. The RANS coefficients are adjusted dynamically to match the LES at the boundary between RANS and LES. This model was shown to be considerably more accurate than the simpler wall models described above [117] and predicted low-order statistics, such as mean velocities, in good agreement with those from LES using resolved wall layers at a much smaller computational cost for several complex flows (i.e., trailing-edge flow [117]).

Another conceptually different model, introduced by Schmidt *et al.* [105], was based on the one-dimensional turbulence (ODT) model of Kerstein [58]. This ODT model introduces fine-scale temporal and spatial variance of velocity fluctuations (in one direction) in the near-wall region by solving the modified ODT evolution equations on one-dimensional wall-normal lines placed in the inner region.

Hybrid RANS/LES Methods

A more recent approach is based on the idea of merging the LES with RANS models into one that can be used to model the near-wall region. One of these approaches is

detached-eddy simulation [111] (DES), which is based on a modification of the length scale in the destruction term of the one-equation eddy viscosity model developed by Spalart and Almaras [110]. This hybrid RANS/LES method combines the advantages of both approaches, so it is a promising solution for complex high-Re flows dominated by large coherent structures. The major drawback of these models is that the solutions of two different fields are difficult to merge at the interface. Major difficulties arise from the fact that the RANS solution at the interface lacks information about small-scale perturbations, information that is required for the LES part of the solution. This problem arises, particularly in near-wall regions where the outer flow is coupled to the wall through a physically incorrect buffer layer [86, 1]. To solve this problem, Piomelli *et al.* [93], Keating and Piomelli [54] and De Prisco *et al.* [18] introduced small fluctuations in the transition region of the model using a backscatter type of forcing. Dahlstrom *et al.* [16] followed the same approach and added instantaneous fluctuations to the momentum equations at the LES interface to feed the LES region with relevant turbulent structures. After an extensive comparative analysis, they found that the interface conditions exhibited improved results over those in the case without forcing. In a recent study [97], however, it was observed that accurate results can be obtained only for flows with complex flow features (i.e., an adverse pressure gradient) without using stochastic forcing at the interface.

LES and RANS eddy viscosity models can also be combined to achieve a smooth transition from RANS near the wall to LES away from it. These models are based on blending functions that need to be fine-tuned to yield good results. However, one problem of this type of RANS/LES application is the lack of resolved eddies at the interface. Hamba [39, 40] applied additional filtering at the interface, increasing the wall-normal fluctuations and thus the turbulent intensity at the bottom of the LES region, providing a more physical velocity field for the LES. Because of this corrected velocity field, the grid scale turbulent stresses increased and as a result, the mean

velocity profile was corrected. Temmerman *et al.* [112] dynamically calculated the eddy viscosity coefficient in the RANS region, which introduced additional unsteadiness and improved the mean flow predictions for channel flow and separated flow around a curved hill. Davidson and Peng [17] performed both types of simulations and observed a mean flow mismatch in the channel flow case.

A new hybrid RANS/LES formulation, rigorously derived by Germano [27], was based on a new additive filter for incompressible flows and extended by Sanchez-Rocha and Menon [103] for compressible flows. In the hybrid RANS/LES formulation, new hybrid terms appear in the governing equations, and models are needed to close the final equation. Studies based on the turbulent boundary layer [103] showed that these terms are quite important and closing them can reduce the effect of the blending function.

1.2 Multiscale Methods

A different approach to overcome the resolution requirement in LES is to use subgrid simulation approaches, which are based on multiscale methods. Several multiscale methods have been proposed in recent years, including the variational multiscale method (VMS) by Hughes *et al.* [45, 46], the dynamic multilevel method (DML) by Dubois *e*t al. [24], the rapid distortion theory (RDT) by Laval *e*t al. [63, 64], and the Two Level Simulation (TLS) model by Kemenov and Menon [56]. All these models are based on decomposition of the flow field into the resolved (large-scale) and unresolved (small-scale) components. From this decomposition, the coupled system of large and small-scale governing equations can be derived. In these models, small scales are explicitly simulated by solving the small-scale equations. In contrast to conventional LES technique where the major effort is concentrated on modeling subgrid scale terms, in the multiscale approaches the major effort is focused on modeling the small-scale velocity itself. This is acquired by decomposing the velocity field into large and

small-scale components.

The VMS proposed by Hughes [45, 46] and clarified by Collis [15] is a promising approach alternative for LES of turbulent flows. The basic idea of VMS, in contrast to traditional LES, is the use of variational projections instead of filtering, thus eliminating several difficulties of the traditional LES, e.g., commutation errors. VMS can be applied to complex flows with the use of the finite element method or discontinuous Galerkin methods [45].

In the RDT approach [63, 64, 65], the flow is decomposed into small (subgrid) and large (resolved) scales in the spirit of LES. In RDT, as in LES, the large and small scale quantities are defined by using a filter function. The large scale equations are obtained by filtering the Navier-Stokes equation and the small scale equations are obtained by subtracting filtered Navier-Stokes equations from full Navier-Stokes equations. The small scale equations are simplified by keeping only the terms involving the product of a large scale and a small scale component and modeling the terms involving the product of two small scale components by a turbulent viscosity [63, 64, 62]. This simplified form of the RDT has been successfully applied to 2D flows, which showed significant reduction of the computational time compared to DNS. However, its extension to non-homogenous flows with complex features is still an open question.

The DML method [24] is based on the study of attractors. The dimension of the attractor coincides with the estimates of the number of degrees of freedom of a turbulent flow [24]. In the DML methodology, the small scales are computed with less accuracy and are updated less often than in DNS simulation.

The TLS approach proposed by Kemenov and Menon [56, 57] uses a special large-scale function in lieu of filtering to separate the large scales from the small scales. This obviates many of the issues related to the filtering operation. From this scale separation, the TLS approach formally derives equations of motion that govern both

the large scale (LS) and the small scale (SS) from the original Navier-Stokes equations. Then, both LS and SS are explicitly simulated and coupled together. For computationally efficient implementation of the TLS approach the SS field is simulated on three one-dimensional (1D) orthogonal lines embedded within the LES three-dimensional (3D) grid. Past studies of decaying and forced isotropic turbulence [56], mixing layers [57] and fully developed channel flow [57] have shown that the baseline TLS model can capture important features of high-Re turbulent flows using relatively coarse grids under a wide range of conditions. Therefore, can be extended as a near-wall approach for LES.

1.3 Motivation and Objectives

Accurate modeling of the near-wall region constitutes the most difficult problem for LES. The maximum production of turbulent kinetic energy occurs in the inner layer, where very high resolution is needed to accurately predict the small but dynamically important eddies in the near-wall region. Most popular methods to overcome this problem very often fail to represent the correct near-wall dynamics where the two-way inner/outer layer interactions are present. The limitations of the near-wall LES models are understandable in light of the fact that all current models, either explicitly or implicitly, consider the inner layer in a Reynolds-averaged sense, and thus most near-wall fluctuations are suppressed. The major objective of this work is to propose a framework which does not suppress the near-wall fluctuations. In this thesis, a new hybrid model that combines a multiscale approach based on TLS [56, 57] in the inner region with conventional LES away from the wall is demonstrated. Some earlier attempts of applying the current approach to simulate non-homogeneous flows, such as canonical channel flows and channel flows with adverse pressure gradient, were reported elsewhere [38, 37, 36]. In particular, the following steps are considered major objectives of the present study:

(1) Development of a new multiscale model for wall-bounded flows at high Reynolds numbers

A new approach is presented here that uses TLS as a near-wall LES model in order to increase accuracy of the prediction of the near-wall turbulence. The proposed near-wall approach should be applicable to wide range of flows with and without adverse pressure gradients and to complex flows (e.g., flows with separation) at high Reynolds numbers without changing the model. Furthermore, the mathematical formulation has to be general. Moreover, the near-wall modeling procedure should be easily incorporated into a general purpose incompressible flow solver.

(2) Analysis of the TLS approach at high Reynolds number flows

Further understanding of the TLS approach is necessary in order to integrate TLS as a near-wall model for LES. In the TLS approach, the properties of the large scale function need to be clearly identified in order to lay the proper groundwork for the hybrid approach. The validity of the simplified 1D representation of the small-scale is an important issue to justify the TLS approach and needs to be addressed for high Re flows. Also the resolution requirement for the TLS approach has to be addressed.

(3) Development of a computational tool that accurately and reliably predict turbulent flows with generalized boundary conditions

The computational code should be efficient and accurate for unsteady turbulent simulations. Since LES and/or TLS of engineering flows in complex domains is of eventual interest, the accuracy of the finite differencing scheme needs to be carefully addressed. The code should be parallelisable for effective simulations of high Re flows. The computational code should be versatile. This means the ability of imposing a variety of boundary conditions, including inflow/outflow, wall boundary, separation, etc.

(4) Validation of the new approach for canonical wall-bounded turbulent flows at high Reynolds number

Fully-developed turbulent channel flow is an important reference test case for testing and developing numerical methods. There exist a wide range of experimental and numerical studies. Therefore, this test flow can be used to evaluate the behavior of the new approach for high Re.

(5) Investigation of the new approach for flows around complex geometries at high Reynolds number

Two different flow configurations are investigated in general; the flow in a channel with a converging-diverging section in the bottom wall and a flow in an asymmetric plane diffuser. These types of flow contain the complex phenomena with unsteady separation, re-attachment, wakes and vortex interactions. Turbulent flow in such a channel permits the examination of flow distortion due to the combined effects of the streamwise pressure gradient and the surface curvature, and therefore, offers a challenge for near-wall models. Furthermore, because of the equilibrium and non-equilibrium behavior of turbulence inside the diffuser, this flow presents a challenging test case for turbulence modeling approaches.

1.4 Outline

This thesis is organized as follows:

1. Chapter 2 introduces the governing equations, including LES and TLS equations for incompressible flows. Moreover, TLS approach in terms of the properties of the LS function and resolution is investigated. The SS model behavior is revisited for a DNS data set at high Re. Finally, the stand-alone SS integrations are performed.

2. Chapter 3 shows the formulation of the hybrid TLS-LES equations for wall-bounded flows and discusses the TLS-LES coupling strategies and the boundary condition treatments for the TLS regions.

3. Chapter 4 presents a background information on the numerical methods employed in developing a new code for numerical solution of LES and TLS approaches and explains the artificial compressibility approach and the spatial and temporal discretization with the dual-time stepping. Furthermore, this chapter presents the numerical results and the validation of the newly developed incompressible flow solver and examines the decaying isotropic turbulence, the turbulent channel flow, and the turbulent re-circulating flows for DNS, coarse-DNS, LES and TLS; and compares the results with those of the experimental data and those of other numerical methods when they are available.

4. Chapter 5 demonstrates the application of the current methodology to the well-developed turbulent channel flow at three Reynolds numbers to evaluate the capabilities of the current approach.

5. Chapter 6 demonstrates the application of the TLS-LES approach to study turbulent flow in a converging-diverging channel among with the full LES studies, and compares results of both with those of DNS.

6. Chapter 7 addresses flow through an asymmetric two-dimensional diffuser with separation, reattachment, and redevelopment using the TLS-LES model. The TLS-LES results are compared with the experimental measurements as well as the conventional LES results.

7. Chapter 8 contains concluding remarks.

8. Chapter 9 outlines possible directions for future research.

CHAPTER II

MATHEMATICAL FORMULATION

The multiscale characteristics of turbulence makes it difficult to simulate high-Re turbulent flows numerically using DNS where the resolution requirement scales as $O(Re^3)$. In order to reduce the cost of these simulations most numerical approaches rely on scale separation between the resolved and the unresolved scales. In the LES approach, the scale separation is achieved by a filtering function, whereas in the TLS approach, it is obtained by a special LS function. In order to lay the proper groundwork for the TLS-LES hybrid model to follow in subsequent chapters a brief introduction to LES and TLS approaches are given in the following sections.

The present chapter is organized as follows. A brief introduction to the Navier-Stokes equations is given in §2.1. The LES approach with its properties and closure models are discussed in detail in §2.2. The TLS approach is briefly discussed in §2.3. The SS model assumptions and their justifications for high Reynolds number flows are investigated in §2.3.2 by performing *a priori* analysis of a DNS data set of isotropic turbulence at Reynolds number of $Re_\lambda = 433$. The numerical approach for SS integration and investigation of LS and SS resolution effects are described in §2.3.3.

2.1 Navier-Stokes Equations

The equations governing the evolution of an incompressible Newtonian fluid are known as the Navier-Stokes equations. The final set of equations represents the

physical concepts of conservation of mass and momentum and can be written as:

$$\frac{\partial u_i}{\partial x_i} = 0 \tag{5}$$

$$\frac{\partial u_i}{\partial t} + \frac{\partial u_i u_j}{\partial x_j} = -\frac{1}{\rho}\frac{\partial p}{\partial x_i} + \nu \frac{\partial^2 u_i}{\partial x_j^2} \tag{6}$$

for $i = 1, 2, 3$. Here u_i denotes the velocity component in the x_i direction, ρ is the density, p is the pressure and ν is the kinematic viscosity $\nu = \mu/\rho$ where μ is the viscosity.

2.2 Large Eddy Simulation

In this section, a brief review of the conventional LES approach is given. For a more in depth discussion, the interested reader is referred to [75, 95, 102].

The LES governing equations are formally obtained by applying a spatial filter to the governing equations. The filtering operation essentially removes the high wave number contributions by acting as a low-pass filter. In the conventional LES, the filtered variable results from the convolution of a variable (e.g., u_i) with a filter kernel as:

$$\overline{u}_i(\mathbf{x}, t) = \int u_i(\mathbf{x}', t) G(\mathbf{x}, \mathbf{x}' : \overline{\Delta}) d\mathbf{x}' \tag{7}$$

The filter kernel, $G(\mathbf{x}, \mathbf{x}' : \overline{\Delta})$ is a weighting function whose support varies depending on the filter type and the filter width $\overline{\Delta}$. There are several filter kernels used in physical space, the most commonly used ones being the top-hat filter and the Gaussian filter. In the present study, the top-hat filter defined as

$$G(\mathbf{x} - \mathbf{x}') = \begin{cases} \frac{1}{\overline{\Delta}} & if \quad |\mathbf{x} - \mathbf{x}'| \leq \frac{\overline{\Delta}}{2} \\ 0 & otherwise \end{cases} \tag{8}$$

is used. The top-hat filtering corresponds to a local volume averaging in three-dimensional domain. One drawback of the top-hat filtering is that it requires full support in spectral space, as opposed to the spectral cut-off filter. Nevertheless, the

top-hat filter provides ease of implementation in implicit LES in which the numerical grid acts as the filter and does not require any explicit filtering.

In LES, filtering operation separates the turbulent velocity into a large-scale component which contains the energy and a sub-grid scale (sgs) or small-scale component, which contains the dissipation along with the unresolved energy. The sgs component, u_i', is defined from the Leonard decomposition as

$$u_i'(\mathbf{x}, t) = u_i(\mathbf{x}, t) - \overline{u}_i(\mathbf{x}, t) \tag{9}$$

which differs from the Reynolds decomposition in that the filtered value of the sgs is not zero:

$$\overline{u'} \neq 0 \tag{10}$$

Moreover, the LES filtered field is not idempotent:

$$\overline{\overline{u}} \neq \overline{u} \tag{11}$$

A typical one-component velocity signal (obtained from a DNS database, described later in Appendix A), u and its filtered version $\overline{u}$ are shown in Fig. 2. The top-hat filtering is used to obtain the filtered field. The subgrid component is obtained from the decomposition, Eq. (9). It is seen that subgrid component has much less kinetic energy than the filtered velocity, but contains all the short wave lengths, and therefore most of the gradients. As previously noted in Eq. (10) filtered subgrid component is not zero (see Fig. 2 (b)). The effect of the filtering operator can be further investigated by looking at the spectral distributions of the kinetic energy and derivatives stored in the filtered and sgs fields. The gradients occur at the small scales and hence appear at the higher wavenumbers, and therefore dissipation occurs primarily at the sgs scales. Therefore, what filtering operation does is to separate the velocity into a large-eddy component, which contains the most of the kinetic energy, and a sgs

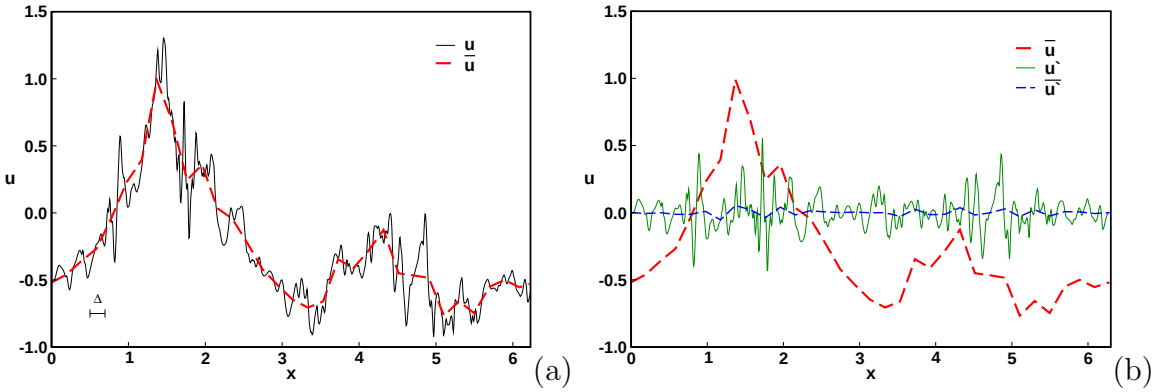

Figure 2: A typical turbulent velocity signal, u, obtained from a DNS data given at 1024 grid points and its filtered version $\overline{u}$. (a) Full and filtered velocity. The filtered variable is represented on 32 grid points using a top-hat filter, the filter width is plotted in the figure also. (b) Filtered velocity, as in (a), subgrid component, $u - \overline{u}$, and the filtered subgrid component $\overline{u'}$.

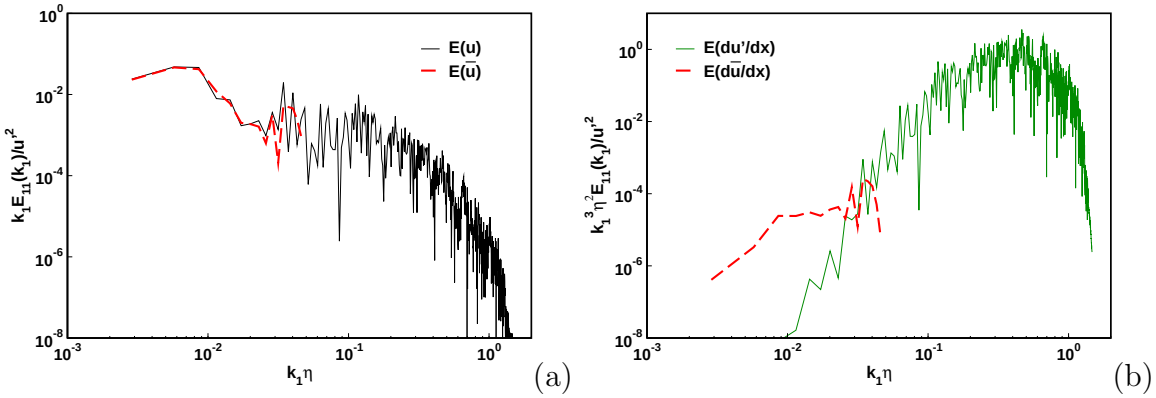

Figure 3: Premultiplied spectra of the filtered signal in Fig. 2 (a) Velocity, (b) Velocity gradients.

component containing most of the dissipation with the remaining unresolved kinetic energy (see Fig. 3).

The spatial filtering as defined above commutes with temporal derivatives in the governing equations

$$\begin{aligned}\overline{\frac{\partial u_i}{\partial t}} &= \int \frac{\partial u_i}{\partial t} G(\mathbf{x}, \mathbf{x}' : \overline{\Delta}) d\mathbf{x}' \\ &= \frac{\partial}{\partial t} \int u_i G(\mathbf{x}, \mathbf{x}' : \overline{\Delta}) d\mathbf{x}' \\ &= \frac{\partial \overline{u}_i}{\partial t} \end{aligned} \tag{12}$$

since the filtering function is independent of time. However, it does not commute with spatial derivatives in general since the kernel function G is a function of space. Thus,

$$\begin{aligned}\overline{\frac{\partial u_i}{\partial x_j}} &= \int \frac{\partial u_i}{\partial x_j} G(\mathbf{x}, \mathbf{x}' : \overline{\Delta}) d\mathbf{x}' \\ &= \int \frac{\partial}{\partial x_j} \big(u_i G(\mathbf{x}, \mathbf{x}' : \overline{\Delta}) \big) d\mathbf{x}' - \int u_i \frac{\partial G(\mathbf{x}, \mathbf{x}' : \overline{\Delta})}{\partial x_j} d\mathbf{x}' \\ &= \frac{\partial}{\partial x_j} \int u_i G(\mathbf{x}, \mathbf{x}' : \overline{\Delta}) d\mathbf{x}' - \int u_i \frac{\partial G(\mathbf{x}, \mathbf{x}' : \overline{\Delta})}{\partial x_j} d\mathbf{x}' \\ &= \frac{\partial \overline{u}_i}{\partial x_j} - \int u_i \frac{\partial G(\mathbf{x}, \mathbf{x}' : \overline{\Delta})}{\partial x_j} d\mathbf{x}' \end{aligned} \tag{13}$$

For spatial derivatives this condition is only satisfied for homogeneous filters whose kernels are constant in physical space. The presence of the second term, the so-called commutation error term, indicates that the filtering function must be independent of the space for commutativity of the spatial derivatives [31]. This condition is barely satisfied for wall-bounded flows in which the spatial grid resolution varies near a wall [31]. In the present LES study, the commutation of the spatial derivatives is assumed to hold.

Applying the filtering operation to the incompressible Navier-Stokes equations and assuming that the filter commutes with differentiation, the general form of the

LES equations are obtained:

$$\frac{\partial \overline{u}_i}{\partial t} + \frac{\partial \overline{u}_i \overline{u}_j}{\partial x_j} = -\frac{1}{\rho}\frac{\partial \overline{p}}{\partial x_i} + \nu \frac{\partial^2 \overline{u}_i}{\partial x_j^2} - \frac{\partial \tau_{ij}^{sgs}}{\partial x_j} \tag{14}$$

$$\frac{\partial \overline{u}_i}{\partial x_i} = 0 \tag{15}$$

where, $\overline{u}_i$ is the filtered velocity and $\overline{p}$ is the filtered pressure. The effect of subgrid fluctuations appears as the sgs stress tensor

$$\tau_{ij}^{sgs} = \overline{u_i u_j} - \overline{u}_i \overline{u}_j \tag{16}$$

in the LES equations and has to be modeled. The sgs stress term (16) resulting from the filtering operation represents the effect of small-scale on the resolved scales in the form of additional stress. This term can be decomposed into its stresses using $u_i' = u_i - \overline{u}_i$, such that

$$\overline{u_i u_j} = \overline{(\bar{u}_i + u_i')(\bar{u}_j + u_j')} \tag{17}$$

$$= \overline{\bar{u}_i \bar{u}_j} + \overline{\bar{u}_i u_j'} + \overline{u_i' \bar{u}_j} + \overline{u_i' u_j'} \tag{18}$$

With this decomposition, the sgs stress tensor can be written in a triple decomposition form (known as the Leonard decomposition [67])

$$\tau_{ij}^{sgs} = L_{ij} + C_{ij} + R_{ij} \tag{19}$$

where

$$L_{ij} = \overline{\bar{u}_i \bar{u}_j} - \bar{u}_i \bar{u}_j \tag{20}$$

$$C_{ij} = \overline{\bar{u}_i u_j'} + \overline{u_i' \bar{u}_j} \tag{21}$$

$$R_{ij} = \overline{u_i' u_j'} \tag{22}$$

The term L_{ij} is the Leonard stress, which represents the interactions between the resolved scales, C_{ij} is the cross stress tensor which represents the interaction between resolved and unresolved scales, and R_{ij}, the sgs Reynolds stress, represents the interactions between the unresolved (small) scales.

The filtered Navier-Stokes equations should be invariant with respect to a Galilean transformation. It can be shown that τ_{ij}^{sgs}, $L_{ij}+C_{ij}$ and R_{ij} are Galilean invariant, but not necessarily L_{ij} or C_{ij}. If we add a constant term U_i to the turbulent field u_i, the transformed components v_i of the velocity are

$$v_i = u_i + U_i \tag{23}$$

$$\bar{v}_i = \bar{u}_i + U_i \tag{24}$$

$$v_i' = u_i' \tag{25}$$

Using this transformed velocity,

$$L_{ij}^* = \overline{\bar{v}_i\bar{v}_j} - \bar{v}_i\bar{v}_j = L_{ij} - U_i\overline{u_j'} - U_j\overline{u_i'} \tag{26}$$

$$C_{ij}^* = \overline{\bar{v}_i v_j'} + \overline{v_i'\bar{v}_j} = C_{ij} + U_i\overline{u_j'} + U_j\overline{u_i'} \tag{27}$$

$$R_{ij}^* = \overline{v_i'v_j'} = R_{ij} \tag{28}$$

It can be seen that $L_{ij}+C_{ij}$ is Galilean invariant, not L_{ij} and C_{ij}. Because of this, the sgs term is not often decomposed into these terms, and instead is directly modeled.

Representation of the sgs stress term in the form of Eq. (16) is the most common form where the nonlinear term in the momentum equation is given as $\bar{u}_i\bar{u}_j$. However, by looking at the terms in the LES equation (14), it can be seen that this term has a spectral support higher than the other terms since, in spectral space, multiplication has a double support. So, this formulation is inconsistent. In the filtered Navier-Stokes equation, there are supports from unresolved scales which are the double size of the applied filter, which alias back to the resolved part of the spectrum. In general, subgrid models can potentially offset this effect. However this condition rarely appears as a modeling constraint [28]. To eliminate this problem, there are studies that apply additional filter of the nonlinear term [19, 72]. This is called explicit filtering, where the subgrid stress term can be defined as:

$$\tau_{ij}^{sgs} = \overline{\overline{u}_i\overline{u}_j} - \overline{u}_i\overline{u}_j \tag{29}$$

Even though, this decomposition is consistent, this form of the stress is not Galilean invariant unless a spectral cut-off filter is used [115, 72]. In the present study, the top-hat filter is used as the filter function; therefore, the decomposition given by Eq. (29) will not be used.

2.2.1 Energy Transfer

The subgrid stress term appearing in the momentum equation affects the transfer of energy between the resolved and unresolved scales. In order to justify this, the kinetic energy of the resolved field can be obtained by multiplying Eq. (14) by $\overline{u}_i$ and defining the kinetic energy of the resolved field $\overline{q}^2 = \overline{u}_i\overline{u}_i/2$ as:

$$\frac{\partial \overline{q}^2}{\partial t} + \frac{\partial \overline{q}^2 \overline{u}_j}{\partial x_j} = \frac{\partial}{\partial x_j}\big(- \overline{pu}_j + \nu \frac{\partial \overline{q}^2}{\partial x_j} - \tau_{ij}^{sgs}\overline{u}_i\big) - \nu \frac{\partial \overline{u}_i}{\partial x_j}\frac{\partial \overline{u}_i}{\partial x_j} + \tau_{ij}^{sgs}\frac{\partial \overline{u}_i}{\partial x_j} \tag{30}$$

The first term appearing on the right hand side is in the divergence form, and thus it conserves $\overline{q}^2$. The second term on the right hand side is the viscous dissipation of the resolved scale energy ,which is typically very small in high Re flows. The last term contains interactions between sgs stress tensor and the filtered velocity field, and describes the energy transfer between the two. This term can be either negative, corresponding to the transfer of energy from the resolved scales (forwardscatter) or positive representing the transfer of energy to the resolved scales (backscatter). On average this transfer is negative [102]. However, backscatter can also contribute to the energy transfer locally in space and time. This last term is commonly referred to as the sgs dissipation. Using the fact that τ_{ij}^{sgs} is a symmetric tensor, the subgrid dissipation can be written as

$$\varepsilon_{sgs} = -\tau_{ij}^{sgs}\frac{\partial \overline{u}_i}{\partial x_j} = -\tau_{ij}^{sgs}\overline{S}_{ij} \tag{31}$$

where $\overline{S}_{ij}$ is the resolved rate of strain tensor

$$\overline{S}_{ij} = \frac{1}{2}\left(\frac{\partial \overline{u}_i}{\partial x_j} + \frac{\partial \overline{u}_j}{\partial x_i}\right) \tag{32}$$

It should be noted that, the sgs stress tensor affects the transfer of both momentum and resolved scale kinetic energy, thus models for τ_{ij}^{sgs} should ideally predict both effects accurately.

2.2.2 Subgrid Modeling

While there are many possibilities for modeling of τ_{ij}^{sgs}, the most common method is to assume the following form

$$\tau_{ij}^{sgs} - \frac{\tau_{kk}}{3}\delta_{ij} = -2\nu_t \overline{S}_{ij} \tag{33}$$

where ν_t is the eddy viscosity (which needs to be determined) and $\overline{S}_{ij}$ is the resolved strain rate (32) with zero trace. Only the deviatoric (or anisotropic) part of the subgrid stress needs to be modeled. The isotropic part $(\tau_{kk}/3)\delta_{ij}$ is usually absorbed into a modified pressure.

This relation (33) implies that there is a perfect correlation between the sgs stress and the resolved rate-of-strain, whereas *a priori* studies of DNS show that the correlation is rather low [75]. Similarly this relation implies that sgs dissipation $\varepsilon_{sgs} = 2\nu_t \overline{S}_{ij}\overline{S}_{ij} \geq 0$, and hence the possibility of backscattering is excluded for positive ν_t.

2.2.3 The Smagorinsky Model

One of the primary approaches to determine the eddy viscosity was introduced by Smagorinsky [109], as

$$\nu_\tau = C_s \overline{\Delta}^2 |S|, \quad |S| = 2(\overline{S}_{ij}\overline{S}_{ij})^{1/2} \tag{34}$$

Here, C_s is the Smagorinsky coefficient and $\overline{\Delta}$ is the filter width ,which is computed as:

$$\overline{\Delta} = (\Delta x_1 \Delta x_2 \Delta x_3)^{1/3} \tag{35}$$

For isotropic turbulence, the model coefficient is determined to be $C_s = 0.16$ from the equilibrium assumption where the energy transfer is equal to the viscous dissipation

[95]. However, for different type of flows, such as in the presence of mean shear, solid boundaries or in transitional flows, this value produces too much dissipation [90]. One *ad hoc* modification is to reduce C_s in such situations. Another way is to determine the model coefficients dynamically. This will be explained in the next section.

2.2.3.1 The Dynamic Procedure

The dynamic approach by Germano [28] is based on estimating C_s directly from the resolved velocity field. Recall that applying a filtering operator to the Navier-Stokes equations at filter width $\overline{\Delta}$ yields an evolution equation for the filtered velocity field $\overline{u}_i$ with the sgs tensor τ_{ij}^{sgs}. Similarly, filtering a second time at filter width $\widehat{\overline{\Delta}}$ yields an equation for $\widehat{\overline{u}_i}$ with the residual stress tensor

$$T_{ij} = \widehat{\overline{u_i u_j}} - \widehat{\overline{u}_i}\widehat{\overline{u}_j} \tag{36}$$

Using the Germano identity [28], the relation between the two stress tensors can be written as

$$L_{ij} = \widehat{\overline{u}_i \overline{u}_j} - \widehat{\overline{u}_i}\widehat{\overline{u}_j} = T_{ij} - \widehat{\tau_{ij}^{sgs}} \tag{37}$$

The key point here is that L_{ij} can be expressed entirely using the LES resolved field. Assuming that both stresses T_{ij}, and τ_{ij}^{sgs} are modeled using the same underlying approach with the same value of the model coefficient, then one can use the Germano identity to compute C_s. Here, it is assumed that, there are some similarities between different length scales [75], which can be true if both filter widths are within the inertial subrange.

Applying the Smagorinsky model for both stresses

$$\tau_{ij}^{sgs} - \frac{\tau_{kk}^{sgs}}{3}\delta_{ij} = -2C_s\overline{\Delta}^2|\overline{S}|\overline{S}_{ij} \tag{38}$$

$$T_{ij} - \frac{T_{kk}}{3}\delta_{ij} = -2C_s\widehat{\overline{\Delta}}^2|\widehat{\overline{S}}|\widehat{\overline{S}_{ij}} \tag{39}$$

Substituting these into the Germano identity, the deviatoric part of the stress (L_{ij}^d)

can be obtained as

$$L_{ij}^{d} - \frac{L_{kk}}{3}\delta_{ij} = 2C_s\widehat{\overline{\Delta}^2|\overline{S}|\overline{S}_{ij}} - 2C_s\widehat{\overline{\Delta}}^2|\widehat{\overline{S}}|\widehat{\overline{S}_{ij}} \tag{40}$$

By assuming constant filter width and a non-spatial variation of the constant (which is strictly invalid) $C\overline{\Delta}^2$ can be taken outside of the test filtering which yields

$$L_{ij}^{d} - C_s M_{ij} = 0, \quad M_{ij} = 2\overline{\Delta}^2\widehat{|\overline{S}|\overline{S}_{ij}} - 2\widehat{\overline{\Delta}}^2|\widehat{\overline{S}}|\widehat{\overline{S}_{ij}} \tag{41}$$

Here, C_s can be determined by minimizing the mean square error [70]

$$\left\langle \epsilon^2 \right\rangle = \left\langle (L_{ij}^{d} - C_s M_{ij})^2 \right\rangle = \left\langle L_{ij}^{d} L_{ij}^{d} \right\rangle - 2C_s \left\langle L_{ij}^{d} M_{ij} \right\rangle + C^2 \left\langle M_{ij} M_{ij} \right\rangle \tag{42}$$

where $\langle . \rangle$ represents the average over homogeneous directions. The minimum can be found by setting $\partial \left\langle \epsilon^2 \right\rangle / \partial C_s = 0$ which yields

$$C_s = \frac{\left\langle L_{ij}^{d} M_{ij} \right\rangle}{\left\langle M_{ij} M_{ij} \right\rangle} \tag{43}$$

In most of the studies, test filter width is taken as twice of the filter width $\widehat{\overline{\Delta}} = 2\overline{\Delta}$.

Dynamic Smagorinsky model has been widely used in many flows and has shown accurate results in most cases. However, the dynamic approach requires at least one homogeneous direction since the denominator of the Eq. (43) will be ill-conditioned without some algorithmic adjustment (e.g., spatial averaging in a homogeneous direction [28, 81]).

2.2.4 The One Equation Model

Another approach to determine the eddy viscosity is based on the sgs kinetic energy

$$k^{sgs} = \frac{1}{2}\left(\overline{u_k u_k} - \overline{u}_k \overline{u}_k\right) \tag{44}$$

where the eddy viscosity can be expressed as follows:

$$\nu_t = C_\nu \overline{\Delta} (k^{sgs})^{1/2} \tag{45}$$

where C_ν is the model coefficient that needs to be determined, and $\overline{\Delta}$ is the filter width.

The sgs kinetic energy is obtained by the following transport equation [77, 106]

$$\frac{\partial k^{sgs}}{\partial t} + \frac{\partial}{\partial x_i}\left(\overline{u}_i k^{sgs}\right) = P^{sgs} - D^{sgs} + \frac{\partial}{\partial x_i}\left(\nu_t \frac{\partial k^{sgs}}{\partial x_i}\right) \tag{46}$$

Here, the three terms on the right-hand side represent the production, the dissipation, and the diffusion of k^{sgs}, respectively. The production term is defined as,

$$P^{sgs} = -\tau_{ij}^{sgs}\left(\frac{\partial \overline{u}_i}{\partial x_j}\right) \tag{47}$$

where τ_{ij}^{sgs} is the sgs tensor which is modeled as [106, 122]

$$\tau_{ij}^{sgs} = -2\nu_t \overline{S}_{ij} + \frac{2}{3} k^{sgs} \delta_{ij} \tag{48}$$

The dissipation term is usually modeled as [106, 122]

$$D^{sgs} = C_\epsilon \frac{(k^{sgs})^{3/2}}{\overline{\Delta}} \tag{49}$$

where $\overline{S}_{ij}$ is the resolved scale strain rate tensor (Eq. (32)) and C_ϵ is another coefficient that needs to determined either from turbulence theory or from the dynamic approach.

2.2.4.1 The Localized Dynamic Procedure

The coefficients C_ν and C_ϵ can be evaluated based on the turbulence theory as $C_\nu = 0.067$ and $C_\epsilon = 0.916$ or adjusted dynamically as part of the solution using a localized dynamic procedure for the subgrid kinetic energy (LDKM) [76, 60]. In the current study, the latter approach is followed where these coefficients are obtained using a scale similarity model. Although the details of the LDKM are given elsewhere [76, 60], for completeness, the key features of the model are summarized here.

The dynamic calculation of the model coefficients C_ν and C_ϵ requires specification of test filter field which is analogous to the dynamic approach explained previously

(see §1.1). However, it should be noted that the LDKM approach differs significantly from the classical dynamic model.

Experimental free jet studies by Liu *et al.*[71], suggested that the subgrid stress τ_{ij}^{sgs} at the grid filter level $\overline{\Delta}$ and the Leonard's stress L_{ij} at the test filter level $\widehat{\Delta}(=2\overline{\Delta})$ are self-similar and simple model $\tau_{ij}^{sgs} = C_L L_{ij}$ was proposed. In the LDKM approach, this scale similarity assumption is used to obtain the model coefficients dynamically.

The test scale Leonard stress is

$$L_{ij} = \widehat{\overline{u}_i \overline{u}_j} - \widehat{\overline{u}}_i \widehat{\overline{u}}_j \tag{50}$$

In the LDKM, the test filter level kinetic energy can be defined from the trace of the Leonard stress Eqn. (50)

$$k_{test} = \frac{1}{2}\left(\widehat{\overline{u}_k \overline{u}_k} - \widehat{\overline{u}}_k \widehat{\overline{u}}_k\right) \tag{51}$$

Here, k_{test} is fully resolved at the test filter level. The scale similarity $\tau_{ij}^{sgs} = C_L L_{ij}$ is extended to the test filter level so that:

$$L_{ij} = -2C_\nu \sqrt{k_{test}}\,\widehat{\Delta}\,\widehat{\overline{S}_{ij}} + \frac{1}{3} L_{kk}\delta_{ij} \tag{52}$$

In Eqn. (52) the only unknown is C_ν. The model coefficient C_ν is again obtained using the least square method:

$$C_\nu = \frac{1}{2}\frac{L_{ij}M_{ij}}{M_{ij}M_{ij}} \tag{53}$$

where

$$M_{ij} = -\widehat{\Delta}\sqrt{k_{test}}\,\widehat{\overline{S}_{ij}} \tag{54}$$

Note that M_{ij} is determined completely from the test filtered quantities.

A similar approach is used to obtain the dissipation coefficient C_ε such that

$$C_\epsilon = \frac{(\nu+\nu_\tau)\widehat{\Delta}[(\partial\overline{u}_i/\partial\widehat{x_j})(\widehat{\partial\overline{u}_i/\partial x_j}) - (\partial\widehat{\overline{u}_i}/\partial x_j)(\partial\widehat{\overline{u}_i}/\partial x_j)]}{k_{test}^{3/2}} \tag{55}$$

Since the denominator of Eqn. (52) and (55) are well defined and non zero at the test filter level, the ill-conditioning problem associated with the Germano's identity is relieved.

2.2.4.2 Realizability conditions

Upper limit for the model coefficient C_ν can be obtained from the realizability conditions [107, 116].

$$\begin{aligned}
\tau_{11}^{sgs} &\geq 0 \\
\tau_{22}^{sgs} &\geq 0 \\
\tau_{33}^{sgs} &\geq 0 \\
|\tau_{12}^{sgs}|^2 &\leq \tau_{11}^{sgs}\tau_{22}^{sgs} \\
|\tau_{13}^{sgs}|^2 &\leq \tau_{11}^{sgs}\tau_{33}^{sgs} \\
|\tau_{23}^{sgs}|^2 &\leq \tau_{22}^{sgs}\tau_{33}^{sgs} \\
det(\tau_{ij}^{sgs}) &\leq 0
\end{aligned} \tag{56}$$

A new condition can be written as

$$|\tau_{12}^{sgs}|^2 + |\tau_{13}^{sgs}|^2 + |\tau_{23}^{sgs}|^2 \leq \tau_{11}^{sgs}\tau_{22}^{sgs} + \tau_{11}^{sgs}\tau_{33}^{sgs} + \tau_{22}^{sgs}\tau_{33}^{sgs} \tag{57}$$

Noting that $\tau_{ij}^{sgs} = 2\nu_t(\overline{S}_{ij}) + 2/3k^{sgs}\delta_{ij}$

$$\begin{aligned}
(2\nu_t)^2(\overline{S}_{12}^2 + \overline{S}_{13}^2 + \overline{S}_{23}^2) &\leq (2\nu_t)^2\big(\overline{S}_{11}\overline{S}_{22} + \overline{S}_{11}\overline{S}_{33} + \overline{S}_{22}\overline{S}_{33}\big) \\
&+ \frac{4}{3}(k^{sgs}2\nu_t)(\overline{S}_{11} + \overline{S}_{22} + \overline{S}_{33}) \\
&+ 3\frac{4}{3}k^{sgs2}
\end{aligned} \tag{58}$$

The flow is divergence free, hence the second term on the right hand side is zero. The first term can be re-expressed as:

$$\overline{S}_{11}\overline{S}_{22} + \overline{S}_{11}\overline{S}_{33} + \overline{S}_{22}\overline{S}_{33} = \frac{1}{2}(\overline{S}_{11} + \overline{S}_{22} + \overline{S}_{33})^2 - \frac{1}{2}(\overline{S}_{11}^2 + \overline{S}_{22}^2 + \overline{S}_{33}^2) \tag{59}$$

The first term on the right hand side is zero also. From this the inequality can be written as:

$$(\nu_t)^2\big(\overline{S}_{12}^2+\overline{S}_{13}^2+\overline{S}_{23}^2+\frac{1}{2}(\overline{S}_{11}^2+\overline{S}_{22}^2+\overline{S}_{33}^2)\big)\leq\frac{1}{3}k^{sgs2} \tag{60}$$

From this condition, the upper limit for C_ν can be obtained as

$$C_\nu\leq\frac{\sqrt{k^{sgs}}}{\sqrt{3}\sqrt{S}\Delta} \tag{61}$$

where S is defined as:

$$S=\frac{1}{2}\big(\overline{S}_{ij}\big)\big(\overline{S}_{ij}\big). \tag{62}$$

2.3 Two-Level Simulation Approach

This section provides a brief review of the TLS approach as presented in Kemenov and Menon [56, 57].

The TLS approach has recently been described by Kemenov and Menon [56, 57] as a novel approach that utilizes a special scale separation in lieu of spatial filtering that is commonly done in LES. The TLS approach provides a different perspective on turbulence modeling in which small-scales are calculated using a small-scale simulation model instead of modeling the effect of small-scale on the large-scales.

In the TLS approach, the velocity field is decomposed into large-scale (LS) and small-scale (SS) components using a special LS function [56]. TLS introduces this two-scale decomposition into the Navier-Stokes equations and derives the exact equations for each range of scales. In the TLS approach, the three-dimensional SS equations are simplified and constructed on three orthogonal one-dimensional (1D) lines embedded in a three-dimensional (3D) domain. This simplification drastically reduces the computational time required for SS calculations while retaining full coupling between the LS and SS fields. The validity of this simplified 1D representation of the SS is an important issue to justify the TLS approach. This consideration motivates us to perform an *a priori* analysis on a flow with a Re as high as possible to obtain some ideas on appropriateness of the model assumptions.

TLS model assumptions needed to reduce the 3D SS governing equations onto the 1D domain were evaluated earlier by Kemenov and Menon [56, 57], who used both *a priori* and *a posteriori* test for homogeneous and in-homogeneous flows. Previous analyses were based on a Reynolds number of $Re_\lambda = 140$ (based on the Taylor length scale) for homogeneous turbulence [56] and $Re_\tau = 640$ (based on the friction velocity) for non-homogeneous wall-bounded turbulence [57]. The purpose of the study discussed in here is to revisit the simplifying model assumptions for higher Re. Thus, this study conducts *a priori* tests using the DNS data set of homogeneous forced isotropic turbulence at a Reynolds number of $Re_\lambda = 433$, which is available at the John Hopkins University (JHU) database (http://turbulence.pha.jhu.edu). Details of the database are given in Appendix A.

2.3.1 Two-scale Decomposition

The TLS approach begins with the definition of a LS function ($\mathcal{F}^L$), which can be defined in various forms. Some examples are presented in detail by Kemenov and Menon [56]. Hereafter, any quantity that belongs to the LS function is denoted by superscript L. From this LS field ($\mathcal{F}^L$), the SS field can be obtained ($\mathcal{F}^S$). The LS and SS fields are complements and together form the total field.

In TLS, scale separation is obtained via a LS function leading to

$$u_i(\mathbf{x},t) = u_i^L(\mathbf{x},t) + u_i^S(\mathbf{x},t) \tag{63}$$

with

$$u_i^L(\mathbf{x},t) = \mathcal{L}^\Delta u_i(\mathbf{x},t) = \mathcal{I}^\Delta \circ \mathcal{S}^\Delta[u_i(\mathbf{x},t)] \tag{64}$$

$$\mathcal{S}^\Delta : u_i(\mathbf{x},t) \rightarrow u_i^L(\mathbf{x}_k,t) \tag{65}$$

$$I^\Delta : u_i^L(\mathbf{x}_k,t) \rightarrow u_i^L(\mathbf{x},t) \tag{66}$$

$$\mathbf{x}_k \in G^\triangle \equiv \{\mathbf{x_1},\ldots,\mathbf{x_N}\} \subset \Omega \tag{67}$$

where operator $\mathcal{L}^\triangle$ consists of the sequential application of a local averaging operator

$\mathcal{S}^{\Delta}$ and an interpolation operator $\mathcal{I}^{\Delta}$ [56, 57]. Applying the local averaging operator on $u_i(\mathbf{x}, t)$ yields a large-scale variable $u_i^L(\mathbf{x}_k, t)$, defined at the degrees of freedom of the large scale grid, which is then interpolated in order to obtain a continuous large scale field $u_i^L(\mathbf{x}, t)$. The corresponding SS field can be obtained from the following decomposition:

$$u_i^S(x,t) = u_i(x,t) - u_i^L(x,t) \tag{68}$$

This decomposition appears analogous to the Reynolds decomposition. However, important differences are that $u^L(x,t)$ is a space and time dependent field and that the averaged (or operated) SS field is not zero:

$$(u^S)^L \neq 0 \tag{69}$$

which can be expressed as the LS part of any SS quantity that is not zero. Also, the SS part of any LS quantity is not zero:

$$(u^L)^S \neq 0 \tag{70}$$

Furthermore, the products always have non-zero LS and SS parts:

$$(u^L u^L)^S \neq 0, \quad (u^S u^S)^L \neq 0 \tag{71}$$

Moreover, the LS operator is not idempotent:

$$(u^L)^L \neq u^L \tag{72}$$

The two-scale decomposition is illustrated in Figs. 4 (a) and (b) for two uncorrelated signals obtained from the DNS database. Here, it should be noted that these one-dimensional fields are just a one-dimensional cut of the exact fully resolved three-dimensional flow field obtained from the DNS data and represented with DNS_{1D}, hereafter. Fully resolved DNS_{1D} data are given on the 1024 grid, and for these examples, the LS fields are explicitly computed on 32 uniformly-spaced grids.

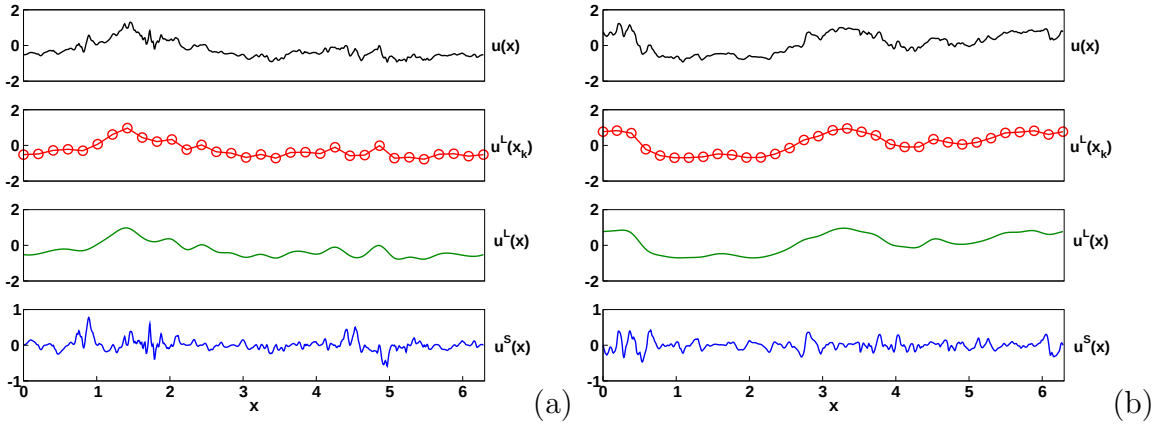

Figure 4: Application of the TLS scale separation operator for a 1D problem in physical space. Fully resolved signals (black) obtained from a 1024^3 DNS of the isotropic turbulence study at $Re_\lambda = 433$. The LS field (red) represented on a 32 grid point, is truncated from the fully resolved signal using the averaging operator ($u^L(x_k) = \mathcal{S}^\Delta[u(x)]$). The LS field (green) represented on the SS grid (1024 grid point) is obtained using the interpolation operator ($u^L(x) = \mathcal{I}^\Delta[u^L(x_k)]$). The SS field (blue) represented on a 1024 grid point is obtained by subtracting the LS field from the fully resolved field ($u^S(x) = u(x) - u^L(x)$).

Here, operator $\mathcal{S}^\Delta$ is the sampling operator (i.e., $u^L(\mathbf{x}_k) = u(x_k)$), and operator $\mathcal{I}^\Delta$ is chosen to be the cubic spline interpolation. The SS fields are obtained from decomposition on the DNS grid. Here, it can be seen that both the LS and SS fields differ for the two signals.

The LS quantity given by (64) is unique for a fixed averaging $\mathcal{S}^\Delta$ and the interpolation $\mathcal{I}^\Delta$. These two degrees of freedom in TLS are similar to traditional LES filtering since the filtered field is also defined uniquely when two parameters, the specific filter function G and the filter width $\overline{\triangle}$, are fixed.

The $\mathcal{S}^\Delta$ operator can be defined in several ways. Specifically, the definition of the discrete LS value depends on the LS grid $G^\triangle$ and the algorithm. The simplest way would be the sampling operator in which the LS velocity is defined as the velocity values of the nodes of the $G^\triangle$, e.g., $u^L(\mathbf{x}_k) = u(x_k)$. The LS operator $\mathcal{S}^\Delta$ can also be defined in more general fashion as an averaging over lines or volumes (in three-dimensional domains).

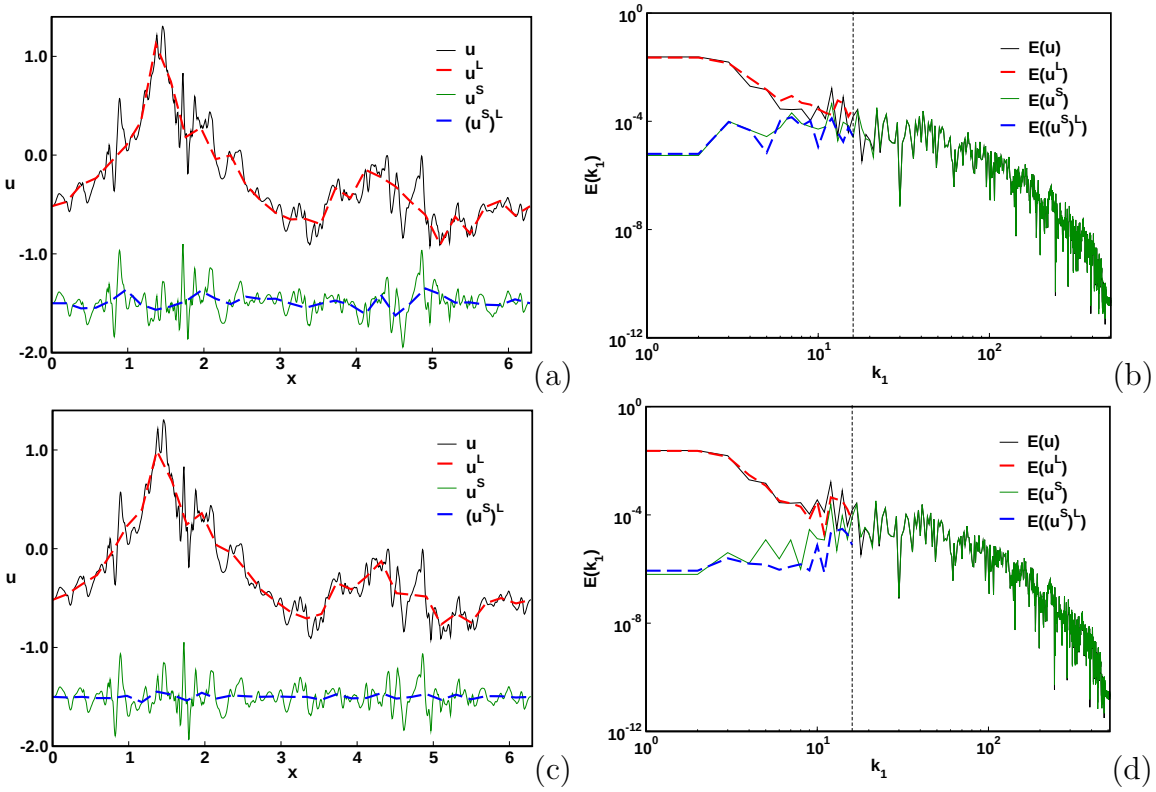

Figure 5: Application of the TLS scale separation for a 1D problem. The LS field is represented on the LS grid using (a,b) sampling approach; (c,d) averaging approach. The LS grid resolution is shown by dotted vertical line. The SS velocity profiles are shifted downwards by -1.5.

The effect of the LS averaging operator (64) is studied for a one-dimensional signal obtained from the DNS database (shown in Fig. 5). In the first example (Figs. 5 (a) and (b)), operator $\mathcal{S}^{\Delta}$ is the sampling operator (i.e., $u^L(\mathbf{x}_k) = u(x_k)$), and in the second (Figs. 5 (c) and (d)), it is an averaging operator along the line at the LS grid cell (i.e.,$u^L(\mathbf{x}_k) = \int_{x-\Delta/2}^{x+\Delta/2} \frac{u(\xi)}{\Delta} d\xi$). In this definition, the length of the averaging window (Δ) is a parameter, but here, the length of the LS cell is used. It should be noted that the second definition of the LS field is similar to that of the filtered (LES) field if the filter function is specified as a top-hat filter, and the filter width is equal to the grid length. The LS fields follow the general trends of the DNS_{1D} field, but the small length scale fluctuations have been removed. They appear in the SS field $u^S(\mathbf{x}, t)$, which is also shown in Figs. 5 (a) and (c). As previously noted,

the LS part of the SS field is non-zero for both definitions of the LS operator. The spectral representations of the LS and SS fields are also shown in Figs. 5 (b) and (d). It is clear that the spectral content of the LS fields are also different. The sampling operator predicts higher energy at high wave numbers, and deviates from the DNS_{1D} spectrum, which appears as a higher spectral support at the low wave numbers for the SS field.

It is noted that both the TLS LS and LES filtered fields are the same if the sampling operator and the filtering operator is a top-hat filter. In this case, the sampling operator $\mathcal{S}^{\Delta}$ and box-filtering are similar. However, using the $\mathcal{S}^{\Delta}$ (64) is more versatile since it can allow non-uniform grids. In the case of box-filtering, the non-uniformity of the filter width can result in the commutativity error [30] that has to be modeled or ignored.

In the TLS approach, the LS and SS fields are uniquely defined for a fixed $\mathcal{S}^{\Delta}$ and $\mathcal{I}^{\Delta}$ operators. In the previous paragraphs, the effects of $\mathcal{S}^{\Delta}$ on the LS and SS fields are described. The effect of $\mathcal{I}^{\Delta}$ is now addressed. For this analysis, $\mathcal{I}^{\Delta}$ is chosen as the cubic spline interpolation. To justify the use of the cubic spline interpolation, the LS energy at the DNS grid after the interpolation ($E^{LSI} = E(u^L(x))$, denoted by superscript LSI) is quantified from the respective LS energy at the LS grid ($E^{LS} = E(u^L(x_k))$, denoted by superscript LS) using the L_2-norm e_0^E:

$$e_0^E = \frac{\|E^{LS} - E^{LSI}\|_0}{\|E^{LS}\|_0} \tag{73}$$

The error in the longitudinal energy ($e_0^{E_{uu}}$) is evaluated analogously. Table 1 shows

Table 1: The deviation from the LS energy for the longitudinal $e_0^{E_{uu}}$ and the total e_0^E energy according to (73) for the linear and cubic spline interpolation methods.

	Longitudinal Energy ($e_0^{E_{uu}}$)	Total Energy (e_0^E)
Cubic Spline Interpolation	1.10%	0.84%
Linear Interpolation	6.12%	4.50%

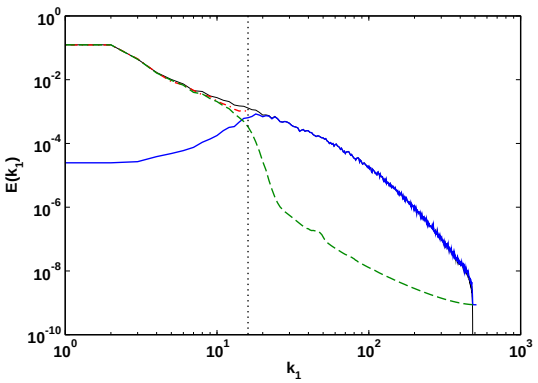

Figure 6: The averaged energy spectra for the lines obtained from the DNS data. SS energy is represented by the solid line, LS energy at the LS grid by the dotted dashed line, LS energy at the SS grid by the dashed line, and total DNS energy by the thin solid line. The LS grid resolution is represented by the dotted vertical line.

the L_2-norm of the deviation of the LS energy at the DNS grid after the interpolation E^{LSI} from the LS energy at the LS grid E^{LS}. A first-order approximation (linear interpolation) introduces a large error in combination with a relatively coarse LS resolution. Higher order interpolation method is considerably closer to the LS energy. Clearly the choice of the LS grid can also play a role in minimizing the error.

The SS field that complements the LS field is obtained from decomposition on the DNS grid. To support this, the spectral representation of the LS and SS fields are investigated and compared with the total DNS field (see Fig. 6). Here, the energy spectrum is obtained by averaging over 250 lines obtained from the DNS database. In spectral space, LS energy in the SS grid decays quickly beyond the maximal grid resolvable mode (shown as a dotted dashed line in the figure). Here, the SS field dominates dynamically relative to the LS field. This figure shows that in spectral space, the SS field complements the LS field.

Following the TLS decomposition (63), the coupled LS and SS equations given for

incompressible flows are (see Kemenov and Menon [56] for more details)

$$\frac{\partial u_i^L}{\partial t} + \frac{\partial}{\partial x_j}(u_i^L + u_i^S)(u_j^L + u_j^S) = -\frac{\partial p^L}{\partial x_i} + \nu \frac{\partial^2 u_i^L}{\partial x_j^2} + F_i^S \tag{74}$$

$$\frac{\partial u_i^S}{\partial t} + \frac{\partial}{\partial x_j}(u_i^L + u_i^S)(u_j^L + u_j^S) = -\frac{\partial p^S}{\partial x_i} + \nu \frac{\partial^2 u_i^S}{\partial x_j^2} + F_i^L \tag{75}$$

where the forcing terms on the right-hand sides are given as

$$F_i^L = \frac{\partial}{\partial x_j}\big[(u_i^L + u_i^S)(u_j^L + u_j^S)\big]^L \tag{76}$$

$$F_i^S = \frac{\partial}{\partial x_j}\big[(u_i^L + u_i^S)(u_j^L + u_j^S)\big]^S \tag{77}$$

The LS and SS fields are coupled through the forcing terms F_i^S and F_i^L, which explicitly depend only on the corresponding LS or SS fields and the non-linear product term [56]. Finally, the LS and SS continuity equations are

$$\frac{\partial u_i^L}{\partial x_i} = 0, \quad \frac{\partial u_i^S}{\partial x_i} = 0 \tag{78}$$

The coupled LS and SS Eqs. (74) and (75) along with the incompressibility constraint (78), supplied with the appropriate boundary conditions, completely define the evolution of the LS and SS fields in the TLS approach. However, solving the full TLS Eqs. ((74) and (75)) is equivalent to performing DNS, so, to reduce the overall cost of simulating the small-scale equations, additional simplifications of the SS field equations are needed. This requires modeling of some of the terms and this is addressed in the next section.

2.3.2 Treatment of Small-Scale Equations

In the TLS model, the small-scale field u_i^S is solved on three 1D lines embedded in the 3D LS domain. In principle, the orientation of these lines can be arbitrary, but in the present study, they are chosen to be orthogonal to each other and parallel to the corresponding LS coordinates. These three lines intersect at the LS grid node, as shown in Fig. 7. All three components of the velocity are represented on these 1D

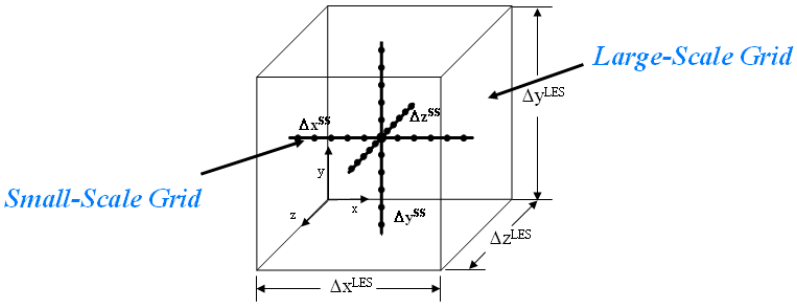

Figure 7: The 1D SS line arrangement within a 3D LS grid in the TLS model.

lines, leading to the following representation of the SS line velocity:

$$u_i^S(x,t) \rightarrow u_{i,l_k}^S(l_k,t), \quad x_n = \bigcap_{i=1}^{3} l_k, \quad k = 1,2,3 \tag{79}$$

Here, u_{i,l_k}^S can be viewed as a snapshot of the SS velocity field along line l_k.

In contrast to LES, the TLS LS equations do not need closure. The LS equations are closed if the SS field is known. However, the SS equations need closure when reduced to 1D lines. For a given line (e.g., $l_1 = \{x_1, x_2 = c_2, x_3 = c_3\}$, where c_2 and c_3 are constants), the first and second derivatives of the SS velocity in directions (l_2 and l_3) orthogonal to l_1 are unknown. Thus, all the derivatives in the orthogonal directions have to be modeled. However, the derivatives along the line can be computed as a part of the solution. Thus, for each SS velocity there is one known derivative (along a given line) and two unknown derivatives (orthogonal to a given line). For example, for the u^S component of the SS velocity $\partial u^S/\partial x_1$ is known, but SS derivatives $\partial u^S/\partial x_2$ and $\partial u^S/\partial x_3$ cannot be found on line l_1.

In the TLS approach, the unknown derivatives are modeled in terms of the known derivatives. From a physical point of view, one should expect local correlation between the SS derivatives in the orthogonal directions. It is known that turbulent flow is characterized by 3D elongated structures with intense vorticity and dissipation; thus if a line intersects such a 3D region, the SS derivatives should be locally high in all three directions inside the region and low outside the region. To express the

unknown (transverse) SS derivatives in terms of the known (longitudinal) derivatives, the following assumptions, proposed by Kemenov and Menon [56], are adopted:

(i) The SS second-order derivative along the line l_k is equal to the averaged sum of the SS second order derivatives along all three orthogonal directions:

$$\frac{\partial^2 u_i^S}{\partial x_k^2} = \frac{1}{3}\sum_j \frac{\partial^2 u_i^S}{\partial x_j^2}, \qquad i,k = 1,2,3 \tag{80}$$

(ii) The convective derivatives of the SS velocity are neglected in directions transverse ($j \neq k$) to the line l_k:

$$\frac{\partial}{\partial x_j}\Big[(u_j^S + u_j^L)(u_i^S + u_i^L)\Big]^S = \frac{\partial}{\partial x_j}\Big[(u_j^S(l_k) + u_j^L)(u_i^S(l_k) + u_i^L)\Big]^S \tag{81}$$

(iii) The SS pressure gradient $\partial p^S/\partial x_i$ is neglected. However, the incompressibility constraint is enforced for the LS velocity [56].

As a result, the SS Eq. (75) takes the following simplified form:

$$\frac{\partial u_i^S}{\partial t} + \frac{\partial}{\partial x_j}\Big(u_j^L + u_j^S(l_k)\Big)\Big(u_i^L + u_i^S(l_k)\Big) \;=\; 3\nu\frac{\partial^2 u_i^S}{\partial x_k^2} + F_i^L\Big(u_j^S(l_k), u_j^L\Big) \tag{82}$$

where

$$F_i^L\Big(u_j^S(l_k), u_j^L\Big) = \frac{\partial}{\partial x_j}\Big[\Big(u_j^L + u_j^S(l_k)\Big)\Big(u_i^L + u_i^S(l_k)\Big)\Big]^L \tag{83}$$

Note that k is a free index and refers to line l_k, which is parallel to the corresponding coordinate x_k ($k = 1,2,3$).

For example, the TLS SS Eq. (82) along l_1 lines (which are parallel to the x coordinate) yields the following equations for the u^S component:

$$\begin{aligned}\frac{\partial u^S}{\partial t} \;+\; & \frac{\partial}{\partial x}\Big(u^L + u^S(l_1)\Big)\Big(u^L + u^S(l_1)\Big) + \frac{\partial}{\partial y}\Big(v^L + v^S(l_1)\Big)\Big(u^L + u^S(l_1)\Big) \\ +\; & \frac{\partial}{\partial z}\Big(w^L + w^S(l_1)\Big)\Big(u^L + u^S(l_1)\Big) = 3\nu\frac{\partial^2 u^S}{\partial x_1^2} \\ +\; & F_u^L\Big(v^S(l_1), w^S(l_1), v^L, w^L\Big)\end{aligned} \tag{84}$$

for the v^S component:

$$\begin{aligned}\frac{\partial v^S}{\partial t} &+ \frac{\partial}{\partial x}\Big(u^L + u^S(l_1)\Big)\Big(v^L + v^S(l_1)\Big) + \frac{\partial}{\partial y}\Big(v^L + v^S(l_1)\Big)\Big(v^L + v^S(l_1)\Big) \\ &+ \frac{\partial}{\partial z}\Big(w^L + w^S(l_1)\Big)\Big(v^L + v^S(l_1)\Big) = 3\nu\frac{\partial^2 v^S}{\partial x_1^2} \\ &+ F_v^L\Big(u^S(l_1), w^S(l_1), u^L, w^L\Big) \end{aligned} \tag{85}$$

and for the w^S component:

$$\begin{aligned}\frac{\partial w^S}{\partial t} &+ \frac{\partial}{\partial x}\Big(u^L + u^S(l_1)\Big)\Big(w^L + w^S(l_1)\Big) + \frac{\partial}{\partial y}\Big(v^L + v^S(l_1)\Big)\Big(w^L + w^S(l_1)\Big) \\ &+ \frac{\partial}{\partial z}\Big(w^L + w^S(l_1)\Big)\Big(w^L + w^S(l_1)\Big) = 3\nu\frac{\partial^2 w^S}{\partial x_1^2} \\ &+ F_w^L\Big(u^S(l_1), v^S(l_1), u^L, v^L\Big) \end{aligned} \tag{86}$$

Here, the validity of the SS model assumptions is evaluated. The model assumptions (i) and (ii) are evaluated using an *a priori* study of a DNS data set at $Re_\lambda = 433$. Although the DNS data set is given on a box of 1024^3 grid points, only a set of randomly chosen 250 grid lines along the x direction is used for the current analysis. Since the field is forced isotropic, lines in the other directions should result in the same statistics. The LS velocity field is obtained using the averaging operator, the length of which varies, depending on the LS resolution. Unless it is explicitly noted, for most of the analyses presented in this section, the LS velocity field is computed on the uniform 32 grid points distributed along the lines. Finally, the constructed LS field is interpolated back on the DNS grid using cubic spline interpolation, and then subtracted from the total DNS velocity field to obtain the SS velocity field.

For a given line, the derivative along the line direction is always known, so we will consider the differences between the SS derivative in a particular direction and the averaged sum of the SS derivatives in all three directions. In fact, the model assumption (i) can be expressed in terms of differences as $\mathcal{S}_{ik} = 0$, where

$$\mathcal{S}_{ik} = \frac{1}{3}\sum_{j=1}^{3}\frac{\partial^2 u_i^S}{\partial x_j^2} - \frac{\partial^2 u_i^S}{\partial x_k^2} \tag{87}$$

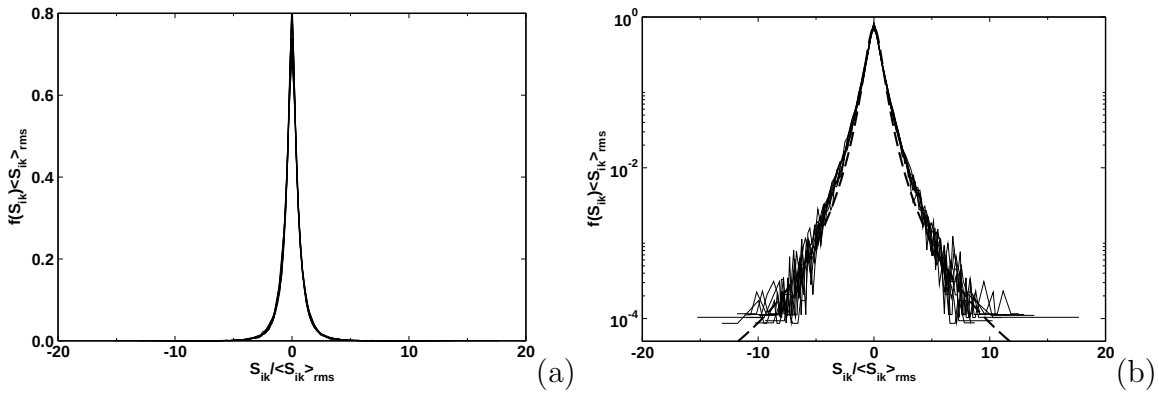

Figure 8: PDFs of the normalized differences of the second SS derivatives compared with the Tsallis distribution (dashed line): (a) in linear scale, (b) in logarithmic scale.

This is supported by Figs. 8 (a) and (b) where all nine $(i, k = 1, 2, 3)$ normalized probability density functions (PDF) of $\mathcal{S}_{ik}$ are shown in linear and logarithmic scales, respectively. All nine PDFs are collapsed and approximated quite well by the Tsallis distribution, which has the form

$$P_T(\xi) = \frac{1}{Z_q[1 + (1/2)\beta(q-1)\xi^2]^{1/(q-1)}} \tag{88}$$

where Z_q is a normalization constant. The Tsallis distribution has a variance 1 for $\beta = 2/(5-3q)$ and reduces to a Gaussian distribution as the $q \to 1$. Tsallis distribution has been used in the context of analyzing the turbulent flows [6]. Therefore, in principle, the distributions of the unknown derivatives of the SS velocity can be prescribed using a chosen Tsallis distributions and was investigated in the past [55]. However, it was also determined that the Tsallis distribution with the same parameters was not a good fit for the non-homogeneous flows as it was for the homogeneous flows [57]. Therefore, instead of modeling the unknown derivatives of the SS velocity with the Tsallis distribution, they are modeled as Eq. (80) in the TLS approach.

Even for this high Re turbulence data set, the most probable state of the modeled SS second derivative is at the origin $\mathcal{S}_{ik} = 0$, suggesting a universality of assumption [57]. The most probable state of the SS second derivative difference suggests that the SS derivatives are either small, as are the differences, or they are not small

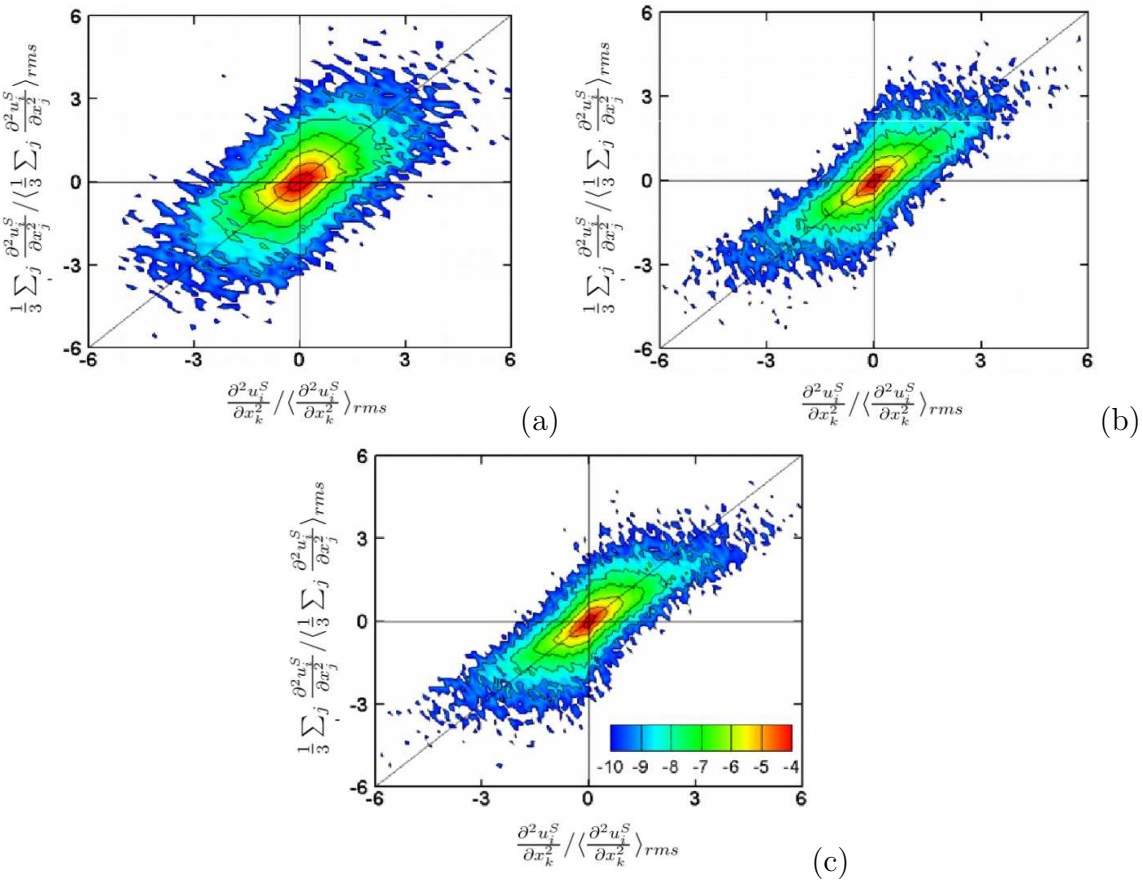

Figure 9: Contour plots of the logarithm of the joint PDF of the SS second derivative along the line l_k and the averaged sum of the SS second derivatives: (a) longitudinal velocity component ($i = k, i = 1, k = 1$), (b) transverse velocity component ($i \neq k, i = 1, k = 2$), (c) transverse velocity component ($i \neq k, i = 1, k = 3$).

but approximately equal. However, from the representation of the SS field through the decomposition, the SS derivatives should be relatively small everywhere except at the locally high gradient, intense turbulent regions, which is justified further by considering the joint PDFs of the SS second derivative along the line l_k, and the averaged sum of the all SS second derivatives (see Figs. 9 (a), (b) and (c)). The joint PDF exhibits a characteristic spike at the origin. Moreover, the probabilities exhibit positive correlations for the second derivative and the averaged sum, suggesting that events in which the second derivative is large in magnitude and has the same sign as the averaged sum are more probable.

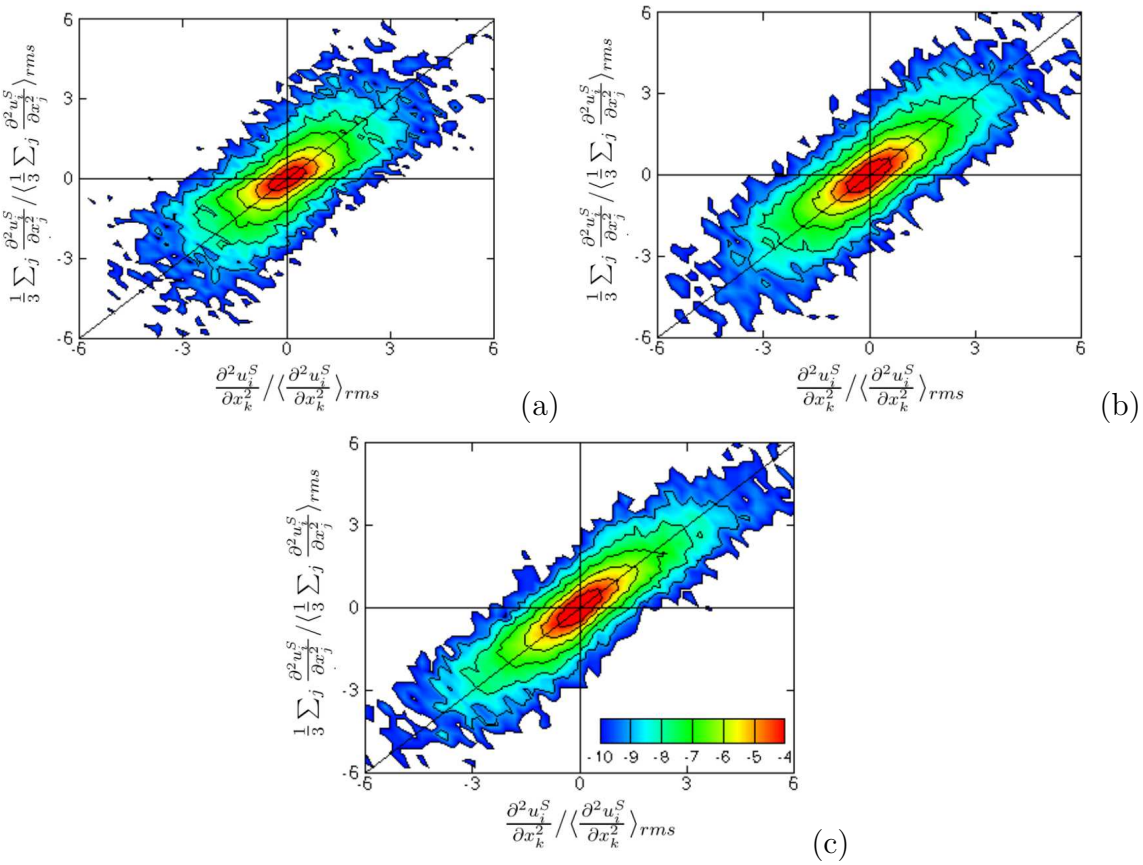

Figure 10: Contour plots of the logarithm of the joint PDF of the SS second derivative along the line l_k and the averaged sum of the SS second derivatives for longitudinal velocity component ($i = k, i = 1, k = 1$); (a) 128 LS grid resolution, (b) 256 LS grid resolution, (c) 512 LS grid resolution.

The bisector of the I and III quadrants corresponds to the model assumption, $\mathcal{S}_{ik} = 0$. These plots show positive correlations between the SS second derivative and the SS total derivatives, suggesting that events described by $S_{ik} = 0$ are highly probable. However, as the magnitude of the SS second derivative increases, the probability decreases, suggesting the presence of highly turbulent regions where the LS resolution becomes inadequate [56]. In order to justify the effect of the LS resolution on the assumptions of the SS model, the model assumption (i) are revisited for four different LS resolutions, as summarized in Table 2. The correlation coefficient is

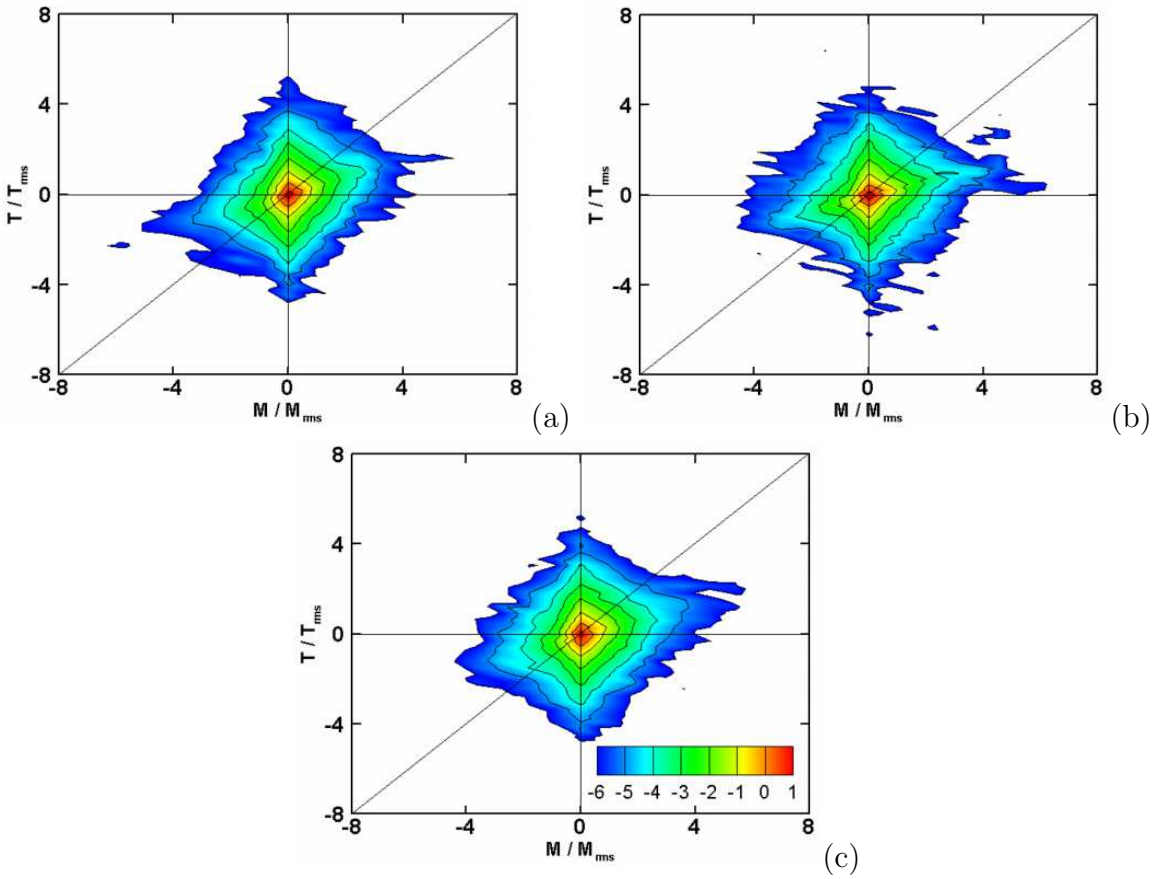

Figure 11: Contour plots of the logarithm of the joint PDF of the total SS advection term $T = \partial[(u_j^S + u_j^L)(u_i^S + u_i^L)]^S/\partial x_j$ and modeled SS advection term $M = \partial[(u_j^S(l_k) + u_j^L)(u_i^S(l_k) + u_i^L)]^S/\partial x_j$: (a) $i = k, j \neq k, i = 1, k = 1, j = 2$, (b) $i \neq j, j \neq k, i = 3, k = 1, j = 2$, (c) $i = j, j \neq k, i = 2, k = 1, j = 2$.

defined as

$$\rho_{ik} = \frac{\langle \mathcal{T}_{ik} \mathcal{M}_{ij} \rangle}{\left[\langle \mathcal{T}_{ik} \rangle_{rms} \langle \mathcal{M}_{ij} \rangle_{rms} \right]^{1/2}}, \quad i, k = 1, 2, 3 \tag{89}$$

Here, for model assumption (i) $\mathcal{T}_{ik} = \partial^2 u_i^S / \partial x_k^2$ and $\mathcal{M}_{ij} = 1/3 \sum_j (\partial^2 u_i^S / \partial x_j^2)$. It is seen that the correlation increases as the LS resolution increases (see Table 2). This is further investigated by considering the joint PDFs of the SS derivative and the average sum at different LS resolutions (see Fig. 10). Along the bisector of the I and III quadrants, the contour lines with high probabilities are approximately oval in shape and elongated. As the LS resolution increases, the joint PDFs elongate significantly along the diagonal of the I and III quadrants, suggesting that the probability of the

Table 2: The correlation coefficients according to (89) for model assumption (i) for different LS resolutions.

LS Resolution	ρ_{11}	ρ_{12}	ρ_{13}
32	0.623	0.814	0.811
64	0.666	0.808	0.809
128	0.737	0.806	0.814
256	0.828	0.801	0.804
512	0.875	0.797	0.802

events described by $S_{ik} = 0$ increase as the LS resolution increases.

On a similar vein, the model assumption (ii) can be analyzed. Joint PDFs of the total and modeled SS convective derivatives are shown in Figs. 11 (a), (b) and (c) for different velocity components in the streamwise line l_1 ($k = 1$). The shape of the PDFs is almost independent of the direction of the SS convective derivative. Assumption (*ii*) appears as a diagonal in the I and III quadrants. It is seen that maximum probability occurs at the origin which corresponds to the small values of the SS convective terms. The probability decreases as the SS convective terms grow. The joint PDFs illustrate that the total and modeled convective terms are positively correlated, indicating that the modeled and total SS convective terms that have the same signs are more dominant. The correlation coefficient can be analyzed in a similar manner as is investigated for model assumption (i) according to Eq. (89). For model assumption (ii), the $\mathcal{T}_{ik}$ and $\mathcal{M}_{ij}$ variables appearing in the Eq. (89) are defined as $\mathcal{T}_{ij} = \partial[(u_j^S + u_j^L)(u_i^S + u_i^L)]^S/\partial x_j$ and $\mathcal{M}_{ij} = \partial[(u_j^S(l_k) + u_j^L)(u_i^S(l_k) + u_i^L)]^S/\partial x_j$. The correlation coefficient indicates that the correlation between the total and modeled SS convective terms is quite low and does not show a major increase as the LS resolution increases (until 256 LS grid points) (see Table 3).

Model assumption (ii) corresponds to a case in which the modeled SS convective terms would admit values higher in magnitude than the most probable values of the total SS convective term. As a result, the modeled SS field is subject to higher

Table 3: The correlation coefficients according to (89) for model assumption (ii) for different LS resolutions.

LS Resolution	ρ_{12}	ρ_{22}	ρ_{23}
32	0.263	0.171	0.247
64	0.288	0.144	0.211
128	0.379	0.234	0.268
256	0.562	0.487	0.493
512	0.703	0.643	0.651

distortion by the SS advection term than the exact field [56].

In summary, both model assumptions qualitatively yield the same results as those obtained in previous studies using much lower Re turbulence data [56, 57], suggesting a universality of the assumptions. Moreover, it is observed that the model assumptions become more accurate as the LS grid resolution increases which makes sense. Results of the current analysis suggest that the TLS approach can simulate forced isotropic turbulence at $Re_\lambda = 433$ at an LS resolution of 128^3 grid points. This resolution (in one direction) is eight times smaller than that required for DNS (1024). This results is consistent with the previous TLS SS analysis by Kemenov and Menon [56], in which they used 32^3 LS grid resolution for the TLS approach at $Re_\lambda = 140$; however, a DNS study used 256^3 grid resolution at the same Re. Therefore, it appears a simple back-of-envelope type estimate can be obtained from these studies as for the LS resolution $N_i^{DNS}/2^3$. Here, N_i^{DNS} is the DNS resolution requirement in each coordinate direction x_i. Although this provides a good starting point for TLS, this requirement may not be universal especially for wall-bounded flows. Nevertheless, this guideline is used latter to simulate other flows of interest.

2.3.3 Numerical Implementation of Small-Scale Equations

In the previous section, TLS SS model assumptions for 1D lines were justified using an *a priori* analysis of the DNS data. In this part of the study, the SS equations with

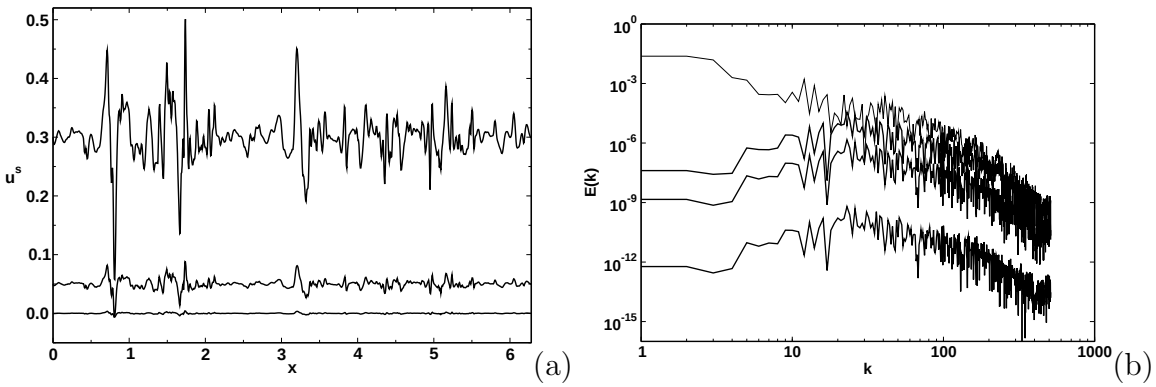

Figure 12: Time evolution of the SS velocity (a) and SS energy (b).

those underlying model assumptions are integrated numerically in order to study the model capability to duplicate the SS velocity on 1D line. The LS velocity field is obtained from the DNS_{1D} field according to the averaging procedure given by Eq. (64). The SS velocity field is re-constructed on lines by solving the SS Eq. (82). The 1D SS equations are solved on each line with periodic boundary conditions, which is consistent with the DNS data. The basic numerical method for solving the SS equations is similar to that used in Kemenov and Menon [56].

Starting from a zero initial state [56], the SS starts growing due to non-linear interactions. SS evolution is illustrated in Figs. 12 (a) and (b), where the evolution of the SS velocity and SS spectral energy are shown for one line in the isotropic turbulent field. Due to the nonlinear interactions between the LS and SS fields, the energy starts cascading down to the SS part of the spectrum until it reaches the viscous cut-off level, thus creating the SS field. On the final stage, the SS energy spectrum matches the SS part of the DNS_{1D} spectrum quite well.

The evolution time needed to properly establish the SS part of the spectrum is determined by matching the kinetic energies of the LS and the SS at the smallest resolvable (cut-off) scale on the LS grid. The *a priori* analysis of the DNS_{1D} data set indicates that the SS energy matches the LS energy at the cut-off, which is illustrated in Figs. 5 (b) and (d), and in Fig. 6 for the 1D signal spectrum and the averaged

spectrum of all the lines obtained from the DNS database, respectively. Furthermore, Figs. 13 (c), (f), (i), and (l), and 14 (a) and (b) also exhibit that the SS energy spectrum matches the LS energy spectrum at the cut-off, independent of the LS grid resolution. These observations indicate that evolving the SS equations up to LS energy near the cut-off can be used as an upper limit for the SS evolution time.

Figure 13 shows the LS and SS velocity fields and spectra with the DNS_{1D} and exact SS velocity field and spectra for four different LS grid resolutions (32, 64, 128, and 256). The exact SS field is explicitly computed from the DNS_{1D} velocity field. Moreover, the probabilities of the SS velocity and the exact SS velocity field are also shown. The overall comparison of the predicted SS field with the exact SS field is quite satisfactory for all LS grid resolutions. Note that the SS becomes more correlated with the exact SS as the LS grid resolution increases. This is understandable since the SS field strongly depends on the LS velocity and its gradient. However, it should be noted that even with the coarsest LS resolution, the predicted SS spectrum compared well with the exact SS spectrum (see Fig. 13 (c)). Overall, the SS spectra exhibit small deviations from the exact SS spectra for all LS grid resolutions. However, close to the dissipation range, small scales can have more energy, and this may be an artifact of adopted model assumption given by Eq. (81) [56]. The LS grid resolution of 128 shows higher correlations than the lower LS grid resolution of 32 and 64 cases, which supports the earlier suggestion for a lower limit for the LS grid resolution. It is seen that the 128 LS grid creates a SS field that correlates well with the DNS_{1D} SS field.

Note that SS fields differ on different lines, since the LS velocity field changes from line to line. In order to demonstrate this, we consider two different lines and look at the predicted SS velocity field and spectrum. The LS field is represented on 32 grid points and the SS field on 1024 grid points. Figure 14 shows that SS fields in physical and spectral space differ, since the LS fields vary from one line to another. Moreover,

the number of time steps in which the SS field evolves differs for each line depending on the kinetic energy of the LS field. This is illustrated in Fig. 15 for three different lines, each of which has different LS kinetic energy depending on the number of grid points representing the LS field. As the number of LS grid points increases, more kinetic energy is stored in the LS field, thus requiring fewer iterations to fully evolve the SS spectrum. Figure 15 shows that the number of SS time steps strongly depends on the LS energy. As the LS energy increases, the number of SS iterations decreases.

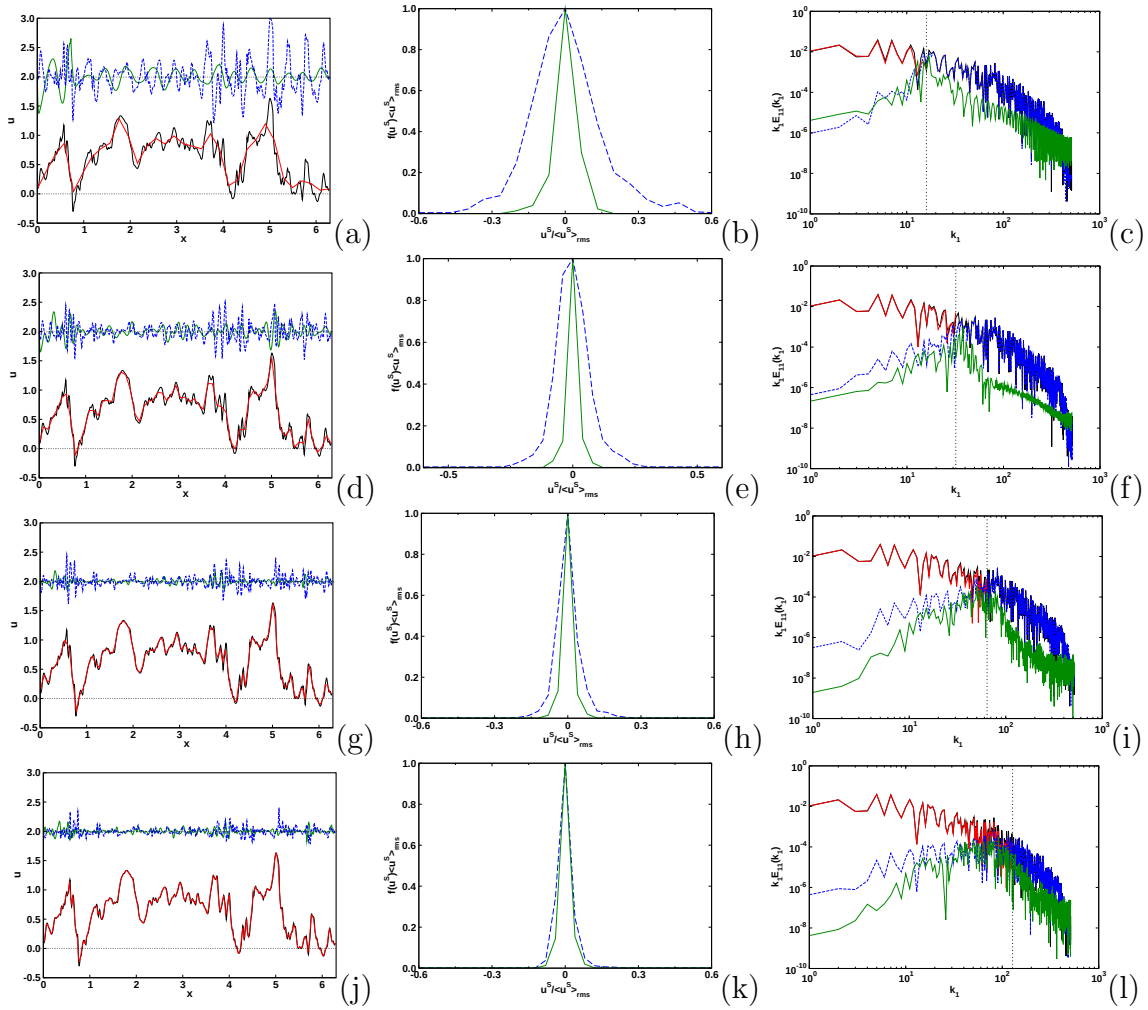

Figure 13: Comparison of the LS (red) and the SS (green) velocity fields with the DNS_{1D} (black) and exact SS (blue) fields for four different LS resolutions: (a,b,c) 32; (d,e,f) 64; (g,h,i) 128; (j,k,l) 256. (SS resolution is 32). The LS grid resolutions are represented by a dotted vertical line. The SS velocity profiles are multiplied and shifted upwards by 2.

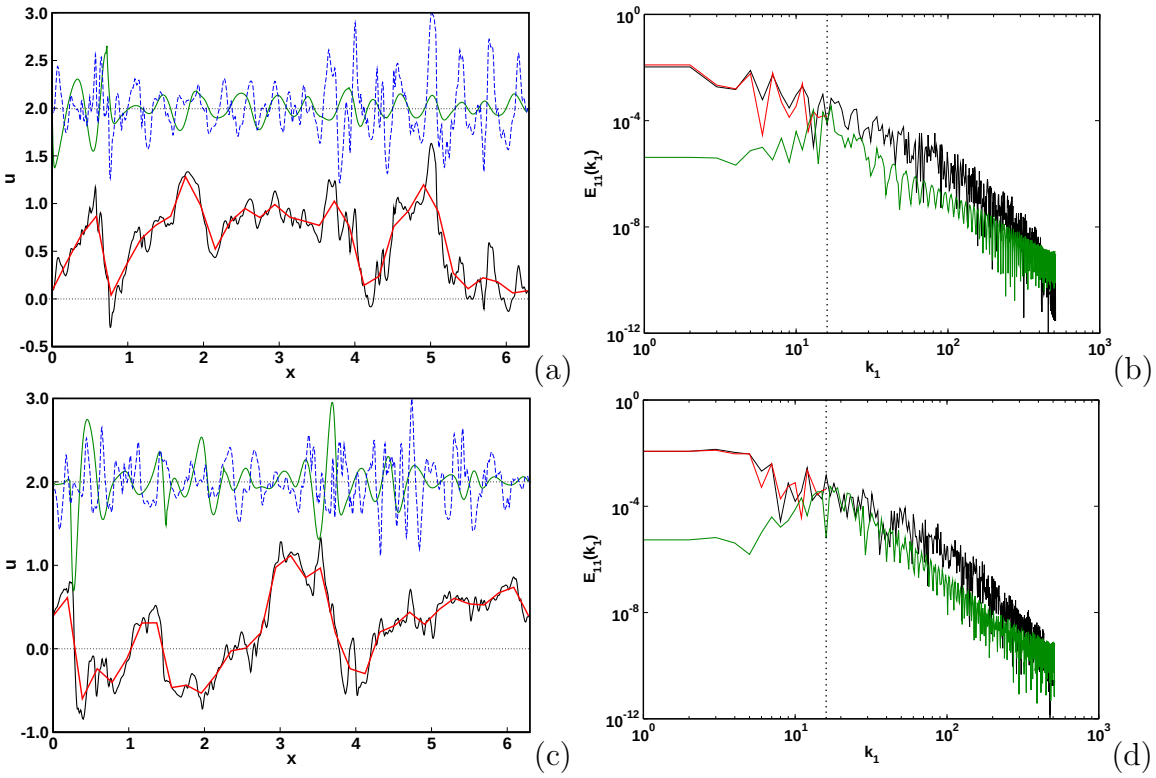

Figure 14: The LS (red) and SS (green) velocity fields and energy spectra compared with the DNS_{1D} field (black) for two different lines. The LS grid resolution is shown by a dotted vertical line. The SS velocity profiles are multiplied and shifted upwards by 2.

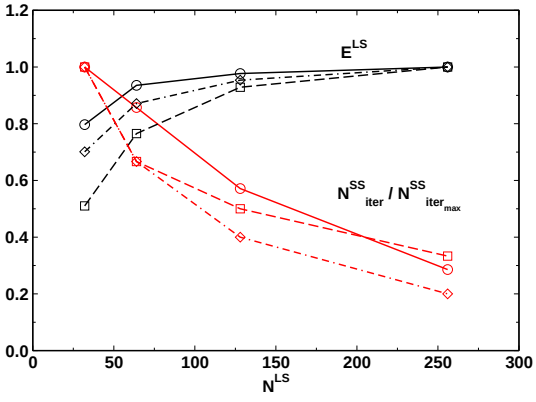

Figure 15: Variation of the LS energy and the number of time steps required for the final SS field with respect to LS resolution. Different line types (solid, dashed, dotted-dashed) represent three different lines in the DNS field.

CHAPTER III

TLS-LES METHOD

In this chapter, a hybrid approach is formulated by coupling the TLS for the near-wall region with conventional LES away from the wall, and is called TLS-LES, hereafter. The idea to couple the inner and the outer layer in wall-bounded flows using a hybrid approach is a recurrent argument in the literature (see [27, 103] and references therein). However, most of these approaches are based on coupling the LES equations with the RANS equations where all the near wall fluctuations are suppressed due to the time-averaging imposed on the RANS field. However, these near-wall fluctuations are of major concern in terms of predicting the correct near-wall dynamics, such as skin friction or turbulence production. The hybrid approach developed and demonstrated in this thesis is a new approach for developing near-wall modeling that does not suppress the near-wall fluctuations.

The organization of the chapter is as follows. The new hybrid operator is described in §3.1. The mathematical formulation of the TLS-LES approach based on this hybrid operator is described in §3.2. Finally, the TLS-LES coupling strategies, the boundary condition treatments for the TLS regions, and the numerical implementation of SS equations in the TLS region are discussed in §3.3.

3.1 Scale Separation

In order to formulate the TLS-LES equations, a new additive scale separation operator is defined based on the TLS-LS operator and LES filtering operator described in the previous chapter. A new hybrid operator is constructed by combining these two

operators with a blending function [27]:

$$\overline{\mathcal{L}} = \mathcal{K}\mathcal{L} + (1-\mathcal{K})F \tag{90}$$

here $\mathcal{L}$ represents the TLS scale separation operator (64) and F denotes the LES filtering operator. In the additive formulation, $\mathcal{K}(\mathbf{x},t)$ is a normalized function that in general, depends on time and space. Moreover, this function is continuous, atleast in first-order derivatives in time and second-order in space (this condition will show itself in the TLS-LES formulation).

Any large scale quantity constructed based on the additive LS operator $\overline{\mathcal{L}}$ is denoted by superscript $\mathcal{L}$ and obtained as:

$$\begin{aligned}
u_i^{\mathcal{L}}(\mathbf{x},t) &= \overline{\mathcal{L}}u_i(\mathbf{x},t) = \mathcal{K}\mathcal{L}(u_i(\mathbf{x},t)) + (1-\mathcal{K})F(u_i(\mathbf{x},t)) \\
\mathcal{L} &: u_i(\mathbf{x},t) \rightarrow u_i^L(\mathbf{x},t) \\
F &: u_i(\mathbf{x},t) \rightarrow \overline{u}_i(\mathbf{x},t) \\
u_i^{\mathcal{L}}(\mathbf{x},t) &= \mathcal{K}u_i^L(\mathbf{x},t) + (1-\mathcal{K})\overline{u}_i(\mathbf{x},t)
\end{aligned} \tag{91}$$

This new additive LS variable ($u_i^{\mathcal{L}}$) represents the TLS-LS variable (u_i^L) when $\mathcal{K}=1$ and LES filtered variable ($\overline{u}_i$) when $\mathcal{K}=0$. Similar to LES and TLS, this additive LS variable gives rise to a new small scale variable based on decomposition

$$u_i^{\mathcal{S}} = u_i - u_i^{\mathcal{L}} \tag{92}$$

Here, the additive SS can be easily shown to be related to the TLS SS and LES fluctuating field as

$$u_i^{\mathcal{S}} = \mathcal{K}u_i^S + (1-\mathcal{K})u_i' \tag{93}$$

It can be further shown that, the additive LS operator follows the properties of the TLS-LS and LES filtering operators. For example, the SS part of the additive operator is not zero:

$$(u_i^{\mathcal{L}})^{\mathcal{S}} \neq 0 \tag{94}$$

Moreover, the additive LS operator is not idempotent:

$$(u_i^{\mathcal{L}})^{\mathcal{L}} \neq u_i^{\mathcal{L}} \tag{95}$$

Here, it is reminded that $(u_i^L)^S \neq 0$ and $(u_i^L)^L \neq u_i^L$ in the TLS approach and $\overline{u}_i' \neq 0$ and $\overline{\overline{u}_i} \neq \overline{u}_i$ (unless the filter kernel is a sharp spectral cut-off) in the LES approach. The additive operator does not commute with differentiation. Such a commutation problem will theoretically arise if the blending function $\mathcal{K}$ is not uniform in space and time, i.e., if $\mathcal{K} = \mathcal{K}(x,t)$. This case is realistic since $\mathcal{K}$ is a blending function with a variation in space and in time. Introducing the commutation error operator [29]:

$$[f,g](u) \equiv f \circ g(u) - g \circ f(u) \tag{96}$$

and

$$\frac{\partial \mathcal{L}(u_i)}{\partial x_i} = \mathcal{K}\big(\frac{\partial u_i^L}{\partial x_i}\big) + u_i^L\big(\frac{\partial \mathcal{K}}{\partial x_i}\big) + (1-\mathcal{K})\big(\frac{\partial \overline{u}_i}{\partial x_i}\big) + \overline{u}_i\big(\frac{\partial \mathcal{K}}{\partial x_i}\big) \tag{97}$$

one obtains the following expression for the commutation error with first-order spatial derivatives:

$$\left[\mathcal{L}, \frac{\partial}{\partial x_i}\right](u_i) = -(u_i^L - \overline{u}_i)\frac{\partial \mathcal{K}}{\partial x_i} \tag{98}$$

Similarly, the commutation error for the first-order time derivatives:

$$\left[\mathcal{L}, \frac{\partial}{\partial t}\right](u_i) = -(u_i^L - \overline{u}_i)\frac{\partial \mathcal{K}}{\partial t} \tag{99}$$

An interesting result is that the commutation error is directly proportional to the gradient of $\mathcal{K}$ and the differences in LS and LES velocities.

The last property of the additive operator is related to its ability to reconstruct the TLS-LS and LES filtered variables if the additive LS field is known. Such as, once the TLS-LS field is known, the LES filtered variable can be obtained by (Eq. 91)

$$\overline{u}_i = \frac{u_i^{\mathcal{L}}}{1-\mathcal{K}} - \frac{\mathcal{K}}{1-\mathcal{K}} u_i^L \tag{100}$$

Therefore, the differences in the commutation error terms can be expressed as

$$u_i^L - \overline{u}_i = u_i^L - u_i^{\mathcal{L}} \tag{101}$$

a difference between the LS and additive LS field.

For a more physical picture of the additive LS scale separation operator consider the velocity field shown in Fig. 16. Here, a 1D field is obtained from the DNS database on a 1024 grid point and represented on the resolved grid in two different ways. In the first one, it is assumed that the blending function $\mathcal{K} = 0$, hence the additive LS field ($u^{\mathcal{L}}$) is equal to the LES filtered field ($\overline{u}$) (which is obtained by applying a top-hat filter to the DNS field). In the second approach, the blending function $\mathcal{K} = 1$, and therefore, the additive LS field ($u^{\mathcal{L}}$) is equal to the TLS-LS field (u^L), which is obtained by applying the scale separation operator (Eq. (64)) to the DNS field. The corresponding TLS SS field for the LS field is obtained from the decomposition. Both TLS-LS and LES filtered fields are on top of each other. As previously noted, the TLS-LS field is similar to the LES field if the filter function is a top-hat filter.

In addition to the physical representation of the LES and TLS fields, the spectral representations are also shown in Figs. 17 (a) and (b). The LES approach can represent scales up to the maximum LS grid resolution At this resolution, the detailed information of the flow is missing and needs to be modeled. However, modeling this information may not be adequately represented by the standard LES approaches that are based on extrapolation of resolved fields to represent subgrid scales. Unlike LES, TLS approach can represent a broad range of scales that can be as many as DNS. Moreover, the TLS-LS equations do not need closure if the SS field is known.

3.2 The Additive TLS-LES Equations

The TLS-LES equations can be obtained by applying the additive operator on the velocity field $u_i = u_i^{\mathcal{L}} + u_i^{\mathcal{S}}$ and pressure field $p = p^{\mathcal{L}} + p^{\mathcal{S}}$. Therefore, the equations for the decomposed field can be written for incompressible flows as

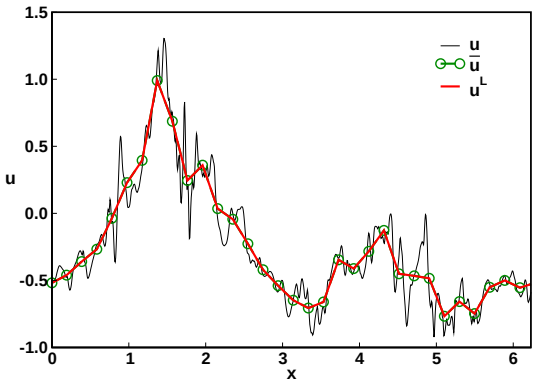

Figure 16: Fully resolved field (thin solid line) obtained from a 1024^3 DNS of isotropic turbulence study at $Re_\lambda = 433$. The resolved field is represented on a 32 grid point. The tophat filtered LES field (dashed line with symbol) is obtained by taking a moving average of the fully resolved field over 32 points. The TLS-LS field (solid line) is truncated from the fully resolved field.

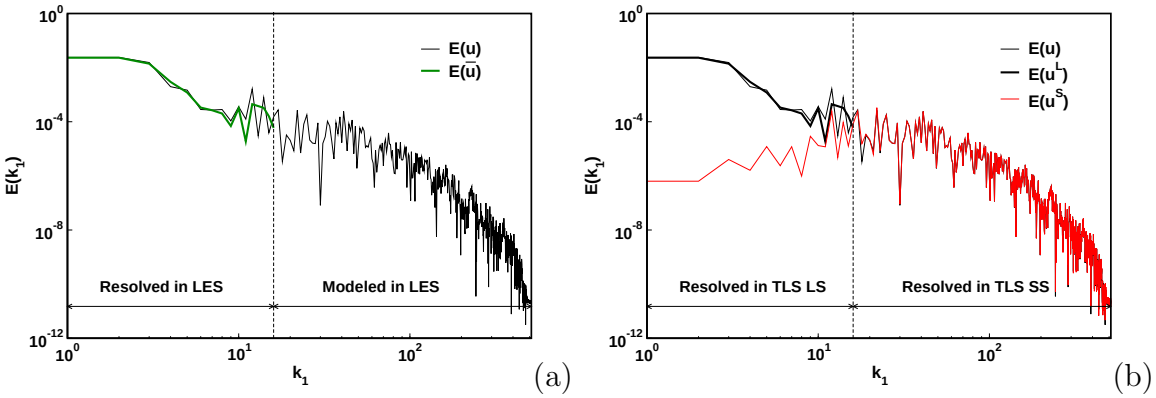

Figure 17: The longitudinal energy spectra of a fully resolved field (thin solid line) and (a) LES energy spectra (thick solid line), (b) The TLS-LS (dashed line) and SS (dotted dashed line) energy spectra (b). The LS grid resolution is shown by dotted vertical line.

$$\frac{\partial}{\partial t}(u_i^{\mathcal{L}} + u_i^{\mathcal{S}}) + \frac{\partial}{\partial x_j}(u_i^{\mathcal{L}} + u_i^{\mathcal{S}})(u_j^{\mathcal{L}} + u_j^{\mathcal{S}}) = -\frac{\partial}{\partial x_i}(p^{\mathcal{L}} + p^{\mathcal{S}}) + \nu\frac{\partial^2}{\partial x_j^2}(u_i^{\mathcal{L}} + u_i^{\mathcal{S}}) \quad (102)$$

$$\frac{\partial}{\partial x_i}(u_i^{\mathcal{L}} + u_i^{\mathcal{S}}) \;\; = \;\; 0 \quad (103)$$

The additive LS equations can be obtained by two different approaches. The first approach is to apply the additive operator to the Navier-Stokes equations. The second, which is followed here, is to apply additive approach introduced in the first section to the set of equations, such as the LS equation in the inner region and the LES equations in the outer region. Before formulating the TLS-LES equations, it is convenient to repeat the LES and TLS equations derived in the previous chapter. The LES equations are derived by filtering the Navier-Stokes equation and given as

$$\frac{\partial \overline{u}_i}{\partial t} + \frac{\partial}{\partial x_j}\left(\overline{u}_i\overline{u}_j\right) = -\frac{\partial \overline{p}}{\partial x_i} + \nu\frac{\partial^2 \overline{u}_i}{\partial x_j^2} - \frac{\partial \tau_{ij}^{sgs}}{\partial x_i}, \quad \frac{\partial \overline{u}_i}{\partial x_i} = 0 \quad (104)$$

In the LES approach most of the effort is on modeling the sgs term. The details of the sgs modeling is given in the previous chapter (Chapter 2, §2.1), and therefore, not repeated here. In LES formulation, the solution of the fluctuating part is not required since only its effect is modeled in the sgs model. The TLS-LS equations are derived following the two-scale decomposition approach by [56]. Within this formulation, the LS equations are

$$\frac{\partial u_i^L}{\partial t} + \frac{\partial}{\partial x_j}\left(u_i u_j\right)^L = -\frac{\partial p^L}{\partial x_i} + \nu\frac{\partial^2 u_i^L}{\partial x_j^2}, \quad \frac{\partial u_i^L}{\partial x_i} = 0 \quad (105)$$

The TLS approach differs from the LES approach in that the LS equations are coupled to the SS equations. Here, it should be noted that the LS equations are in fact the LES equations since the LS momentum equation can also be written in the following form

$$\frac{\partial u_i^L}{\partial t} + \frac{\partial}{\partial x_j}(u_i^L u_j^L) \;\; = \;\; -\frac{\partial p^L}{\partial x_i} + \nu\frac{\partial^2 u_i^L}{\partial x_j^2} - \frac{\partial \tau_{ij}^L}{\partial x_j} \quad (106)$$

where $\tau_{ij}^L = (u_i u_j)^L - (u_i^L u_j^L)$ is the unresolved term appearing in the momentum equation.

Both TLS-LS and LES filtered equations are given in the same functional form. With same initial and boundary conditions and subgrid modeling, both equations will give the same LS/LES field. Hence, the TLS-LES formulation can be defined with one set of LS equation. The closure of these equations, however are different. In the outer region, conventional LES sgs model is used whereas in the inner region, the SS 1D model is used.

The transition between these two regions can be obtained by using the blending approach given in [27]. The governing equations themselves can be blended [29] such that the LS equations are valid in the inner region and the LES equations hold in the outer region. This hybrid model can be symbolically written as:

$$TLS - LES = \mathcal{K}(LS) + (1 - \mathcal{K})(LES) \tag{107}$$

The TLS-LES equations for the additive LS velocity ($u_i^{\mathcal{L}}$) and LS pressure ($p^{\mathcal{L}}$) are:

TLS-LES Continuity:

$$\frac{\partial u_i^{\mathcal{L}}}{\partial x_i} = \frac{\partial \mathcal{K}}{\partial x_i}(u_i^L - \overline{u}_i) \tag{108}$$

TLS-LES Momentum:

$$\begin{aligned} \frac{\partial u_i^{\mathcal{L}}}{\partial t} + \frac{\partial u_i^{\mathcal{L}} u_j^{\mathcal{L}}}{\partial x_j} \quad &+ \quad \frac{\partial p^{\mathcal{L}}}{\partial x_j} - \nu \frac{\partial^2 u_i^{\mathcal{L}}}{\partial x_j^2} = \\ &- \quad \frac{\partial \tau_{ij}^{\mathcal{L}}}{\partial x_j} + \frac{\partial \mathcal{K}}{\partial x_i}(p_i^L - \overline{p}_i) + \frac{\partial \mathcal{K}}{\partial x_i}((u_i u_j)^L - \overline{u_i u_j}) \\ &- \quad 2\nu \frac{\partial \mathcal{K}}{\partial x_i}\frac{\partial}{\partial x_j}(u_i^L - \overline{u}_i) - \nu \frac{\partial^2 \mathcal{K}}{\partial x_j^2}(u_i^L - \overline{u}_i) \end{aligned} \tag{109}$$

where

$$\begin{aligned}(u_iu_j)^{\mathcal{L}} &= u_i^{\mathcal{L}}u_j^{\mathcal{L}} + \tau_{ij}^{\mathcal{L}} \\ \overline{u_iu_j} &= \overline{u}_i\overline{u}_j + \tau_{ij}^{sgs} \\ (u_iu_j)^{L} &= (u_i^{L}u_j^{L})^{L} + \tau_{ij}^{L}\end{aligned} \tag{110}$$

Here, the right hand side of the momentum and continuity equation represents the hybrid effect. The additive turbulent stress associated to the new TLS-LES formulation are:

$$\begin{aligned}\tau_{ij}^{\mathcal{L}} &= \mathcal{K}\tau_{ij}^{sgs} + (1-\mathcal{K})\tau_{ij}^{L} \\ &+ \mathcal{K}(1-\mathcal{K})(\overline{u}_i - u_i^{L})(\overline{u}_j - u_j^{L})\end{aligned} \tag{111}$$

where the first two hybrid turbulent stress terms blend together the LES subgrid model and TLS stresses while the third term is like a similarity turbulent stress term [27].

TLS and LES stress terms can be defined as

$$\begin{aligned}TLS: \quad \tau_{ij}^{L} &= (u_i^{L}u_j^{S})^{L} + (u_i^{S}u_j^{L})^{L} + (u_i^{S}u_j^{S})^{L} \\ LES: \quad \tau_{ij}^{sgs} &= -2\nu_t S_{ij}\end{aligned} \tag{112}$$

The specific closures for these terms associated with LES and TLS approaches are described in the previous chapter; therefore, will not be repeated here.

The hybrid terms appear due to the commutation error of the blending function with the space derivatives. As noted, the commutation error consist of the differences of the TLS-LS field and the LES filtered field, thus, can be further reduced to a difference of the additive LS field and TLS-LS field (Eq. 101). In the TLS-LES formulation both, u_i^L and p_i^L can be calculated from the TLS-LS equations, and therefore, these hybrid terms can be directly obtained. However, to do this computationally, the TLS-LS variables (u_i^L, p_i^L) have to be carried explicitly in the whole domain along

with the main variables $(u_i^{\mathcal{L}}, p^{\mathcal{L}})$. This will dramatically increase the computational requirement for the TLS-LES approach, and therefore, not pursued at present.

In the present study, neither of these hybrid terms are included. This reduction simplifies the governing equations Eqs. (108) and (109) of the TLS-LES approach

$$\frac{\partial u_i^{\mathcal{L}}}{\partial t} + \frac{\partial u_i^{\mathcal{L}} u_j^{\mathcal{L}}}{\partial x_j} = -\frac{\partial p^{\mathcal{L}}}{\partial x_j} + \nu \frac{\partial^2 u_i^{\mathcal{L}}}{\partial x_j^2} - \frac{\partial \tau_{ij}^{\mathcal{L}}}{\partial x_j}, \quad \frac{\partial u_i^{\mathcal{L}}}{\partial x_i} = 0 \tag{113}$$

The additive turbulent stress (Eq. 111) takes the following simplified form:

$$\tau_{ij}^{\mathcal{L}} = \mathcal{K}\tau_{ij}^{L} + (1-\mathcal{K})\tau_{ij}^{sgs} \tag{114}$$

Here, $\mathcal{K}$ is a space and time dependent variable. This function can be pre-defined in advance or it can calculated dynamically based on the characteristic length scale of the flow. The second approach is not followed here since it requires the integration of SS lines in the whole computational domain as well as the calculation of the subgrid stress model. Rather, the TLS-SS region is limited only near the wall, which drastically reduces the computational time and provides a more physical closure for the near-wall dynamics.

In this thesis, the first approach employs and evaluates two blending functions. First one is a step function in which an abrupt change from TLS to LES is performed:
Step Function

$$\mathcal{K} = \begin{cases} 1 & if \quad y > y^{TLS} \\ 0 & if \quad y < y^{TLS} \end{cases} \tag{115}$$

and *tanh* function, which provides a smooth transition:
Tanh Function

$$\mathcal{K} = \frac{1}{2}\left[1 - tanh\left(\frac{c_1(y/d - c_2)}{(1-c_2)y/d + c_2}\right)/tanhc_1\right] \tag{116}$$

where y^{TLS} represents the pre-defined interface for the TLS-LES model. Here, c_1 and c_2 are constants and chosen as 2 and 0.2, respectively. Moreover, the d represents the location at which the transition function is zero.

3.3 TLS-LES Coupling

In the TLS-LES approach, the TLS equations are used in the high-gradient near-wall region, while standard LES equations are used in the outer flow region. From a geometric standpoint, the current TLS-LES model has similarities to the two-layer wall-stress model - which also applies an embedded grid in an inner region (in that case, the embedded grid extends only to the first LES cell). However, the equations governing the TLS-LES in the inner region are fundamentally different. The present model does not apply an eddy viscosity for the turbulent transport. In addition, the TLS-LES model is strongly bi-directional. For transition of the fields, any type of blending function can be used. This pre-definition of the interface is the case in all hybrid simulations. For example, in DES, the switch between the LES and RANS is based on a pre-defined length [111].

In the LES region, the subgrid stress term (τ_{ij}^{sgs}) is closed by using a eddy viscosity model that employs the dynamic Smagorinsky model [28] while the TLS closure is based on the simulation of the unresolved term.

3.3.1 Boundary Conditions for the TLS Region

Since the resolved motion equations have the same functional form for TLS and LES, the implementation of the TLS-LES approach is easy by switching from the explicit SS reconstruction to subgrid stress closure in the outer layer. However, there are issues regarding boundary conditions that have to be addressed. The end points

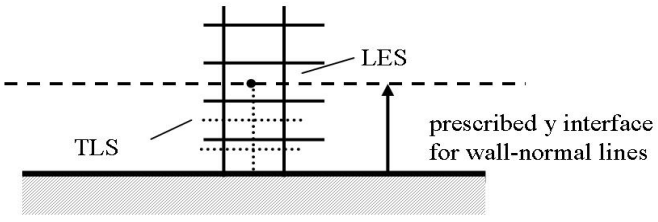

Figure 18: Illustration of wall-normal discretization for the TLS-LES model.

of the wall-normal lines in the TLS region lie inside the flow domain where the SS boundary conditions are not known. It is expected that the reconstructed SS velocity field would be insensitive to the boundary conditions at the interior endpoint since it is mostly defined by the LS velocity gradients. However, further analysis is needed.

Regardless, the wall-normal TLS lines begin at the no-slip wall ($y = 0$) and extend up to the edge of the near-wall region ($y = y^{TLS}$) (see Fig. 18). At $y = y^{TLS}$, two boundary conditions have been evaluated: the first one is a zero gradient boundary condition for the small scale velocities and the second one is the direct calculation of the small scale velocities in terms of the local subgrid kinetic energy k^{sgs} (obtained from the eddy viscosity). This second approach assumes that small scales are isotropic at the edge of the inner region. Given these assumptions, the boundary condition for the SS field on the wall-normal lines are:

at $y = 0$:

No-slip boundary condition: $u_i^S = 0,\ i = 1, 2, 3$

and at $y = y^{TLS}$ either by:

Zero gradient boundary condition: $\partial u_i^S / \partial y = 0, \qquad i = 1, 2, 3$

or fluctuating boundary condition: $u_i^S = \sqrt{\frac{2}{3} k^{sgs}} W_i, \qquad i = 1, 2, 3$

Here, W_i represents a random number with zero mean.

3.3.2 Numerical Implementation of SS Equations

If the SS lines are oriented with the LS grid, then these SS equations (82) become particularly simple, and boundary conditions for SS equations can be imposed at the three-dimensional domain boundaries.

Numerical implementation of the TLS equations is based on integration of LS equations and coupling the SS dynamics on the LS grid. The coupling is done by assuming that the knowledge of the SS field is only important at the LS time in order

to close the LS equation. This is similar to the classical LES approach closure of the sgs terms. The detailed information of the numerical implementation can be found elsewhere [56, 57].

Here, for completeness, the four main steps of the numerical implementation of TLS equations summarized as follows:

(1) At a given time step, the LS field on each 1D SS line is approximated by linear interpolation of the LS field.

(2) The SS field on each line is evolved from zero initial condition and corresponding boundary condition until the SS energy matches with the LS energy near the grid scale cut off.

(3) Using the SS field, the unclosed terms $u_i^S u_j^S, u_i^S u_i^L$ and $u_j^S u_i^L$ in the LS equation are calculated on the LS grid by averaging over the lines intersecting at the LS grid point.

(4) The LS velocity is advanced to the next time level $t_{n+1}^L = t_n^L + \Delta t^L$ by integrating the LS equation using a conventional three-dimensional finite-volume or finite-difference scheme.

CHAPTER IV

NUMERICAL METHOD

One of the major objectives of this thesis is to construct an accurate finite difference flow solver for incompressible unsteady turbulent flow simulations using LES or TLS. In this chapter, the algorithm for solving incompressible Navier-Stokes equations is presented. The equations are non-linear and are solved by numerical techniques applicable to general engineering applications. The algorithm used here to solve the non-linear equations is the artificial compressibility method. This method will be presented for time accurate problems. Temporal advancement in pseudo-time is conducted using a fifth-order Runge-Kutta method and in the physical time second-order backward differencing. The implementation is general enough to allow the simulation of flows in complex geometries. The code is parallelized (MPI) for distributed-memory machines.

The major difference between the incompressible and compressible formulation is the lack of the time derivative in the continuity equation in the incompressibility formulation. Therefore, satisfying the mass conservation is the main issue in solving the incompressible flow equations. Physically, incompressible flows are characterized by elliptic behavior of the pressure waves, where the disturbances propagate with infinite speed. In the incompressible formulation, the pressure field is desired to be a part of the solution. However, the pressure can not be obtained directly from the governing equations.

There are two main approaches to solve the incompressible equations: vorticity-stream function approach and primitive-variable approach. In the vorticity-stream function approach, the velocity components in the governing equations are replaced

with the vorticity (ω) and the stream function (ψ) in the two-dimensional formulation. With this new set of equations, the solution is obtained in terms of the vorticity and stream function. Then, the velocity field can be calculated back using the definition of stream functions. The pressure term is not explicitly present in the formulation. Therefore, a new equation for pressure is derived from the Poisson equation for pressure (obtained by taking the divergence of the momentum equation) in which the pressure is a function of velocity components or vorticity-stream function.

The extension of the vorticity-stream function approach for three-dimensional flow is not straightforward since the stream function does not exist in three-dimensional flow. For three-dimensional flows, the most common approach to overcome this limitation is to use vorticity-potential method where the formulation is generalized using a vector potential. This method may require computational effort much more than the primitive variable approach since the vorticity equation in the two-dimensional formulation must be replaced with a set of three equations for the components of the vorticity vector, each of which become more complicated than the two-dimensional formulation due to the vortex stretching terms that occur in three-dimensional formulation.

The main difficulties with the vorticity-stream function approach are the issues related to the extension of the approach to three-dimensional problems and the definition of the boundary conditions in terms of vorticity. On the other hand, the primitive variable approach does not have such complicated formulation when it applied to three-dimensional formulation. Therefore, in most cases, the methods with primitive variables are preferable.

In the primitive variable approach the incompressible Navier-Stokes equations are solved in their primitive variable form (u, v, w, p). In general, computational fluid dynamic methods for solving incompressible flows in the primitive formulation have followed two distinct evolutionary paths: pressure based methods and artificial

compressibility method.

The pressure based method for incompressible flow was developed by Harlow and Welch [41] called marker-and-cell (MAC) method for the calculation of unsteady flows. The extension of this method to steady flows has been introduced by Patankar [88] and called semi implicit method for pressure linked equations (SIMPLE). Numerous variants have been developed since (SIMPLEC, SIMPLER and primitive variable implicit separator (PISO)).

In the pressure based methods, the basic idea is to use pressure as a mapping parameter to satisfy the continuity equation. The pressure Poisson equation is solved to satisfy the continuity at the next time level. Numerically the intermediate velocity field is computed first, then the pressure correction is obtained by solving the Poisson equation. With this pressure correction, new pressure and velocity fields are computed.

In this approach, the time step is advanced in multiple steps which is convenient in terms of computations. However, the governing equations are not coupled which will affect the robustness and limit the maximum available time step. Additionally, in this approach the Poisson equation solver portion is usually the most expensive part of the computation. Therefore, many studies have been focused on accelerating the convergence of the Poisson equation calculations.

Two different grid types have been used in implementations of pressure based methods: staggered grids with different control volumes for velocity and pressure, and collocated grids with the same control volume for all variables. The use of staggered grids introduces significant complexities in code development, increases the number of storage allocations, and requires intense interpolations. Furthermore, the use of staggered grids in 3D complex geometries becomes computationally prohibitive. The SIMPLE method and its variants are designed for collocated grid systems and have been widely used. Nevertheless, there are some critical issues when using the

collocated system, due to collocated grid system, leading to numerical oscillations in the solution. To avoid these oscillations one might need artificial damping terms or a momentum interpolation procedure [99].

In the artificial compressibility formulation [14], the continuity equation is modified by adding a pseudo-time derivative of the pressure to the continuity equation. With the addition of the pseudo-time derivative, the continuity equation changes from an elliptic to a hyperbolic type in the space-time domain. Algorithms that have been developed for solving the compressible flow equations can then be directly applied to the new set of equations, taking advantage of all the development in compressible flow algorithms.

The artificial compressibility approach was introduced by Chorin [14]. It was originally developed for steady flow computations but can be used for unsteady flows by using a dual-time stepping procedure. A few examples of its time accurate capabilities are given in [78].

Dual time stepping artificial compressibility methods have been employed by many authors for studying unsteady flows. Rogers and Kwak [101] proposed a dual time artificial compressibility scheme, which uses second-order backward differencing for time derivative along with Euler-implicit temporal discretization of the spatial derivatives. This type of method is strongly stable and dissipative. The artificial compressibility with dual time stepping was used to pertain a DNS of three-dimensional, swirling flow in a closed cylinder with a rotating lid [101]. They used second-order backward differencing for the physical time derivatives along with a point-wise implicit Runge-Kutta iteration scheme that has been successfully applied to a variety of complex flow simulations. Kim and Menon [60] employed a dual time artificial compressibility method to carry out LES of complex turbulent flows using a five-stage Runge-Kutta algorithm. They investigated several convergence acceleration techniques including local dual time stepping, implicit residual smoothing, and multi-grid acceleration.

In the present chapter, the spatial and temporal discretization for the parallel incompressible flow solver is defined.

The organization of the chapter is as follows. The artificial compressibility method for incompressible flows is briefly explained in §4.1. The governing equations for incompressible flows in generalized coordinates are presented in §4.2. Issues concerning the spatial and temporal discretization and boundary conditions are then covered in the §4.3, 4.4, and 4.5, respectively. The validation of the incompressible solver for decaying isotropic turbulence, turbulent re-circulating flows, and turbulent channel flows are presented in §4.7.

4.1 Artificial Compressibility Method

In this thesis, the solution algorithm used to solve the governing equations of the incompressible flows is based on the scheme by Rogers and Kwak [101]. The algorithm employs the method of artificial compressibility in which an artificial compressibility parameter is introduced into the continuity equation along with a time derivative for the pressure.

To introduce a pressure derivative in the continuity equation, consider the Navier-Stokes equations for compressible flows:

$$\frac{\partial \rho}{\partial t} + \frac{\partial \rho u_i}{\partial x_i} = 0 \tag{117}$$

Following the assumption of small compressibility and isothermal conditions, the state equation in the linearized form is given by

$$p = p(\rho) \approx p_0 + c_0^2(\rho - \rho_0) \tag{118}$$

By substituting this relation to the continuity equation, we can now eliminate the density in the conservation equation.

$$\frac{1}{\beta}\frac{\partial p}{\partial t} + \frac{\partial u_i}{\partial x_i} = 0 \tag{119}$$

where $\beta = c_0^2 \rho_0$ is an artificial compressibility or a pseudo-compressibility parameter. Together with the unsteady momentum equations, this forms a hyperbolic-parabolic type of pseudo-time dependent system of equation. Physically this means that waves of finite speed are introduced into the incompressible flow field as a medium to distribute the pressure. For a truly incompressible flow, wave speed is infinite, whereas the speed of propagation of these pseudo-waves depend on the magnitude of the artificial compressibility parameter.

The pseudo speed of sound, c is found to be

$$c = \sqrt{u^2 + \beta} \tag{120}$$

The pseudo Mach number, M can be expressed as

$$M = \frac{u}{c} = \frac{u}{\sqrt{u^2 + \beta}} < 1 \tag{121}$$

The pseudo Mach number is always less than 1 for all $\beta > 0$. Therefore, the pseudo-compressibility does not introduce shock waves to the system.

The addition of the pseudo-time derivative term directly couples the pressure and the velocity. The set of governing equations become hyperbolic in space and time, which is the same form of the compressible equations. This similarity allows to use the methods developed for compressible flows. For steady-state solutions, the pseudo-time derivative will vanish as the solution converges, satisfying the conservation of mass. For time dependent flows, sub-iterations are performed to satisfy continuity for each physical step in time. The time integration scheme will be discussed in more detail in a later section.

4.2 Governing Equations in Generalized Coordinates

The primitive-variable form of the Navier-Stokes Eqs. (5, 6), itself has many different sub-forms that are formally equivalent analytically but which can lead to different algorithmic behaviors when replaced by discrete approximation. In this section an

overview of these various forms is provided and later the equations for generalized coordinates are formulated.

For purposes of comparisons, the Navier-Stokes equations in a symbolical form is expressed as follows:

$$\frac{\partial u_i}{\partial t} + (Conv.)_i + (Pres.)_i + (Visc.)_i = 0 \tag{122}$$

$$(Cont.) = 0 \tag{123}$$

where

$$(Cont.) \equiv \frac{\partial u_i}{\partial x_i}, \tag{124}$$

$$(Pres.)_i \equiv \frac{\partial p}{\partial x_i}, \tag{125}$$

$$(Visc.)_i \equiv \frac{\partial \tau_{ij}}{\partial x_j}. \tag{126}$$

The convective term in the Navier-Stokes equation transports energy without dissipation. So, special care needs to be taken to discretize the convective terms. A discrete form is needed in which the convection conserves the total energy (in the absence of physical dissipation).

The convective term in the momentum equation can be represented by four different forms. These forms are defined as

$$(Div.)_i \equiv \frac{\partial u_i u_j}{\partial x_j}, \tag{127}$$

$$(Adv.)_i \equiv u_j \frac{\partial u_i}{\partial x_j}, \tag{128}$$

$$(Skew.)_i \equiv \frac{1}{2}\frac{\partial u_i u_j}{\partial x_j} + \frac{1}{2} u_j \frac{\partial u_i}{\partial x_j}, \tag{129}$$

$$(Rot.)_i \equiv u_j(\frac{\partial u_i}{\partial x_j} - \frac{\partial u_j}{\partial x_i}) + \frac{1}{2}\frac{\partial u_i u_j}{\partial x_j}. \tag{130}$$

where $(Div.)_i$, $(Adv.)_i$, $(Skew.)_i$ and $(Rot.)_i$ are the divergence, advective, skew-symmetric and rotational forms, respectively.

For incompressible flows, the continuity equation (123) appears in the divergence form where the mass is conserved *a priori*. With the same approach, the pressure and viscous terms are conservative in the momentum equation. However, the convective term is only conservative *a priori* if it is given in divergence form. The other forms of the convective terms can be connected with each other through the following relations:

$$(Adv.)_i = (Div.)_i - u_i(Cont.), \tag{131}$$

$$(Skew.)_i = \frac{1}{2}(Div.)_i + \frac{1}{2}(Adv.)_i, \tag{132}$$

$$(Rot.)_i = (Adv.)_i. \tag{133}$$

Although all these forms are equivalent at the continuous level, their discretized forms do not have the same properties of conservation and stability.

The advective form provides the simplest form for discretization and is widely used; but such discretizations generally do not conserve either momentum or kinetic energy. On the other hand, straightforward discretizations of the divergence form do conserve momentum.

The rotational form is widely used in the context of pseudo-spectral approximations to the Navier-Stokes equations where it is necessary for stability [12]. The skew-symmetric form is constructed as the average of the conserved and unconserved forms. This form leads to discrete conservation of kinetic energy and, like the rotational form, enhances stability of pseudo-spectral methods.

It is a well-known fact that kinetic energy conservation is a key feature for the stability of unsteady calculations of incompressible flows. In the absence of viscous

terms, the Navier-Stokes (or Euler) equations would preserve conservation; so, especially for high-Re flows, it is advantageous for discretization of the convective terms to be conservative.

Recently Morinishi [82] derived conservative second- and fourth-order schemes for advective form of the Navier-Stokes equations. Hence, with this formulation, discrete conservation of both momentum and kinetic energy is easily achieved. So it has the potential for simulating very high-Re flows. In this research, the advective form of the Navier-Stokes equations is considered. The spatial discretization will be given in later sections. In the following section, the governing equations in the advective form are extended for generalized coordinates.

The cartesian space (x, y, z) is mapped onto a generalized curvilinear space (ξ, η, ζ) using the conventional methods. Hence, the governing Eq. (113) for the additive LS variable $u^{\mathcal{L}}$ are rewritten as

$$\frac{\partial}{\partial \xi}\left(\frac{U}{J}\right) + \frac{\partial}{\partial \eta}\left(\frac{V}{J}\right) + \frac{\partial}{\partial \zeta}\left(\frac{W}{J}\right) = 0, \tag{134}$$

$$\begin{aligned} \frac{1}{J}\frac{\partial q}{\partial t} + \left(\frac{U}{J}\right)\frac{\partial q}{\partial \xi} + \left(\frac{V}{J}\right)\frac{\partial q}{\partial \eta} + \left(\frac{W}{J}\right)\frac{\partial q}{\partial \zeta} = -\frac{\partial}{\partial \xi}(e - e_v) &- \frac{\partial}{\partial \eta}(f - f_v) \\ &- \frac{\partial}{\partial \zeta}(g - g_v) \end{aligned} \tag{135}$$

where J is the Jacobian of the transformation, and U, V, and W are the contravariant velocities along the streamwise, wall-normal and spanwise directions, respectively, in the computational domain.

$$\begin{aligned} U &= \xi_x u^{\mathcal{L}} + \xi_y v^{\mathcal{L}} + \xi_z w^{\mathcal{L}} \\ V &= \eta_x u^{\mathcal{L}} + \eta_y v^{\mathcal{L}} + \eta_z w^{\mathcal{L}} \\ W &= \zeta_x u^{\mathcal{L}} + \zeta_y v^{\mathcal{L}} + \zeta_z w^{\mathcal{L}} \end{aligned} \tag{136}$$

Here, q is the velocity vector, and the vectors e, f, and g and e_ν, f_ν, and g_ν contains

the pressure and viscous terms, respectively.

$$q = \begin{bmatrix} u^{\mathcal{L}} \\ v^{\mathcal{L}} \\ w^{\mathcal{L}} \end{bmatrix}, e = \begin{bmatrix} \xi_x p^{\mathcal{L}} \\ \xi_y p^{\mathcal{L}} \\ \xi_z p^{\mathcal{L}} \end{bmatrix}, f = \begin{bmatrix} \eta_x p^{\mathcal{L}} \\ \eta_y p^{\mathcal{L}} \\ \eta_z p^{\mathcal{L}} \end{bmatrix}, g = \begin{bmatrix} \zeta_x p^{\mathcal{L}} \\ \zeta_y p^{\mathcal{L}} \\ \zeta_z p^{\mathcal{L}} \end{bmatrix} \tag{137}$$

$$\begin{aligned}
e_v &= \begin{bmatrix} \xi_x(\tau_{xx} - \tau^{\mathcal{L}}_{xx}) + \xi_y(\tau_{xy} - \tau^{\mathcal{L}}_{xy}) + \xi_z(\tau_{xz} - \tau^{\mathcal{L}}_{xz}) \\ \xi_x(\tau_{xy} - \tau^{\mathcal{L}}_{xy}) + \xi_y(\tau_{yy} - \tau^{\mathcal{L}}_{yy}) + \xi_z(\tau_{yz} - \tau^{\mathcal{L}}_{yz}) \\ \xi_x(\tau_{xz} - \tau^{r}_{xz}) + \xi_y(\tau_{yz} - \tau^{\mathcal{L}}_{yz}) + \xi_z(\tau_{zz} - \tau^{\mathcal{L}}_{zz}) \end{bmatrix} \\
f_v &= \begin{bmatrix} \eta_x(\tau_{xx} - \tau^{\mathcal{L}}_{xx}) + \eta_y(\tau_{xy} - \tau^{\mathcal{L}}_{xy}) + \eta_z(\tau_{xz} - \tau^{\mathcal{L}}_{xz}) \\ \eta_x(\tau_{xy} - \tau^{\mathcal{L}}_{xy}) + \eta_y(\tau_{yy} - \tau^{\mathcal{L}}_{yy}) + \eta_z(\tau_{yz} - \tau^{\mathcal{L}}_{yz}) \\ \eta_x(\tau_{xz} - \tau^{\mathcal{L}}_{xz}) + \eta_y(\tau_{yz} - \tau^{\mathcal{L}}_{yz}) + \eta_z(\tau_{zz} - \tau^{\mathcal{L}}_{zz}) \end{bmatrix} \\
g_v &= \begin{bmatrix} \zeta_x(\tau_{xx} - \tau^{\mathcal{L}}_{xx}) + \zeta_y(\tau_{xy} - \tau^{\mathcal{L}}_{xy}) + \zeta_z(\tau_{xz} - \tau^{\mathcal{L}}_{xz}) \\ \zeta_x(\tau_{xy} - \tau^{\mathcal{L}}_{xy}) + \zeta_y(\tau_{yy} - \tau^{\mathcal{L}}_{yy}) + \zeta_z(\tau_{yz} - \tau^{\mathcal{L}}_{yz}) \\ \zeta_x(\tau_{xz} - \tau^{\mathcal{L}}_{xz}) + \zeta_y(\tau_{yz} - \tau^{\mathcal{L}}_{yz}) + \zeta_z(\tau_{zz} - \tau^{\mathcal{L}}_{zz}) \end{bmatrix}
\end{aligned} \tag{138}$$

In the above equations, τ^L_{ij} is the additive turbulent stress (Eq. 114) and τ_{ij} is the viscous stress term $\tau_{ij} = 2\nu S_{ij}$, where S_{ij} is the additive LS strain rate tensor $S_{ij} = \frac{1}{2}(\frac{\partial u^L_i}{\partial x_j} + \frac{\partial u^L_j}{\partial x_i})$ which is written in the transformed coordinates as

$$S_{xx} = \xi_x u^L_\xi + \eta_x u^L_\eta + \zeta_x u^L_\zeta, \quad etc. \tag{139}$$

where the velocity gradients are written as

$$u^{\mathcal{L}}_\xi = \frac{\partial u^{\mathcal{L}}}{\partial \xi}, \quad etc. \tag{140}$$

and the metrics of the transformation are defined by

$$\xi_x = \frac{\partial \xi}{\partial x}, \quad etc. \tag{141}$$

4.3 Spatial Grid System and Discretization

There are three main types of grid structure that have been employed in attempts to numerically solve the Navier-Stokes equations. These grid structures are (*i*) unstaggered, (*ii*) staggered and (*iii*) collocated.

In the staggered grid approach, the location at which each independent variable is computed is different for all variables. This type of grid was introduced by Harlow and Welch [41] in constructing the MAC method. In particular, this type of grid is used for the pressure correction methods. The problem of pressure-velocity decoupling seen on the unstaggered grid does not occur. On the other hand, the implementation of the boundary conditions are not straightforward. One of the major problem is the fact that, the no-slip boundary condition cannot be exactly satisfied with the staggered grid.

In the collocated grid system, while all variables are computed at the same location, this location corresponds to the cell center rather than a grid point at a cell vertex. The collocated grid system supposedly has the merits of both staggered and unstaggered grid systems, and has been mainly used for steady flow simulations. It is important to recognize that independent of whether it has been used for steady or unsteady problems, collocated variables lead to inability to exactly satisfy all boundary conditions.

In this thesis, the unstaggered grid structure is used. In the unstaggered grid all variables are defined at grid points at the cell vertices. With all discrete variables defined at each vertex, implementation of boundary conditions is straightforward. In particular, grid points will coincide with the discrete boundary points, implying that boundary conditions can be implemented without any approximation, which is highly desirable situation in the context of numerical discretization.

Accurate simulation of turbulent flows is a very difficult task due to the wide

range of scales present in the flow. Spectral methods are believed to provide accurate approximations to the problems. However, spectral solvers are limited by their applicability to simple geometries with generally periodic boundary conditions. To accurately resolve all the important length scales, higher-order difference schemes [98, 66, 82] are desirable for spatial discretization. In the present study, the convective terms are approximated using two different finite difference methods: fifth-order accurate, upwind-biased finite differencing suggested by Rai and Moin [98] and fourth-order accurate energy conservative scheme suggested by Morinishi *e*t al. [82].

4.3.1 Morinishi Operators

The discrete spatial operators used here are based on the unstaggered regular grid of Morinishi *e*t al. [82] and Vasilyev [114].

The finite-difference operator with stencil n acting on ϕ with respect to x_i is defined as

$$\frac{\delta_n \phi}{\delta_n x_i} = \frac{\phi(x_i + nh_i/2) + \phi(x_i - nh_i/2)}{nh_i} \tag{142}$$

and the interpolation operator with stencil n acting on ϕ in the x_i direction is

$$\overline{\phi}^{nx_i} = \frac{\phi(x_i + nh_i/2) + \phi(x_i - nh_i/2)}{2} \tag{143}$$

4.3.2 Upwind-Biased Finite Difference Scheme

The convective terms are approximated using fifth-order accurate, upwind-biased finite differences with a seven point stencil. For example, the first term in the momentum equation, $(U/J)_{q_\xi}$, is evaluated as;

$$\begin{aligned}\left(\frac{U}{J}q_\xi\right)_{i,j,k} = \frac{(U/J)_{i,j,k}}{120}\big(&- 6q_{i+2,j,k} + 60q_{i+1,j,k} + 40q_{i,j,k} \\ &- 120q_{i-1,j,k} + 30q_{i-2,j,k} - 4q_{i-3,j,k}\big)\end{aligned} \tag{144}$$

if $U_{i,j,k} > 0$, and

$$\left(\frac{U}{J}q_\xi\right)_{i,j,k} = \frac{(U/J)_{i,j,k}}{120}\big(\quad 4q_{i+3,j,k} - 30q_{i+2,j,k} + 120q_{i+1,j,k} - 40q_{i,j,k} - 60q_{i-1,j,k} + 6q_{i-2,j,k}\big) \tag{145}$$

if $U_{i,j,k} < 0$. The remaining convective terms are evaluated in a similar manner.

The viscous terms are evaluated using central differences, which are approximated to fourth-order accuracy using half-point differencing. The first viscous term in the u-momentum equation $(cu_\xi)_\xi$, where $c = 2\nu\xi_x/J$, is discretized as

$$[(cu_\xi)_\xi]_{i,j,k} = \frac{1}{24}\big[\; - \; (cu_\xi)_{i+3/2,j,k} + 27(cu_\xi)_{i+1/2,j,k} - 27(cu_\xi)_{i-1/2,j,k} + (cu_\xi)_{i-3/2,j,k}\big] \tag{146}$$

Additionally, u_ξ, which is defined at the half-points, is computed using a fourth-order accurate finite-difference given as

$$(u_\xi)_{i+1/2,j,k} = \frac{1}{24}\big(- u_{i+2,j,k} + 27u_{i+1,j,k} - 27u_{i,j,k} + u_{i-1,j,k}\big) \tag{147}$$

The viscous terms uses seven grid points, therefore, can be approximated to sixth-order accuracy on uniform grids.

The velocity derivatives in the continuity equation and the pressure derivatives in the momentum equations are computed using fourth-order central difference scheme. For example,

$$\left[\left(\frac{U}{J}\right)_\xi\right]_{i,j,k} = \frac{1}{12}\big[\; - \; \left(\frac{U}{J}\right)_{i+2,j,k} + 8\left(\frac{U}{J}\right)_{i+1,j,k} - 8\left(\frac{U}{J}\right)_{i-1,j,k} + \left(\frac{U}{J}\right)_{i-2,j,k}\big] \tag{148}$$

$$\left[\left(\frac{\xi_x p}{J}\right)_\xi\right]_{i,j,k} = \frac{1}{12}\big[\; - \; \left(\frac{\xi_x p}{J}\right)_{i+2,j,k} + 8\left(\frac{\xi_x p}{J}\right)_{i+1,j,k} - 8\left(\frac{\xi_x p}{J}\right)_{i-1,j,k} + \left(\frac{\xi_x p}{J}\right)_{i-2,j,k}\big] \tag{149}$$

4.3.3 Fully Conservative Finite Difference Scheme

With (142) and (143), for an unstaggered grid system, the advective term in the momentum equation is discretized as

$$u_j \frac{\partial u_i}{\partial x_j} \equiv (Adv.)_i = \frac{4}{3}\overline{\overline{u_j}^{1x_j} \frac{\delta_1 u_i}{\delta_1 x_j}}^{1x_j} - \frac{1}{3}\overline{\overline{u_j}^{2x_j} \frac{\delta_2 u_i}{\delta_2 x_j}}^{2x_j} \tag{150}$$

The pressure term is discretized by

$$\frac{\partial p}{\partial x_i} \equiv (Pres.)_i = \frac{9}{8}\frac{\delta_1 p}{\delta_1 x_i} - \frac{1}{8}\frac{\delta_3 p}{\delta_3 x_i} \tag{151}$$

and the discrete divergence operator in the continuity equation is

$$\frac{\partial u_i}{\partial x_i} \equiv (Cont.)_i = \frac{9}{8}\frac{\delta_1 u_i}{\delta_1 x_i} - \frac{1}{8}\frac{\delta_3 u_i}{\delta_3 x_i} \tag{152}$$

The viscous terms are written using the generic form

$$\begin{aligned} \frac{\partial}{\partial x_j}\left(\mu \frac{\partial u_i}{\partial x_j}\right) \equiv (Visc.)_i &= \frac{9}{8}\frac{\delta_1}{\delta_1 x_j}\left[\mu\left(\frac{9}{8}\frac{\delta_1 u_i}{\delta_1 x_i}\right)\right] \\ &- \frac{1}{8}\frac{\delta_3}{\delta_3 x_j}\left[\mu\left(\frac{9}{8}\frac{\delta_1 u_i}{\delta_1 x_i}\right)\right] \end{aligned} \tag{153}$$

For example, the fourth order accurate kinetic energy conservative form for the convective terms are approximated as

$$\left(\frac{U}{J}q_\xi\right)_{i,j,k} = \frac{1}{2}\left(\frac{U}{J}q_\xi\right)_{i,j,k} + \frac{1}{2}\left[q\left(\frac{U}{J}\right)_\xi\right]_{i,j,k} + \frac{1}{2}\left(\frac{U}{J}q\right)_\xi \tag{154}$$

where the derivatives are approximated using 4th order central scheme and given as

$$\begin{aligned} \left(\frac{U}{J}q_\xi\right)_{i,j,k} &= \frac{(U/J)_{i,j,k}}{24}\left(-q_{i+2,j,k} + 8q_{i+1,j,k} - 8q_{i-1,j,k} + q_{i-2,j,k}\right) \\ &+ \frac{q_{i,j,k}}{24}\left[\left(\frac{U}{J}\right)_{i+2,j,k} - 8\left(\frac{U}{J}\right)_{i+1,j,k} + 8\left(\frac{U}{J}\right)_{i-1,j,k} - \left(\frac{U}{J}\right)_{i-2,j,k}\right] \\ &+ \frac{1}{24}\left[-\left(\frac{U}{J}q\right)_{i+2,j,k} + 8\left(\frac{U}{J}q\right)_{i+1,j,k} - 8\left(\frac{U}{J}q\right)_{i-1,j,k} + \left(\frac{U}{J}q\right)_{i-2,j,k}\right] \end{aligned} \tag{155}$$

Unlike central difference, all upwind and upwind-biased differences have truncation error terms that are dissipative in nature. However, it is an essential requirement to

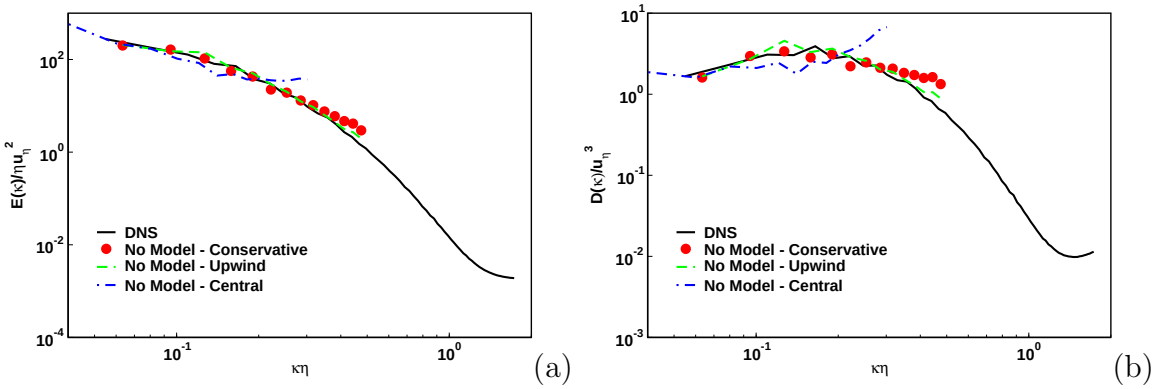

Figure 19: Decay of isotropic turbulence: (a) Normalized energy spectra (b) Normalized dissipation spectra at time $t = 2.67$

have the numerical dissipation of the finite difference scheme lower than the turbulent dissipation. The dissipation of the numerical schemes can overwhelm the true dissipation in the turbulent flow and, therefore, needs to be evaluated carefully.

Figures 19 and 20 present the three dimensional normalized energy and dissipation spectrum in the decaying isotropic turbulence (the detailed description of this flow field will be presented in the section 5.3). Results obtained on a 32^3 grid resolution using three different convective schemes (implemented with and without employing sgs model) are shown together with the DNS results on a 128^3 grid.

It can be seen from Figs. 19 (a) and (b) that the numerical dissipation of the finite-difference scheme is lower than the turbulent dissipation if the convective terms are discretized using either with the fifth-order upwind or fourth-order conservative schemes. The fourth-order central scheme for the convective terms without employing any sgs model shows unphysical build-up at the high wave-numbers. It is known that central schemes are not dissipative and need to be combined with artificial viscosity. However, the fourth-order conservative scheme does not require any artificial damping. Figures 19 (a) and (b) indicate that the upwind scheme is more dissipative than the conservative one.

The numerical dissipation of the conservative scheme is lower than the turbulent

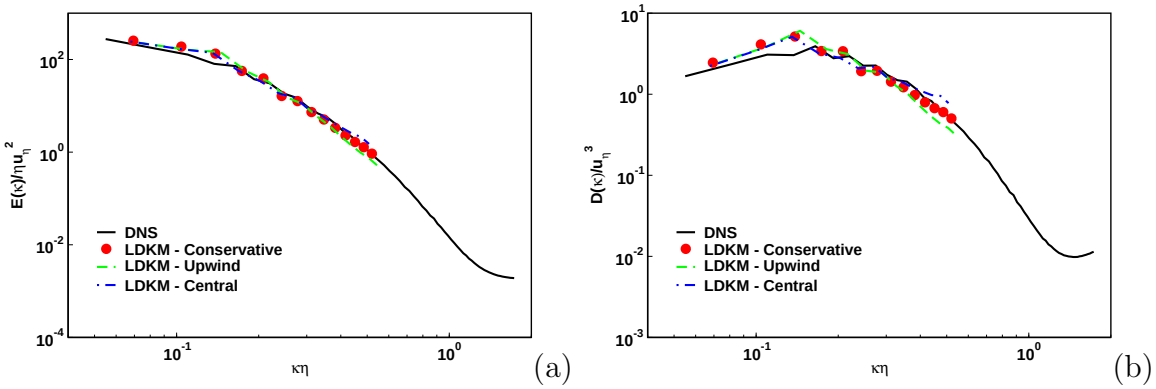

Figure 20: Decay of isotropic turbulence: (a) Normalized energy spectra (b) Normalized dissipation spectra at time $t = 2.67$

dissipation, which is an essential requirement for turbulent simulation solvers. As shown in Figs. 20 (a) and (b), the conservative scheme with the sgs model agrees very well with the DNS data. However, with the addition of the subgrid terms, upwind scheme produces more dissipation and under predicts the energy and dissipation spectrum at the high wave-numbers. The fully central scheme behaves well for low wave numbers but energy and dissipation builds up at the high-wave numbers.

In summary, these results demonstrate that the numerical dissipation of the solver is lower than the turbulent dissipation if the convective terms are dicretized using the fourth-order conservative scheme. Also, the LES data agrees well with the DNS. This demonstrates the need for the conservative algorithm and the capability of the sgs model.

4.4 Time Integration

Artificial compressibility method used for the solution of the unsteady incompressible Navier-Stokes equations. Several examples can be found in [78]. In order to conduct unsteady flow computations, the dual time stepping technique of Jameson [48] is combined with the pseudo-compressibility approach.

4.4.1 Dual-time Stepping

In the unsteady flow, the continuity equation remains the same, while the momentum equation takes the following form [101]

$$\frac{\partial q}{\partial \tau} = -\frac{\partial q}{\partial t} - R^*(q) = -R(q) \tag{156}$$

where R^* represents the residual in the momentum equations, which includes convective and viscous terms. This is called dual time stepping where t is the physical time, while τ is the pseudo-time. In this unsteady formulation, the governing equations are marched in the pseudo-time (i.e., subiterated) until the divergence free flow field is obtained. The convergence in the pseudo integration can be accelerated by the use of proper β. It is found that for large values of the physical time step dt, the unsteady system behaved like the steady one, therefore, convergence can be accelerated by using β of the order u. For small values of the physical time step dt, convergence can be significantly accelerated by letting β much larger than its conventional values in spite of the fact that this requires a corresponding reduction in the pseudo-time step $d\tau$.

For pseudo-compressibility approach one needs to recognize that inviscid part of the flow would converge at a very different rate compared to that of the near wall viscous region because of different speeds of wave propagation. Therefore, sufficient number of pseudo-time iterations has to be performed so that the viscous part and inviscid part of the flow field are fully converged at each real-time step.

The integration in the pseudo-time is carried out by a five-stage Runge-Kutta time stepping scheme. If m is the index associated with pseudo-time, the five-stage Runge-Kutta can be written in the following form

$$q^{(0)} = q^m, \tag{157}$$

$$q^{(k)} = q^{(0)} - \alpha_k \Delta\tau R(q^{(k-1)}), \quad k = 1...5, \tag{158}$$

$$q^{m+1} = q^5 \tag{159}$$

Here, the coefficients are chosen as $\alpha_1 = 0.059$, $\alpha_2 = 0.145$, $\alpha_3 = 0.273$, $\alpha_4 = 0.5$, and $\alpha_5 = 1.0$.

The physical time derivatives in the momentum equations are computed using a second order backward difference that results in an implicit scheme,

$$\frac{\partial q}{\partial \tau} = -\frac{3q^{n+1} - 4q^n + q^{n-1}}{2\Delta t} - R^*(q^{n+1}) = -R(q^{n+1}) \tag{160}$$

where the superscript n denotes the physical time level.

4.4.2 Local time Stepping

To accelerate the convergence in pseudo-time marching at each physical time step, efficient acceleration techniques for explicit steady-state solvers, such as local time-stepping is employed. Local time-stepping involves using the locally maximum allowable time step. The local time step for viscous flow is computed as:

$$\Delta\tau = CFL \frac{1}{\lambda_\xi + \lambda_\eta + \lambda_\zeta + 2(\nu + \nu_T)J^2(S_\xi^2 + S_\eta^2 + S_\zeta^2)} \tag{161}$$

where CFL is the Courant-Friedrichs-Lewy number, λ_ξ, λ_η, and λ_ζ are the spectral radii in the ξ, η, and ζ directions, respectively and defined as:

$$\begin{aligned}
\lambda_\xi &= |U| + \beta\sqrt{\left(\xi_x^2 + \xi_y^2 + \xi_z^2\right)} \\
\lambda_\eta &= |V| + \beta\sqrt{\left(\eta_x^2 + \eta_y^2 + \eta_z^2\right)} \\
\lambda_\zeta &= |W| + \beta\sqrt{\left(\zeta_x^2 + \zeta_y^2 + \zeta_z^2\right)}
\end{aligned} \tag{162}$$

Also:

$$\begin{aligned}
S_\xi &= \sqrt{x_\xi^2 + y_\xi^2 + z_\xi^2} \\
S_\eta &= \sqrt{x_\eta^2 + y_\eta^2 + z_\eta^2} \\
S_\zeta &= \sqrt{x_\zeta^2 + y_\zeta^2 + z_\zeta^2}
\end{aligned} \tag{163}$$

Note that the local time step $\Delta\tau$ is limited to be less than the physical time step Δt to make the scheme stable.

4.5 Boundary Conditions

Once the numerical algorithm has been developed, the next most important aspect is the proper implementation of the boundary conditions. In the present study, boundary conditions are imposed at the geometrical boundaries. At the inflow, the velocities are specified and the pressure is extrapolated from the interior. For internal flow at the outflow boundary velocities are extrapolated from the interior. However, the pressure is calculated from the mass conservation equation. On a solid surface, the usual no-slip condition is applied. The pressure at the wall is obtained by setting the wall-normal gradient of the pressure equal to zero at the no-slip wall.

4.6 Parallel Computing Performance of the Solver

Even with current technological advances in computer hardware, large simulations can require an extraordinary amount of computer resources. Therefore, in order to decrease simulation time and lower the memory requirements, the code needs to be parallelized. This is accomplished by utilizing the Message Passing Interface (MPI) library. MPI is a library of functions for Fortran that distributes information from a single processor to multiple processors.

The parallel computing performance of the solver is investigated for turbulent channel flow at $Re_\tau = 395$ for two different grid sizes and a number of processors. This test case is used due to its geometric simplicity which allows for a wide variety of processor distributions. Also, this case is successfully validated for LES-LDKM and TLS-LES approaches. For this case, the TLS-LES resolution is eight times smaller than the LES-LDKM resolution. The TLS SS region extends to three LES cells near the walls. The TLS-LES and LES-LDKM studies are validated against the DNS of Moser *et* al. [83] and will be presented in the following chapters.

Figure 21 shows the parallel performance of the developed code as recorded on the Cray XT4 cluster. The Cray XT4 is a quad-core machine, therefore the lowest

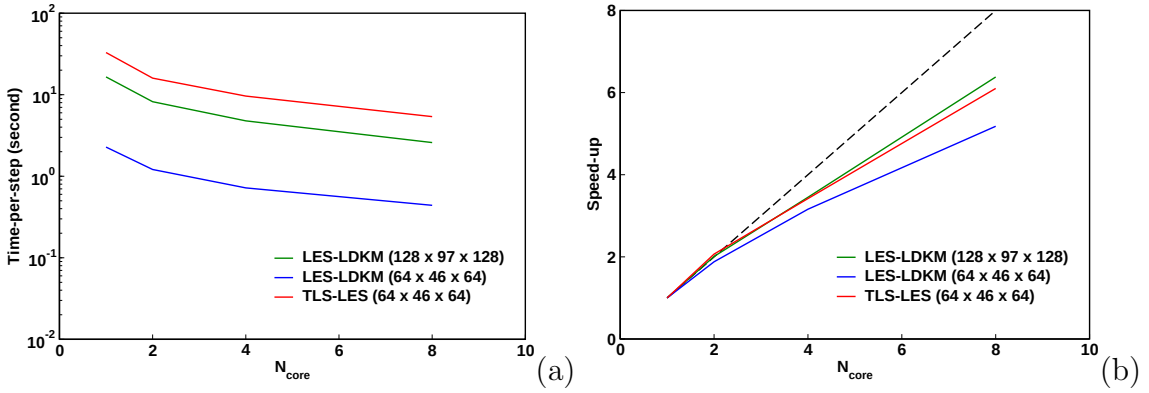

Figure 21: (a) The solver-timing plots for different grid sizes and models (b) Overall speedup of the solver

simulations are performed on a single core with four processor. Figure 21 (a) shows the average time for one iteration step as a function of number of cores for TLS-LES and LES-LDKM cases. For a given number of cores, an increase in domain size for LES-LDKM results in an increase in the time needed to complete one iteration. This is expected due to the increase number of grid points per processor. Here, it is noted that the average time required for TLS-LES case is higher than the LES-LDKM case due to the extra work coming from the SS integration in the TLS region. For both cases, for a given grid size, there is a decrease in average time for one iteration step with increase in number of cores. This is due to the reduced computational load per processor.

The speed-up efficiency of the code is evaluated and presented in Fig. 21 (b). The speed-up is defined as the time per iteration for one core divided by the time per iteration on multiple cores. In the current study, the minimum numbers of cores used for evaluating the speed-up is one. The speed-up efficiency of the solver is shown in Fig. 21 (b) for TLS-LES and LES-LDKM studies. The ideal performance is also shown in form of a dashed line. Good speed-up characteristics is observed especially for TLS-LES and LES-LDKM fine grid studies.

In summary, the incompressible flow solver performance in terms of scaling and

speed-up efficiency is documented for the TLS-LES and LES algorithms. It is noted that, the TLS-LES solver demonstrated that the solver scales well (approximately 70%) with increase in mesh size. Overall, the algorithm demonstrates reasonable parallel computing performance.

4.7 Code Validation Studies

To validate the incompressible flow solver developed in this study, *a posteriori* tests of decaying isotropic turbulence, turbulent re-circulating flows, and turbulent channel flows are performed. These benchmark cases were chosen to facilitate the evolution of the solver and the turbulence approaches (LES, TLS and TLS-LES) under various conditions of increasing complexity. Comparisons with experimental data and DNS results (wherever available) are carried out to demonstrate the capability of the solver.

4.7.1 Decaying Isotropic Turbulence

Decaying isotropic turbulence is an idealized problem for studying turbulence theory and model. The primary reason for this is that decaying isotropic turbulence is governed by two basic elements: non-linearity and viscosity, without any more complexities, like physical boundaries.

Decaying isotropic turbulence has two periods. First one is the energy propagation period where the energy at the large scales propagate to the smaller scales due to the nonlinear coupling. In this period, the non-linearity is dominant although there is a decay of the total energy. Second one is the final decay period where the viscous effects are dominant and nonlinear energy transfer could be neglected. The energy in the final decay period exhibits an asymptotical form.

The main objective of this study is to investigate the second period of the decaying isotropic turbulence using direct numerical and large eddy simulations with the incompressible solver developed in this study.

All numerical simulations are conducted in a three-dimensional periodic cube with

various resolutions: N^3. The initial incompressible velocity field is obtained from a 128^3 DNS turbulent field at $Re_\lambda = 86$.

DNS of decaying isotropic turbulence is performed at a resolution of 128^3. In decaying isotropic turbulence, the total kinetic energy E

$$E = \frac{u_i^2}{2} \tag{164}$$

and dissipation D

$$D = 2\nu S_{ij} S_{ij} \tag{165}$$

always decay with time. This is shown in Figs. 22 (a) and (b). In the final decay period, they are expected to decay as

$$\frac{E}{E_0} \quad \propto (t - t_0)^{-n} \tag{166}$$

$$\frac{D}{D_0} \quad \propto (t - t_0)^{-n-1} \tag{167}$$

In this study, the decay exponent for energy and dissipation are predicted as 1.6 and 2.6, respectively, which falls well within the classical results.

The corresponding Reynolds number based on Taylor micro-scale also decreases with time (see Fig. 22 (c)). However, the Taylor micro-scale decreases first and then grows slowly (see Fig. 22 (d)). These results are in good agreement with theory and past studies. In the energy propagation period, the Taylor micro-scale decreases which implies the development of small scales in turbulent motion. And, in the final decay period, the Taylor micro-scale grows which implies the decay of the small-scale motions.

The velocity derivative skewness S

$$S = -\frac{\langle \left(\frac{\partial u_i}{\partial x_i}\right)^3 \rangle}{\langle \left(\frac{\partial u_i}{\partial x_i}\right)^2 \rangle^{3/2}} \tag{168}$$

and the velocity derivative flatness F

$$F = -\frac{\langle \left(\frac{\partial u_i}{\partial x_i}\right)^4 \rangle}{\langle \left(\frac{\partial u_i}{\partial x_i}\right)^2 \rangle^{2}} \tag{169}$$

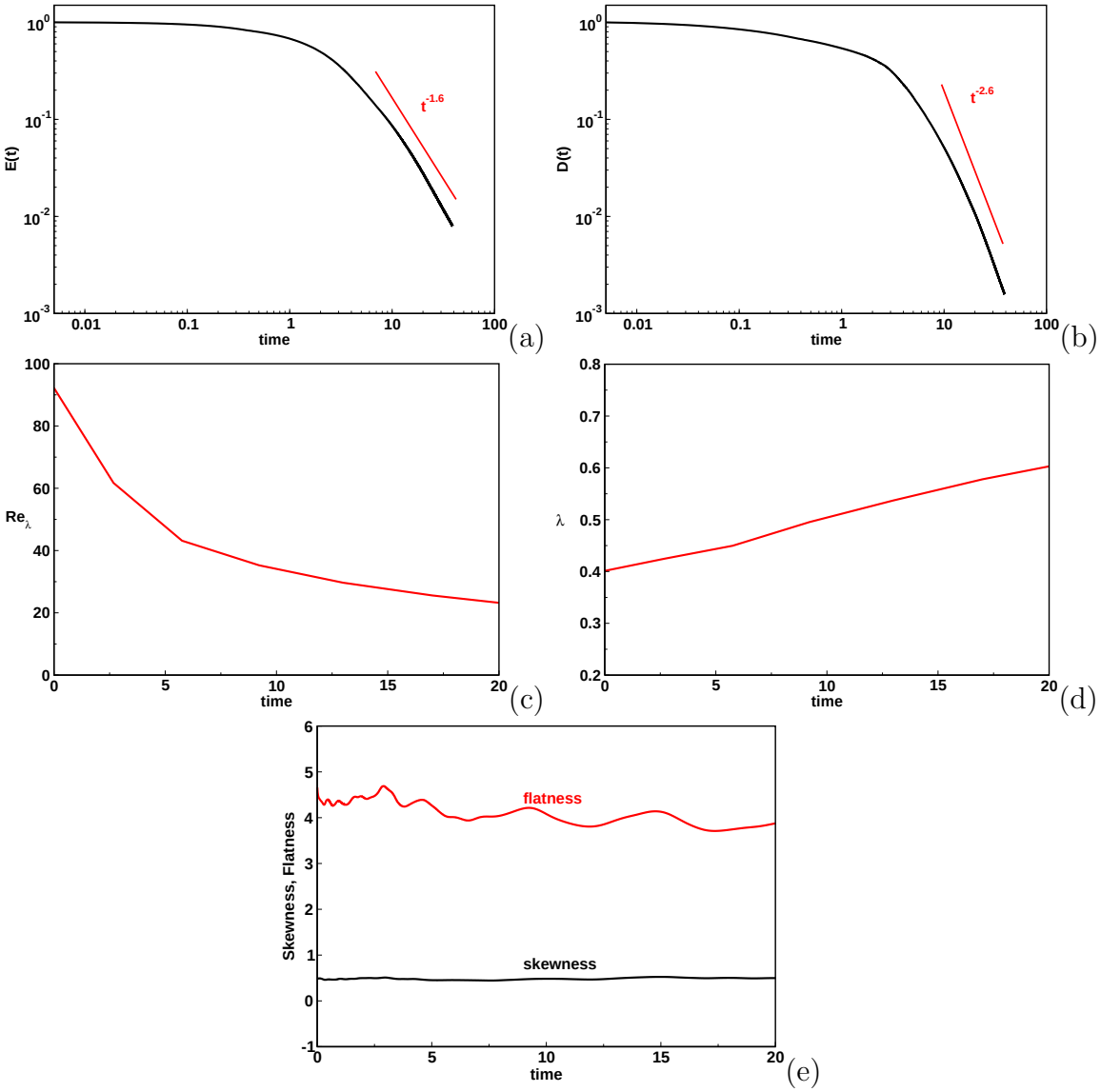

Figure 22: Decay of isotropic turbulence: (a) Turbulent kinetic energy (b) Dissipation (c) Reynolds number based on Taylor micro-scale (d) Taylor micro-scale (e) Skewness and Flatness.

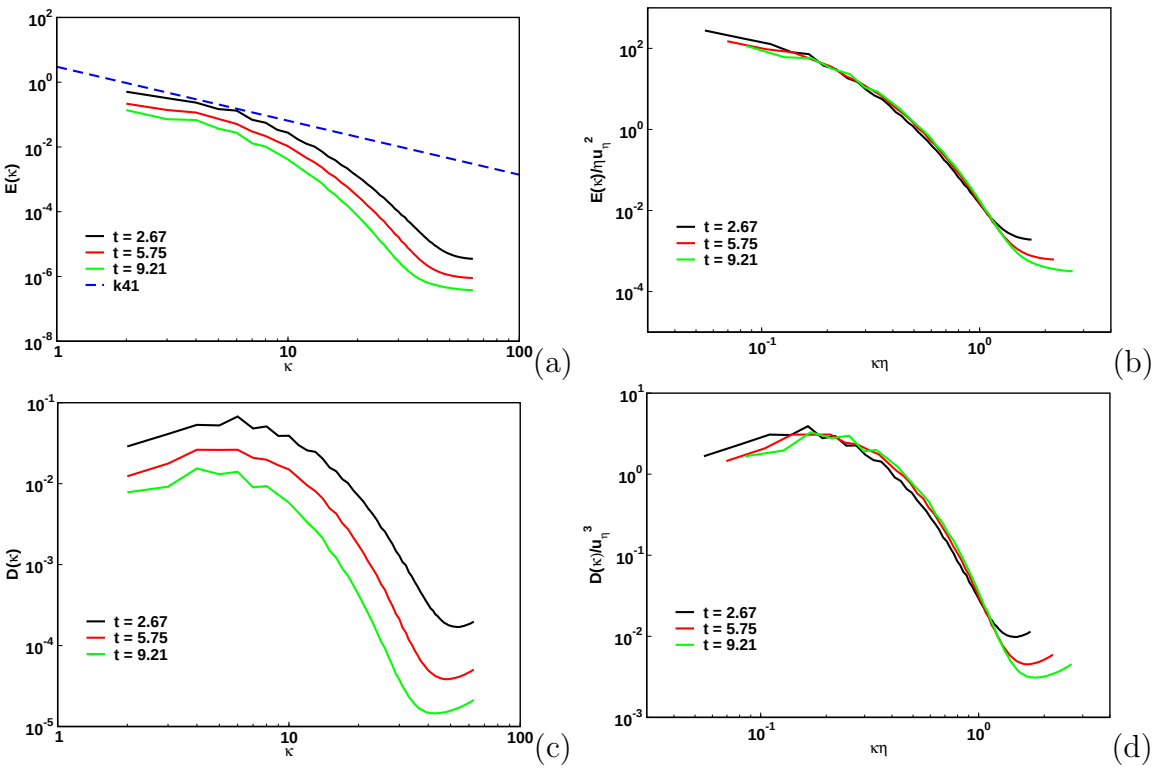

Figure 23: Decay of isotropic turbulence: (a) Three dimensional energy spectra (b) Normalized energy spectra (c) Three dimensional dissipation spectra (d) Normalized dissipation spectra for three instants of time $t = 2.67$, 5.75 and 9.21.

are presented in Fig 22 (e). The velocity derivative skewness is directly related to the production of dissipation, and is also a measure of the non-linearity of the Navier-Stokes equation. In the energy propagation period, the skewness rapidly drops, which implies the development of turbulence. Meanwhile, in the final period, it varies slowly which implies that turbulence remains to some level at this period. The final decay period for skewness is well predicted in this study.

The three-dimensional energy spectra $E(\kappa)$:

$$E(\kappa) = \frac{1}{2} \sum_{\kappa - 1/2 < |\kappa| \leq \kappa + 1/2} \widehat{u}(\kappa)\widehat{u}^*(\kappa) \tag{170}$$

and the dissipation spectra $D(\kappa)$:

$$D(\kappa) = 2\nu\kappa^2 E(\kappa) \tag{171}$$

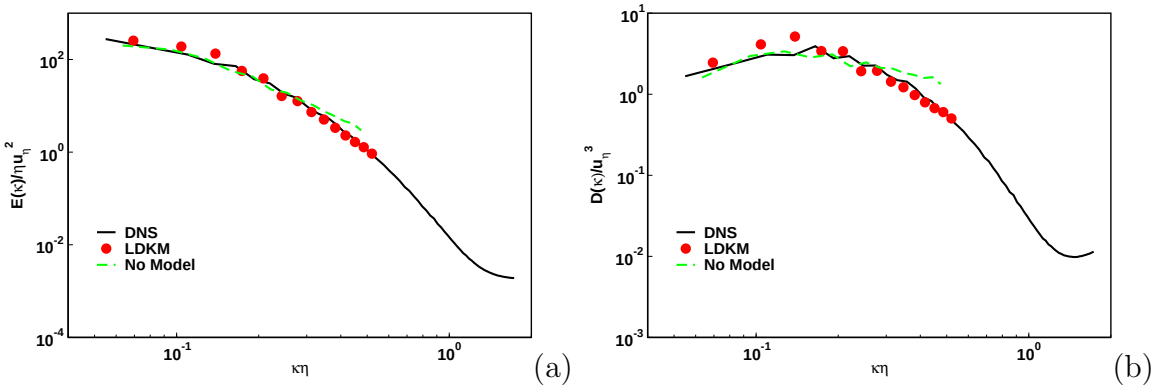

Figure 24: Decay of isotropic turbulence predicted with LES-LDKM: (a) Normalized energy spectra (b) Normalized dissipation spectra at time $t = 2.67$

are shown in Fig. 23. It is known that the energy and dissipation spectrum are collapse at high wave numbers for different Reynolds numbers if they are normalized with the Kolmogorov length and velocity scales. This behavior is observed and presented for three instants of time in Fig. 23 (b) and (d) for energy and dissipation, respectively.

The energy and dissipation spectrum predicted with the LES-LDKM at a grid resolution of 32^3 is shown in Fig. 24. It is noted that the LES results perfectly match with the DNS spectrum.

Snapshots of the second invariant of velocity gradient tensor (174) at the level of $Q = 150$ for three instants of time are shown in Fig. 25. The positive values of the second invariant of the velocity gradient tensor indicates the regions of intense enstrophy and weak shear. It is seen from Fig. 25 that the tube-like structures in the field gradually die out.

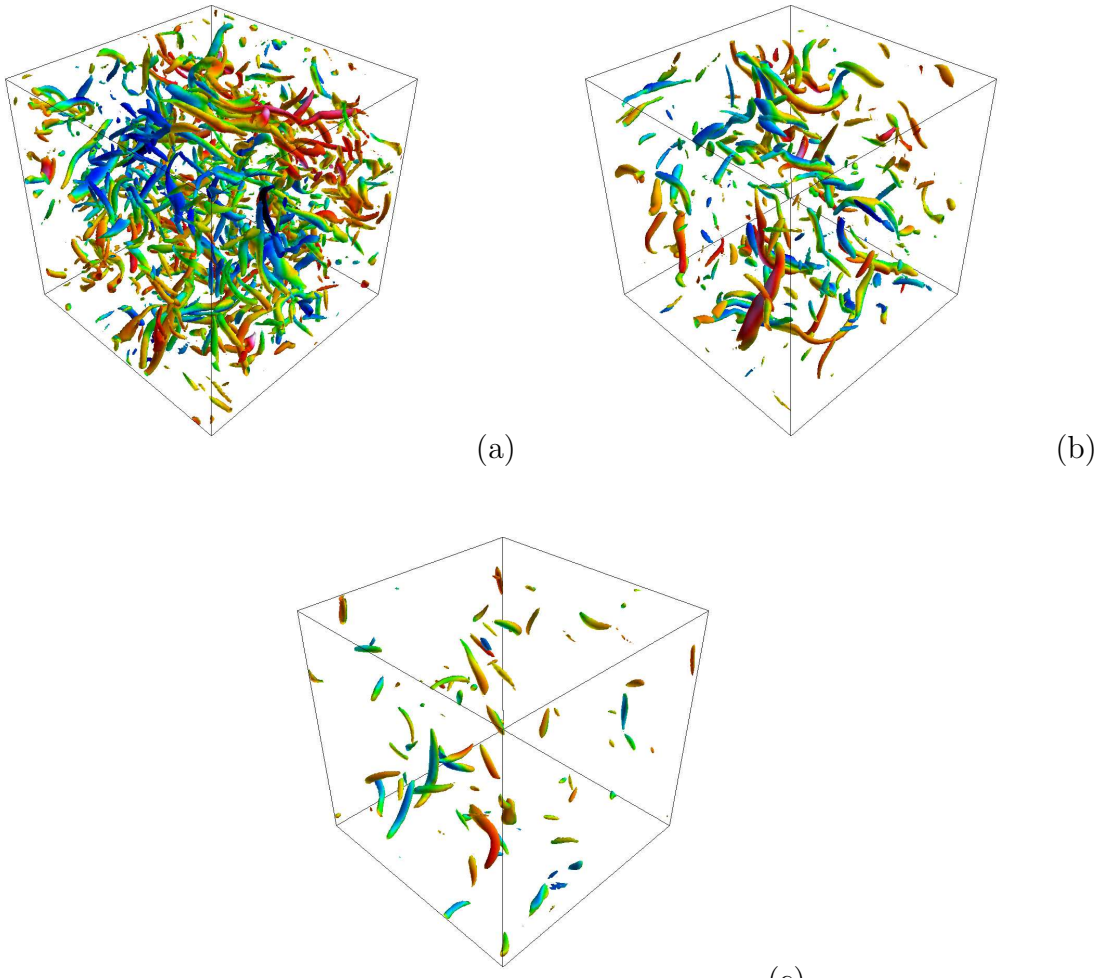

Figure 25: Decay of isotropic turbulence: Second invariant of the velocity gradient tensor at a level of $\Omega = 150$ colored with streamwise velocity in the range of -5 to $+5$ for three instants of time $t = 0, 0.42$ and 2.44.

4.7.2 Lid-driven Cubical Cavity Flow

The study of three-dimensional lid-driven cavity flows is of interest not only of its simple geometry but also the complex flow physics, such as multiple counter-rotating re-circulating regions at the corners of the cavity depending on the Re, Taylor Gortler-type vortices, flow bifurcations and transition to turbulence. A detailed review of the fluid mechanics of driven cavities is provided by [96, 68, 8].

In these flow, the Re is usually defined to be $Re = U_0 2h/\nu$, where U_0 is the maximum velocity and h is the cavity half height. At some critical Re, the turbulence develops near the cavity walls, and at Re higher than 10000, the flow near the downstream corner eddy becomes fully turbulent. The highest Re attained with experiment [96] was 10000, and with DNS [68] was 12000. These DNS and experimental studies are taken as the reference solutions to evaluate the performance of the sgs model and the numerical scheme. The sgs modeling in the case of a flow with laminar, transitional and turbulent zones represents a challenging problem.

The results presented herein correspond to the numerical simulation of lid-driven cavity flow at the Re of 12000. At this Re, turbulence develops near the cavity walls and flow near the downstream corner eddy becomes fully turbulent. The flow domain is represented in a cubical cavity where the width, the depth and the length of the domain are $2h$. The flow is driven by imposing a non-zero velocity parallel to the streamwise direction on the top wall. The other walls (i.e. the upstream and downstream walls, which are perpendicular to the streamwise direction, the side walls, which are perpendicular to the spanwise direction and the bottom wall, which is perpendicular to the wall-normal direction) remain stationary. In order to avoid severe discontinuities along the top edges due to unit velocity, the velocity on the lid (top-wall) is given by a polynomial expansion

$$u_x(x,h,z) = U_0 \left(1 - \left(\frac{x}{h}\right)^n\right)^2 \left(1 - \left(\frac{z}{h}\right)^n\right)^2, \quad u_y = u_z = 0 \tag{172}$$

In this study, n is taken as 18.

The kinetic energy is provided to the flow by the shear stress at the top lid through viscous diffusion. The high momentum fluid near the lid induces a region of strong pressure in the upper corner of the downstream wall as the flow has to change direction and moves vertically downwards. The sudden change of the flow direction dissipates energy in that region. Along the downstream wall the plunging flow behaves like a wall jet and produces two elliptical jets on both sides of the symmetry plane. These jets hit the bottom wall where they produce turbulence. This turbulence region is convected upwards by the main vortex towards the upstream wall where the flow slows down and re-laminarizes during the fluid rise. The flow is also characterized by multiple counter rotating vortices at the corners and edges of the cavity.

In this study, all simulations are conducted using $64 \times 64 \times 64$ grids. The DNS solution [68] was obtained with a Chebshev collocation method on grid composed of 129^3 collocation points in each direction. The grid used in this study has therefore twice less points per space direction than the DNS study [68]. However, it is important to note that DNS using a finite-difference solver would require more than 129^3 grid points due to the lower order of the finite-difference scheme as compared to the Chebyshev collocation method. The space discretization used in this study is equivalent to the one used for the other LES studies reported in [123, 60] for a lower Re of 10000. In order to resolve the boundary layer along the lid and both walls, the grid is stretched in all directions using 5.5% $tanh$ stretching. For LES-KSGS and LES-LDKM studies small random velocity perturbations are initially prescribed to prevent the initial k_{sgs} field becoming zero. The spatial discretization relies on the fourth-order kinetic energy conservative form for convective terms.

Before comparing the results obtained for the LES-LDKM, partial results for the no-model (without including any model effect) and LES-KSGS studies are presented

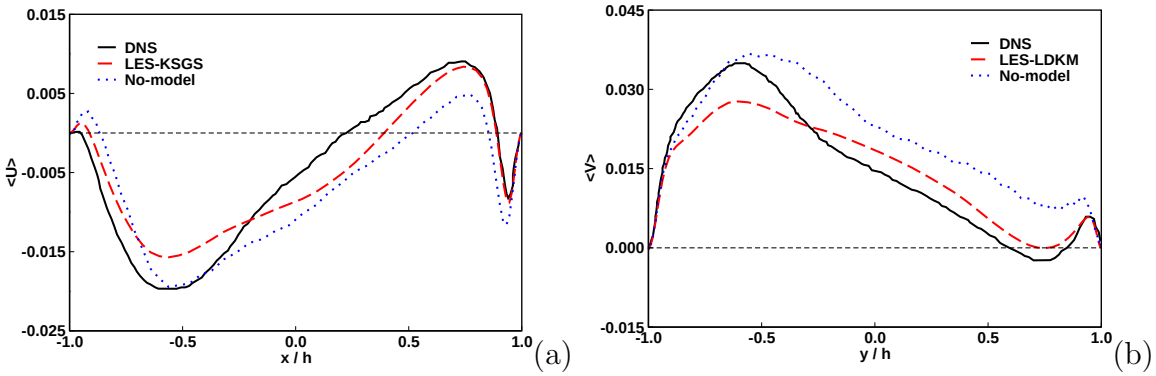

Figure 26: In the midplane $z/h = 0$: $< U >$ on the horizontal centerline $y/h = 0$ (a), $\langle V \rangle$ on the vertical centerline $x/h = 0$ (b); experiment (crosses), DNS (black), No-model (blue), LES-KSGS (red).

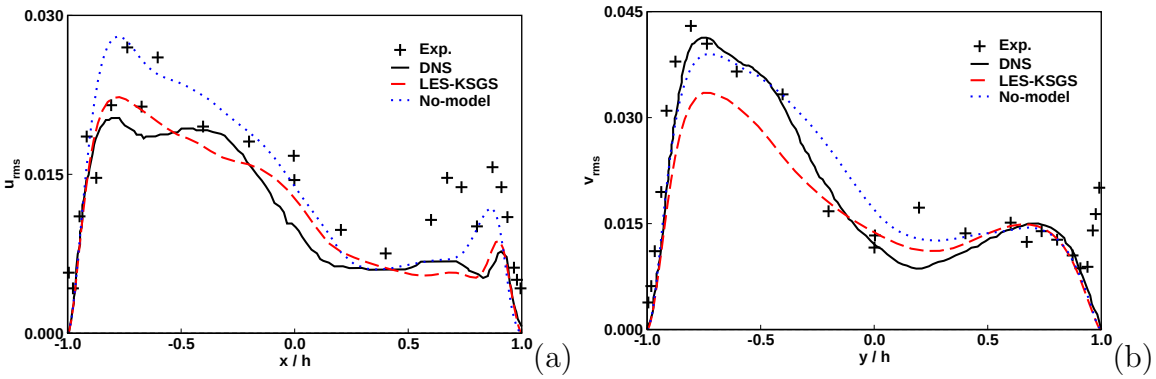

Figure 27: In the midplane $z/h = 0$: $\sqrt{\langle u^2 \rangle}$ on the horizontal centerline $y/h = 0$ (a), $\sqrt{\langle v^2 \rangle}$ on the vertical centerline $x/h = 0$ (b); experiment (crosses), DNS (black), No-model (blue), LES-KSGS (red).

first. For the LES-KSGS the value of the model constant (C_ν) is taken as its theoretical value of 0.067. The statistics for all studies are based on sampling over an integration range of $40h/U_0$ after the initial transition.

The results presented in Figs. 26 and 27 are one-dimensional profiles of the average velocity field and its fluctuations in the midplane $z/h = 0$. DNS results by Leriche [68] and experimental results by Prasad and Koseff [96] are used for direct comparison. The DNS results are presented by solid black line in the figures, whereas, dashed and dotted-dashed lines refer to the no-model and LES-KSGS, respectively.

These results show that no-model is not capable of predicting the physics of this

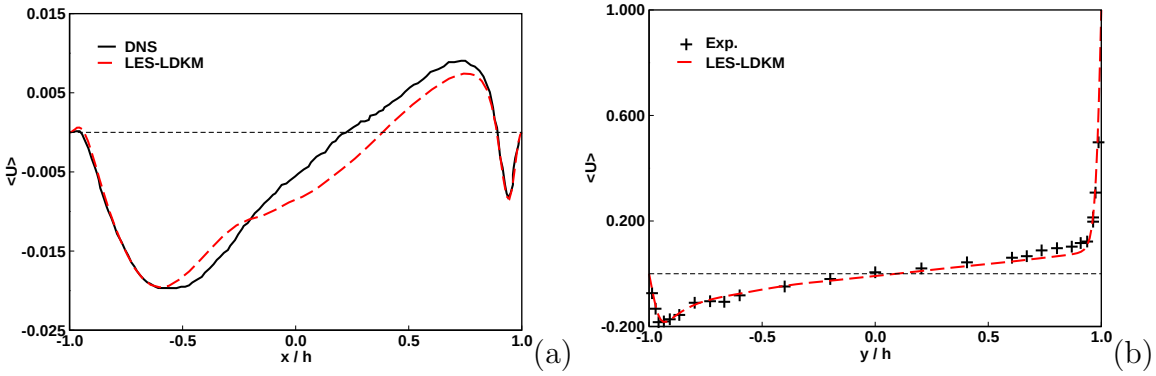

Figure 28: In the midplane $z/h = 0$: $\langle U \rangle$ on the horizontal centerline $y/h = 0$ (a), $\langle U \rangle$ on the vertical centerline $x/h = 0$ (b); experiment (crosses), DNS (black), LES-LDKM (red).

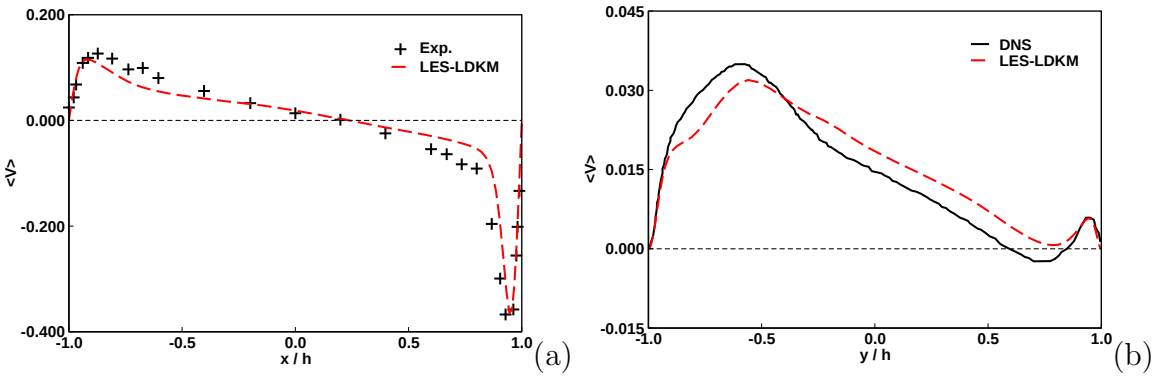

Figure 29: In the midplane $z/h = 0$: $\langle V \rangle$ on the horizontal centerline $y/h = 0$ (a), $\langle V \rangle$ on the vertical centerline $x/h = 0$ (b); experiment (crosses), DNS (black), LES-LDKM (red).

flow. Both first and second order statistics are not captured correctly by this approach. LES-KSGS shows a real improvement predicting the flow fields over no-model but still, the results do not agree well with the experimental and numerical data.

The LES-LDKM results are then compared with the DNS and experimental data. Figures 28-32 indicate that the LES-LDKM model predicts results close to the DNS results even for the rms fluctuations and Reynolds stresses.

The comparisons of the DNS results in the previous section are now extended to the whole midplane $z/h = 0$ (see Figs. 33 and 34). The DNS (left column) and the LES-LDKM (right column) results are plotted for identical series of contour levels for

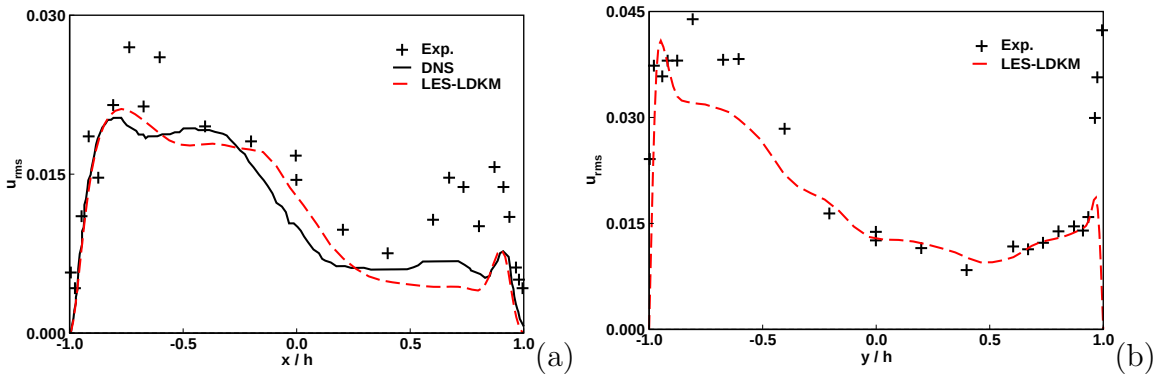

Figure 30: In the midplane $z/h = 0$: $\sqrt{\langle u^2 \rangle}$ on the horizontal centerline $y/h = 0$ (a), $\sqrt{\langle u^2 \rangle}$ on the vertical centerline $x/h = 0$ (b); experiment (crosses), DNS (black), LES-LDKM (red).

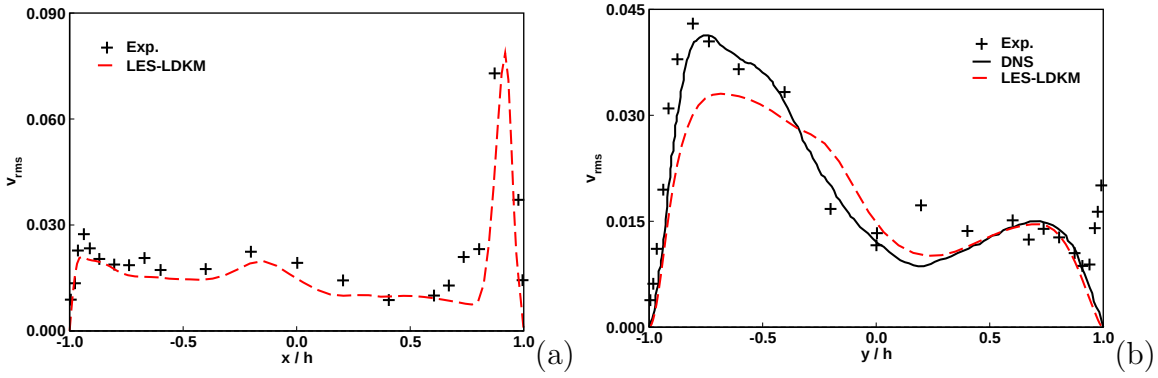

Figure 31: In the midplane $z/h = 0$: $\sqrt{\langle v^2 \rangle}$ on the horizontal centerline $y/h = 0$ (a), $\sqrt{\langle v^2 \rangle}$ on the vertical centerline $x/h = 0$ (b); experiment (crosses), DNS (black), LES-LDKM (red).

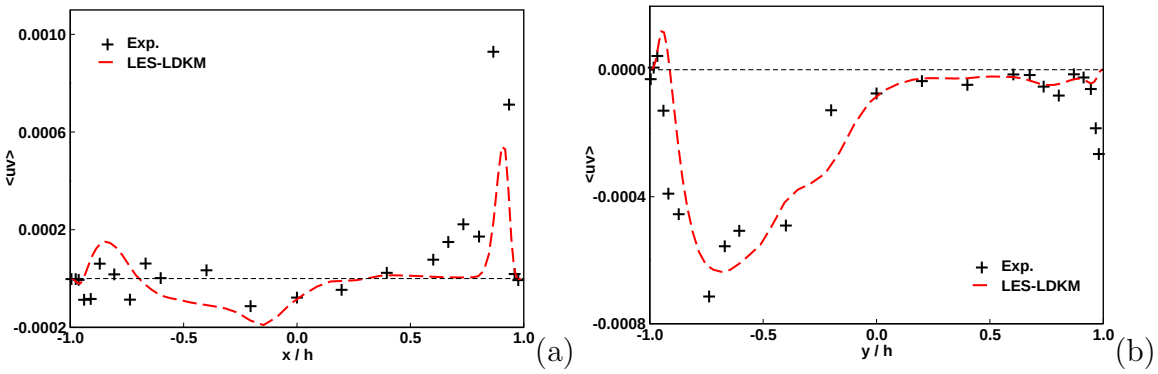

Figure 32: In the midplane $z/h = 0$: $\langle uv \rangle$ on the horizontal centerline $y/h = 0$ (a), $\langle uv \rangle$ on the vertical centerline $x/h = 0$ (b); experiment (crosses), DNS (black), LES-LDKM (red).

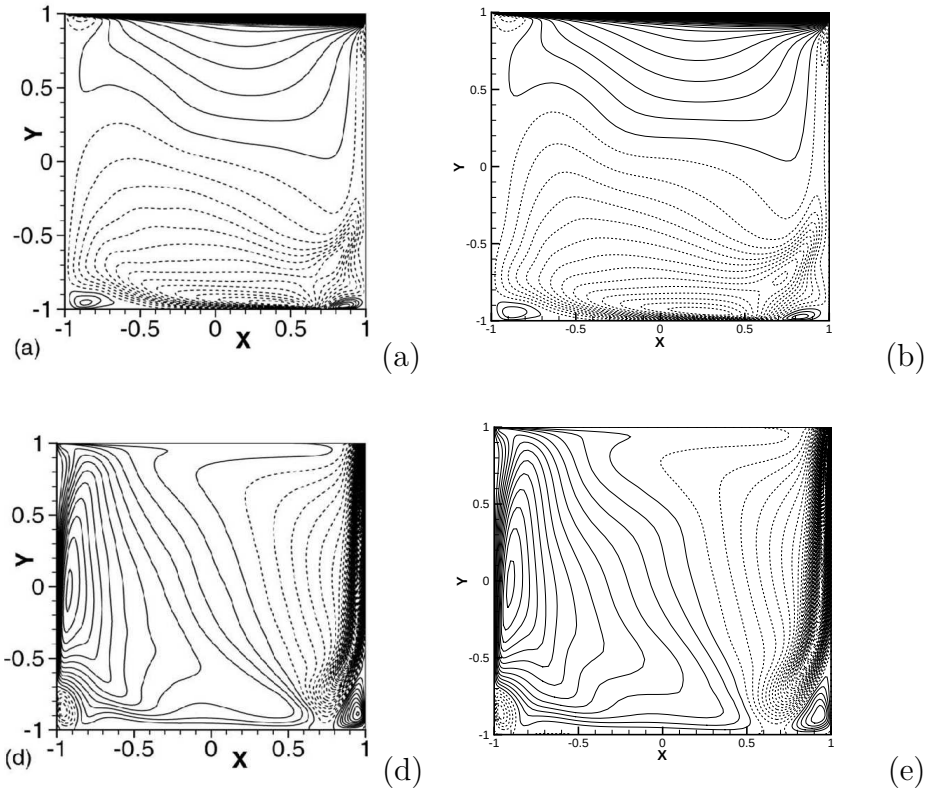

Figure 33: Contours of average velocity in the midplane $z/h = 0$; DNS (left), LES-LDKM (right); 100 contours equally spaced between -0.4 and 1 for $\langle U \rangle$(top) and between -0.7 and 0.2 for $\langle V \rangle$(bottom).

mean velocities and their fluctuations.

The results provided by the LES-LDKM are very close to the reference DNS results. Secondary corner eddies located above the bottom wall and below the lid next to the upstream wall are correctly captured in the mean flow. The high gradient region for the mean flow just below the lid is also accurately resolved. Moreover, in the downstream wall region where two elliptical jets are impinging on the bottom wall, the high gradients of velocity fluctuations are well reproduced. The maximum turbulent production occurs in this region of the flow domain.

This is further analyzed by investigating the turbulent kinetic energy and eddy viscosity in the half of the domain. It is seen that the maximum sgs kinetic energy occurs in the region where two elliptical jets are impinging on the bottom wall.

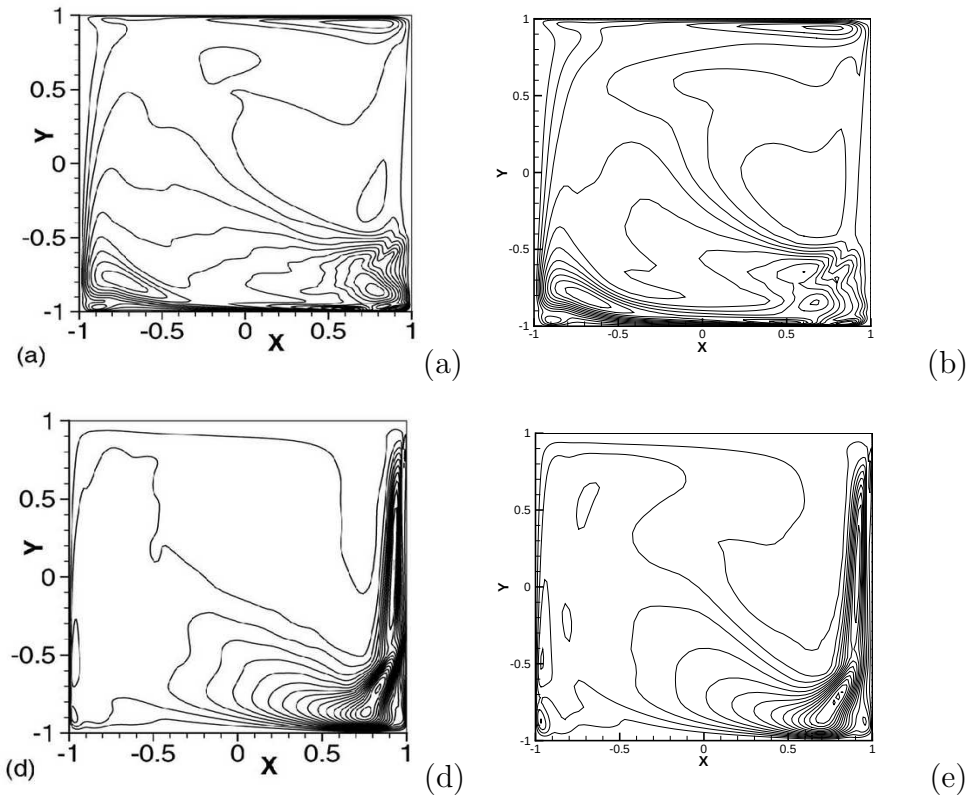

Figure 34: Contours of rms fluctuations of the velocity in the midplane $z/h = 0$; DNS (left), LES-LDKM (right); 20 contours equally spaced between 0 and 0.1 for u-rms (top) and between 0 and 0.15 for v-rms (bottom).

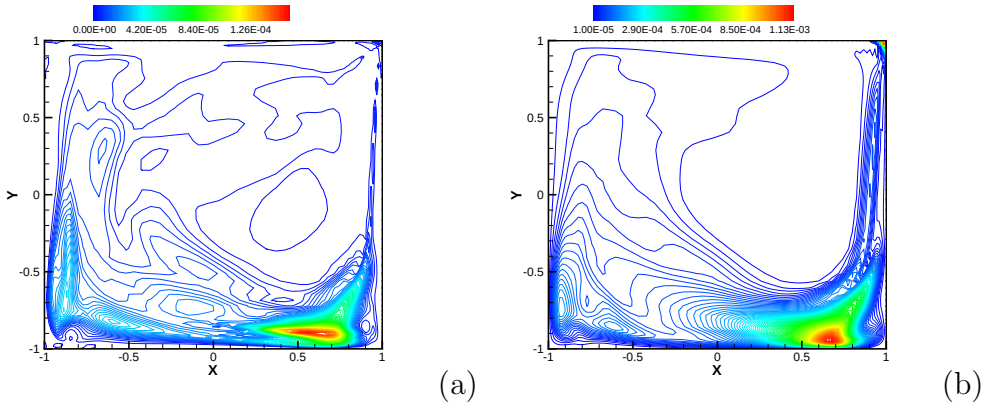

Figure 35: Contours of the averaged (a) eddy viscosity and (b) subgrid kinetic energy for LES-LDKM in the midplane $z/h = 0$.

4.7.3 Turbulent Channel Flow

The capabilities of the new flow solver are investigated next for a turbulent channel flow. The fully developed channel flow has been widely studied in the past. The flow characteristics are thus, well documented, see for example [83, 22, 44]. Therefore, the validation of the flow solver and the numerical method are possible. In this study, the results for statistically stationary flow are compared with DNS data of Moser *et* al. [83].

The fully developed channel flow of length $2\pi\delta$ and width $\pi\delta$, where δ is the channel half-height, matching the domain size of DNS of Moser *et* al. [83] is simulated by applying periodic boundary conditions in the streamwise and spanwise directions and no-slip conditions in the cross-stream direction. Flow is driven by a pressure gradient in the streamwise direction. The Reynolds number based on the friction velocity is $Re_\tau = 395$. The computational domain is discretized with uniformly distributed grid in the periodic directions and stretched grid using 4.5% *tanh* streching in the wall-normal direction to capture the boundary layers properly. To assess the capability of the solver and the LES and TLS approaches, simulations on different grids with and without the turbulence modeling are performed. Three different grids are used. The simulation parameters are summarized in Table 4.

Table 4: Simulation parameters for turbulent channel flow at $Re_\tau = 395$.

		Grid	Spatial Resolution		
			$\triangle x^+$	$\triangle y^+$	$\triangle z^+$
DNS[83]		$256 \times 193 \times 192$	10	0.029	6.5
No-model		$192 \times 151 \times 128$	12.9	0.58	9.69
LES		$128 \times 97 \times 128$	19.4	1.1	9.69
TLS	Large Scale	$64 \times 46 \times 64$	38.76	5.45	19.38
	Small Scale		4.86	0.68	2.42

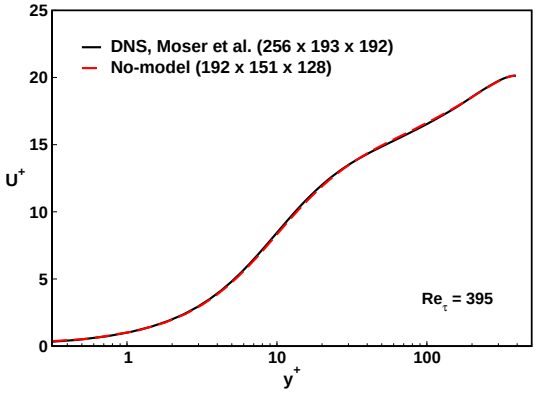

Figure 36: Mean velocity of the turbulent channel flow for no-model case (dotted line) and the DNS of Moser *et* al. [83] (solid line).

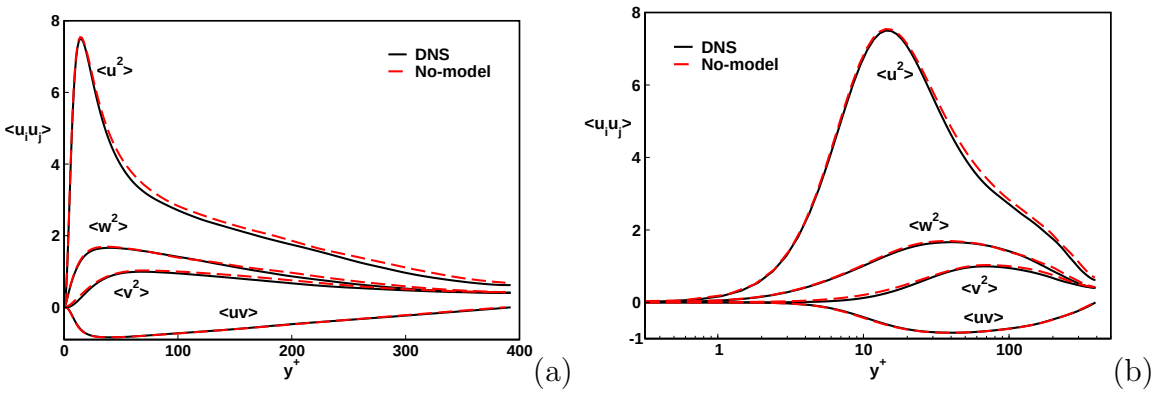

Figure 37: Rms velocity fluctuations of the turbulent channel flow for no-model case (dotted line) and the DNS of Moser *et* al. [83] (solid line).

4.7.3.1 No-model Results

Here, the results based on the no-model approach (without including any model effect) are presented first. This study is performed in order to challenge the numerical scheme for turbulent flows with periodic boundary conditions. Removal of the turbulence model is a way to test its influence on the results. While it does not bring out the errors due to the turbulence modeling, at least it provides some measure of the importance of the modeling. The computational domain is discretized by $192 \times 151 \times 128$ grid cells. Obviously the grid is too coarse to perform real a DNS study. The simulation parameters are summarized in Table 4.

The mean velocity distribution is given in Fig. 36 and compared with the DNS of Moser. The present result is in good agreement with the data. Figure 36 shows that the mean velocity profile agrees well with the DNS profile up to $y^+ = 50$. However, in the outer layer ($y^+ > 50$) the profile is over predicted due to the coarse resolution of the grid at that region.

The root mean square (rms) of velocity fluctuations are shown in Figs 36 (a) and (b) in the linear and logarithmic plots, respectively and compared with DNS [83]. The agreement between the current results and the DNS is quite satisfactory for the purpose of the code validation. There are some discrepancies in the log layer which are expected due to the coarse resolution. The Reynolds shear stress and viscous shear stress are shown in Fig. 38. The present results agree well with those of Moser *e*t al. [83]. Figures 39-40 show the Reynolds stresses and some related statistics obtained from the no-model simulation of channel flow.

For fully developed channel flow, the balance equation for turbulent kinetic energy (see appendix C) takes the following simplified form:

$$0 = P - \varepsilon + \nu \frac{d^2 k}{dy^2} - \frac{d}{dy}\langle \frac{1}{2} vu.u \rangle - \frac{1}{\rho}\frac{d}{dy}\langle vp' \rangle \tag{173}$$

Here, P denotes the turbulent kinetic energy production, ε is the pseudo-dissipation, the third term is the viscous diffusion of the turbulent kinetic energy, the fourth is the kinetic energy convection, and the last is the pressure transport. Figure 41 shows the turbulent kinetic energy budget for the viscous wall region. Overall a good agreement

Table 5: Mean flow variables for turbulent channel flow at $Re_\tau = 395$.

	Re_b	C_f	$e_0^{C_f}$
DNS[83]	13728	0.65×10^{-2}	
No-model	13905	0.62×10^{-2}	3.8%
LES	13800	0.61×10^{-2}	4.2%
TLS	13855	0.63×10^{-2}	2.5%

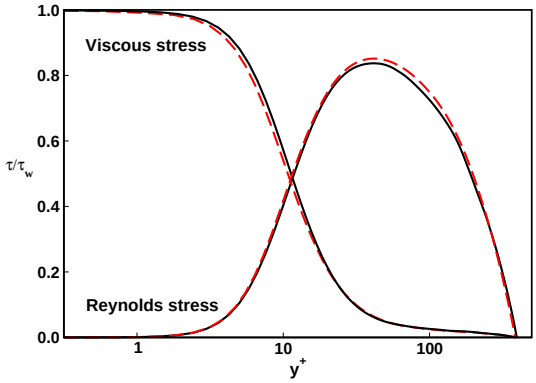

Figure 38: Profiles of shear stress and Reynolds stress of the turbulent channel flow; No-model (dotted line) and the DNS of Moser *et* al. [83] (solid line).

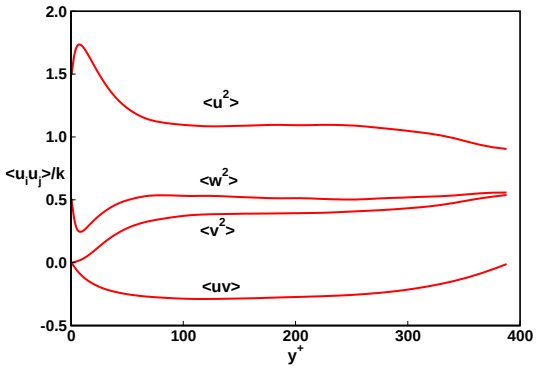

Figure 39: Reynolds stresses normalized by the turbulent kinetic energy predicted with the no-model case.

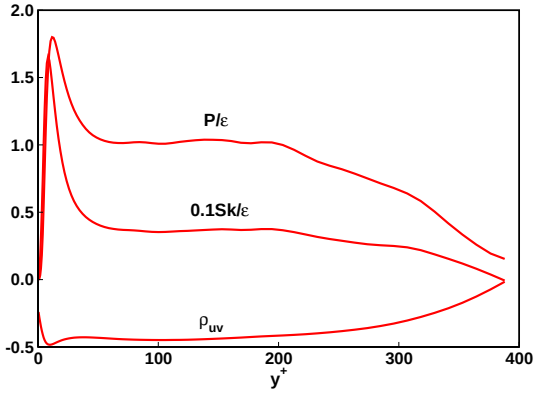

Figure 40: Ratio of production to dissipation, normalized mean shear rate, and shear stress correlation coefficient predicted with the no-model case.

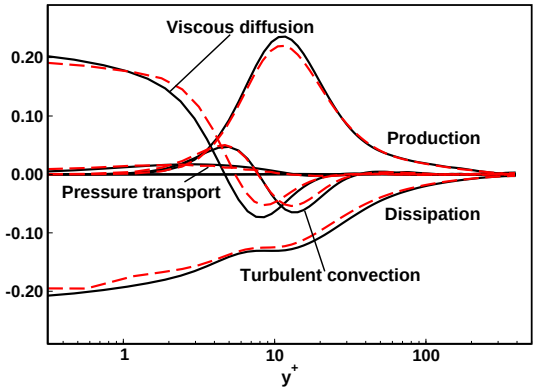

Figure 41: The turbulent kinetic energy budget in the viscous wall region of the turbulent channel flow; No-model (dotted line) and the DNS of Moser *et* al. [83] (solid line).

with the DNS [83] results is observed.

Two-dimensional velocity spectra are usually used to investigate the details about flow structures in the channel. These are shown in Figs. 42 and 43 for $y^+ = 14$ and $y/h = 1.0$, respectively and compared to DNS results for $Re_\tau = 550$ [22]. The shaded contours represent the no-model results, whereas line contours correspond to the DNS [22]. Note that this DNS domain is larger ($8\pi\delta \times 2\delta \times 4\pi\delta$) and employs a much higher resolution ($1536 \times 257 \times 1536$) than the resolution used for the no-model case ($192 \times 151 \times 128$).

2D plots (see Figs. 42 and 43) show that the energy distribution in the no-model study is qualitatively similar to the DNS with the large structures being the most energetic. The u-spectrum in the near-wall region lies approximately along the power law $\lambda_x^+ \sim (\lambda_z^+)^3$, implying that, while the structures of the streamwise velocity widen as they become longer, they also become more elongated since they progressively separate from the spectral locus of two-dimensional isotropy $\lambda_x^+ = \lambda_z^+$.

Individual one dimensional spectrum, $E^{1D}(\lambda)$, is obtained by summing $E^{2D}(\lambda_x, \lambda_z)$ either over the spanwise or the streamwise wave-numbers. The streamwise velocity spectrum (44) is slightly wider and much longer, and strongest at $y^+ = 10 - 20$ which

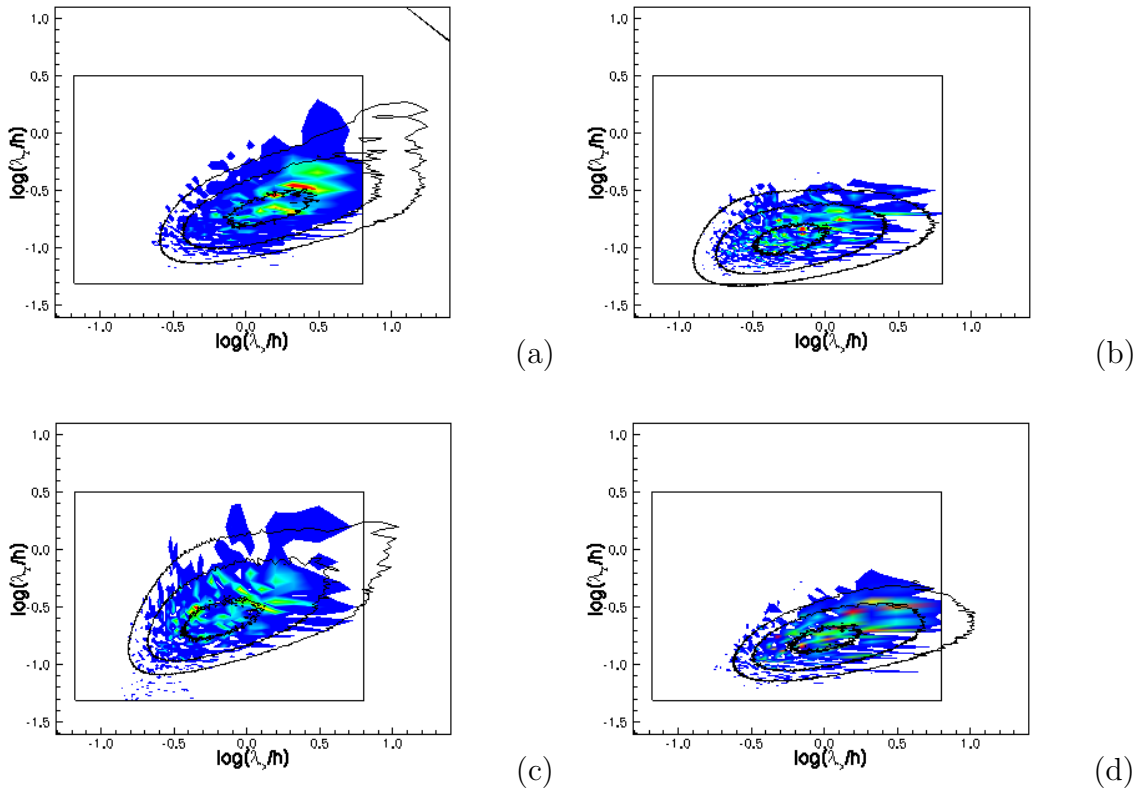

Figure 42: Premultiplied two-dimensional velocity spectra and co-spectra, $k_x k_z E^{1D}(\lambda)$ as functions of the streamwise and spanwise wavelengths. $y^+ = 14$. Shaded contours, no-model at $Re_\tau = 395$; line contours, DNS at $Re_\tau = 550$ [22]. The contours are 0.2(0.2)0.8 times the common maximum value of the corresponding spectrum for the full channel. (a) Streamwise velocity; (b) Wall-normal velocity; (c) Spanwise velocity; (d) Reynolds-stress co-spectrum.

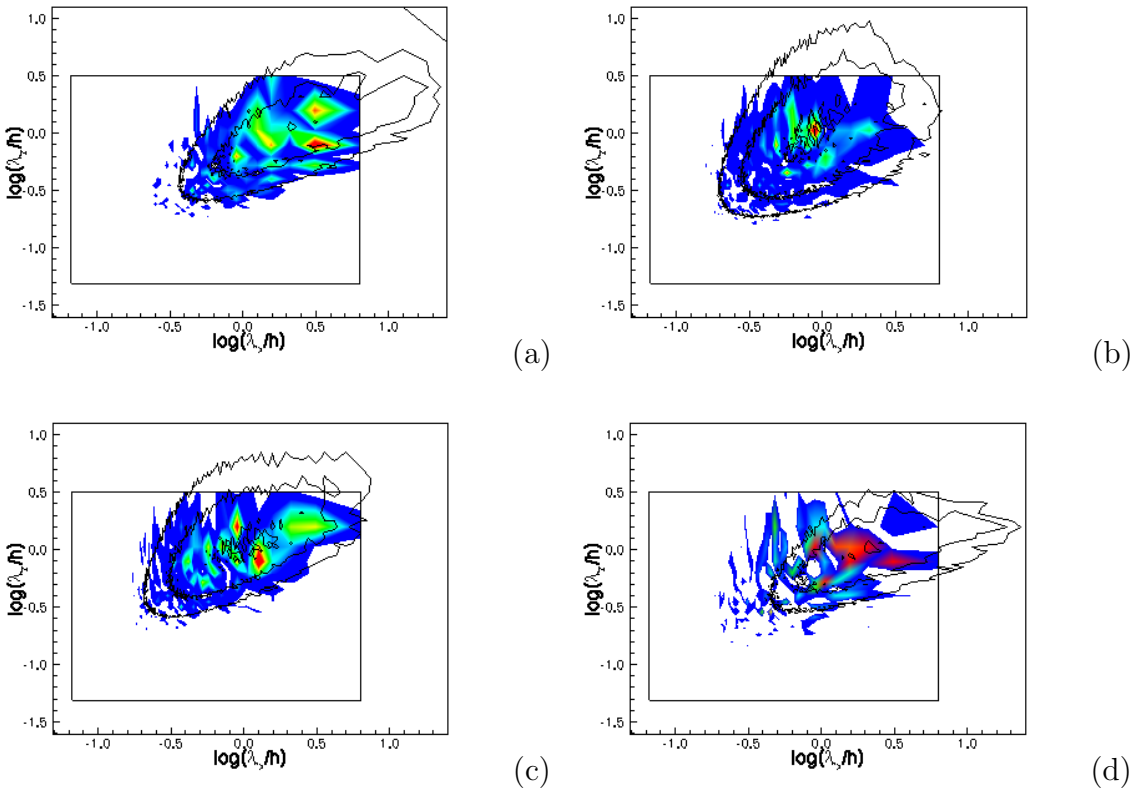

Figure 43: Premultiplied two-dimensional velocity spectra and co-spectra, $k_x k_z E^{1D}(\lambda)$ as functions of the streamwise and spanwise wavelengths. $y/h = 1.0$. Shaded contours, no-model at $Re_\tau = 395$; line contours, DNS at $Re_\tau = 550$ [22]. The contours are 0.2(0.2)0.8 times the common maximum value of the corresponding spectrum for the full channel. (a) Streamwise velocity; (b) Wall-normal velocity; (c) Spanwise velocity; (d) Reynolds-stress co-spectrum.

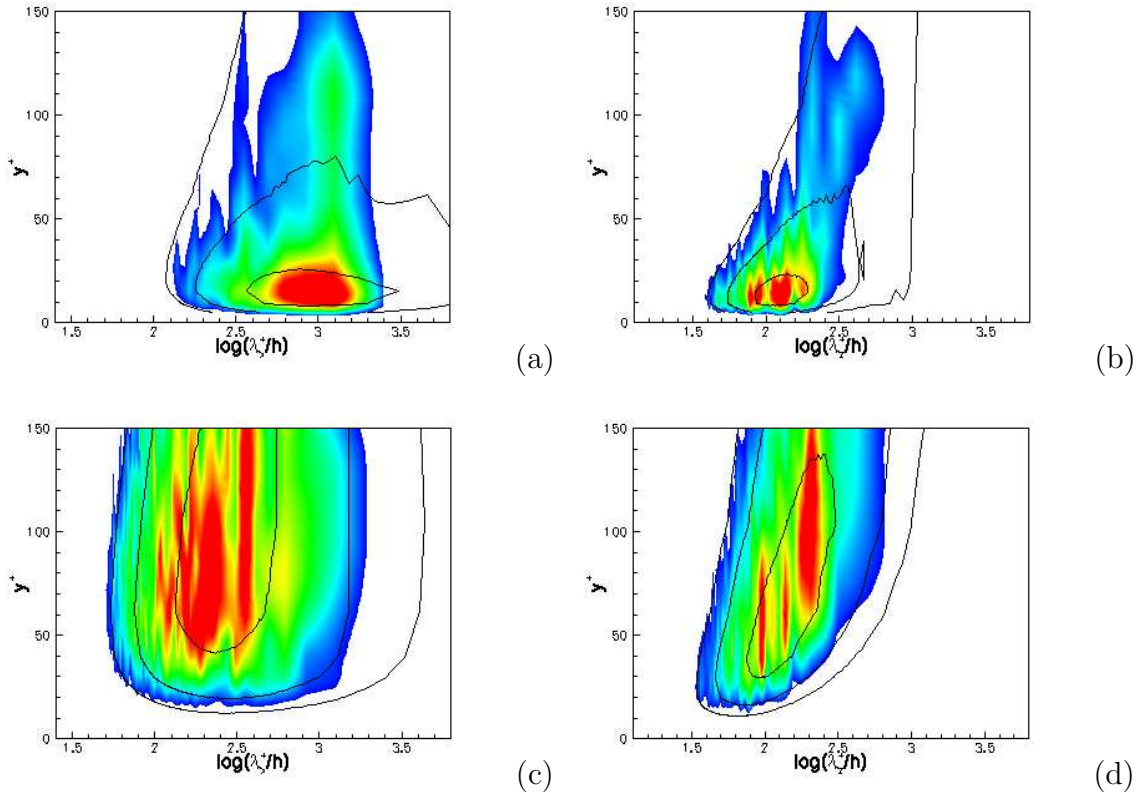

Figure 44: Premultiplied one-dimensional spectra $kE^{1D}(\lambda)$ as functions of the wavelength and of the wall distance. Shaded contours, no-model at $Re_\tau = 395$; line contours, DNS at $Re_\tau = 550$ [22]. The contours are 0.2(0.2)0.8 times the common maximum value of the corresponding spectrum for the full channel. (a,b) Streamwise velocity. (c,d) Wall-normal velocity.

can be interpreted as the signature of the near-wall streaks.

Considering the flow statistics shown in Figs. 36 - 41, the incompressible flow solver using the fourth-order kinetic energy conservation predicts reasonable agreement with the DNS of Moser *e*t al. [83].

4.7.3.2 LES and TLS Results

In order to validate the implementation of the full TLS approach, the TLS of the turbulent channel flow at $Re_\tau = 395$ is performed. The LES with LDKM subgrid model of same of flow is also performed. The flow statistics are compared to the DNS results of Moser *e*t al. [83].

As in the previous study and the DNS study of Moser *e*t al. [83], the computational domain is defined as $2\pi\delta \times 2\delta \times \pi\delta$. The computational domain is discretized with $64 \times 46 \times 64$ LS grid points for TLS and $128 \times 97 \times 128$ for LES-LDKM. The grid points are uniformly distributed in the streamwise and spanwise directions and stretched using 5% *tanh* streching in the wall-normal direction. A uniform grid of 8 SS cells per LS cell is used in the periodic directions and a variable grid of 12 near the wall to 3 in the center of the channel is used in the wall-normal direction. The full TLS approach simulated the SS field in the whole simulation domain. The simulation and mean flow properties are given in Tables 4 and 5, respectively.

Figure 45 shows the mean streamwise velocity and rms velocity fluctuations predicted with the TLS and LES approaches. LES results compared very well with the DNS [83]. It is noted that, for a given coarse resolution, the TLS approach is able to predict the mean and rms velocity profiles reasonably well.

Finally, isosurfaces of the streamwise vorticity contours are shown for LS and SS in Fig. 46 for the full TLS study. The SS vorticity is estimated at the LS grid nodes. In spite of being reconstructed only at the LS grid level, the SS streamwise vorticity demonstrates qualitatively correct near-wall structures which is populated by high-

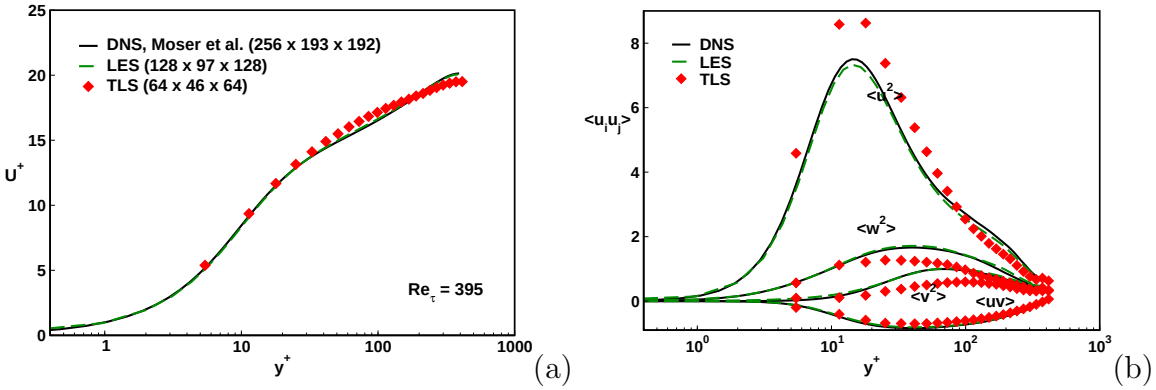

Figure 45: (a) Mean streamwise velocity and (b) rms velocity fluctuations for channel flow. TLS results are compared with those of LES and DNS [83].

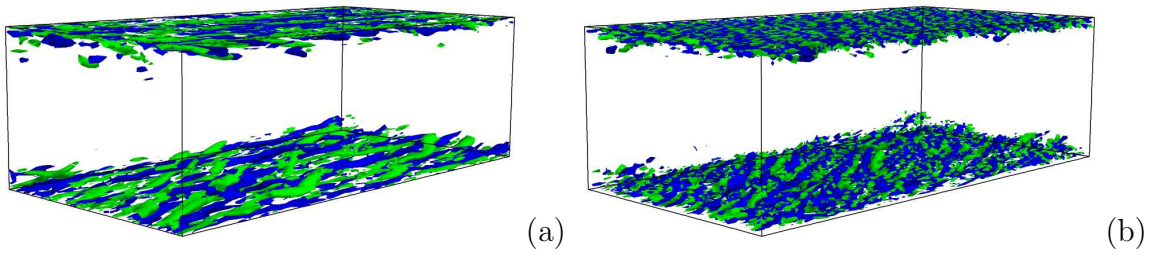

Figure 46: (a) Isosurfaces of the LS streamwise vorticity $w_x^L = +40$ (green), $w_x^L = -40$ (blue); (b) Isosurfaces of the SS streamwise vorticity $w_x^S = +1$ (green), $w_x^S = -1$ (blue).

and low-speed streaks.

This chapter addresses the numerical model development and its validation for a range of turbulent flow problems with and without walls. The kinetic energy conserving algorithm is shown to be accurate for DNS/LES studies. The numerical algorithm is shown to be robust, stable and computationally efficient for these problems. Due to the general implementation, it can be used for complex flows.

CHAPTER V

APPLICATION OF TLS-LES TO TURBULENT CHANNEL FLOWS

The fully developed channel flow is an important reference case for testing and developing numerical models. The accurate representation of the near-wall dynamics, and the prediction of skin friction are required for most of engineering applications, and flows in nature. There exists a wide range of experimental and numerical (DNS) studies for validation of models [83, 22, 44]. Therefore, this test flow is used to evaluate the behavior of the near-wall TLS-LES approach.

In this chapter, the results based on the new TLS-LES approach are presented for three Reynolds numbers: $Re_\tau = 590$, 1200, and 2400. A pseudo-spectral solver [56, 57] is used for the calculations presented in this chapter. For the new TLS-LES application, the TLS model is localized in the near-wall region and combined with the Germano's dynamic subgrid model [28] in the outer region. The details of the solver are given in the previous studies [56, 57]. However, for consistency a brief review of the solver is given first.

This chapter is organized as follows. The numerical approach for the pseudo-spectral solver along with the modeling procedure is explained briefly in §5.1. The channel flow geometry and its discretization parameters are given in §5.2. The results section contains three subsections. First, the TLS-LES parameters, such as LS and SS grid resolutions, and the extension of SS lines in the wall-normal directions are investigated in §5.3.1. Then, the TLS-LES results are compared with the full TLS and LES results for $Re_\tau = 590$ in §5.3.2. Finally, the channel flow results are extended to higher Reynolds number flows in §5.3.3.

5.1 Numerical Approach

The numerical method is similar to that used in Kemenov and Menon [56]. It is based on a second order accurate finite volume discretization of the incompressible Navier-Stokes equations. A third-order polynomial interpolation and a second-order central differencing are used for convective flux and diffusion terms, respectively. Spatial discretization is done on the staggered grid in order to ensure the decoupling between pressure and velocity. Time integration is based on third-order, low storage Runge-Kutta time stepping scheme with implicit treatment of diffusion terms in the wall-normal direction using Crank-Nicolson scheme.

In the TLS region, the SS equations are integrated with an explicit, two-step component-wise TVD scheme. In the LES region, the eddy viscosity is calculated based on Germano's dynamic model [28].

All simulations are performed on an IBM Cluster 1600 machine. The LS integrations are performed on single-processors and SS integrations are on multi-processors with the master-slave approach [56].

5.2 Geometry

The fully developed channel flow of length $2\pi h$ and width πh is simulated by applying periodic boundary conditions in the streamwise and spanwise directions, and no-slip conditions in the cross-stream direction. Here, h denotes the channel half-height. Calculations are performed for Reynolds numbers of $Re_\tau = 590, 1200$, and 2400, where $Re_\tau = u_\tau h/\nu$ and $u_\tau = \sqrt{\nu du/dy|_{y=0}}$ is the friction velocity. Near-wall TLS-LES results for statistically steady flow are compared to DNS data of [83] for $Re_\tau = 590$, [22] for $Re_\tau = 950$ and [44] for $Re_\tau = 2003$.

The computational domain is discretized by $32 \times 40 \times 32$ LS grid cells for both $Re_\tau = 590$ and 1200 with a uniform grid in the periodic directions (streamwise and spanwise) and nominal stretched grid in the wall normal direction. As the Reynolds

number increases, it is observed that only a smaller portion of kinetic energy can be captured on the LS grid. Thus, for the high Reynolds number ($Re_\tau = 2400$) case, the resolution is increased to $64 \times 50 \times 64$.

In the first part of the channel study, the effect of the SS discretization, first LS location in the cross-stream direction, and the LS extension in the TLS region is explored. Therefore, no specific parameters on the SS resolution is given here. This will be explained in more details in §(5.3.1). In the second part of the study, a uniform grid of 8 SS cells per LS cell is used in the periodic directions for all cases. Also a variable grid ranging from 12 SS cells near the wall to 10 SS cells in the last LS cell is used in the wall normal direction. The near-wall region for TLS-LES is represented by 3 LS cells extending up to $y^+ = 50$.

5.3 Results

The results are given in three subsections. In the first section, the TLS-LES parameters are investigated for $Re_\tau = 590$. The second section provides comparison of the mean and rms velocity predictions obtained by TLS-LES, TLS, and LES. Finally, in the last section, the TLS-LES results for three distinct Reynolds numbers ($Re_\tau = 590$, 1200, and 2400) are presented.

5.3.1 Investigation of TLS-LES Parameters

The LS and SS are coupled through the forcing terms and residual stresses. Thus, the correct representation of the LS plays an important role to get a physically correct SS field. For this reason, a detailed study for turbulent channel flow at $Re_\tau = 590$ is performed. Throughout the study, three important parameters are investigated: the effect of the first LS location, the SS resolution for wall-normal lines, and the extension of near-wall TLS region. The TLS-LES simulation parameters are summarized in Table 6. Both cases are discretized with $32 \times 40 \times 32$ LS grid. The effect of the first LS location in the wall-normal direction is investigated for Cases I, II, and III. In

Case I, the location of the first LS grid node is 7.685. This is increased to 9.385 for Case II, and 11.386 for Case III. Figure 47 shows that the mean velocity profile does not exhibit any major change from Case I to Case II. However, case III depicts an overprediction in the mean flow. It is seen that as the first LS grid node moves outside of the buffer layer, the friction is underpredicted. This results in an overprediction at the mean flow. The friction coefficient is thus sensitive to the first LS location, which effectively controls the turbulence intensity. Thus, the optimum value of the first LS location is found by adjusting this parameter to obtain a good match to the DNS friction coefficient and mean velocity profile (Fig. 47).

The effect of SS resolution on the first order statistics is investigated in detail for Case III, where the mean velocity is over predicted in the log-layer. The purpose of this study is to analyze the SS resolution effect on the first order statistics. For Case III, 12 SS cells are used in the near-wall region, whereas, for Cases IV and V, 16 and 14 SS cells are used, respectively.

As it can be seen from Fig. 48, the SS resolution has a minor effect on the prediction of the mean flow. This is consistent with the previous observations [57] that the LS plays the dominant role for reconstruction of the SS field. The predicted SS strongly depends on the LS field, and the SS simulation or model can not overcome

Table 6: Simulation parameters for TLS-LES of turbulent channel flow at $Re_\tau = 590$.

	LS resolution Δy^{+LS}_{min}	SS resolution Δy^{+SS}_{min}	Near-wall TLS extension
Case I	7.685	0.482	3
Case II	9.385	0.782	3
Case III	11.386	1.423	3
Case IV	11.386	0.711	3
Case V	11.386	0.948	3
Case VI	9.385	0.782	1
Case VII	9.385	0.782	2
Case VIII	9.385	0.782	5

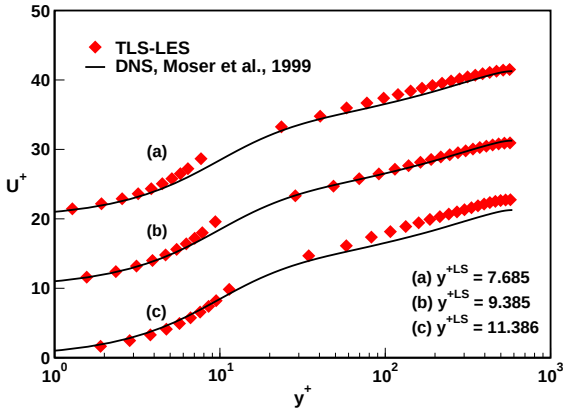

Figure 47: Sensitivity of the TLS-LES approach to the first LS location.

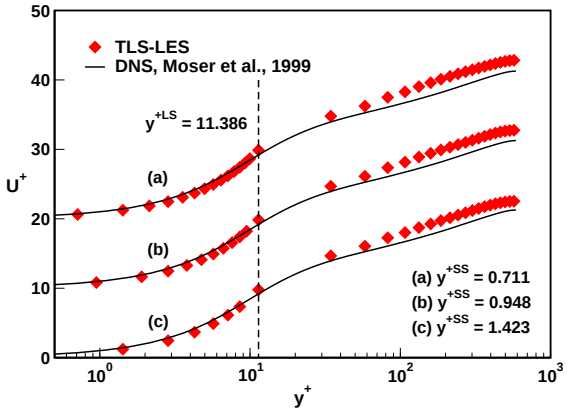

Figure 48: Sensitivity of the TLS-LES approach to the small scale resolution.

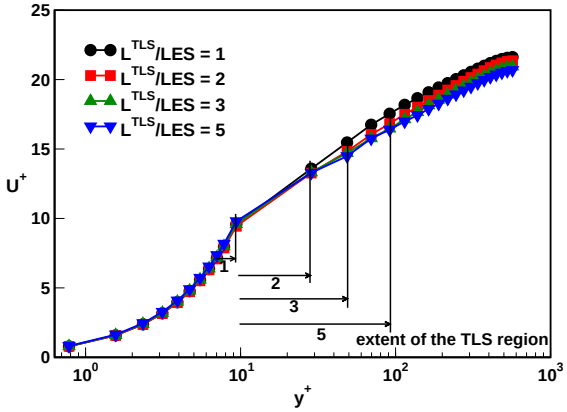

Figure 49: Sensitivity of the TLS-LES approach to the extension of the TLS region.

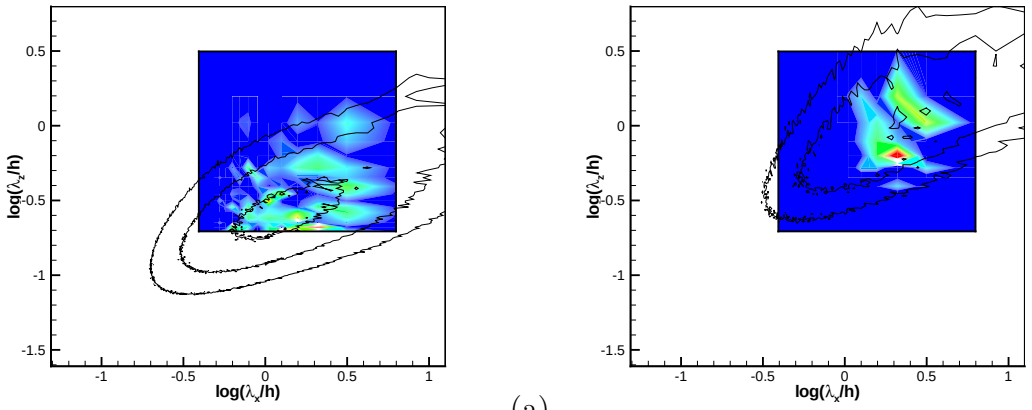

Figure 50: Premultiplied two-dimensional streamwise velocity spectra as functions of the streamwise (λ_x) and spanwise (λ_z) wavelengths at (a) $y^+ = 9.38$ and (b) $y/h = 1$. Shaded contours: TLS-LES at $Re_\tau = 590$; line contours: DNS [22] at $Re_\tau = 550$. The contours are the 0.2(0.2)0.8 times the common maximum value of the corresponding spectrum for the full channel.

the coarse LS resolution effect. Therefore, it is concluded that there is a lower limit for the LS resolution. This is consistent with earlier observations on the decaying isotropic turbulent flow presented in the chapter 2.

To determine the appropriate extension of near-wall TLS region, a simple parametric study is performed and the results are illustrated in Fig. 49. Four different simulations (Case II, VI, VII, and VIII, see Table 6 for details) are performed by keeping the LS and SS resolutions constant and by changing the near-wall TLS region. It can be seen from Fig. 49 that a considerable change is observed as the TLS region is extended from one to three LS cells, but very little difference is seen as this extension is increased to three to five LS cells.

To investigate this further, one- and two-dimensional energy spectra for streamwise velocity (see Figs. 50 and 51) are examined further. For this case, the TLS region extends to three LS cells ($y^+ = 50$). Figure 50 displays the premultiplied two-dimensional energy spectra of streamwise velocity $E_{uu} = k_x k_z \langle \hat{u}(k_x, k_z, y) \hat{u}^*(k_x, k_z, y) \rangle$

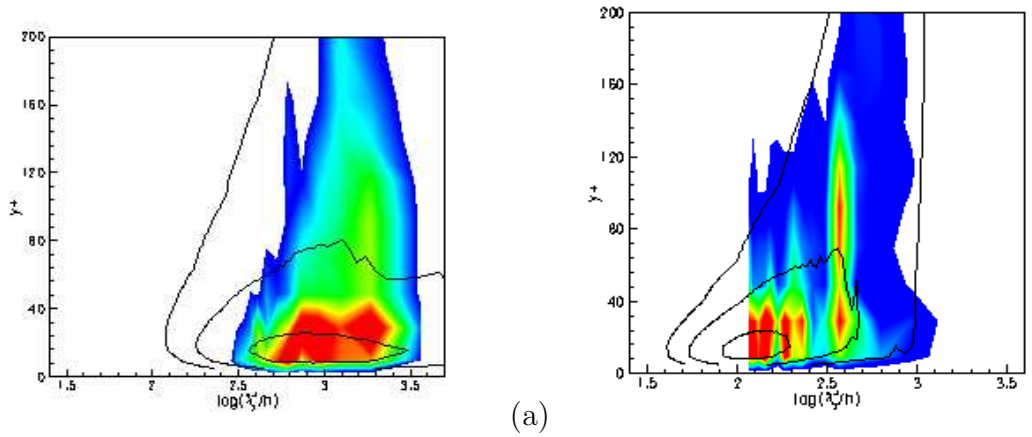

Figure 51: Premultiplied one-dimensional streamwise velocity spectra as functions of the wavelength and of the wall distance. Shaded contours: TLS-LES at $Re_\tau = 590$; line contours: DNS [22] at $Re_\tau = 550$. The contours are the 0.2(0.2)0.8 times the common maximum value of the corresponding spectrum for the full channel.

where $\hat{u}$ is the Fourier coefficient of u, and k_x and k_z are the streamwise and the spanwise wavenumbers, respectively. The two-dimensional velocity spectra is usually used to investigate the details of the flow structures in the channel flow since it provides information about the streamwise kinetic energy contained in a wavelength interval centered at λ_x and λ_z. These are shown in Figs. 50(a) and 50(b) for Case II computed at the first near-wall point ($y^+ = 9.38$) and at the half of the channel ($y/h = 1.0$) and compared to DNS results for $Re_\tau = 550$ [22]. The shaded contours represent the TLS-LES results, whereas line contours correspond to the DNS results [22]. The wall distance in the Fig. 50 (a) $y^+ = 9.3$ is the location of first LS cell. At this location, it is seen that most of the energy is not captured at the LS resolution. This resolution can be considered as a coarse resolution for LES (this will be shown in the next section). The plot shows that the energy distribution in the TLS-LES at the half of the channel is qualitatively similar to the DNS with the large structures being the most energetic. However, especially in the near-wall region, most of the energy is not captured with this LS resolution (see Fig. 50 (a)). It is believed that the SS

plays the dominant role to correct the LS effect in this region.

The wall-normal distribution of the one-dimensional u-spectrum is shown in Fig. 51. Here, Figs. 51 (a) and (b) show the $1D$ streamwise velocity spectrum ($E^{1D}(\lambda)$) obtained by summing $E^{2D}(\lambda_x, \lambda_z)$ over the streamwise and the spanwise wavenumbers, respectively. It can be seen that the streamwise velocity spectra is slightly wider and much longer, and strongest at $y^+ = 10 - 20$ which is interpreted as the signature of the near-wall streaks. These results are consistent with the earlier observation [57] that only the very near-wall energetic region needs to be resolved using TLS. The energy distribution on the wall-normal direction shows that maximum energy occurs near the wall. Therefore, the TLS region extending up to $y^+ \approx 50$ is sufficient to represent the near-wall region. As shown earlier in Fig. 49, further extension of the TLS region does not improve the mean prediction.

5.3.2 Full TLS Results

The LS and SS parameters defined for Case II are sufficient for $Re_\tau = 590$ and therefore, for the studies presented in this section, the same LS resolution of $32 \times 40 \times 32$ is used. In this section, the TLS-LES approach is compared with the full TLS approach and a conventional LES approach. The LES approach uses the dynamic Smagorinsky model based on the classical Germano identity. The full TLS approach simulates the SS field in the whole simulation domain, whereas, in the TLS-LES approach, the SS lines are restricted to the near wall region and LES subgrid modeling is used in the outer region. The simulation parameters and mean flow characteristics

Table 7: Simulation parameters for LES, TLS and TLS-LES of turbulent channel flow at $Re_\tau = 590$.

	Grid	Number of SS lines	C_f	$CPU/iter(sec)$
LES	$32 \times 40 \times 32$		0.00517	1.23
TLS	$32 \times 40 \times 32$	3584	0.00576	2.796
TLS-LES	$32 \times 40 \times 32$	2432	0.00566	2.195

are summarized in Table 7. For comparison purposes, the total number of SS lines used for TLS-LES and full TLS studies are also presented in the table.

The critical part of the TLS based approaches is the computational cost of the SS integrations. Assuming that the LS grid has resolution of $N_x^L \times N_y^L \times N_z^L$ points in each coordinate direction x, y, and z, then one needs a system of $N_x^L N_y^L + N_y^L N_z^L + N_x^L N_z^L$ SS lines to represent the SS fields in the full TLS approach. The number of SS lines can be drastically reduced in the TLS-LES approach, since the SS lines are restricted to the near wall regions. If the SS region in the TLS-LES approach represented by N_w^L points in the y direction, then the number of SS lines becomes $N_x^L N_w^L + N_w^L N_z^L + N_x^L N_z^L$ where $N_w^L < N_y^L$. Here, it has to be noted that this system of SS lines are given only for one family of lines in the TLS-LES approach. For the problems like turbulent channel flows, there are two wall-boundaries, therefore, one needs two sets of SS lines; one in the lower wall and one in the upper wall. Hence, the number of SS lines for turbulent channel flow is calculated as $2 \times (N_x^L N_w^L + N_w^L N_z^L + N_x^L N_z^L)$ which is still less than the SS lines required for the full TLS approach (see Table 7).

The computational cost of the TLS-LES model relative to the LES model depends on the Reynolds number, the LS resolution and the effective parallelization of SS integration and relative to the full TLS model depends on the number of SS lines. For a specified Reynolds number and LS resolution, TLS-LES approach is computationally more expensive than LES model because of the extra work from the SS integrations in the TLS region. However, it is noted that the LS resolution, for the studies considered here, corresponds to a wall-underresolved LES. So, it is expected that the TLS-LES approach will be computationally more effective than performing a wall-resolved LES (which requires Re_τ^2 resolution). Similarly, since the coupled TLS-LES model requires less number of SS lines, it is also computationally less expensive than the full TLS approach.

First, the mean streamwise velocities are analyzed. Mean values are obtained by

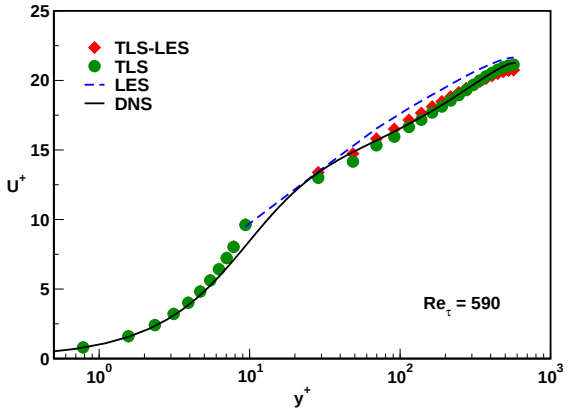

Figure 52: Comparison of the normalized mean streamwise velocity obtained from TLS-LES, TLS, LES and DNS at $Re_\tau = 590$.

averaging the streamwise velocities over all time steps for the statistical period as well as over the homogeneous directions. The mean values are non-dimensionalized by u_τ, which is calculated for each simulations. Figure 52 shows mean streamwise velocities obtained in the LES, TLS and TLS-LES studies. The DNS data of Moser [83] is used for direct comparison. Both results show considerable agreement with the DNS data. It has to be noted that there is hardly noticeable difference between TLS and TLS-LES, which confirms observations in [57]. In both approaches, the energy containing near-wall regions are simulated with the TLS approach. This is in contrast to the LES with Germano's dynamic model, which tends to overpredict the mean velocity in the log region.

The turbulent intensities for streamwise, wall-normal and spanwise velocities are shown in Fig. 53. The rms values are scaled by u_τ^2. As for the mean streamwise velocity, hardly any difference between the TLS and TLS-LES approaches can be recognized. The only noticeable difference is produced by the LES approach. As seen in the Fig. 53, the streamwise velocity fluctuation is overpredicted, whereas the wall-normal and spanwise velocity fluctuations in the outer region are underpredicted. This behavior of the Germano's dynamic model has long been known and argued to be due to the insufficient LS resolution [28].

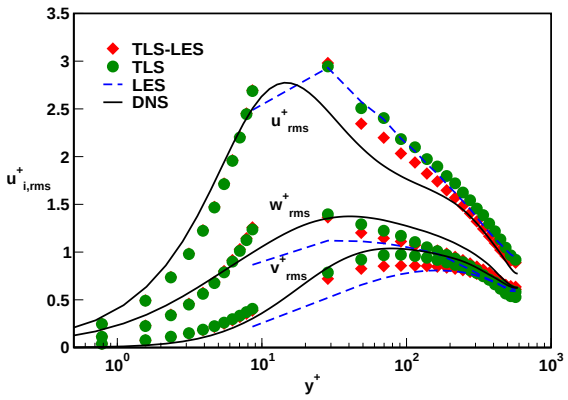

Figure 53: Comparison of the normalized rms velocities obtained from TLS-LES, TLS, LES and DNS at $Re_\tau = 590$.

Overall, the performance of full TLS model is found to be reasonably good. It is noted that TLS based models (full TLS and TLS-LES) correctly predict the location and the peak value of the streamwise rms-velocity fluctuation for $Re_\tau = 590$, but produce a broader profile. It appears that TLS-LES combines the TLS and LES results and it can be concluded that Overall, it can be concluded that TLS-LES predicts mean velocity profiles and rms velocity fluctuations similar to the full TLS but with a lower computational cost. For a similar LES resolution, the dynamic Germano's model shows more discrepancy from DNS data. Clearly, increasing the LES resolution could improve the prediction, but this is not the focus of this study.

5.3.3 TLS-LES Results

In the previous sections, the TLS-LES approach is investigated in detail for the lower Reynolds number case ($Re_\tau = 590$). Here, the TLS-LES approach is applied to much higher Reynolds number flows ($Re_\tau = 1200$ and 2400). The standard LES with dynamic Germano subgrid model is used in the outer region for TLS-LES.

Table 8 summarizes the parameters of the present simulations as well as those of the DNS studies used for comparison. A wall-resolved LES could be performed with a typical grid size of $\Delta_x^+ \approx 100$ and $\Delta_z^+ \approx 30$ with the spectral methods [89, 61].

Table 8: Simulation parameters for TLS-LES of turbulent channel flow.

	Re_τ	Grid		Spatial Resolution		
				$\triangle x^+$	$\triangle z^+$	$\triangle y^+\|_{min}$
DNS[83]	590	$256 \times 193 \times 192$		9.7	4.8	7.2(max)
TLS-LES	590	$32 \times 40 \times 32$	LS	115.78	57.89	9.38
			SS	14.48	7.23	0.78
DNS[22]	934	$3072 \times 385 \times 2304$		9.2	3.8	7.6(max)
TLS-LES	1200	$32 \times 40 \times 32$	LS	235.5	117.75	15.86
			SS	29.43	14.72	1.32
DNS[44]	2003	$6144 \times 633 \times 4608$		8.2	4.1	8.9(max)
TLS-LES	2400	$64 \times 50 \times 64$	LS	235.5	117.75	17.24
			SS	29.43	14.72	1.44

For the highest Re case, the LES resolution requires at least 128 grid points in the streamwise direction and 192 grid points in the spanwise direction which would be six times larger than the resolution used here for the LS grid in the homogeneous directions (64 for both streamwise and spanwise directions). Obviously, the wall-normal resolution used here would be too-coarse for a well-resolved LES. Here it should be noted that both cases correspond to an underresolved simulations in terms of the LS resolutions. Table 9 summarizes the number of SS lines, sampling times and computational costs of the TLS-LES studies. For both studies TLS-LES region is extended up to three LES cells near the walls. The sampling times are given in terms of turnover periods for eddies of size h and of velocity u_τ. The simulations ran on 32 processors of the IBM cluster 1600 machine. It is seen from the table that the highest Re case requires at least six times more CPU hours than the lowest Re case due to increased number of SS lines for the high Re case.

Figure 54 shows the skin friction coefficients obtained by the current approach, and its comparison with the DNS data of Moser [83] and the turbulent correlation of Dean [20]. The Reynolds number used in this plot is based on the bulk velocity

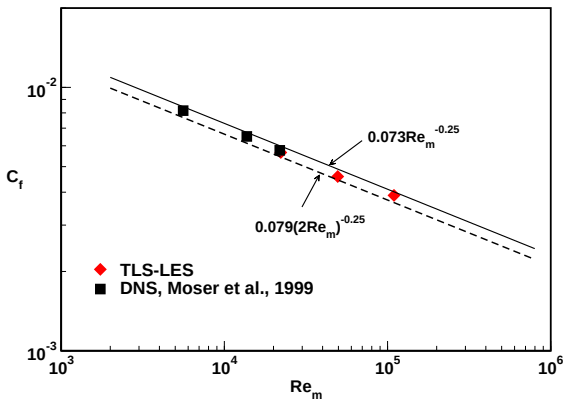

Figure 54: Near-wall mean quantities: Friction coefficient C_f.

and the channel width. The friction coefficient is defined as $C_f = 2(u_\tau/U_{ref})^2$. The present results are in good agreement with the DNS data and the empirical correlation proposed by Dean [20].

Figure 55 presents the TLS-LES results for the mean velocity profiles over the Reynolds-number range indicated in Table 8. The TLS-LES predictions are compared with the DNS data of [83], [22] and [44]. For all cases, the inner law, $u^+ = y^+$, and log law, $u^+ = 2.44lny^+ + 5.2$, are also plotted for comparison purposes.

The TLS-LES model predicts slightly higher values in the buffer region ($10 < y^+ < 30$) which might be caused by the coarse LS grid (which is chosen deliberately as a worst case scenario) employed for all Reynolds numbers. When the flow is well resolved, the details of the model are of little importance to the LS flow since most of the energy is resolved on the LS grid. For $Re_\tau = 1200$, mean streamwise velocity from

Table 9: Simulation parameters for TLS-LES of turbulent channel flow at $Re_\tau = 590, 1200$ and 2400.

	Re_τ	Number of SS lines	tu_τ/h	CPU/iter(sec)
TLS-LES	590	2432	11.3	2.709
TLS-LES	1200	2432	10.2	3.051
TLS-LES	2400	8960	9.8	13.773

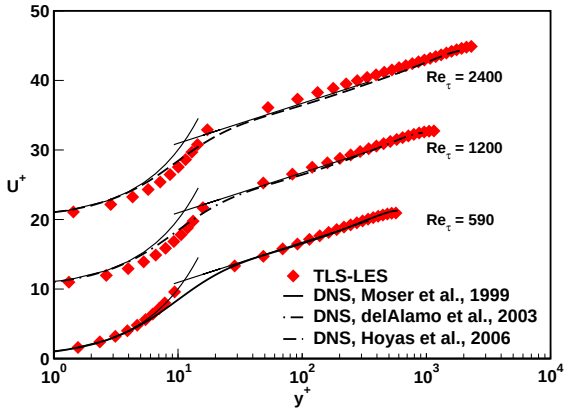

Figure 55: Near-wall quantities: Mean velocity $\langle U^+ \rangle$.

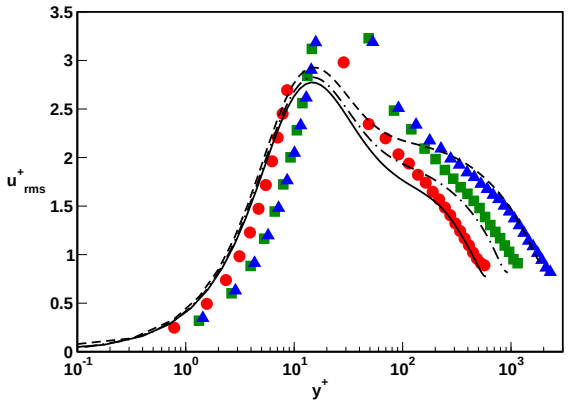

Figure 56: Comparison of the normalized streamwise rms velocities u'^+ obtained from TLS-LES (symbols) and from DNS (lines).

the TLS-LES still shows good agreement with the DNS data, but some deviations appear. The overall mean velocities are predicted quite well with the near-wall TLS-LES model. At all Reynolds numbers, the physically realistic viscous sublayer is captured reasonably well.

In Figs. 56, 57 and 58, the rms-velocity fluctuations obtained by the TLS-LES approach are compared to the DNS results of [83, 22, 44]. The streamwise velocity intensity is overpredicted in the buffer layer, whereas, the wall-normal and spanwise intensities are underpredicted. It is believed that this discrepancy is due to the coarse LS resolutions. On the coarse LS grids, the fine turbulent structures near the wall,

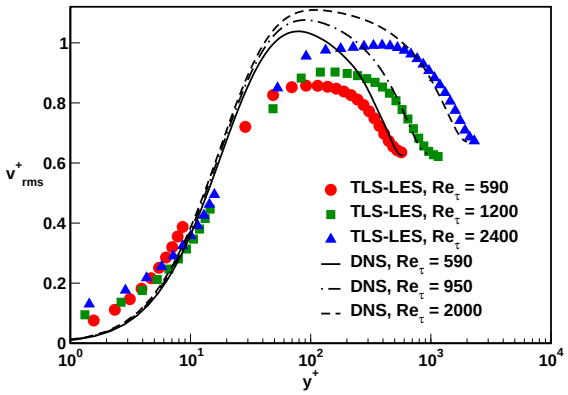

Figure 57: Comparison of the normalized wall-normal rms velocities v'^{+} obtained from TLS-LES (symbols) and from DNS (lines).

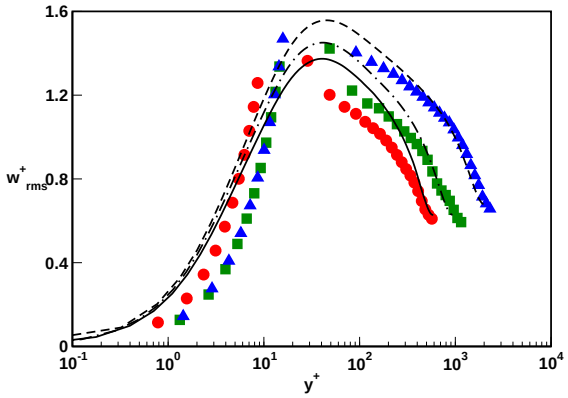

Figure 58: Comparison of the normalized spanwise rms velocities w'^{+} obtained from TLS-LES (symbols) and from DNS (lines).

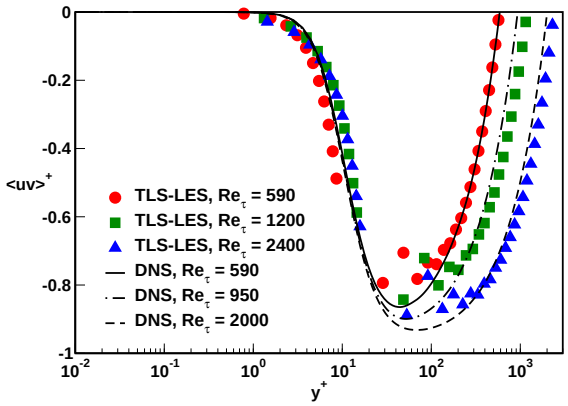

Figure 59: Comparison of the normalized Reynolds stress $u'v'^{+}$ obtained from TLS-LES (symbols) and from DNS (lines).

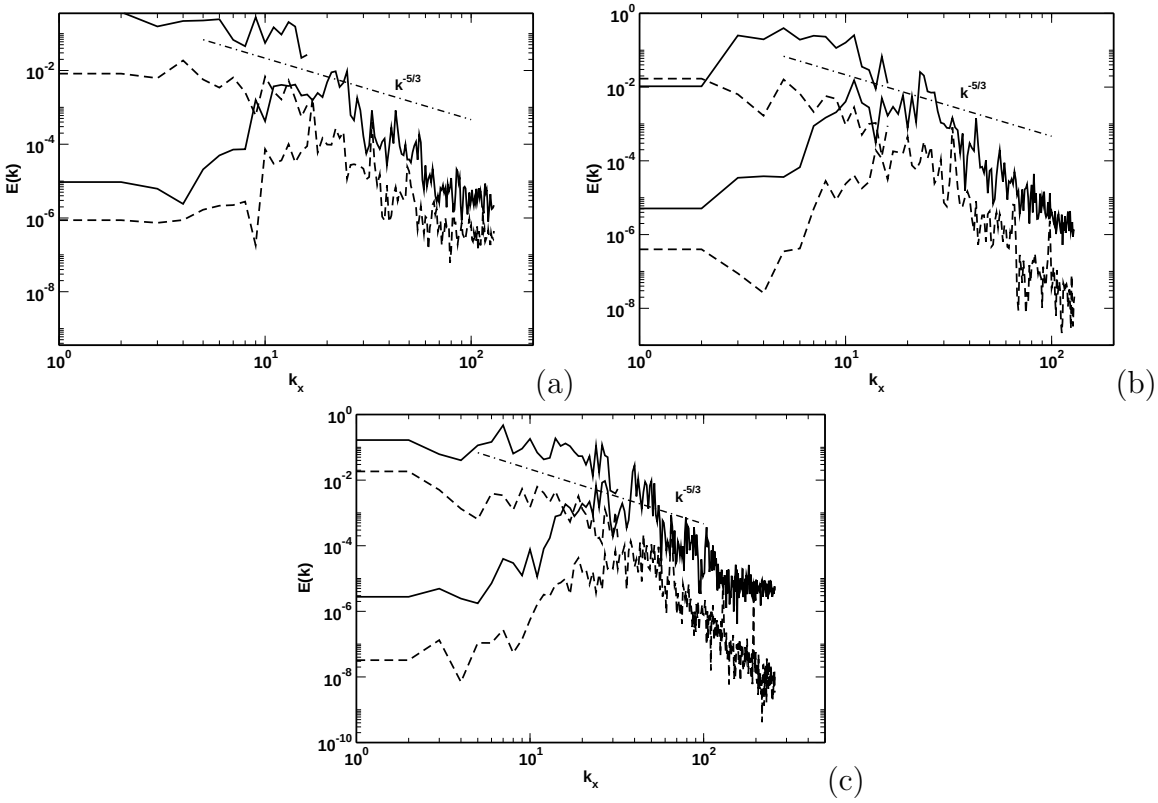

Figure 60: Instantaneous (solid lines) and volume averaged (dashed lines) streamwise spectra for (a) $Re_\tau = 590$ at $y^+ = 9.38$, (b) $Re_\tau = 1200$ at $y^+ = 15.86$ and (c) $Re_\tau = 2400$ at $y^+ = 17.23$

which generate high strain rates and thus, an important part of the skin friction cannot be represented numerically [79].

The Reynolds shear stress is shown in Fig. 59. As the Reynolds number increases, the peak value of the Reynolds shear stress increases and its position moves away from the wall.

One dimensional energy spectra of LS and SS velocities in the near-wall region are shown in Fig. 60, where k_x is the wave number in the streamwise direction. Note that along with the single spectra plane, averaged spectra over the spanwise directions are also shown. Both energy spectra show that TLS-LES approach recovers both LS and SS spectra.

Figure 61 represents the visualization of coherent eddies in turbulent channel flows

considering the regions in which the second invariant of velocity gradient tensor, defined as

$$Q = \frac{1}{2}\big(\Omega_{ij}\Omega_{ij} - S_{ij}S_{ij}\big) \tag{174}$$

$$\Omega_{ij} = \frac{1}{2}\big(\frac{\partial u_i}{\partial x_j} - \frac{\partial u_j}{\partial x_i}\big), \quad S_{ij} = \frac{1}{2}\big(\frac{\partial u_i}{\partial x_j} + \frac{\partial u_j}{\partial x_i}\big) \tag{175}$$

is positive. Here, Ω_{ij} and S_{ij} are the rate of rotation and rate of strain tensors, respectively. Since the velocity gradient tensor represents the balance between rotation and strain rate, flow visualization based on velocity gradient tensor can provide interesting evidence of direct linkage between inner and outer regions of the turbulent flow field. Furthermore, the usage of the velocity gradient tensor is justified because of the motions characterized by high rates of kinetic energy dissipation and high entropy densities are of particular interest. Figure 61 shows the computed second invariant of velocity gradient tensor at the level of $Q^L = 200$ for LS and $Q^S = 0.01$ for SS for three Reynolds numbers. It can be seen that organized tube-like fine eddies are distributed randomly over the turbulent flow field. These coherent fine eddies are assumed to be responsible for controlling self-sustained mechanism of turbulence, control of drag, and many other physical attributes in turbulence. The intensity of the coherent structures are enhanced with an increase in the Reynolds number. It has to be noted that the SS structures are similar to LS ones but with a lower magnitude and higher intensity.

Overall trend of the TLS-LES results show the capabilities of the model for near-wall applications using relatively coarse grids.

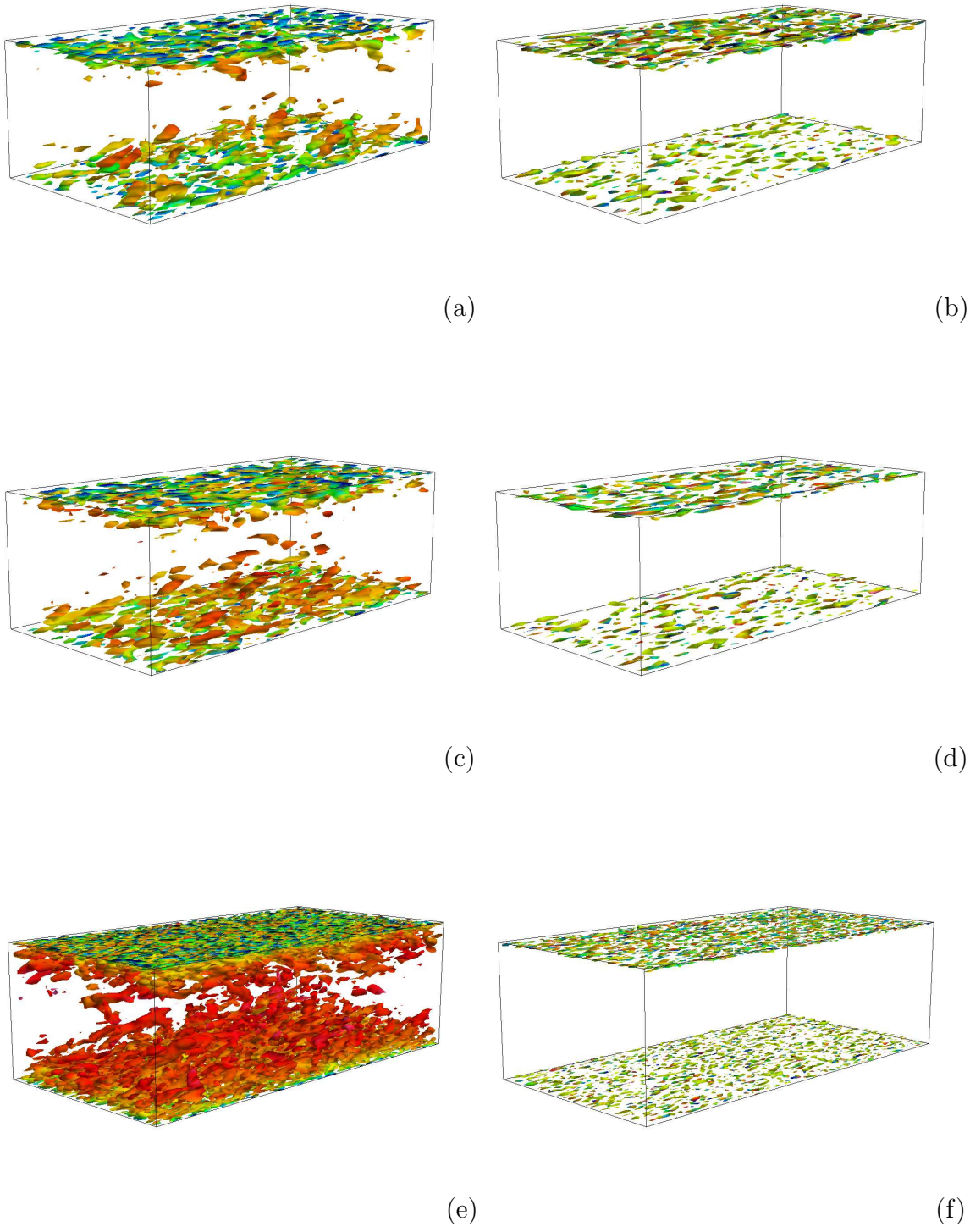

Figure 61: (a,c,e) Second invariant of the LS velocity gradient tensor at a level of $Q = 200$ colored with streamwise velocity in the range of 0 to 30 (b,d,f) Second invariant of the SS velocity gradient tensor at a level of $Q = 0.01$ colored with streamwise velocity in the range of -0.1 to 0.1 for Re_τ, 590 (a,b), 1200(c,d) and 2400 (e,f).

CHAPTER VI

APPLICATION OF TLS-LES TO TURBULENT CHANNEL FLOW WITH ADVERSE PRESSURE GRADIENT

To show the capability of the TLS-LES approach for complex geometries, the flow in a channel with a converging-diverging section at the bottom wall, investigated experimentally by Bernard *et* al. [7], is chosen. Turbulent flow in such a channel permits the examination of flow distortion due to the combined effects of the streamwise pressure gradient and the surface curvature, and therefore, offers a challenge for near-wall models. In this study, LES using an LDKM subgrid model is first performed to show the baseline capabilty of the code for complex flows. Then, this flow is simulated with the new TLS-LES approach.

6.1 Introduction

Most practical engineering flows involve combined effects of longitudinal surface curvature, streamwise pressure gradient and surface roughness. Boundary layers grow much faster on concave surfaces than on flat ones, and conversely, grow more slowly on convex surfaces. Wall shear stress is also affected by curvature, increasing on concave surfaces and decreasing on convex surfaces. Moreover, the turbulence intensities are also affected by surface curvature, increasing on the concave surface and decreasing on the convex surface.

There is a considerable number of experimental and numerical studies that have explored the combined effects of these perturbations on two-dimensional turbulent boundary layers. Baskaran *et* al. [5] and Webster *et* al. [118] have examined a

similar flow geometry in which the surface hill/bump provided significant surface curvature and streamwise pressure gradient effects. In the experiment by Baskaran *et* al. [5], the flow was separated from the downstream of the hill. However, in the experimental study by Webster *et* al. [118], the boundary layer grew rapidly on the downstream of the bump but did not separate. Generally, when there is a sudden change in boundary conditions, such as a change in the pressure gradient or surface curvature, the boundary layer responds by forming an internal layer that grows from the wall, which is shown by knee points in the turbulent stress profile. In both of these experimental studies [5, 118], it was observed that an internal boundary layer, which was triggered by the change from concave to convex surface curvature, grew in the convex region of the hill/bump. In the experiment by Bernard *et* al. [7], the adverse pressure gradient is obtained by a bump which generates first a strong favorable pressure gradient and then an adverse pressure gradient. In the experiment, care was taken to bring the boundary layer on the verge of separation but to prevent it from separating. The experiment is conducted at $Re_\tau \approx 6500$ ($Re_\theta \approx 20000$) at which the flow didn't separate.

DNS of these type of flows is very challenging because of the requirement of a very fine grid to capture the smallest intense spatial and temporal scales. Neumann *et* al. [85] have performed a DNS of flow over sharp-edged and rounded steps to investigate the effect of flow control on the flow separation. It is concluded that, to control separation the smallest structures of the flow have to be captured, which means that either a DNS or wall-resolved LES has to be used. Wu *et* al. [121] performed a LES of a boundary layer over a smooth bump, which was investigated earlier by Webster *et* al. [118]. Results show considerable agreement with the experiment, however, very small coherent structures close to the wall cannot be captured accurately due to the use of coarse resolution with an eddy viscosity type of model. Recently, Marquillie *et* al. [74] performed a DNS study over a smooth profile to investigate the effect of

pressure gradient and curvature on the turbulent structures in a channel.

In the present study, the bump shape is designed to reproduce a comparable pressure distribution as in the experiment by Bernard *e*t al. [7]. However, the Re of the simulation used in this study and in the DNS study of Marquillie *e*t al. [74] is one order of magnitude lower than the experiment. For this Re, a slight separation on the bump but not at the opposite wall is observed in the DNS [74], which allows a comparison of the statistics of turbulence in the two configurations.

6.2 Geometry

The adverse pressure gradient is created by a surface bump with concave and convex regions. The geometry of the whole simulation domain is shown in Fig. 62. The inlet plane is located at $x = 0$ where the channel height is 2δ. The bump is characterized by a convex surface between $x = 2.4\delta$ and $x = 5.4\delta$ with two concave regions at the front and at the rear. The length of the computational domain is chosen the same as in the study of Marquillie *e*t al. [74], as $L_x = 4\pi\delta$. Within this length, the outflow boundary condition effect can be negligible. Nevertheless, the flow at the outflow cannot recover the canonical channel flow as in the inflow [74]. The spanwise width is chosen as $L_z = \pi\delta$, matching the spanwise length in Marquillie *e*t al. [74].

Simulations are performed on two different meshes. For all cases, the streamwise and spanwise directions are discretized with uniform grids. In the wall-normal direction, the grid points are moderately stretched towards both solid walls using a *tanh*

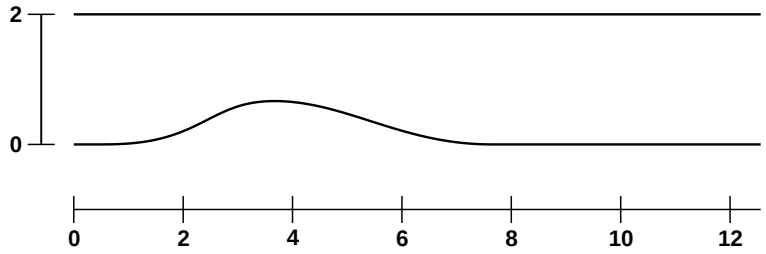

Figure 62: Channel geometry with converging-diverging section in the lower wall.

Table 10: Simulation parameters for channel flow with adverse pressure gradient.

		Grid	Spatial Resolution		
			$\triangle x^+$	$\triangle y^+$	$\triangle z^+$
DNS[74]		$1536 \times 257 \times 384$	3	4.8(max)	3
LES		$128 \times 97 \times 128$	35	1.2	9.8
No-model		$64 \times 46 \times 64$	77.4	5.4	19.2
TLS-LES	Large Scale	$64 \times 46 \times 64$	77.4	5.4	19.2
	Small Scale		9.6	0.68	2.42

function. For the near-wall TLS-LES case, the number of grid points is less than 75% of the grid that is used in the DNS study ($\approx 151M$) [74]. We will compare the results from a set of three simulations for which the grid and the turbulence model are varied, see Table 10.

6.3 Boundary Conditions

At the walls, no-slip boundary conditions are assumed for the velocity and zero gradient boundary condition for pressure. At the inflow, a time dependent inflow velocity vector is prescribed. This time dependent inflow data are taken from a separate simulation of fully developed turbulent channel flow (details of this will be given in the next section). At the outflow boundary, a convective boundary condition

$$\frac{\partial u}{\partial t} + U_c \frac{\partial u}{\partial x} = 0 \tag{176}$$

is prescribed. The convective speed (U_c) is calculated so that overall mass conservation is maintained (i.e., the mass flux through the outflow boundary equals to the mass flux through the inflow boundary). The outflow pressure is extrapolated from interior cells. Periodic boundary conditions are assumed on the spanwise direction.

6.4 Inflow Turbulence

The inflow boundary condition is obtained from LES and TLS-LES of plane channel flow at $Re_\tau = 395$, based on friction velocity. This database is then used as an inflow

Table 11: Simulation parameters for inflow turbulent channel flow at $Re_\tau = 395$.

		Grid	Spatial Resolution		
			$\triangle x^+$	$\triangle y^+$	$\triangle z^+$
DNS[83]		$256 \times 193 \times 192$	10	0.029	6.5
LES		$128 \times 97 \times 128$	19.4	1.1	9.69
TLS-LES	Large Scale	$64 \times 46 \times 64$	38.76	5.45	19.38
	Small Scale		4.86	0.68	2.42

data for the actual simulations of the channel flow with adverse pressure gradient.

The inflow channel simulations are conducted in a domain size of $2\pi\delta \times 2\delta \times \pi\delta$ which is spatially discretized using $128 \times 97 \times 128$ grid points for LES and $64 \times 46 \times 64$ for TLS-LES. The LDKM sgs model is used for LES and for TLS-LES in the outer region. The grid points are uniformly distributed in the homogeneous directions, and moderately clustered using 5.6% *tanh* streching in the wall-normal direction. The simulation parameters are given in Table 13. In the TLS-LES, the interface location is pre-defined in advance so that the TLS SS region extends up to $y^+ \approx 30$. After the initial transient, simulations are integrated and statistically averaged over a physical time of 27.5 s and 16 s which correspond to approximately 88 and 52 flow-through times for LES-LDKM and TLS-LES, respectively. For one flow-through time, around 0.022 and 0.012 for a single quad-core hours per iteration per grid point are needed on a Cray XT4 cluster for TLS-LES and LES-LDKM, respectively. Although the TLS-LES model is expensive it is still considered substantially lower than a conventional LES model that employs a well wall-resolved LS grid.

Figure 63 shows the results for the channel flow simulations. The mean velocity profiles and turbulent fluctuations obtained with LES-LDKM and TLS-LES show good agreement with the classical DNS data [83]

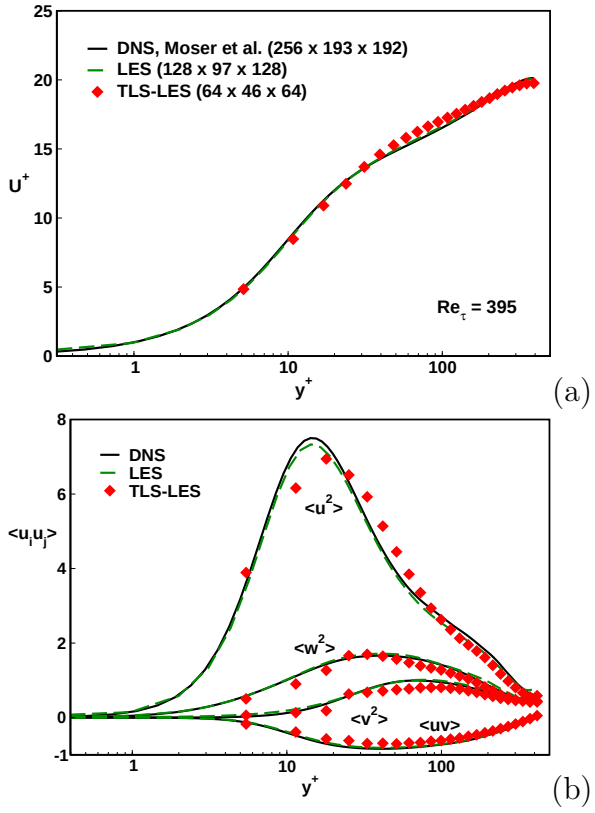

Figure 63: (a) Mean streamwise velocity and (b) rms velocity fluctuation for channel flow. LES and TLS-LES results are compared with DNS [83].

6.5 Results

The fully developed turbulent channel flow field is introduced at one bump height upstream of the forward curvature. The flow is then subject to three changes in the sign of streamwise pressure gradient and four changes in the sign of surface curvature. In general, an adverse pressure gradient and concave surfaces destabilize a boundary layer while favorable pressure gradient and convex surfaces tend to attenuate turbulence.

In the following section, the LES results obtained with a fine-grid resolution will be presented first in order to show the capability of the solver to produce DNS comparable results with the LES-LDKM model. Then, the TLS-LES results will be given for a coarse-grid simulation, and compared with case without any model (No-model)

and the fine grid LES case.

All simulations are performed on an Cray XT4 cluster. The simulations are integrated and statistically averaged over a physical time 2.34 s and 3.37 s which correspond to approximately 3.8 and 5.6 flow-through time for LES-LDKM and TLS-LES, respectively. For a single flow-through time, around 0.43 and 0.64 single quad-core hours per iteration per grid point are needed for LES-LDKM and TLS-LES. Although the computational cost of the TLS-LES model is significant, it is still considered substantially lower than a conventional LES model that employs a well wall-resolved grid. For high Re flows this advantage is beneficial and critical.

6.5.1 LES Results

The bump flow, in spite of the geometrical simplicity, is complex and three-dimensional. The vorticity contours show the complex three-dimensionality of the flow (see Figs. 64 and 65). Figure 65 shows the near-wall streaks for lower and upper wall. Near the summit of the bump, low and high speed streaks are present but they are shortened by the separation. The destruction of the streaks in the separation region has been pointed in the previous DNS studies for highly separated boundary layer flow [84] and in the DNS study of [74] for thin separated region. A similar behavior is also observed in the LES-LDKM study. On the upper wall, the situation is similar but less significant. In the diverging section, short low speed streaks are visible, but with a perceivable difference in structure between the upper and lower walls.

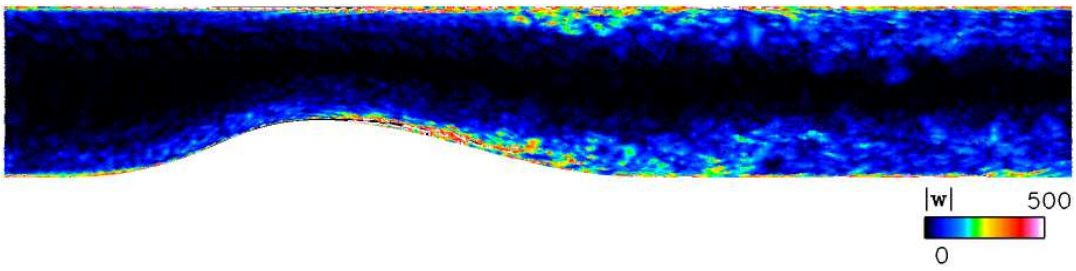

Figure 64: Vorticity magnitude predicted with LES-LDKM.

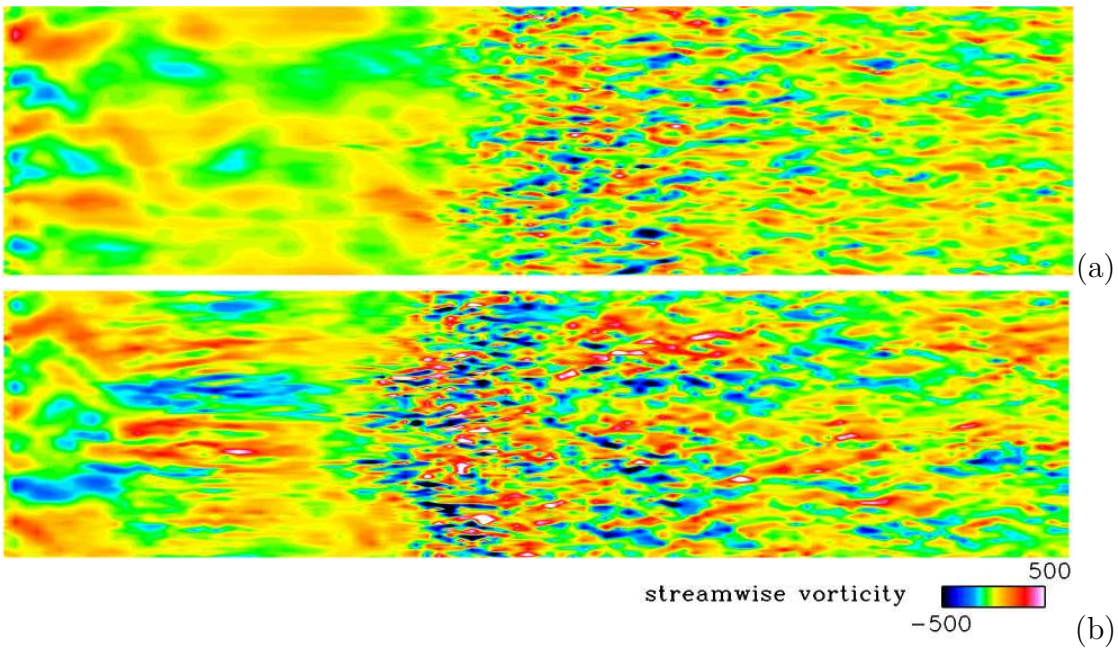

Figure 65: Streamwise vorticity contours in a plane at $y^+ = yu_\tau/\nu = 5$ from (a) the upper wall and (b) the lower wall predicted with LES-LDKM.

The surface static pressure coefficient is defined as

$$C_p = \frac{\langle P \rangle - \langle P_{ref} \rangle}{\frac{1}{2} U_{ref}^2} \tag{177}$$

where U_{ref} is the maximum velocity at the inlet, and P_{ref} is a reference pressure near the outlet ($x/\delta = 12$, $y/\delta = 1$). The pressure coefficient of the current LES-LDKM is compared with the DNS data of Marquillie *et* al. [74] and the experiment of Bernard *et* al. [7] in Fig. 66. The agreement is reasonably good. The streamwise pressure gradient is mildly adverse over the upstream channel, hence C_p increases slowly. From the middle of the upstream concave surface to the bump summit, C_p decreases monotonically to its minimum value. At this point the pressure gradient is favorable. The minimum value at the summit of the bump is predicted 30% lower for the DNS [74] and the current LES, as compared to the experiment [7]. The difference between the numerical and experimental studies is expected since the Re and inflow conditions are not identical. Downstream of the bump summit, the pressure gradient becomes strongly adverse and changes to mildly favorable over the exit channel.

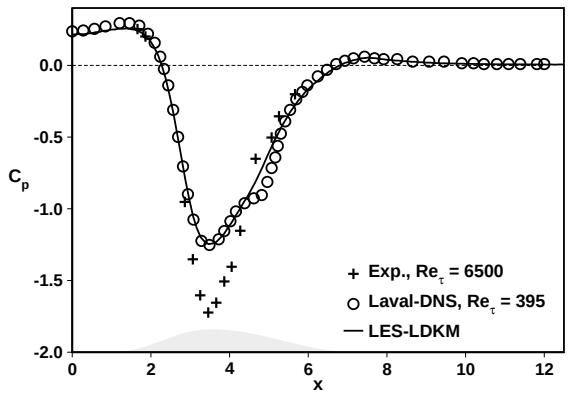

Figure 66: Pressure coefficient predicted with the LES-LDKM. The bump profile at the lower wall is plotted in Grey as reference.

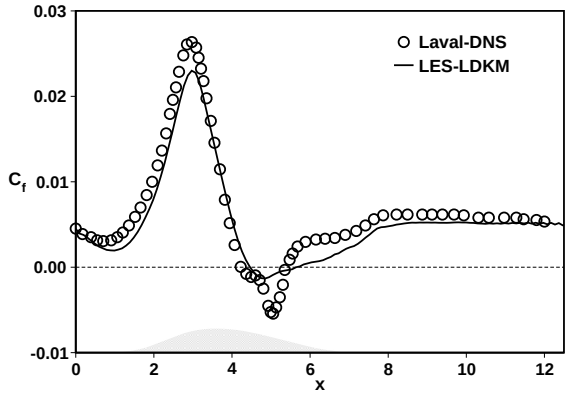

Figure 67: Skin friction coefficient predicted with the LES-LDKM.

The surface skin friction coefficient;

$$C_f = \frac{\tau_w}{\frac{1}{2}U_{ref}^2} \tag{178}$$

(with $\tau_w = \mu \frac{d\langle U \rangle}{dy}|_{y=0}$) is shown in Fig. 67. The friction coefficient exhibits an interesting response to the combined effects of pressure gradient and curvature. In this study there are two pressure gradient changes, which are from adverse to favorable. Two sudden jumps in C_f are found at the locations where the pressure gradient changes from adverse to favorable, as in [118]. C_f tends to decrease when a flow is subjected to adverse pressure gradient or convex curvature and tends to increase for a favorable pressure gradient or concave curvatures. Based on the adverse pressure gradient

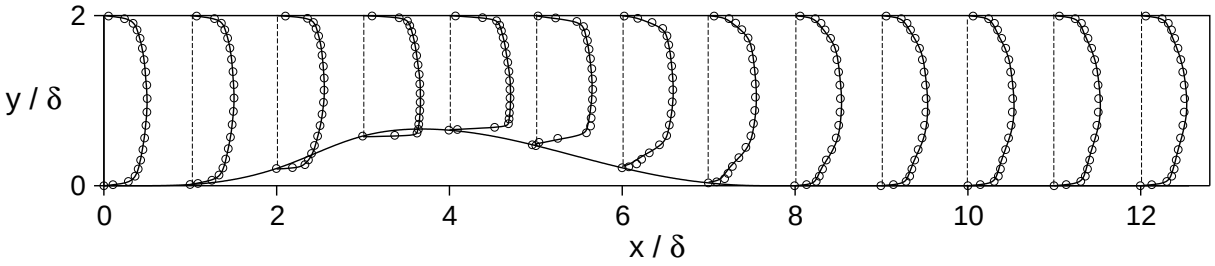

Figure 68: Profiles of mean streamwise velocity $x/\delta + 0.5 \times U/U_c$; LES-LDKM (solid lines) and DNS [74] (symbols).

alone, the wall shear stress should decrease for $0 < x/\delta < 1.25$ (adverse $\bigtriangledown p$), increase for $1.25 < x/\delta < 3.6$ (favorable $\bigtriangledown p$), decrease for $3.6 < x/\delta < 7.5$ (adverse $\bigtriangledown p$) and increase thereafter. If the effect of pressure gradient is ignored, the wall shear stress should decrease in the upstream of the bump because of the increasing Re, increase for $0.5 < x/\delta < 2$ because of concave curvature, then decrease for $2 < x/\delta < 5$ due to convex curvature, increase for $5 < x/\delta < 7.5$ because of concave surface and decrease in the downstream channel.

From Fig. 67 the combined effect of the pressure gradient and the surface curvature on the skin friction can be seen clearly. The decrease for $0 < x/\delta < 0.5$ is consistent with both the effects of curvature and streamwise pressure gradient. The increase for $0.5 < x/\delta < 1.5$ is due to the dominance of concave surface over adverse pressure gradient. C_f keeps increasing for $1.5 < x/\delta < 2$, which is consistent with both effects. The favorable pressure gradient causes C_f to increase at $2 < x/\delta < 3$ as well. Then between $3 < x/\delta < 3.5$, C_f starts to decrease due to the dominance of convex curvature over favorable pressure gradient. The decrease for $3.5 < x/\delta < 4.5$ is consistent with both adverse pressure gradient and convex curvature effect, the flow separates in this region. Finally, the increase for $5 < x/\delta < 7.5$ is because of the dominance of concave curvature over adverse pressure gradient where the intense vortices evolving close to the bump strongly decrease the skin friction.

Wall-normal profiles of mean streamwise velocity are compared with the DNS data

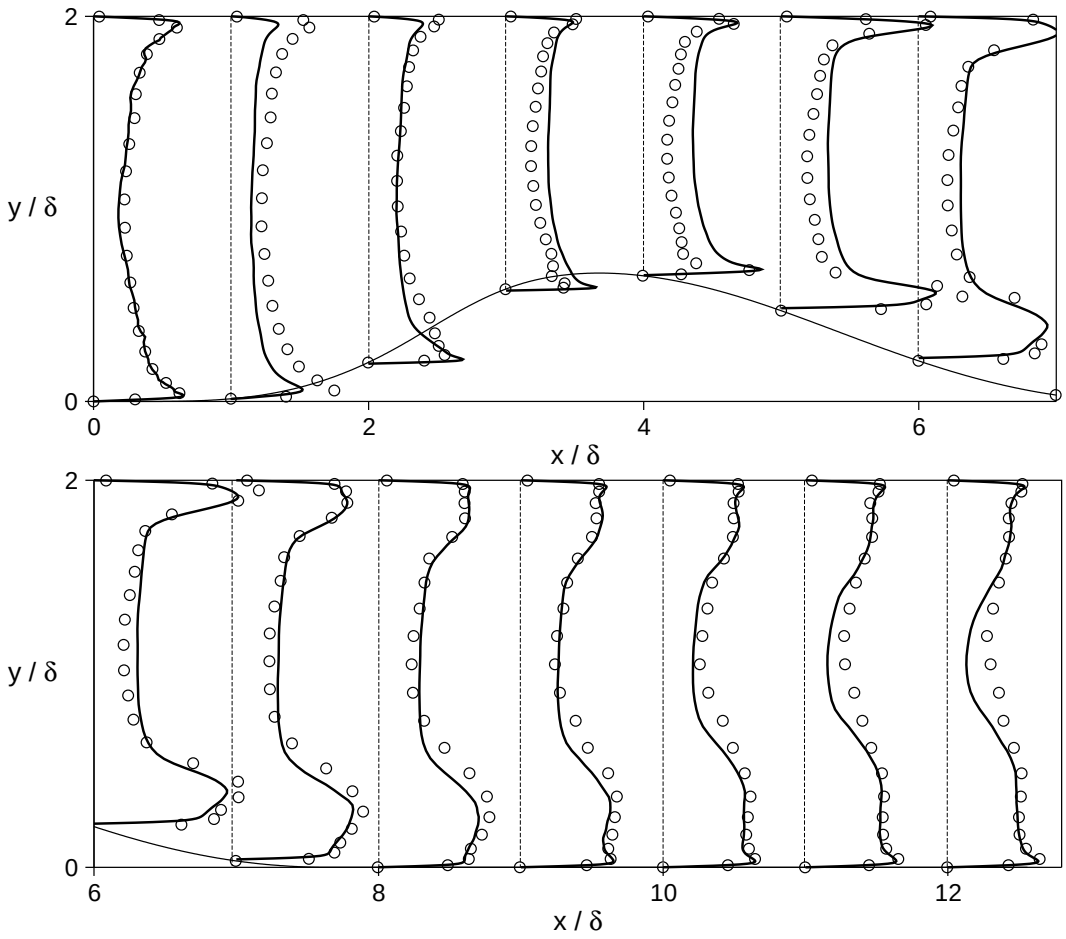

Figure 69: Profiles of the streamwise velocity fluctuation $x/\delta + 4 \times u_{rms}/U_b$; LES-LDKM (solid lines) and DNS [74] (symbols).

in Fig. 68. The velocity profiles are normalized by the inflow velocity, U_c. which is defined as the maximum value of the mean velocity at the inflow. On the inlet section, the profile yields a well-defined mean flow corresponding closely to the inflow turbulent channel flow. Over the downstream side of the bump, the agreement between LES predictions and DNS results is excellent. In the outlet channel, the mean velocity from LES compares reasonably well with DNS, and the slight under-prediction could be due to the effect of the outflow boundary condition.

Figures 69, 70, and 71 show the wall-normal profiles of turbulent intensities of streamwise velocity, wall-normal velocity and spanwise velocity, respectively. The

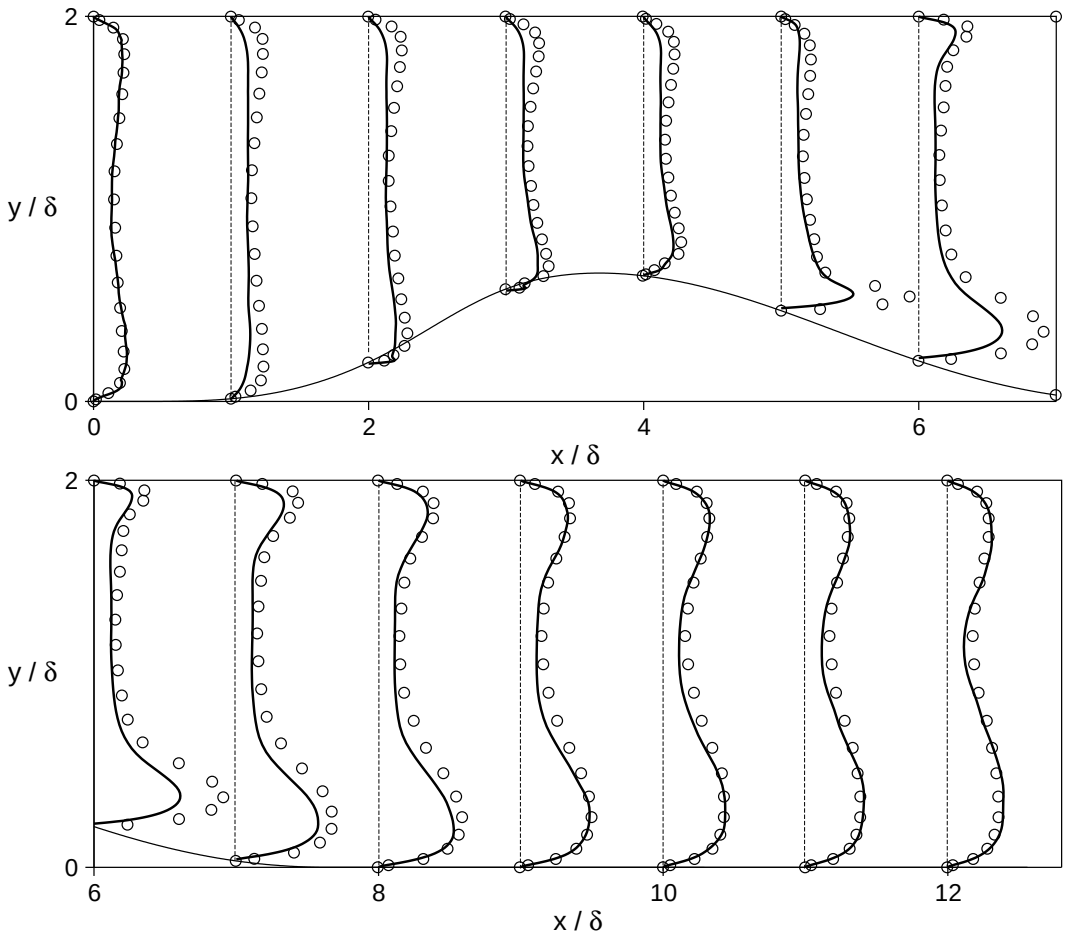

Figure 70: Profiles of the wall-normal velocity fluctuation $x/\delta + 4 \times v_{rms}/U_b$; LES-LDKM (solid lines) and DNS [74] (symbols).

current LES computations are in reasonably good agreement with the DNS data by Marquillie *e*t al. [74] at the inflow boundary. At twelve downstream stations predictions are also in good agreement with the DNS data and accurately reproduce several interesting features in the streamwise variations as found in other numerical studies [74, 121] and experimental studies [118, 5]. Similar to Baskaran *e*t al. [5], due to the mild adverse pressure gradient over the upstream channel, the streamwise fluctuations increase while decreasing wall-normal and spanwise fluctuations. On the middle of the upstream concave surface, streamwise fluctuation is reduced by favorable pressure gradient while wall-normal and spanwise fluctuations are enhanced by the

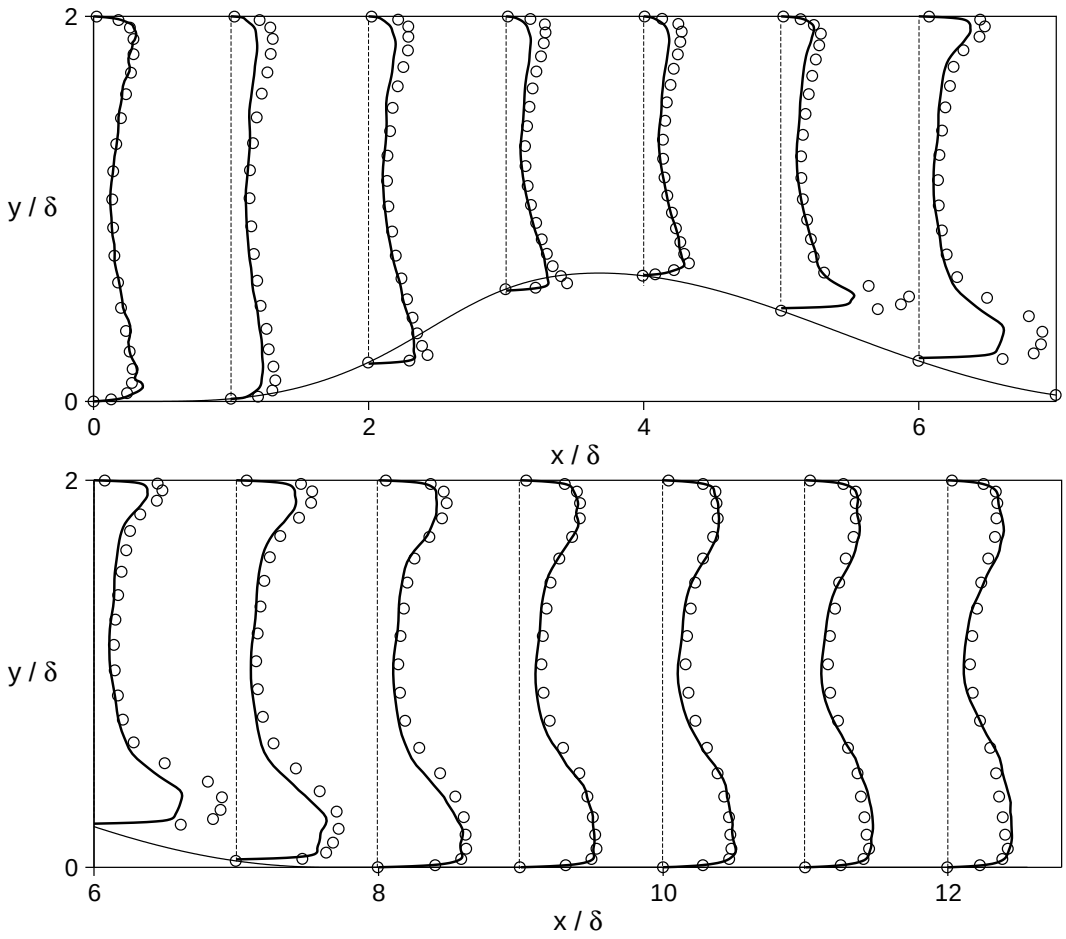

Figure 71: Profiles of the spanwise velocity fluctuation $x/\delta + 4 \times w_{rms}/U_b$; LES-LDKM (solid lines) and DNS [74] (symbols).

concave curvature. Over the upstream convex surface, the wall-normal and spanwise intensities decrease monotonically with the downstream evolution due to the convex curvature, while the streamwise fluctuations exhibit a development. Downstream of the bump summit both intensities decreases because of the convex curvature effect. On the onset of separation both intensities show a sudden increase. This near-wall peak in the streamwise fluctuation is responsible for the sudden increase in C_f (see Fig. 67). And it is also responsible for formation of a new internal layer and the decay of the peak away from the wall. In the reverse flow region closed to the wall, wall-normal and spanwise fluctuations are enhanced and the streamwise fluctuation is decreased

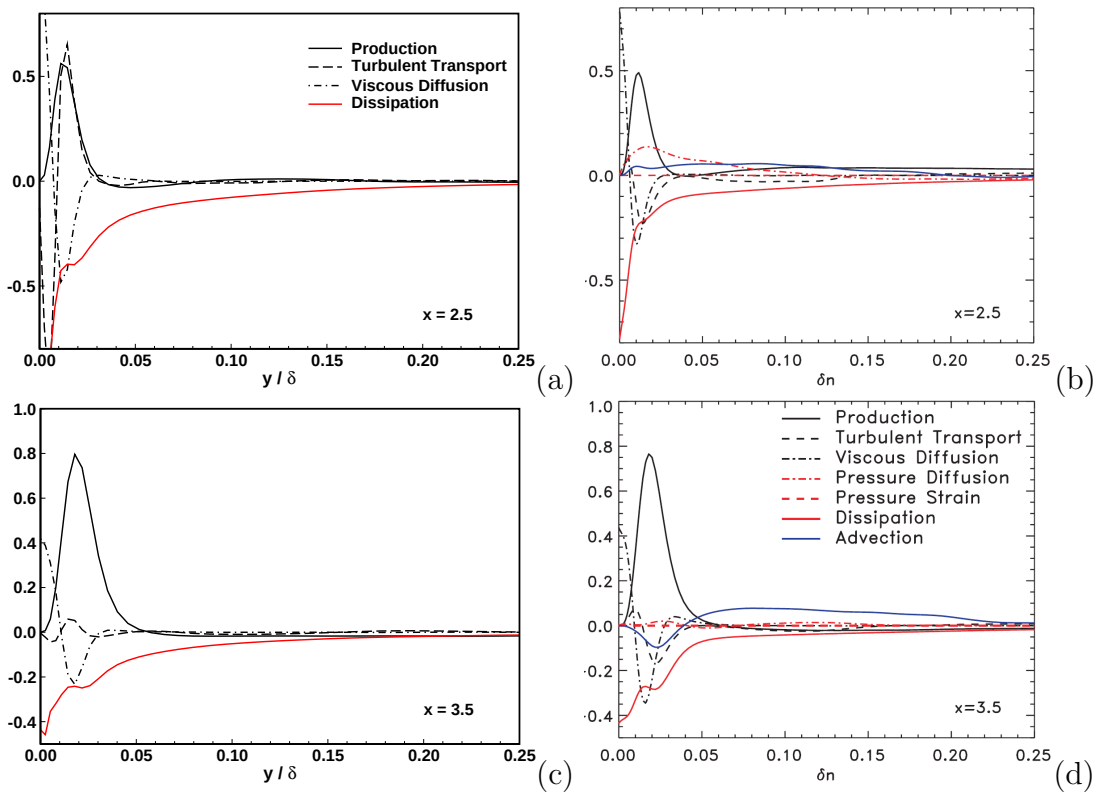

Figure 72: Profiles of the turbulent kinetic energy in the converging section; LES-LDKM (left) and DNS [74] (right).

due to the adverse pressure gradient. The outward shift in the peak streamwise fluctuation occurs in turbulent boundary layers experiencing strong adverse pressure gradient [5, 108]. As seen from the intensities (see Figs. 69, 70, and 71) close to the outflow boundary, the profiles cannot recover the inlet conditions and the flow is still in non-equilibrium.

In order to better characterize the turbulence evolution along the channel, the turbulent kinetic energy budget is computed and compared with the DNS budget [74]. The definitions for the budget is given in appendix C. The budget is first investigated in the converging part of the channel at the lower wall (see Fig. 73). As it has been previously mentioned, the streamwise turbulent intensity is reduced significantly in this region. This decrease is consistent with the turbulent kinetic energy budget which exhibits high dissipation at the wall.

The kinetic energy budget is also presented in the diverging section at four different locations for the lower wall (see Fig. 73). Near the summit of the bump ($x/\delta = 4$), the production reaches its maximum value at $y/\delta = 0.03$ which is also consistent with the streamwise turbulent intensity. It is seen that at $x/\delta = 4$, the production is over predicted when compared with the DNS budget. This is consistent with the previous observations on the streamwise intensities (see Fig. 69). At this location dissipation is lower than the production.

The maximum turbulent energy production, along the bump, is obtained at $x/\delta = 5$ which corresponds to the minimum of the skin friction coefficient for the DNS simulation. However, for the current LES-LDKM study the minimum of the skin friction is predicted earlier. In any case, the LES-LDKM predictions are compared with the DNS results at $x/\delta = 5$. At this location, the production is almost four times higher than the dissipation, and this excess of energy is transported away from the wall by the turbulent transport. It should be noted that the peak location moves away from the wall.

After the reattachment, $x/\delta = 6$, the production shows two peaks. The first peak is located close to the wall. The intensity of the first peak is predicted lower than the DNS results in the current study. The second peak is the one observed at $x/\delta = 4$ and $x/\delta = 5$ which moves farther away from the wall. The intensity of this peak decreases significantly as compared to the high value observed at $x/\delta = 5$. Further downstream of the reattachment, $x/\delta = 7$, the second peak of the production extends away from the wall.

Overall the behavior of the turbulent kinetic budget is predicted quite well with the LES-LDKM approach.

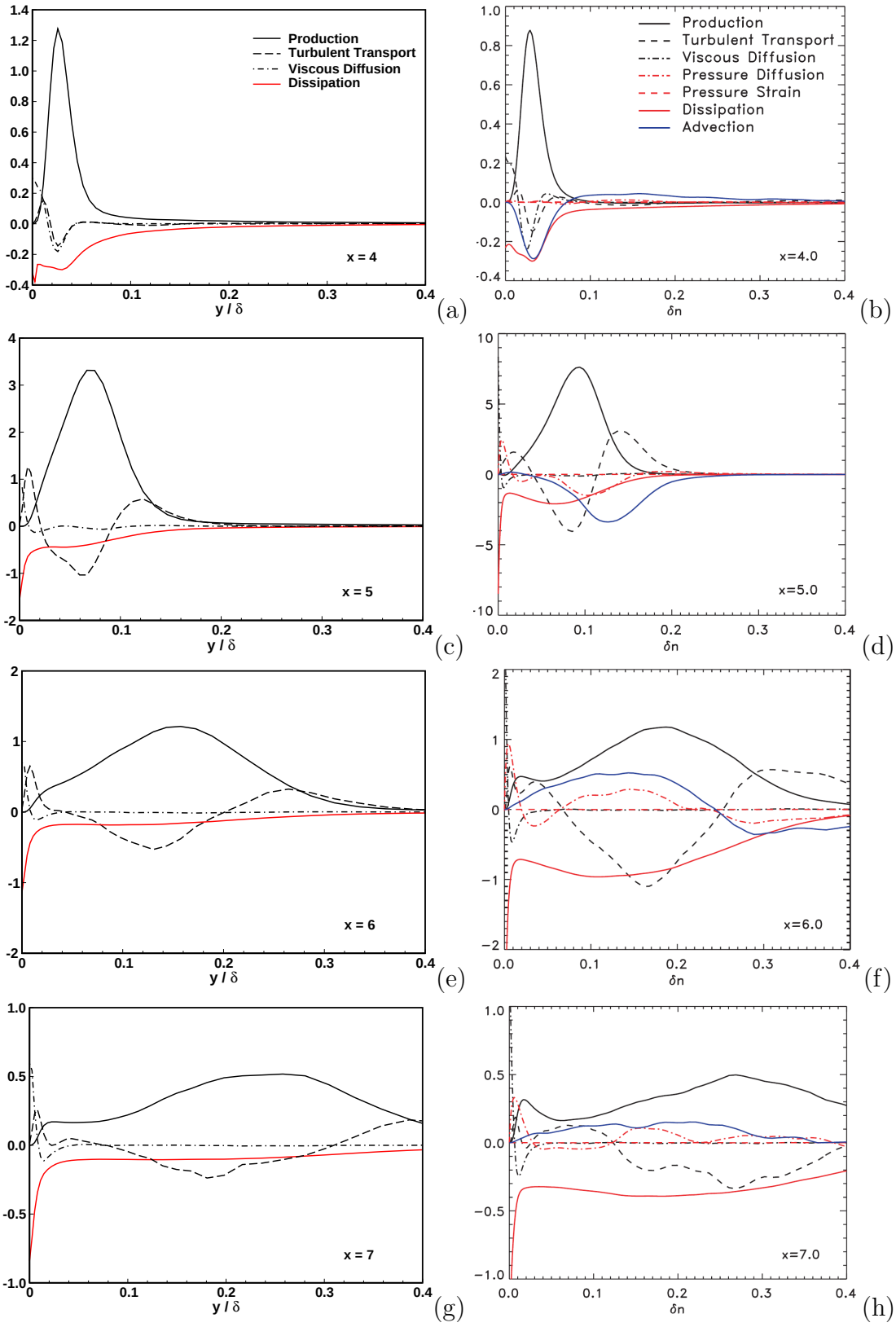

Figure 73: Profiles of the turbulent kinetic energy in the diverging section; LES-LDKM (left) and DNS [74] (right).

6.5.2 TLS-LES Results

In this section, TLS-LES results obtained with a coarse-grid (see Table 10) are presented in order to show the capability of the model to produce LES comparable results with a coarse LS grid.

The TLS-LES resolution ($64 \times 46 \times 64$) is considered very coarse even for a LES (the DNS resolution is $1536 \times 257 \times 387$ [74]). This grid is chosen in order to challenge the ability of the TLS-LES approach to deal with high Re flows with complex flow features using very coarse grids. With this coarse grid, near-wall turbulent field is not expected to be captured properly in the resolved field. Therefore, the burden of the correct reconstruction of the near-wall field is on the SS model. A uniform grid of 8 SS cells per LS cell is used in all directions, which gives a minimal resolution on wall-normal lines about $\Delta y^{+SS}_{min} = 0.68$. The near-wall SS regions are represented by sixteen LS cells extending up to $y^+ \approx 150$ from both walls. Thus, the near-wall dynamics is expected to be resolved on the SS lines.

Two types of transition functions are investigated for the TLS-LES study. First one is the step function (Eq. 115) and second one is the *tanh* function (Eq. 116). Figure 74 illustrates how the near-wall modeling is conceptualized for two different transition functions. It is noted that the transition function effect is not seen in the mean flow, and hence, not shown here. However, the effect of transition function can be clearly seen in the intensities. The *tanh* function provides smooth transition between the TLS and LES regions. Therefore, all the results presented in the rest of the section are for the TLS-LES approach with the *tanh* function.

In order to investigate the SS behavior near the wall, the velocity profiles on a spanwise line located in the separation region are examined further. Figure 75 shows the LS and SS streamwise velocities and SS energy spectrum. For a given LS field, the SS field starts from zero initial condition and evolves till the energy of the SS matches with the energy of the LS near the cut-off. This is illustrated in Fig. 75 for

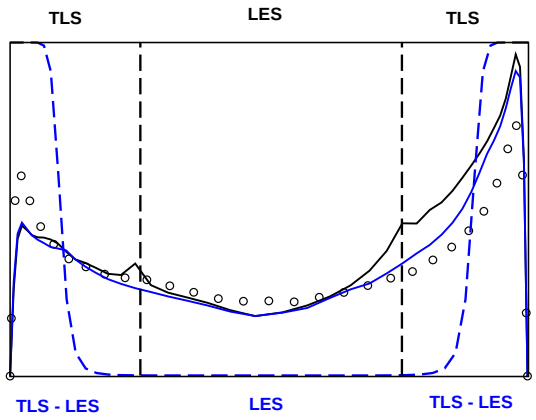

Figure 74: Profiles of streamwise velocity fluctuation at $x/\delta = 1$ and transition functions; Step function (black), Tanh function (blue), and DNS [74] (symbols).

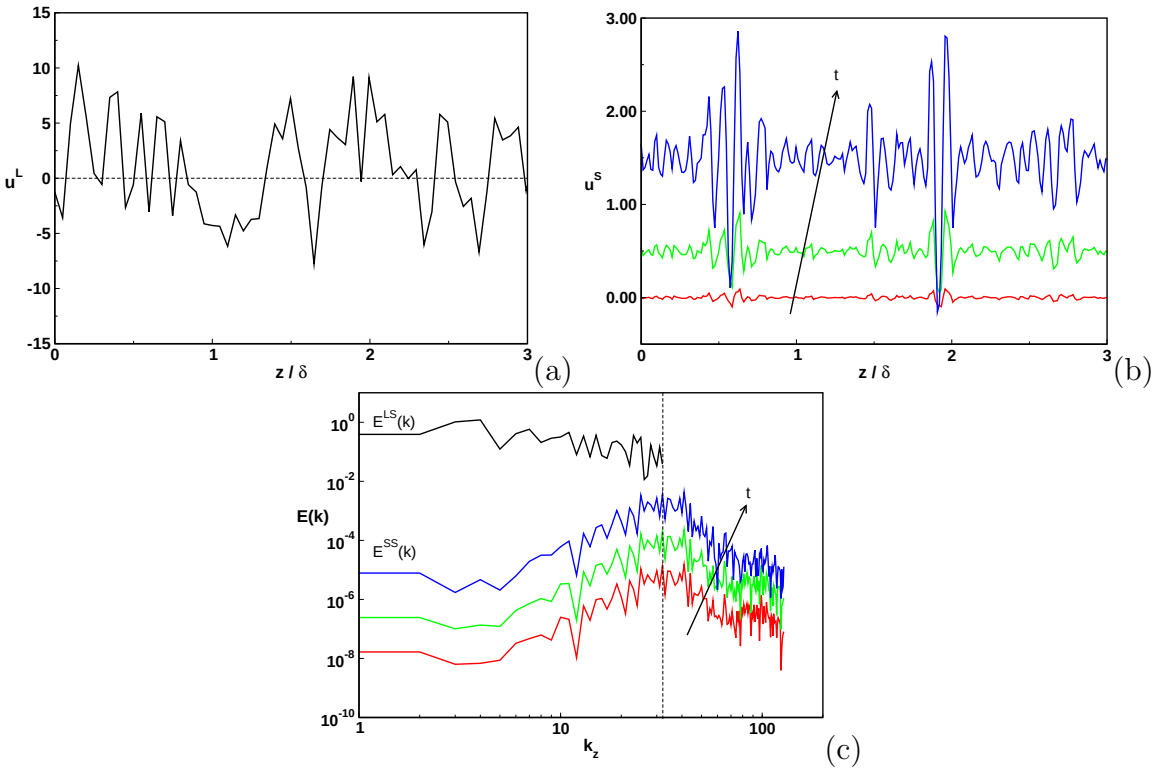

Figure 75: (a) LS streamwise velocity; (b) Evolution of the SS streamwise velocity at three instants of time for a given LS field (a); (c) Evolution of the SS energy spectra at three instants of time for a given LS field (a) along a spanwise line in the separation region at $y^+ = 15$.

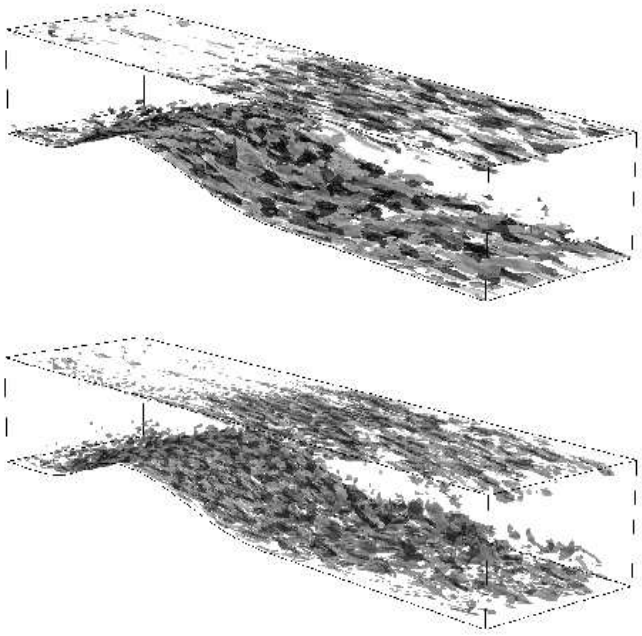

Figure 76: (a) Isosurfaces of the LS streamwise vorticity $w_x^L = +50$ (black), $w_x^L = -50$ (grey); (b) Isosurfaces of the SS streamwise vorticity $w_x^S = +2.5$ (black), $w_x^S = -2.5$ (grey).

three instants of time (and described in more detail in Chapter 2). It should be noted that SS velocity profiles show higher gradients in the regions where the LS gradient is high.

The near-wall vorticity contours for LS and SS (Figs. 76 (a) and (b)) demonstrate intense coherent structures near the separation region. The near-wall SS velocity field exhibits strong streamwise vortical structures that are smaller but similar to those present in the LS field. It is seen that the simulated SS field responds to the LS field by creating fine scale SS field at the high gradient LS regions. These results suggest that TLS-LES is capable of reconstructing physically correct flow field by combining the LS and SS fields in the near-wall region. A similar observation in channel flow is also shown in the previous chapters as well as by the TLS approach [57].

In order to investigate the mean flow predictions by the TLS-LES model, various properties such as the pressure and skin friction coefficient, the mean streamwise

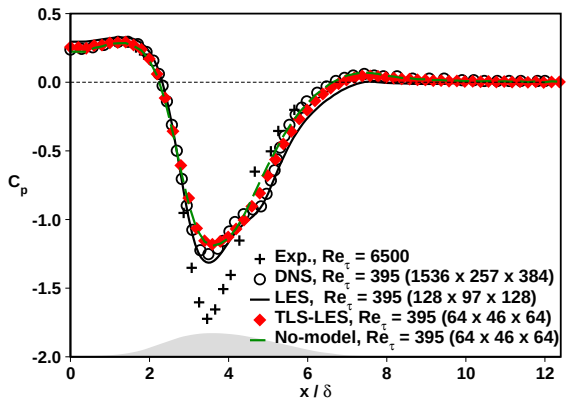

Figure 77: Pressure coefficient; TLS-LES-Tanh (red filled symbols), LES (black solid line), No-model (green dotted line), DNS [74] (symbols).

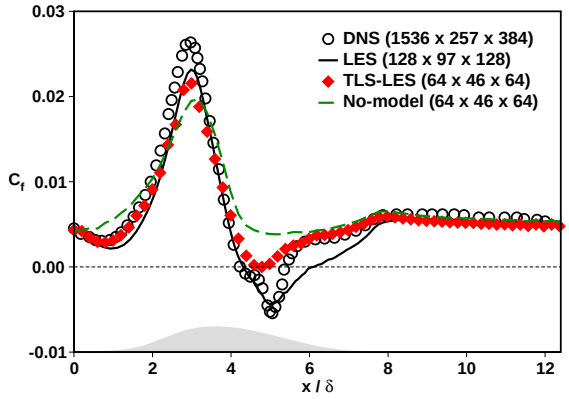

Figure 78: Skin friction coefficient; TLS-LES-Tanh (red filled symbols), LES (black solid line), No-model (green dotted line), DNS [74] (symbols).

velocity, and the turbulent intensities are analyzed. Here, TLS-LES results are compared with a run without any model effect included (No-model) and the LES study presented in the previous section as well as the DNS study of [74]. The simulations conditions are summarized in Table 10.

The comparison for the pressure coefficient at the lower wall is shown in Fig. 77 for TLS-LES, LES and No-model case. As the turbulent flow approaches the leading edge of the bump, the pressure increases slowly in this region. The pressure then decreases near the summit of the bump, forcing the flow to accelerate over the bump. The position of pressure minima is predicted accurately by the TLS-LES calculation.

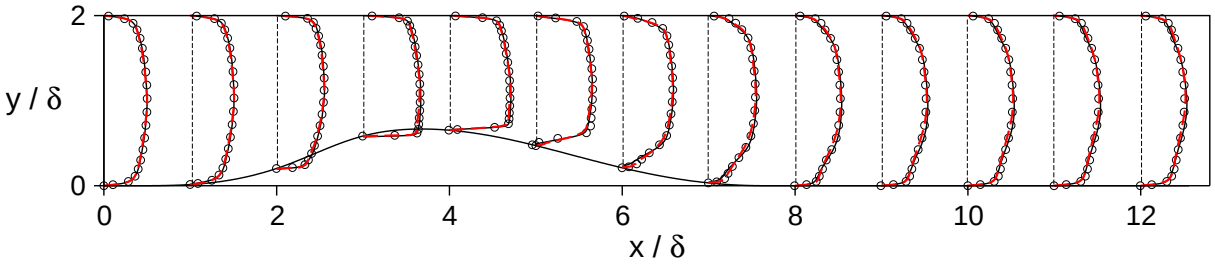

Figure 79: Profiles of the mean streamwise velocity; $x/\delta + 0.5 \times U/U_c$; TLS-LES-Tanh (dotted lines), LES-LDKM (solid lines) and DNS [74] (symbols).

The pressure increases in the downstream of the bump summit. Overall, all results show considerable agreement with the DNS results.

Figure 78 shows the skin friction coefficient predicted with the three approaches along the bump. It is seen that TLS-LES and No-model are not able to capture the separation due to the very coarse LS resolution used in the computations. It is seen that the TLS-LES approach predicts the skin friction quite well, except than the separation region. Overall, it can be concluded that the behavior of the coarse grid simulations is due to an under-resolved pressure gradient at the separation region. No-model case over-predicts the friction at the lower wall. It is seen that without the subgrid modeling or the TLS-LES interaction terms to dampen the effect of turbulence, basic flow properties are missed. Therefore, further analysis of this case is not necessary.

Mean streamwise velocity profiles are shown in Fig. 79 for TLS-LES and LES cases at various streamwise locations along the channel. Overall, it is observed that the profiles with the TLS-LES and LES approaches are quite similar, and matches quite well to the reference DNS data [74]. From the summit of the bump, the current predictions exhibit slight deviations from the reference data, in particular towards the mid of the channel.

Turbulent intensities for streamwise, wall-normal and spanwise velocities are shown in Figs. 80, 81 and 82, respectively. The TLS-LES results are compared with the

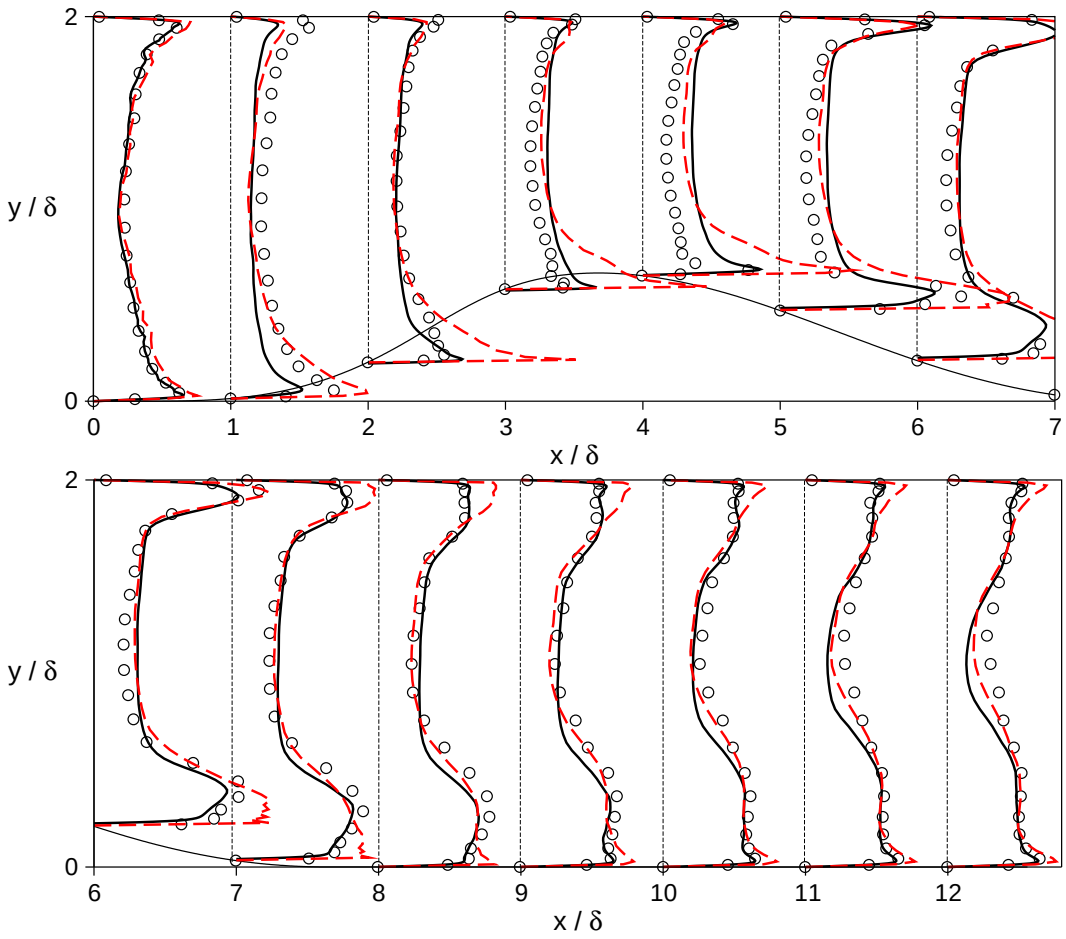

Figure 80: Profiles of the streamwise velocity fluctuation; $x/\delta + 4 \times u_{rms}/U_b$; TLS-LES-Tanh (dotted lines), LES-LDKM (solid lines) and DNS [74] (symbols).

DNS data. TLS-LES results agree well with the LES and the DNS data at most of the locations.

It is noted TLS-LES results tend to overpredict the streamwise velocity fluctuations near the lower wall, especially before the summit of the bump. It is interesting to note that the agreement between the reference DNS and the current approaches increases after this point. Also, the predictions in general agree well with the DNS at the channel mid-height.

The situations looks similar for the wall-normal and spanwise velocity fluctuations (see Figs. 81 and 82). TLS-LES results exhibit a notable deviation from the DNS

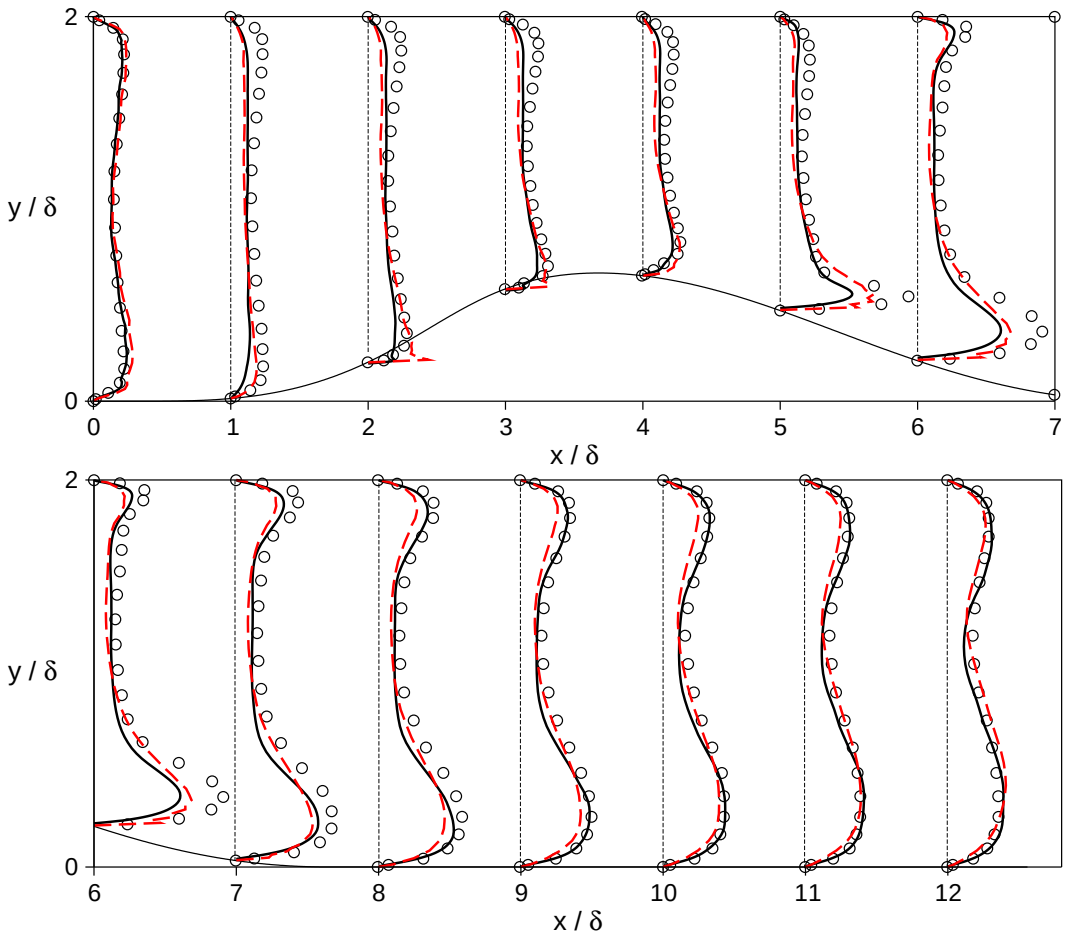

Figure 81: Profiles of the wall-normal velocity fluctuation; $x/\delta + 4 \times v_{rms}/U_b$; TLS-LES-Tanh (dotted lines), LES-LDKM (solid lines) and DNS [74] (symbols).

data closer to the upper wall especially before the summit of the bump. Further downstream in the diverging part, the deviations from the DNS data become more distinct. However, particularly towards the end of the outlet channel, very good match is obtained with the TLS-LES and LES approaches.

The new TLS-LES approach is used to simulate flow in a converging-diverging channel. This type of flow represents a challenging test case, in particular due to the flow separation and subsequent reattachment. The results obtained by TLS-LES has been compared with DNS and a more conventional LES. Results suggest that the TLS-LES approach has the potential for capturing the near-wall dynamics even when

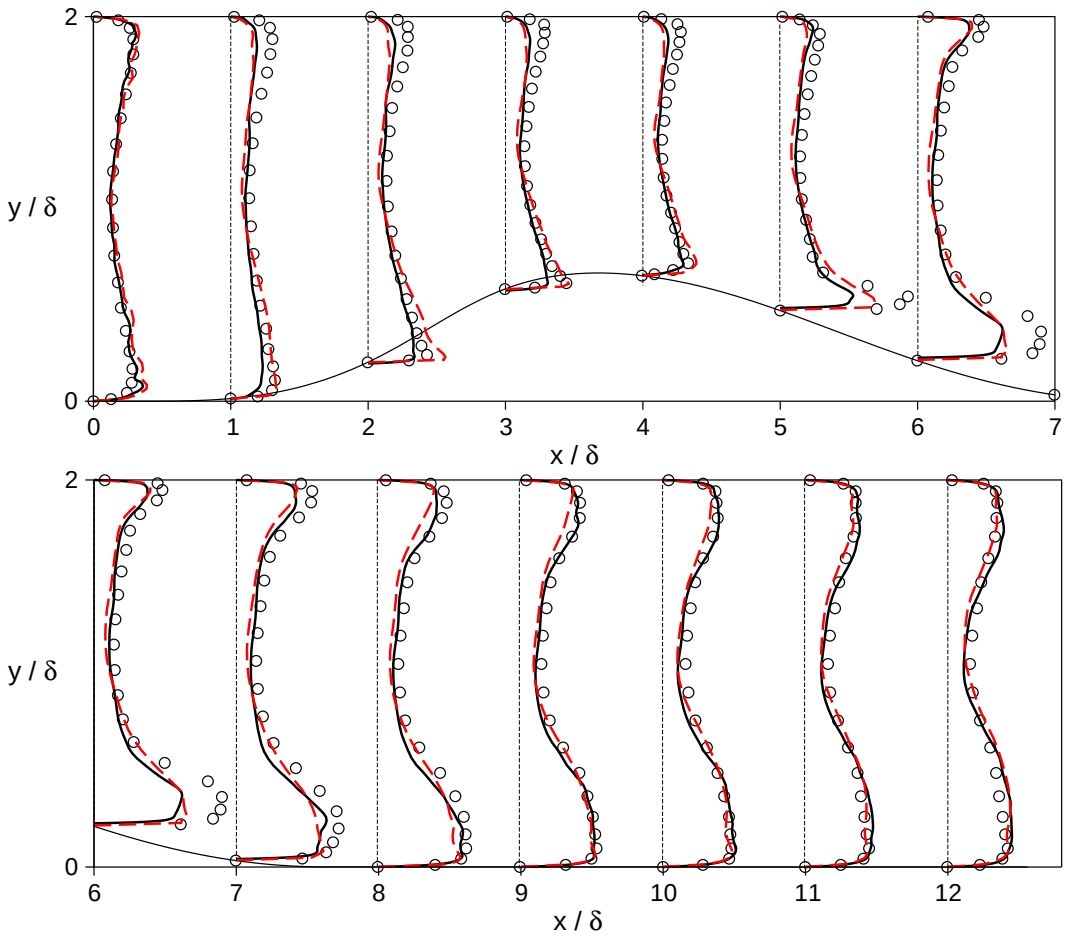

Figure 82: Profiles of the spanwise velocity fluctuation; $x/\delta + 4 \times w_{rms}/U_b$; TLS-LES-Tanh (dotted lines), LES-LDKM (solid lines) and DNS [74] (symbols).

using very coarse grid. Some limitations of using very coarse grids in the near-wall region have been identified. Overall, current results show the capability of the model for flows with complex flow features.

CHAPTER VII

APPLICATION OF TLS-LES TO TURBULENT FLOW IN A DIFFUSER

The TLS-LES approach is further investigated for a diffuser flow, which has been a test case for a number of experimental [87, 9, 35] as well as numerical studies [52, 104, 120, 33]. This types of flow contain complex phenomena with unsteady separations, reattachments, wakes, and vortex interactions. High Re flows of this type are of considerable interest because of their relevance to practical flows.

7.1 Introduction

The main features of the diffuser flow can be summarized as the following

- A large unsteady separation bubble due to an adverse pressure gradient starts about halfway down the deflected wall and reattaches within the outlet channel. The separation point is determined mainly by two factors: the pressure gradient and the level of turbulence. The turbulent transport of mean momentum towards the near-wall region delays the flow separation.

- A sharp variation in streamwise pressure gradient is seen with changes suddenly from a slightly favorable to strongly adverse at the diffuser throat, and then relaxes to a mildly adverse gradient afterward.

- A slow developing internal layer according to the numerical study by Wu et al. [120]. One prerequisite for internal layer formation is the abrupt change in pressure gradient. The studies by Wu et al. [120] and Wu and Squires [121] suggest that internal layers may emerge in the relaxation zone downstream of a

sudden change in streamwise pressure gradient, which is the case here, as well.

Experimental studies on the plane asymmetric diffuser was carried out by Obi *e*t al. [87] and Buice and Eaton [9]. They both considered a fully developed inflow with a $Re_b = 9000$ (based on the bulk velocity and the inlet channel height). Both cases have an inclination angle of 10^o. There has also been a new experimental study [35] for an increased inflow of $Re_b = 20000$ and a decreased opening angle of 8.5^o to study the control of flow separation. DNS of the full diffuser flow at this Re is still prohibitively expensive due to the wide range of spatial and temporal scales. Numerical studies based on RANS were described earlier in [25, 47].

Kaltenbach *e*t al. [52] performed LES of the Obi case and showed satisfactory agreement with the experimental data. They used dynamic Smagorinsky model to account for the unresolved scales and a LES grid of $352 \times 64 \times 128$. More recently, Schluter *e*t al. [104] and Wu *e*t al. [120] performed similar studies applying the dynamic Smagorinsky model, however, using a discretization scheme different from Kaltenbach *e*t al. [52]. They report consistently that a reasonable prediction of the mean separation is possible on even rather coarse LES grids (e.g., $160 \times 64 \times 64$). Some results for the Obi diffuser was also obtained by Gravemeier [32, 33] using a LES based on the VMS. Results showed considerable agreement with the experiments using coarser grid (e.g., $290 \times 64 \times 80$), however, the simulation seemed to be clearly influenced by the exact details of the sgs model. Herbst *e*t al. [43] studied the effect of Re on various diffuser flow characteristics by performing LES using the numerical method as in Kaltenbach *e*t al. [52]. They considered the slightly modified geometry of the diffuser of [35]. Their observations showed that there is a trend towards a larger separation region by increasing the Re. This Re dependence compares well with the experimental findings by Obi *e*t al. [87].

For turbulent channel flows, the minimum resolution requirement depends on the numerical scheme. Spectral methods can produce reliable results for moderate Re

with near wall spacing on the order of $\Delta x^+ = 100$ and $\Delta z^+ = 30$ based on wall units [89, 61]. However, this spacing must be reduced by at least a factor of two to achieve reasonable predictions using second order finite difference schemes [**?**, 73]. In channel flows, the effect of wall imposes a limit on the size of spatial scales. For vertical scales, the channel height is the natural length scale. For spanwise scales, approximately three channel height of domain width is sufficient for spanwise auto correlation to drop to zero. For diffuser flow, the ratio of the width to height increases towards to the outlet channel. Therefore, the effect of the spanwise resolution is felt gradually in the expanding section. However, for flows with mild separation, the flow upstream of separation is generally unaffected by the conditions downstream [108].

Inside the diffuser turbulence structure changes strongly due to effect of adverse pressure gradient. It is well known that the turbulent length scales grow in a decelerating flow [108, 23]. Also, the mean shear decreases and production of turbulence shifts away from the wall. All these conditions interpret that the resolution requirement inside the diffuser is not as strict as it is for a pure channel. The experimental study by Dengel *e*t al. [23], as well as the numerical study by Kaltenbach *e*t al. [52] showed that separation from a smooth wall is very sensitive to changes in the upstream condition.

In the inlet channel section, the flow is in equilibrium and so production and dissipation are at the same rate. However, inside the diffuser, the flow is out of equilibrium, production exceeds dissipation throughout most of the expansion [52]. Both equilibrium and non-equilibrium behavior of turbulence inside the diffuser makes this flow a challenging test case for the sgs models.

Since the correct prediction of the separation point and the extent of the recirculation region is particularly challenging for computational models, the diffuser flow problem was selected as a test case at a workshop in 1999 [42]. Therefore, these observations also provide the motivation for studying this flow to investigate

the capability of both current LES (LDKM) model and the new TLS-LES approach developed in this thesis.

7.2 Geometry

The computational geometry of the diffuser case is similar to the setup employed in the experimental study by Obi *et* al. [87] and Buice and Eaton [9], as well as in the numerical setup in Kaltenbach *et* al. [52] and Wu *et* al. [120]. This geometry is shown in Fig. 83. The origin of the $x - axis$ is located at the intersection of the tangents to the straight and inclined wall. The $y - axis$ originates from the bottom wall of the downstream channel. Simulations are performed for a diffuser inclined wall opening angle of $\phi = 10^o$. The inlet plane is located at $x = -5$ where the channel inflow height is 2δ. The expansion start at $x = 0$ and ends at $x = 42\delta$ where the channel has reached a height of 9.4 corresponding to an expansion ratio of 4.7. The length of the computational domain is $L_x = 105\delta$ allowing the flow to recover over approximately 58δ before exiting the domain. The outlet channel length is chosen as in Wu *et* al. [120], which is considerably longer than the one in Kaltenbach *et* al. [52]. Nevertheless, even with longer outlet channel the recovery into a canonical channel flow may not be reached [9, 52]. The edges at $x = 0$ and $x = 42\delta$ are smoothed with a curvature radii of 19.4 similar as in the experiment [9]. The spanwise width is

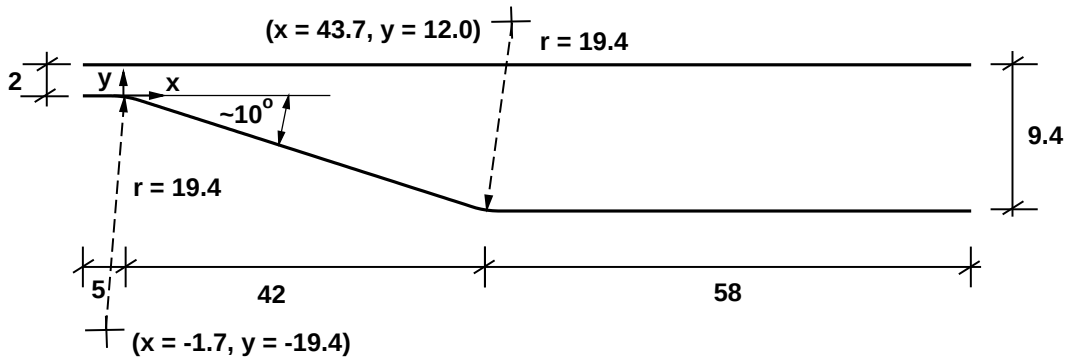

Figure 83: Diffuser geometry in x-y plane.

chosen as $L_z = 4\delta$ for the fine LES study and $L_z = 8\delta$ for the TLS-LES and coarse LES studies, matching the spanwise length in Wu *e*t al. [120]. $L_z = 8\delta$ is the largest value for the spanwise length investigated by Kaltenbach *e*t al. [52].

Various calculations of the diffuser flow are performed and summarized in Table 12. For all cases the geometry of the diffuser is unchanged, however, the grid resolution differs depending upon the simulation method and test conditions are given in table. The grid points are uniformly distributed in the spanwise direction. In the wall-normal direction, the grid points are moderately clustered towards both solid walls. The stretching factor is kept around 5% in order to keep the discretization errors small. In the streamwise direction, the grid is clustered so that the streamwise spacing decreases linearly towards to the diffuser throat then increases linearly with downstream distance from the diffuser throat inside the expansion, and then uniformly distributed in the outlet channel. For the coarse-LES and LS grid for TLS-LES, the number of grid points ($164 \times 56 \times 40$) is less than 42% of the fine grid of Wu *e*t al. [120] ($590 \times 100 \times 110$).

7.3 Boundary Conditions

At the walls, no-slip boundary conditions are imposed for the velocity and zero gradient boundary condition for pressure. At the inflow, a time dependent inflow velocity field is prescribed. This time dependent inflow data is taken from a separate simulation of fully developed turbulent channel flow. Details of this will be given in the next

Table 12: Simulation parameters for turbulent flow in a diffuser.

		Grid	Spatial Resolution			
			$\triangle x^+$	$\triangle y^+$	$\triangle z^+$	L_z
LES		$278 \times 80 \times 80$	25	0.98	25	4δ
LES-coarse		$164 \times 56 \times 40$	54	5.4	50	8δ
TLS-LES	Large Scale	$164 \times 56 \times 40$	54	5.4	50	8δ
	Small Scale		6.7	0.72	6.2	

subsection. At the outflow boundary a convective boundary condition of the form

$$\frac{\partial u}{\partial t} + U_c \frac{\partial u}{\partial x} = 0 \tag{179}$$

is prescribed. The convective speed is calculated such that overall mass conservation is maintained. The outflow pressure is extrapolated from interior cells. According to the numerical study by Kaltenbach *e*t al. [52], the flow is idealized in the spanwise direction as being homogeneous. This assumption is valid if the flow is statistically two-dimensional. Periodic boundary conditions are assumed on the spanwise direction.

7.4 Inflow Turbulence

The inflow boundary conditions are located as $x/\delta = -5$. The time dependent data is taken from a separate simulation of fully developed turbulent channel flow. For this simulation, the same numerical scheme (fourth order kinetic energy conservative scheme) and turbulence approach (LES-LDKM) is applied as it is used for the diffuser calculations. This computation is performed using a mass-flux and Re identical to that of the channel upstream of the diffuser. The Re based on the turbulent wall-shear velocity $u_\tau = \sqrt{\tau_w}$, where τ_w denotes the wall-shear stress, and the channel half-width δ is $Re_\tau = u_\tau \delta/\nu = 500$. The flow data is recorded in a $y - z$ plane and stored in a database.

The inflow channel is spatially discretized using $192 \times 128 \times 192$ grid points in streamwise, wall-normal and spanwise directions, respectively. As in Kaltenbach *e*t

Table 13: Simulation parameters for inflow turbulent channel flow at $Re_\tau = 500$.

	Grid	Spatial Resolution		
		$\triangle x^+$	$\triangle y^+$	$\triangle z^+$
DNS[83]	$384 \times 257 \times 384$	10	0.029	6.5
LES	$192 \times 128 \times 192$	31	1.0	20.9

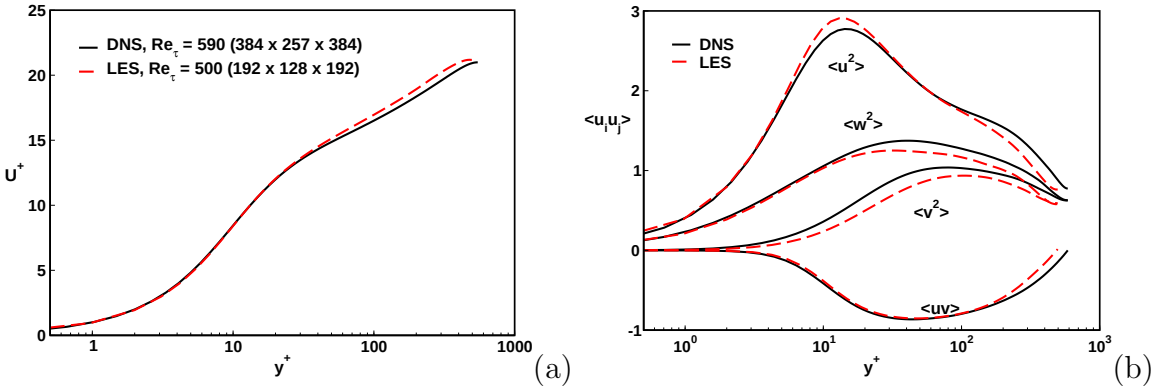

Figure 84: (a) Mean streamwise velocity and (b) rms velocity fluctuation for channel flow. LES results are compared with DNS [83].

al. [52], the channel length is chosen to be 12δ, while the channel height and width are identical to that of diffuser as 2δ and 8δ, respectively. The grid points are uniformly distributed in the homogeneous directions (streamwise and spanwise). In the wall-normal direction, the distribution of the grid points obeys a *tanh* function, clustered to the walls.

The inflow turbulent channel flow results obtained with LES show good agreement with the classical DNS data [83] (see Figs. 84 (a) and (b)).

7.5 Results

In the diffuser, mean streamwise velocity is evaluated at twelve different locations. These locations correspond to the locations where experimental results are available. The mean velocity in the diffuser is obtained by averaging over time as well as over the spanwise homogeneous direction. This is represented by $\langle\cdot\rangle$. As in previous numerical studies [52, 120], mean velocity is scaled by the inlet bulk mean velocity U_b defined as the area-averaged mean streamwise velocity at $x/\delta = -5$. All the results are compared to the experimental data from Buice experiment [9].

7.5.1 LES Results

The well-resolved LES results are first compared with the experimental data.

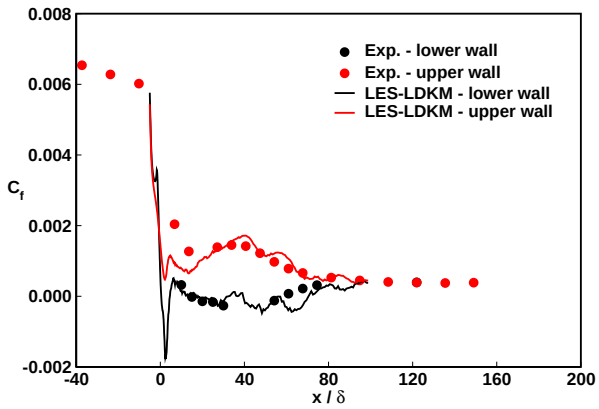

Figure 85: Skin friction coefficient along the upper and lower wall of the diffuser. Symbols: experimental data from Buice and Eaton [9]; Lines: LES.

The wall static pressure coefficient defined as

$$C_p = \frac{\langle P_w \rangle - \langle P_w \rangle (x/\delta = -5)}{\frac{1}{2}\rho U_b^2} \tag{180}$$

where P_w represents the pressure value at the walls, and the skin friction coefficient evaluated as

$$C_f = \frac{\tau_w}{\frac{1}{2}\rho U_b^2} \tag{181}$$

where τ_w denotes the wall shear stress. In both these formulations, the fluid density ρ is assumed to be of unit value.

The skin friction along both walls agree well with Buice's measurements (see Fig. 85). There is a small separation region indicated by negative C_f near the diffuser throat on the deflected wall. This region, which is completely disconnected from the separation region, is also observed in other numerical studies [52, 120]. Skin friction coefficient over the upper flat wall displays a strong drop from $x/\delta = 0$ to 10 upstream and a long plateau starting near the separation region in the bottom wall, extending from $x/\delta = 15$ to 45 and a more gradual decrease downstream of $x/\delta = 45$.

The pressure coefficient curves from LES and experiment agrees reasonably well, as shown in Fig. 86. The pressure increases suddenly due to the expansion and exhibits a characteristic plateau in the separation region. The change from strongly

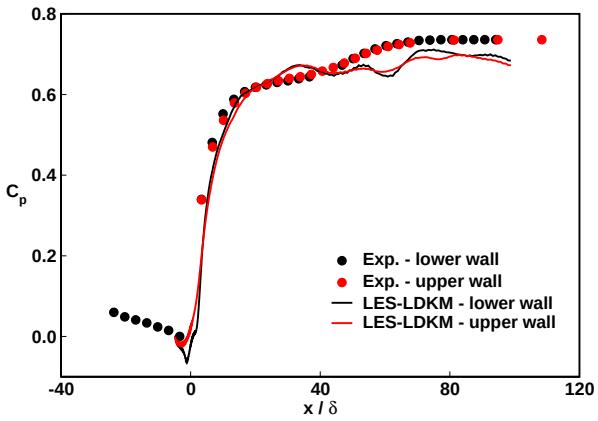

Figure 86: Wall static pressure coefficient along the upper and lower wall of the diffuser. Symbols: experimental data from Buice and Eaton [9]; Lines: LES.

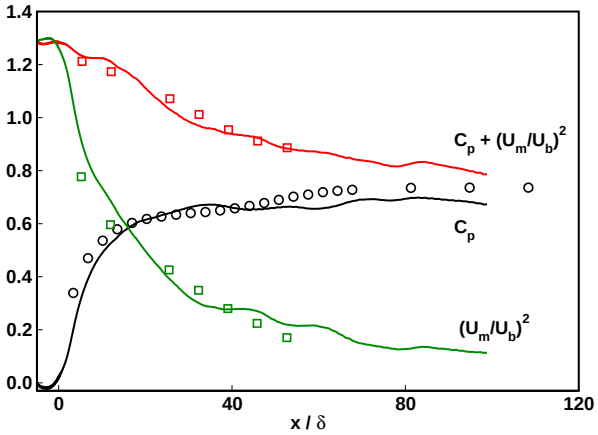

Figure 87: Wall static pressure, maximum velocity and total pressure along the upper wall. Symbols: experimental data from Buice and Eaton [9]; Lines: LES.

adverse to weakly adverse pressure gradient starts near $x/\delta = 10$. The behavior of C_p for diffuser shows similar pattern as C_p found in the bump flows [5, 118].

Figure 87 shows the total pressure, C_p and the maximum value of the streamwise velocity along the upper wall. For incompressible, inviscid flow, the energy conservation reveals that the total pressure remains constant along a stream tube. However, for viscous flows, the total pressure will generally decrease in the streamwise direction as a result of frictional losses. Figure 87 shows that the total pressure decreases about 30% over the length of the domain. LES and measurements exhibit about the same

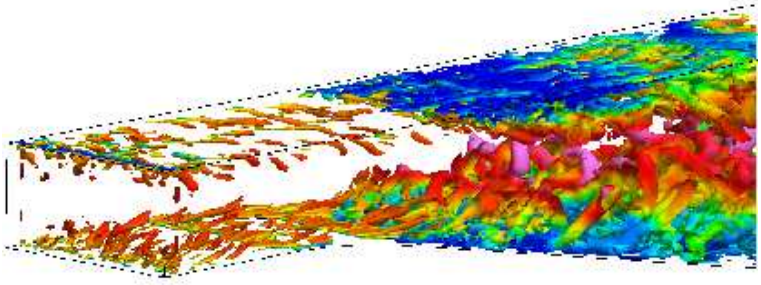

Figure 88: Isosurfaces of the second invariant of the streamwise velocity gradient tensor predicted with LES approach. Isosurfaces are colored with local streamwise velocity in the range of 0 to 25.

total pressure and maximum velocity.

Overall there is a quite good agreement of mean profiles between simulation and experiment. The location and height of the separation bubble agree well up to $x/\delta = 55$. However, reattachment is observed further downstream in the simulation compared to the experiment.

In order to study the global motion of the turbulent structures, isosurfaces of the second invariant of the velocity gradient tensor (Eq. (174)) is presented in Fig. 88. The vortices generated near the diffuser throat are more intense than the ones generated in plane channel flow. The long near-wall streamwise streaks coming from the upstream channel are destroyed at the throat of the diffuser.

7.5.2 TLS-LES Results

In this section, the TLS-LES results for the coarse grid are presented. LES with the same coarse resolution is also performed to compare with the TLS-LES approach. Comparing the discretization of the diffuser to the finer discretization in [120] ($590 \times 100 \times 110$), it is noted that this LS resolution is considered very coarse and, therefor, the near-wall turbulent field is not expected to be captured properly in the resolved field. Thus, most near-wall dynamics is expected to be resolved on the SS lines. A

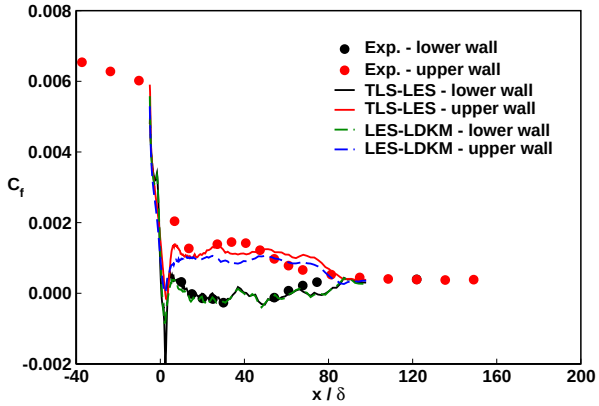

Figure 89: Skin friction coefficient along the upper and lower wall of the diffuser. Symbols: experimental data from Buice and Eaton [9]; Dashed lines: LES-coarse; Solid lines: TLS-LES.

uniform grid of 8 SS cells per LS cell is used in all directions, which gives a minimal resolution on wall-normal lines about $\Delta y^{+SS}_{min} = 0.72$. The near-wall TLS regions for lower and upper walls are represented by 16 LS cells extending up to $y^+ = 160$.

TLS-LES and LES results are compared with the experimental data. Figure 89 presents the computed surface distribution of the skin friction (C_f) and the corresponding experimental result for lower and upper walls. There is a good similarity in both features and magnitudes between TLS-LES and the experimental data. It is interesting to note that the TLS-LES shows better prediction of the skin friction compared with the coarse LES results at the top wall. Skin friction coefficient over the upper flat wall displays a strong drop and a long plateau starting near the separation region in the bottom wall, and a more gradual decrease downstream. The separation location is predicted quite well by all (TLS-LES and LES) simulations but reattachment is observed further downstream. These discrepancies in the lower wall where the flow is reattaching can be the artifact of the coarse LS grid resolution.

Figure 90 presents the TLS-LES and coarse LES results for the pressure coefficient along the lower wall. It is clear from this figure that the TLS-LES is capable of predicting approximately the correct pressure distribution along the lower wall. The

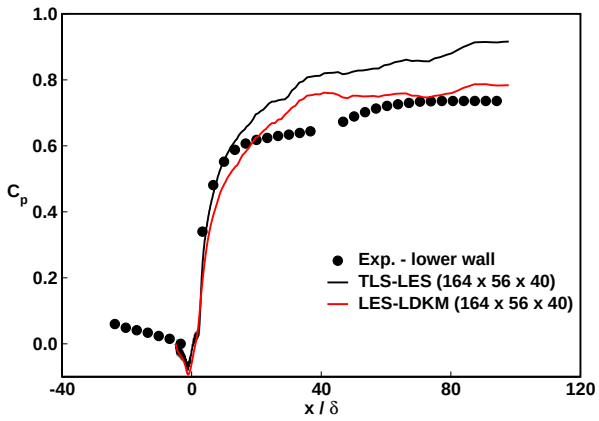

Figure 90: Wall static pressure coefficient along the lower wall. Symbols: experimental data from Buice and Eaton [9]; Dashed lines: LES-coarse; Solid lines: TLS-LES.

pressure increases suddenly due to the expansion and exhibits a characteristic plateau in the separation region. These features are not captured well with the coarse LES approach. However, the pressure coefficient is over-predicted in the TLS-LES study. This over-prediction of the pressure coefficient is also observed in the LES study of Kaltenbach *et* al. [52] for their coarse grid resolution. It was noted there that the simulation results strongly depend on the quality of the inflow or the streamwise grid resolution provided in the inlet channel [52]. In the current study, the resolution in the inlet channel is approximated from the previous TLS-LES analysis (see, Chapter 5) of the channel flow at $Re_\tau = 590$. Thus, it is likely that this resolution might be too coarse for the TLS-LES of this flow.

Figure 91 shows the pressure coefficient, the maximum streamwise velocity and the total pressure along the upper wall. The pressure coefficient is closely related to the maximum value of the mean velocity profile. It is seen that the maximum velocity is under-predicted in the separation region and shows itself as an over-prediction in the pressure coefficient and the total pressure distributions.

Snapshots of the second invariant of the LS and SS velocity gradient tensor isosurfaces at a level of $Q^L = 75$ and $Q^S = 0.5$ are shown in Fig. 93. Isosurfaces are

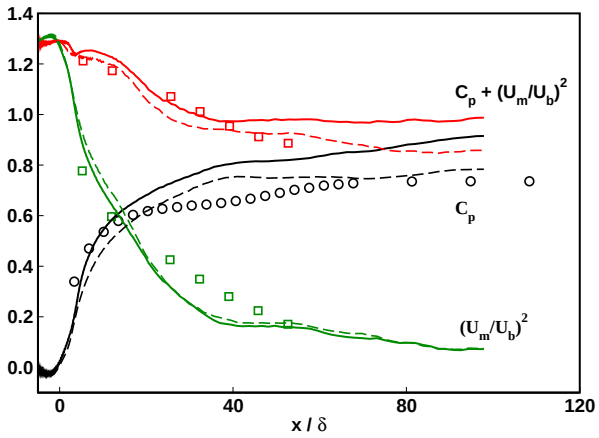

Figure 91: Wall static pressure, maximum velocity and total pressure along the upper wall. Symbols: experimental data from Buice and Eaton [9]; Dashed lines: LES-coarse; Solid lines: TLS-LES.

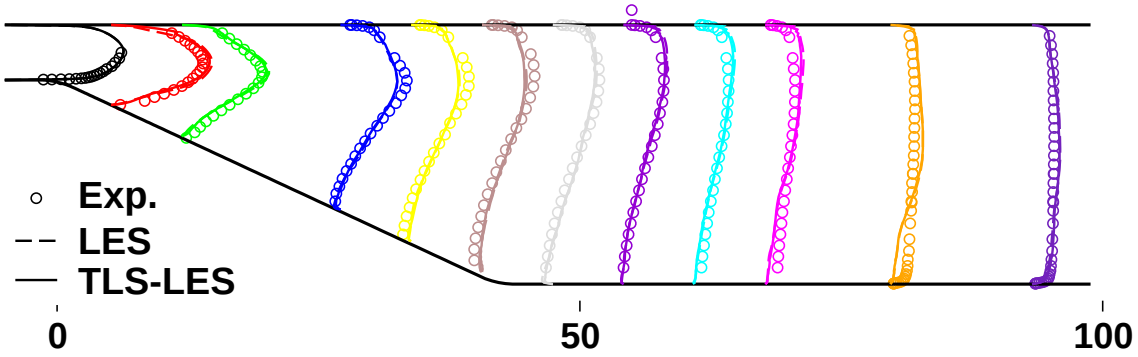

Figure 92: Profiles of mean streamwise velocity $x/\delta + 10 \times U/U_b$. Symbols: experimental data from Buice and Eaton [9]; Dashed lines: LES-coarse; Solid lines: TLS-LES.

colored with local streamwise velocity. It is seen that the simulated SS field responds to the LS field by creating fine scale SS field at the high gradient LS regions.

Current results show that TLS-LES shows qualitative agreement with the experimental results for this complex flow. Clearly the resolution of LS/SS for this type of flow needs to be revisited. Nevertheless, the fact that the same TLS-LES approach is used here without any changes offers some proof of the potential of this method to handle complex flows with reasonable grid resolution. Current results show the capability of TLS-LES for complex flows. The TLS-LES shows qualitative agreement

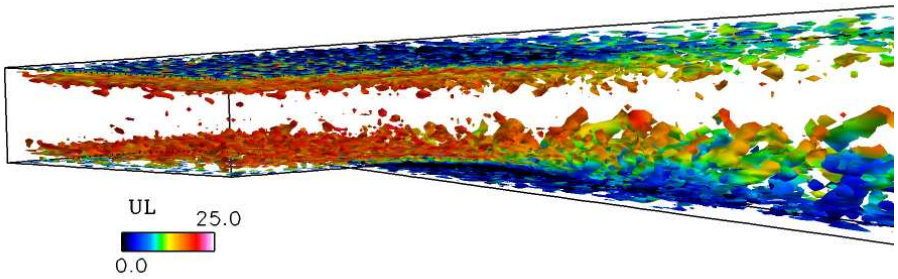

(a)

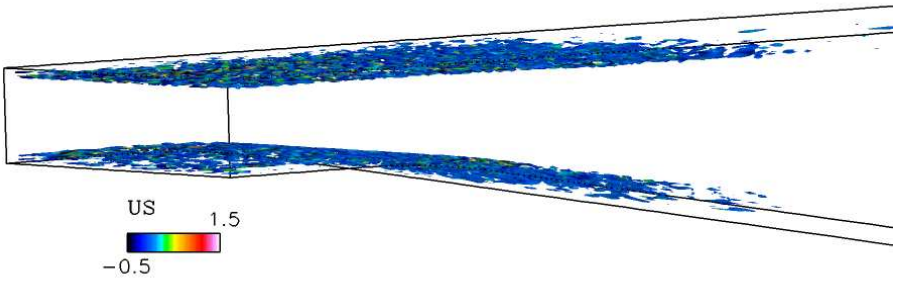

(b)

Figure 93: Isosurfaces of the second invariant of the (a) LS and (b) SS velocity gradient tensor predicted with TLS-LES approach. Isosurfaces are colored with local streamwise velocity.

with the experimental results. Overall results look reasonable for this kind of coarse resolution. A finer resolution is expected to provide better results and needs to be addressed.

CHAPTER VIII

CONCLUSION

In this study, a new hybrid approach (TLS-LES) for numerical simulations of complex wall-bounded flows has been developed. The TLS-LES approach is formulated by coupling the TLS for the near-wall region with conventional LES away from the wall. The TLS-LES equations are derived based on the definition of a new scale separating operator. The key attribute of this approach is that unlike other near-wall LES models, the near-wall fluctuations are not suppressed, a unique capability, particularly near the wall.

The TLS approach is first investigated in detail to analyze the properties of the LS functions and resolution. The TLS SS assumptions are revisited using *a priori* analysis of a forced isotropic turbulence DNS data at $Re_\lambda = 433$. Current analysis show that SS model assumptions become more closely correlated with their true values as LS resolution increases. The LS resolution requirement is estimated as $N_i^{DNS}/2^3$ in coordinate direction x_i. Here, N_i^{DNS} is the resolution requirement in each coordinate direction x_i for a DNS. Finally, stand-alone SS equations are integrated on one-dimensional lines in order to study the model capability to duplicate the SS velocity on 1D line. The predicted SS field becomes more correlated with the exact SS field (obtained from the DNS_{1D} field) as the LS grid resolution increases. Furthermore, it is observed that the SS evolution time strongly depends on the energy stored in the LS. As the LS energy increases, the number of iterations for the SS evolutions decreases.

A new incompressible flow solver is entirely developed as part of this thesis because the pseudo-spectral code (used in Chapter 5) is not capable of simulating complex

flows of present interest, since it is limited to the flows with simple boundary conditions. Therefore, a new code for LES and/or TLS of incompressible, unsteady, turbulent flows using massively parallel computers is developed. The implementation is general enough to allow the simulation of flows in complex geometries. The code uses an artificial compressibility approach to solve incompressible three-dimensional Navier-Stokes equations. The advective derivatives are discretized using fourth-order energy conservative finite differences. Temporal advancement in pseudo-time is conducted using a fifth-order Runge-Kutta method and in the physical time second-order backward differencing. The code is parallelized using MPI for distributed-memory machines. The capability of the incompressible code is extended to perform LES, TLS, and TLS-LES methods. The TLS SS equations are integrated with an explicit, two-step component-wise TVD scheme in parallel as well. The accuracy and efficiency of the code is evaluated by performing *a posteriori* tests of decaying isotropic turbulence, turbulent re-circulating flows, and turbulent channel flows. These test flows are chosen to evaluate the code and the turbulence modeling approaches (LES, TLS and TLS-LES) under various conditions of increasing complexity. Comparisons with the experimental data and DNS results (wherever available) are carried out to demonstrate the capability of the code.

To evaluate the behavior of the near-wall TLS-LES approach, the fully developed channel flow for a range of Re is investigated. This simulation is used for validation purposes and results are compared with the DNS data. Studies based on the location of the first LS grid shows that as the first LS grid node moves outside of the buffer layer, the friction is underpredicted, thus, the mean flow is overpredicted. The effect of the SS discretization is also explored using this test case. It is observed that the SS simulation cannot overcome the coarse LS resolution, which is consistent with the previous observations in the *a priori* analysis of the TLS approach. Fully coupled TLS-LES simulations of turbulent channel flow at $Re_\tau = 395, 590, 1200$ and

2400 suggest that explicit reconstruction of the SS velocity in the near-wall region allows accurate prediction of the LS turbulence dynamics. Results from these channel flow simulations suggest that near-wall implementation of TLS is a viable alternative approach for LES of wall bounded flows.

Finally, the TLS-LES approach is investigated for flows with much more complex flow features, such as separation and re-attachment. First, a turbulent channel flow containing a convergent-divergent bump on the bottom wall is investigated. LES using LDKM subgrid model is first performed to show the baseline capability of the code for complex flows. The LES results show good agreement with the DNS data. Then, this flow is simulated with the new TLS-LES approach using a much coarser LS grid. Results suggest that the TLS-LES approach has the potential for capturing the near-wall dynamics even when a very coarse LS grid is used. The TLS-LES model is further investigated for a diffuser flow and results show that the TLS-LES approach shows qualitative agreement with the experimental results for this complex flow. The separation location is predicted quite well with the TLS-LES, however, reattachment is observed further downstream. Also, the the pressure coefficient is over-predicted along the lower wall. These discrepancies between the TLS-LES results and experimental results can be the artifact of the coarse LS grid resolution. Clearly, the resolution of LS and SS for this type of flows needs to be revisited. Nevertheless, current studies show that the TLS-LES approach can be extended to complex flows without making any change on the model. This is an important aspect in terms of the numerical approaches since most of the turbulence models requires special tuning for one flow to another.

CHAPTER IX

FUTURE WORK

The additive TLS-LES equations are formulated by blending two equations: TLS-LS equation in the inner region and the LES equation in the outer region. New hybrid terms are identified in the TLS-LES equations due to the commutation error of the blending function with the space derivatives. In the TLS-LES formulation these hybrid terms can be directly calculated from the differences of the TLS LS and TLS-LES additive LS fields. However, due to the additional computational cost of this approach (TLS-LS variables have to be carried explicitly), these terms are not included in the present study. Therefore, including these terms to the solution of the TLS-LES equations needs to be addressed.

In the final form of the additive TLS-LES equations, the time dependency of the blending function $\mathcal{K}$ is neglected. However, for a more general approach a dynamic blending function can be used in order to remove the pre-definition of the blending approach before starting the simulation. The dynamic calculation of the blending function requires the integration of SS lines in the whole computational domain which will increase the computational time drastically. Further simplifications will be required in that case. For example, the placing of the 1D lines to simulate the SS field can be adjusted dynamically to match the blending function.

The TLS resolution requirement for the wall-bounded flows needs to be addressed for high Re flows ($Re \approx 10^5$). From the current analysis of the forced isotropic turbulence, it is argued that the LS resolution is $\mathrm{O}(N_i^{DNS}/2^3)$ for one direction. Although this estimate provides a good starting point, this requirement may not be universal for wall-bounded flows and, therefore, needs to be investigated in detail.

The turbulent channel flow with adverse pressure gradient is investigated for $Re_\tau = 395$ using the LES-LDKM and TLS-LES approaches. However, this Re is lower than the Re of the experiment, which is performed at $Re_\tau = 6500$. It is believed that even with the advent of massively parallel computers DNS of this flow is still not possible in the near future. Therefore, TLS-LES approach can be used to investigate the channel flow with adverse pressure gradient since the current studies show that TLS-LES resolution requirement can be eight times smaller than the DNS requirement and, with a coarse grid, TLS-LES is still able to capture low-order statistics. The TLS-LES LS and SS resolution requirements need to be revisited in the simulation of diffuser flow. Preliminary results presented in this study show the capability of the TLS-LES approach for the first order statistics. Further studies should investigate the TLS-LES approach for a diffuser flow with an inclination angle, which is smaller than the current study. The reason for choosing a smaller inclination angle is to check the sensitivity of the TLS-LES approach to predict separation and reattachment.

The parallel incompressible solver developed in this study needs to be further optimized for computations of high Re complex flows.

APPENDIX A

JHU DNS DATABASE

The database consists of forced isotropic turbulence simulations at Reynolds number of $Re_\lambda = 433$. A detailed description of the DNS methodology has been given in [69].

The analysis are performed based on the DNS velocity along particular lines across the 3D domain. These velocities are obtained using the web-service tool $GetVelocity$. Detailed description of this tool can be found in [69]. We take 250 grid lines along the x direction which are randomly distributed along both y and z directions. In each query, the velocity vectors at 1024 grid points for each line is obtained from the database. Therefore, there are 250 database queries in total in which each of obtains 1024 grid points. In total, about 0.26 million spatial locations are requested. These points are given on the grid and are equally spaced on the x direction. Since the points are given on the grid no interpolation method was needed. For the analysis here, only data at a single time $t = 0.564$ are used. We modified the sample FORTRAN code given in JHU DNS database (http://turbulence.pha.jhu.edu) for our purpose. A part of the code is given in the following example:

```
  integer, parameter :: NoTInt = 0 ! No temporal interpolation
  integer, parameter :: NoSInt = 0 ! No spatial interpolation
  character*100 :: dataset = 'isotropic1024coarse' // CHAR(0)
  character*100 :: authkey = 'jhu.edu.pha.turbulence.testing-200804' // CHAR(0)
  real :: time = 0.564
!
  call soapinit() ! Initialize the gSOAP runtime.
!
  pi = 4.0*(atan(1.0D0))
  dxmin = 2.0 * pi / 1024
......
......
  do i = 1, 1024, 1
     points(1, i) = dxmin * (i - 1)  ! x location
     points(2, i) = dxmin * (jj - 1) ! y location
```

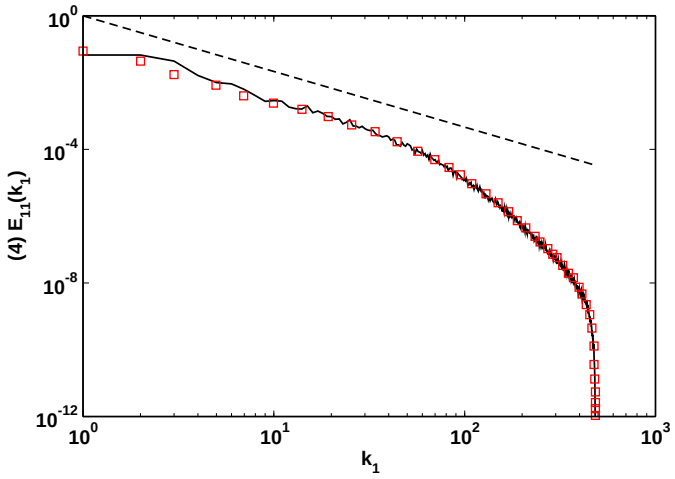

Figure 94: One-dimensional energy spectra calculated through database queries averaged over 250 lines and compared with [69] (symbols). Thin dashed line has slope $-5/3$.

```
     points(3, i) = dxmin * (kk - 1) ! z location
  end do
  write(*, *) 'Velocity at 1024 particle locations'
  call getvelocity(authkey, dataset,  time, NoSInt, NoTInt, 1024, points, dataout3)
  write(12,1010) points(1,i), dataout3(1,i), dataout3(2,i), dataout3(3,i)
.....
.....
!
  call soapdestroy() ! Destroy the gSOAP runtime.
!
```

In order to illustrate the correct loading of the data we looked at the longitudinal one dimensional spectrum and compared with the data given in [69]. The longitudinal spectrum is defined as $E_{11}(k_1) = \langle \hat{u}^*(k_1)\hat{u}(k_1)\rangle$, where $\hat{u}(k_1)$ is the one dimensional Fourier transformation of the streamwise velocity and $\hat{u}^*(k_1)$ is its complex conjugate. The average is taken over all the lines in y, z plane. The result is shown in Fig. 94. The rescaled longitudinal spectrum calculated with the data used in this study is equal to that calculated in [69], suggesting that there is no error in loading the data.

APPENDIX B

COMPRESSIBLE TLS FORMULATION

The governing equations of motion for unsteady, compressible fluid are the Navier-Stokes equations describing the conservations of mass, momentum and total energy, are given as follows:

$$\frac{\partial \rho}{\partial t} + \frac{\partial \rho u_i}{\partial x_i} = 0 \tag{182}$$

$$\frac{\partial \rho u_i}{\partial t} + \frac{\partial}{\partial x_j}(\rho u_i u_j) = -\frac{\partial p}{\partial x_j}\delta_{ij} + \frac{\partial \tau_{ij}}{\partial x_j} \tag{183}$$

$$\frac{\partial \rho E}{\partial t} + \frac{\partial}{\partial x_i}(\rho E u_i) = -\frac{\partial}{\partial x_i}(p u_i) - \frac{\partial q_i}{\partial x_i} + \frac{\partial}{\partial x_i}(\tau_{ij} u_j) \tag{184}$$

where ρ is the mass density, p is the pressure, E is the total energy per unit mass, u_i is the velocity vector, q_i is the heat flux vector ($q_i = -k\frac{\partial T}{\partial x_i}$), and τ_{ij} is the viscous stress tensor

$$\tau_{ij} = \mu(\frac{\partial u_i}{\partial x_j} + \frac{\partial u_j}{\partial x_i}) - \frac{2}{3}\mu\frac{\partial u_k}{\partial x_k}\delta_{ij}. \tag{185}$$

where μ is the molecular viscosity coefficient.

Also, the equation of state is:

$$p = \rho R T \tag{186}$$

where R is the universal gas constant per unit mass.

B.1 TLS Equations

Although the original TLS formulation by Kemenov and Menon [56] is for incompressible flows, to give the current TLS approach more generality, it is extended to fully compressible flows [38]. In the TLS approach [56], all flow variables are decomposed

into large-scale (LS, superscript L) and small-scale (SS, superscript S) components as:

$$\begin{aligned}
\rho(x,t) &= \rho^L(x,t) + \rho^S(x,t) \\
p(x,t) &= p^L(x,t) + p^S(x,t) \\
u_i(x,t) &= u_i^L(x,t) + u_i^S(x,t) \\
T(x,t) &= T^L(x,t) + T^S(x,t) \\
\rho u_i(x,t) &= (\rho u_i)^L(x,t) + (\rho u_i)^S(x,t) \\
\rho E(x,t) &= (\rho E)^L(x,t) + (\rho E)^S(x,t)
\end{aligned} \tag{187}$$

Here, the LS field is obtained by applying a LS operator $L^{\triangle}$ to the total velocity, which is defined by Kemenov and Menon [56] as:

$$u_i{}^L(x) = [u_i(x)]^L = L^{\triangle} u_i(x) \tag{188}$$

Similar to decomposition given in Eq. (187), any variable can be decomposed into LS and SS components:

$$\begin{aligned}
\Big((\rho u_i)^L + (\rho u_i)^S\Big)(u_j^L + u_j^S) &= \Big[\Big((\rho u_i)^L + (\rho u_i)^S\Big)(u_j^L + u_j^S)\Big]^L \\
&+ \Big[\Big((\rho u_i)^L + (\rho u_i)^S\Big)(u_j^L + u_j^S)\Big]^S
\end{aligned} \tag{189}$$

By substituting the decomposition given in Eq. (187) to the Navier-Stokes equations (182), the baseline TLS equations are given explicitly for both large and small scales, respectively as:

Large Scale Equations:

$$\frac{\partial \rho^L}{\partial t} + \frac{\partial}{\partial x_i}(\rho u_i)^L = F_{c,i}^S \tag{190}$$

$$\frac{\partial}{\partial t}(\rho u_i)^L + \frac{\partial}{\partial x_j}\Big((\rho u_i)^L + (\rho u_i^S)\Big)(u_j^L + u_j^S) = -\frac{\partial p^L}{\partial x_i} + \frac{\partial \tau_{ij}^L}{\partial x_j} + F_{m,i}^S \tag{191}$$

$$\begin{aligned}
\frac{\partial}{\partial t}(\rho E)^L + \frac{\partial}{\partial x_i}\Big((\rho E)^L + (\rho E)^S\Big)(u_i^L + u_i^S) &= -\frac{\partial}{\partial x_i}(p^L + p^S)(u_i^L + u_i^S) \\
&- \frac{\partial q_i^L}{\partial x_i} + \frac{\partial}{\partial x_i}(\tau_{ij}^L + \tau_{ij}^S)(u_j^L + u_j^S) \\
&+ F_{e,i}^S
\end{aligned} \tag{192}$$

Small Scale Equations:

$$\frac{\partial \rho^S}{\partial t} + \frac{\partial}{\partial x_i}(\rho u_i)^S = F^L_{c,i} \tag{193}$$

$$\frac{\partial}{\partial t}(\rho u_i)^S + \frac{\partial}{\partial x_j}\Big((\rho u_i)^L + (\rho u_i)^S\Big)(u^L_j + u^S_j) = -\frac{\partial p^S}{\partial x_i} + \frac{\partial \tau^S_{ij}}{\partial x_j} + F^L_{m,i} \tag{194}$$

$$\begin{aligned}\frac{\partial}{\partial t}(\rho E)^S + \frac{\partial}{\partial x_i}\Big((\rho E)^L + (\rho E)^S\Big)(u^L_i + u^S_i) &= -\frac{\partial}{\partial x_i}(p^L + p^S)(u^L_i + u^S_i) \\ &- \frac{\partial q^S_i}{\partial x_i} + \frac{\partial}{\partial x_i}(\tau^L_{ij} + \tau^S_{ij})(u^L_j + u^S_j) \\ &+ F^L_{e,i}\end{aligned} \tag{195}$$

where, F^S and F^L are the small-scale and large-scale forcing terms. In these equations the subscript c, m and e represents the source terms in the continuity, momentum and energy equation, respectively. These forcing terms are mathematically the coupling between the large and small-scale equations and can be expressed as: Large Scale Forcing Terms:

$$F^L_{c,i} = \frac{\partial \rho^L}{\partial t} - \frac{\partial}{\partial x_i}(\rho u_i)^L \tag{196}$$

$$F^L_{m,i} = -\frac{\partial}{\partial t}(\rho u_i)^L - \frac{\partial p^L}{\partial x_i} + \frac{\partial \tau^L_{ij}}{\partial x_j} \tag{197}$$

$$F^L_{e,i} = -\frac{\partial}{\partial t}(\rho E)^L - \frac{\partial q^L_i}{\partial x_i} \tag{198}$$

Small Scale Forcing Terms:

$$F^S_{c,i} = \frac{\partial \rho^S}{\partial t} - \frac{\partial}{\partial x_i}(\rho u_i)^S \tag{199}$$

$$F^S_{m,i} = -\frac{\partial}{\partial t}(\rho u_i)^S - \frac{\partial p^S}{\partial x_i} + \frac{\partial \tau^S_{ij}}{\partial x_j} \tag{200}$$

$$F^S_{e,i} = -\frac{\partial}{\partial t}(\rho E)^S - \frac{\partial q^S_i}{\partial x_i} \tag{201}$$

Note that, the TLS equations (190, 193) are different forms of the Navier-Stokes equations (182) written for different unknown velocities and they do not involve any

type of filtering. Thus, the TLS formulation is free of the commutativity issue, which is the main restriction of LES to the wall-bounded flows and non-uniform grids. This makes TLS a viable model for all types of flows, specifically for wall-bounded flows. These features have been extensively discussed and validated in earlier studies [56].

In order to have the same structure as the LES equations, the TLS equations can also be re-written in a different equivalent form. Substituting Eq. (189) into Eqs. (190, 193) gives another form of TLS equations as follows:

Large Scale Equations:

$$\frac{\partial \rho^L}{\partial t} + \frac{\partial}{\partial x_i}(\rho u_i)^L = G^S_{c,i} \tag{202}$$

$$\frac{\partial}{\partial t}(\rho u_i)^L + \frac{\partial}{\partial x_j}\Big[\Big((\rho u_i)^L + (\rho u_i)^S\Big)(u^L_j + u^S_j)\Big]^L = -\frac{\partial p^L}{\partial x_i} + \frac{\partial \tau^L_{ij}}{\partial x_j} + G^S_{m,i} \tag{203}$$

$$\begin{aligned}\frac{\partial}{\partial t}(\rho E)^L + \frac{\partial}{\partial x_i}\Big[\Big((\rho E)^L + (\rho E)^S\Big)(u^L_i + u^S_i)\Big]^L &= \Big[\frac{\partial}{\partial x_i}(p^L + p^S)(u^L_i + u^S_i)\Big]^L \\ &- \frac{\partial q^L_i}{\partial x_i} + \Big[\frac{\partial}{\partial x_i}(\tau^L_{ij} + \tau^S_{ij})(u^L_j + u^S_j)\Big]^L \\ &+ G^S_{e,i}\end{aligned} \tag{204}$$

Small Scale Equations:

$$\frac{\partial \rho^S}{\partial t} + \frac{\partial}{\partial x_i}(\rho u_i)^S = G^L_{c,i} \tag{205}$$

$$\frac{\partial}{\partial t}(\rho u_i)^S + \frac{\partial}{\partial x_j}\Big[\Big((\rho u_i)^L + (\rho u_i)^S\Big)(u^L_j + u^S_j)\Big]^S = -\frac{\partial p^S}{\partial x_i} + \frac{\partial \tau^S_{ij}}{\partial x_j} + G^L_{m,i} \tag{206}$$

$$\begin{aligned}\frac{\partial}{\partial t}(\rho E)^S + \frac{\partial}{\partial x_i}\Big[\Big((\rho E)^L + (\rho E)^S\Big)(u^L_i + u^S_i)\Big]^S &= -\Big[\frac{\partial}{\partial x_i}(p^L + p^S)(u^L_i + u^S_i)\Big]^S \\ &- \frac{\partial q^S_i}{\partial x_i} + \Big[\frac{\partial}{\partial x_i}(\tau^L_{ij} + \tau^S_{ij})(u^L_j + u^S_j)\Big]^S \\ &+ G^L_{e,i}\end{aligned} \tag{207}$$

Here the LS and SS forcing terms are given by: Large Scale Forcing Terms:

$$G^L_{c,i} = F^L_{c,i} \tag{208}$$

$$G^L_{m,i} = F^L_{m,i} - \frac{\partial}{\partial t}(\rho u_i)^L - \frac{\partial}{\partial x_j}(\rho u_i u_j)^L \tag{209}$$

$$G^L_{e,i} = F^L_{e,i} - \frac{\partial}{\partial x_i}(\rho E u_i)^L - \frac{\partial}{\partial x_i}(p u_i)^L + \frac{\partial}{\partial x_i}(\tau_{ij} u_j)^L \tag{210}$$

Small Scale Forcing Terms:

$$G^S_{c,i} = F^S_{c,i} \tag{211}$$

$$G^S_{m,i} = F^S_{m,i} - \frac{\partial}{\partial t}(\rho u_i)^S - \frac{\partial}{\partial x_j}(\rho u_i u_j)^S \tag{212}$$

$$G^S_{e,i} = F^S_{e,i} - \frac{\partial}{\partial x_i}(\rho E u_i)^S - \frac{\partial}{\partial x_i}(p u_i)^S + \frac{\partial}{\partial x_i}(\tau_{ij} u_j)^S \tag{213}$$

and note that both are equivalent to the original Navier-Stokes equations (182) written as [56]

$$G^L_{c,i} + G^S_{c,i} = 0 \tag{214}$$

$$G^L_{m,i} + G^S_{m,i} = 0 \tag{215}$$

$$G^L_{e,i} + G^S_{e,i} = 0 \tag{216}$$

These equations hold only when each LS and SS forcing terms are simultaneously zero ($i.e., G^L_{c,i} = 0, G^S_{c,i} = 0, G^L_{m,i} = 0, G^S_{m,i} = 0, G^L_{e,i} = 0, G^S_{e,i} = 0$). If not, the small scale field obtained by solving SS equations will have contributions at the small wave numbers (i.e., at the large scales). The details and justification of these arguments are given by Kemenov and Menon [56]. By substituting Eq. (214) into the LS and the SS equations, the final form of the TLS equations can be obtained as:

Large Scale Equations:

$$\frac{\partial \rho^L}{\partial t} + \frac{\partial}{\partial x_i}(\rho u_i)^L = 0 \tag{217}$$

$$\frac{\partial}{\partial t}(\rho u_i)^L + \frac{\partial}{\partial x_j}\Big[\Big((\rho u_i)^L + (\rho u_i^S)\Big)(u_j^L + u_j^S)\Big]^L = -\frac{\partial p^L}{\partial x_i} + \frac{\partial \tau^L_{ij}}{\partial x_j} \tag{218}$$

$$\frac{\partial}{\partial t}(\rho E)^L + \frac{\partial}{\partial x_i}\Big[\Big((\rho E)^L + (\rho E)^S\Big)(u_i^L + u_i^S)\Big]^L = -\Big[\frac{\partial}{\partial x_i}(p^L + p^S)(u_i^L + u_i^S)\Big]^L - \frac{\partial q_i^L}{\partial x_i} + \Big[\frac{\partial}{\partial x_i}(\tau^L_{ij} + \tau^S_{ij})(u_j^L + u_j^S)\Big]^L \tag{219}$$

Small Scale Equations:

$$\frac{\partial \rho^S}{\partial t} + \frac{\partial}{\partial x_i}(\rho u_i)^S = 0 \tag{220}$$

$$\frac{\partial}{\partial t}(\rho u_i)^S + \frac{\partial}{\partial x_j}\Big[\Big((\rho u_i)^L + (\rho u_i^S)\Big)(u_j^L + u_j^S)\Big]^S = -\frac{\partial p^S}{\partial x_i} + \frac{\partial \tau_{ij}^S}{\partial x_j} \tag{221}$$

$$\frac{\partial}{\partial t}(\rho E)^S + \frac{\partial}{\partial x_i}\Big[\Big((\rho E)^L + (\rho E)^S\Big)(u_i^L + u_i^S)\Big]^S = -\Big[\frac{\partial}{\partial x_i}(p^L + p^S)(u_i^L + u_i^S)\Big]^S - \frac{\partial q_i^S}{\partial x_i} + \Big[\frac{\partial}{\partial x_i}(\tau_{ij}^L + \tau_{ij}^S)(u_j^L + u_j^S)\Big]^S \tag{222}$$

APPENDIX C

BUDGET OF THE TURBULENT KINETIC ENERGY EQUATION

The turbulent kinetic energy equation is obtained by multiplying the momentum equation for the fluctuating velocity

$$\frac{\partial \langle u_i' u_i' \rangle}{\partial t} + \langle u_j' \rangle \frac{\partial \langle u_i' u_i' \rangle}{\partial x_j} = P + T + D + D_\rho + \Phi - \varepsilon \tag{223}$$

where the left-hand side term is the advection and the right-hand side terms are defined as follows:

Production: $$P = -\langle u_i' u_j' \rangle \frac{\partial \langle u_i \rangle}{\partial x_j} - \langle u_i' u_j' \rangle \frac{\partial \langle u_i \rangle}{\partial x_j}$$

Turbulent Transport: $$T = -\frac{\partial \langle u_i' u_i' u_j' \rangle}{\partial x_j}$$

Viscous diffusion: $$D = \nu \frac{\partial^2 \langle u_i' u_i' \rangle}{\partial x_j x_j}$$

Pressure diffusion: $$D_\rho - \frac{1}{\rho} \left(\frac{\partial \langle u_i' p' \rangle}{\partial x_i} \right)$$

Pressure strain: $$\Phi = \left\langle \frac{p'}{\rho} \left(\frac{\partial u_i'}{\partial x_i} + \frac{\partial u_i'}{\partial x_i} \right) \right\rangle$$

Dissipation: $$\varepsilon = 2\nu \left\langle \frac{\partial u_i'}{\partial x_j} \frac{\partial u_i'}{\partial x_j} \right\rangle$$

REFERENCES

[1] Baggett, J. S., "On the feasibility of merging les with rans in the near-wall region of attached turbulent flows," in *Center For Turbulent Research, Annual Research Briefs*, pp. 267–277, 1998.

[2] Baggett, J. S., Jimenez, J., and Kravchenko, A. G., "Resolution requirements in large-eddy simulations of shear flows," in *Center For Turbulent Research, Annual Research Briefs*, pp. 51–66, 1997.

[3] Balaras, E., Benocci, C., and Piomelli, U., "Two-layer approximate boundary conditions for large-eddy simulations," *AIAA J.*, vol. 34, pp. 1111–1119, 1996.

[4] Bardina, J., Ferziger, J., and Reynolds, W., "Improved subgrid scale models for large eddy simulations," *AIAA Paper 80–1357*, 1980.

[5] Baskaran, V., Smits, A., and Joubert, P., "A turbulent flow over a curved hill. part 1. growth of an internal boundary layer," *Journal of Fluid Mechanics*, vol. 182, pp. 47–83, 1987.

[6] Beck, C., "Superstatistics in hydrodynamic turbulence," *Physica D*, vol. 193, pp. 195–207, 2004.

[7] Bernard, A., Foucaut, J. M., Dupont, P., and Stanislas, M., "Decelerating boundary layer: A new scaling and mixing length model," *AIAA Journal*, vol. 41, no. 2, pp. 248–255, 2003.

[8] Bouffanais, R., "Large-eddy simulation of the flow in a lid-driven cubical cavity," *Physics of Fluids*, vol. 19, pp. 1–20, 2007.

[9] Buice, C. U. and Eaton, J. K., "Experimental investigation of flow through an asymmetric plane diffuser," *Journal of Fluids Engineering*, vol. 122, pp. 433–435, 2000.

[10] Cabot, W., "Large-eddy simulations with wall models," in *Center For Turbulent Research, Annual Research Briefs*, pp. 41–49, 1995.

[11] Cabot, W. and Moin, P., "Approximate wall boundary conditions in the large-eddy simulation of high reynolds number flows," *Flow Turbulence Combustion*, vol. 63, pp. 269–291, 2000.

[12] Canuto, C., Hussaini, M., Quarteroni, A., and Tang, T. in *Spectral Methods in Fluid Dynamics*, 1988.

[13] Chapman, D. R., "Computational aerodynamics development and outlook," *AIAA Journal*, vol. 17, pp. 1293–1313, 1979.

[14] Chorin, A. J., "A numerical method for solving incompressible viscous flow problems," *Journal of Computational Physics*, vol. 2, pp. 12–26, 1967.

[15] Collis, S. S., "Monitoring unresolved scales in multiscale turbulence modeling," *Physics of Fluids*, vol. 13, pp. 1800–1806, 2001.

[16] Dahlstrom, S. and Davidson, L., "Hybrid les-rans with additional conditions at the matching region," in *Turbulence Heat and Mass Transfer 4*, pp. 689–696, Begell House, 2003.

[17] Davidson, L. and Peng, S., "Hybrid les-rans modelling: a one equation sgs model combined with a $k - \omega$ model for predicting recirculating flows," *International Journal of Numerical Methods in Fluids*, vol. 43, pp. 1003–1018, 2003.

[18] De Prisco, G., Piomelli, U., and Keating, A., "Improved turbulence generation techniques for hybrid rans/les calculations," *Journal of Turbulence*, vol. 9, no. 5, pp. 1–20, 2008.

[19] De Stefano, G. and Vasilyev, O. V., ""Perfect" modeling framework for dynamic SGS model testing in large eddy simulation," *Theoretical and Computational Fluid Dynamics*, vol. 18, no. 1, pp. 27–41, 2004.

[20] Dean, R. B., "Reynolds number dependence of skin friction and other bulk flow variables in two-dimensional rectangular duct flow," *Journal of Fluids Engineering*, vol. 100, pp. 215–228, 1978.

[21] Deardorff, J. W., "A numerical study of three-dimensional turbulent channel flow at large reynolds numbers," *Journal of Fluid Mechanics*, vol. 41, pp. 453–480, 1970.

[22] del Alamo, J., Jimenez, J., Zandonade, P., and Moser, R., "Scaling of the energy spectra of turbulent channels," *Journal of Fluid Mechanics*, vol. 500, pp. 135–144, 2004.

[23] Dengel, P. and H., F. H., "An experimental investigation of an incompressible turbulent boundary layer in the vicinity of separation," *Journal of Fluid Mechanics*, vol. 212, pp. 615–636, 1990.

[24] Dubois, T., Jauberteau, F., and R., T., "Dynamic multilevel methods and the numerical simulation of turbulence," Cambridge University Press, 1999.

[25] Durbin, P., "Separated flow computations with the $k - \epsilon - \nu^2$ model," *AIAA Journal*, vol. 33, pp. 659–664, 1995.

[26] Fureby, C. and Tabor, G., "Mathematical and physical constraints on large-eddy simulations," *Theoretical and Computational Fluid Dynamics*, vol. 9, pp. 85–102, 1997.

[27] Germano, M., "Properties of the hybrid rans/les filter," *Theoret. Comput. Fluid Dynamics*, vol. 17, pp. 225–231, 2004.

[28] Germano, M., Piomelli, U., Moin, P., and Cabot, W. H., "A dynamic subgrid-scale eddy viscosity model," *Physics of Fluids A*, vol. 3, no. 11, pp. 1760–1765, 1991.

[29] Germano, M. and Sagaut, P., "Formal properties of the additive rans/dns filter," in *Direct and Large-Eddy Simulations VI*, Springer Netherlands, 2006.

[30] Ghosal, S., "Mathematical and physical constraints on large eddy simulation of turbulence," *AIAA Journal*, vol. 37, pp. 425–433, 1999.

[31] Ghosal, S. and Moin, P., "The basic equations for the large eddy simulation of turbulent flows in complex geometry," *Journal of Computational Physics*, vol. 118, pp. 24–37, 1995.

[32] Gravemeier, V., "A consistent dynamic localization model for large eddy simulation of turbulent flows based on a variational formulation," *Journal of Computational Physics*, vol. 218, pp. 677–701, 2006.

[33] Gravemeier, V., "Variational multiscale large eddy simulation of turbulent flow in a diffuser," *Comput. Mech.*, vol. 39, pp. 477–495, 2007.

[34] Groetzbach, G., "Direct numerical and large eddy simulation of turbulent channel flows," in *Encyclopedia of Fluid Mechanics*, pp. 1337–1391, 1987.

[35] Gullman-Strand, J., Tornblom, O., Lindgren, B., Amberg, G., and A.V., J., "Numerical and experimental study of separated flow in a plane asymmetric diffuser," *International Journal of Heat and Fluid Flow*, vol. 45, pp. 451–460, 2004.

[36] Gungor, A. G. and Menon, S., "Multi-scale simulation of near-wall turbulent flows," in *Direct and Large Eddy Simulation VII (to appear)*, 2008.

[37] Gungor, A. G., Sanchez-Rocha, M., and Menon, S., "Hybrid two level and large eddy simulation of wall bounded turbulent flows," in *Advances in Turbulence XI*, pp. 322–325, 2007.

[38] Gungor, A. and Menon, S., "Direct simulation of subgrid turbulence in high-re, wall-bounded flows," *AIAA paper 2006-3538*, 2006.

[39] Hamba, F., "A hybrid rans/les simulation of turbulent channel flow," *Theoret. Comput. Fluid Dynamics*, vol. 16, pp. 387–403, 2003.

[40] Hamba, F., "A hybrid rans/les simulation of high-reynolds-number channel flow using additional filtering at the interface," *Theoret. Comput. Fluid Dynamics*, vol. 20, no. 2, pp. 89–101, 2006.

[41] Harlow, F. H. and Welch, J. E., "Numerical calculation of time-dependent viscous incompressible flow with free surface," *Physics of Fluids*, vol. 8, no. 12, pp. 2182–2189, 1965.

[42] Hellsten, A. and Rautaheimo (eds), P. in *Proceedings of the 8th ERCOFTAC/IAHR/COST workshop on refined turbulence modeling. Helsinki University of Technology, Espoo, Finland, June 17-18*, 1999.

[43] Herbst, A., Schlatter, P., and Henningson, D., "Simulations of turbulent flow in a plane asymmetric diffuser," *Flow Turbulence Combustion*, vol. 79, pp. 275–306, 2007.

[44] Hoyas, S. and Jimenez, J., "Scaling of the velocity fluctuations in turbulent channels up to $Re_\tau = 2003$," *Physics of Fluids*, vol. 18, p. 011702, 2006.

[45] Hughes, T., Mazzei, L., and Oberai, A., "The multiscale formulation of large-eddy simulation: Decay of homogeneous isotropic turbulence," *Physics of Fluids*, vol. 13, no. 2, pp. 505–512, 2001.

[46] Hughes, T., Oberai, A., and Mazzei, L., "Large eddy simulation of turbulent channel flows by variational multiscale method," *Physics of Fluids*, vol. 13, no. 6, pp. 1784–1799, 2001.

[47] Iaccarino, G., "Predictions of a turbulent separated flow using commercial cfd codes," *Journal of Fluids Engineering*, vol. 123, pp. 819–828, 2001.

[48] Jameson, A., "Time dependent calculation using multigrid, with application to unsteady flows past airfoils and wings," *AIAA Paper 91–1596*, 1991.

[49] Jimenez, J., "Computing high-reynolds-number turbulence: will simulations ever replace experiments?," *Journal of Turbulence*, vol. 4, no. 22, 2003.

[50] Jimenez, J., "Recent developments on wall-bounded turbulence," *Rev. R. Acad. Cien. Serie A. Mat*, vol. 101, no. 2, pp. 187–203, 2007.

[51] Jimenez, J. and Moin, P., "The minimal flow unit in near-wall turbulence," *Journal of Fluid Mechanics*, vol. 255, pp. 221–240, 1991.

[52] Kaltenbach, H.-J., Fatica, M., Mittal, R. Lund, T. S., and Moin, P., "Study of flow in a planar asymmetric diffuser using large-eddy simulation," *Journal of Fluid Mechanics*, vol. 390, pp. 151–185, 1999.

[53] Kaneda, Y., Ishihara, T., Yokokawa, M., Itakura, K., and Uno, A., "Energy dissipation rate and and energy spectrum in high resolution direct numerical simulation of turbulence in a periodic box," *Physics of Fluids*, vol. 15, no. 2, pp. L21–L24, 2003.

[54] Keating, A. and Piomelli, U., "A dynamic stochastic forcing method as a wall-layer model for large-eddy simulation," *Journal of Turbulence*, vol. 7, no. 12, pp. 1–24, 2006.

[55] Kemenov, K., Gungor, A., and Menon, S., "Two level simulation of high-re wall bounded flows and isotropic turbulence," *AIAA paper 2005-5318*, 2005.

[56] Kemenov, K. and Menon, S., "Explicit small-scale velocity simulation for high-re turbulent flows," *Journal of Computational Physics*, vol. 220, pp. 290–311, 2006.

[57] Kemenov, K. and Menon, S., "Explicit small-scale velocity simulation for high-re turbulent flows.part 2: Non-homogeneous flows," *Journal of Computational Physics*, vol. 222, pp. 673–701, 2007.

[58] Kerstein, A., "One-dimensional turbulence: model formulation and application to homogeneous turbulence, shear flows and buoyant stratified flows," *Journal of Fluid Mechanics*, vol. 392, pp. 277–334, 1999.

[59] Kim, H., Kline, S., and Reynolds, W., "The production of turbulence near a smooth wall in a turbulent boundary layer," *Journal of Fluid Mechanics*, vol. 50, pp. 133–166, 1971.

[60] Kim, W.-W. and Menon, S., "An unsteady incompressible navier-stokes solver for large-eddy simulation of turbulent flows," *International Journal of Numerical Fluid Mechanics*, vol. 31, pp. 983–1017, 1999.

[61] Kravchenko, A. G., Moin, P., and Moser, R., "Zonal embedded grids for numerical simulations of wall-bounded turbulent flows," *Journal of Computational Physics*, vol. 127, pp. 412–423, 1996.

[62] Laval, J., Dubrule, B., and Nazarenko, "Fast numerical simulations of 2d turbulence using a dynamic model for subfilter motions," *Journal of Computational Physics*, vol. 196, pp. 184–207, 2004.

[63] Laval, J., Dubrule, B., and Nazarenko, S., "Nonlocality of interaction of scales in the dynamics of 2d incompressible fluids," *Phys.Rev.Let*, vol. 83, pp. 4061–4064, 1999.

[64] Laval, J., Dubrule, B., and Nazarenko, S., "Nonlocality and intermittency in three-dimensional turbulence," *Physics of Fluids*, vol. 13, pp. 1995–2012, 2001.

[65] Laval, J., Dubrule, B., Nazarenko, S., and Kevlahan, N.-R., "A dynamic subfilter-scale model for plane parallel flows," *Physics of Fluids*, vol. 13, pp. 2045–2064, 2001.

[66] Lele, S., "Compact finite difference schemes with spectral-like resolution," *Journal of Computational Physics*, vol. 103, pp. 16–42, 1992.

[67] Leonard, A., "Energy cascade in large eddy simulation of turbulent fluid flow," *Advances in Geophysics*, vol. 18, pp. 237–248, 1974.

[68] Leriche, E., "Direct numerical simulation in a lid-driven cubical cavity at high reynolds number by a chebyshev spectral method," *Journal of Computational Physics*, vol. 27, pp. 335–345, 2006.

[69] Li, Y., Perlman, E., Wan, M., Yang, Y., Meneveau, C., Burns, R., Chen, S., Szalay, A., and Eyink, G., "A public turbulence database cluster and applications to study lagrangian evolution of velocity increments in turbulence," *Journal of Turbulence*, vol. 9, no. 31, pp. 1–29, 2008.

[70] Lilly, D. K., "A proposed modification to the germano subgrid-scale closure method," *Physics of Fluids*, vol. 4, pp. 633–635, 1992.

[71] Liu, S., Meneveau, C., and Katz, J., "On the properties of similarity subgrid-scale models as deduced from measurements in a turbulent jet," *Journal of Fluid Mechanics*, vol. 275, pp. 83–119, 1994.

[72] Lund, T. S., "The use of explicit filters in large eddy simulation," *Computers & Mathematics with Applications*, vol. 46, pp. 603–616, 2003.

[73] Lund, T. and Kaltenbach, H.-J., "Experiments with explicit filtering for les using a finite difference methos," in *Center For Turbulent Research, Annual Research Briefs*, pp. 91–105, 1995.

[74] Marquillie, M., Laval, J.-P., and Dolganov, R., "Direct numerical simulation of a separated channel flow with a smooth profile," *Journal of Turbulence*, vol. 9, no. 1, pp. 1–23, 2008.

[75] Meneveau, C. and Katz, J., "Scale-invariance and turbulence models for large-eddy simulation," *Annual Review of Fluid Mechanics*, vol. 32, pp. 1–32, 2000.

[76] Menon, S. and Kim, W.-W., "High reynolds number flow simulations using the localized dynamic subgrid-scale model," *AIAA Paper 96–0425*, 1996.

[77] Menon, S., Yeung, P.-K., and Kim, W.-W., "Effect of subgrid models on the computed interscale energy transfer in isotropic turbulence," *Computers and Fluids*, vol. 25, no. 2, pp. 165–180, 1996.

[78] Merkle, C. L. and Athavale, M., "Time-accurate unsteady incompressible flow algorithms based on artificial compressibility," *AIAA Paper 87–1137*, 1987.

[79] Meyers, J. and Sagaut, P., "Is plane-channel flow a friendly case for the testing of large-eddy simulation subgrid-scale models.," *Physics of Fluids*, vol. 19, p. 048105, 2007.

[80] Moin, P. and Mahesh, K., "Direct numerical simulation: A tool in turbulence research," *Annual Review of Fluid Mechanics*, vol. 30, pp. 539–578, 1998.

[81] Moin, P., Squires, K., Cabot, W., and Lee, S., "A dynamic subgrid-scale model for compressible turbulence and scalar transport," *Physics of Fluids A*, vol. 11, pp. 2746–2754, 1991.

[82] Morinishi, Y., Lund, T. S., Vasilyev, O. V., and Moin, P., "Fully conservative higher order finite difference schemes for incompressible flows," *Journal of Computational Physics*, vol. 143, pp. 90–124, 1998.

[83] Moser, R., Kim, J., and Mansour, N., "Direct numerical simulation of turbulent channel flow up to $Re_\tau = 590$," *Physics of Fluids*, vol. 11, pp. 943–945, 1999.

[84] Na, Y. and Moin, P., "Direct numerical simulation of a separated boundary layer," *Journal of Fluid Mechanics*, vol. 374, pp. 379–405, 1998.

[85] Neumann, J. and H., W., "Chorent structures in controlled separated flow over sharp-edged and rounded steps," *Journal of Fluid Mechanics*, pp. 1–24, 2004.

[86] Nikitin, N., Nicoud, F., Wasistho, B., Squires, K., and Spalart, P., "An approach to wall modeling in large eddy simulations," *Physics of Fluids*, vol. 12, pp. 1629–1632, 2000.

[87] Obi, S., Aoki, K., and Masuda, S., "Experimental and computational study of turbulent separating flow in an asymmetric plane diffuser," *9th Symposium on Turbulent Shear Flows, Kyoto, Japan, August 16-19*, p. 305, 1993.

[88] Patankar, S. V. Hemisphere Publishing, New York, 1980.

[89] Piomelli, U., "High reynolds number calculations using the dynamic subgrid-scale stress model," *Physics of Fluids A*, vol. 5, no. 6, pp. 1484–1484, 1993.

[90] Piomelli, U., "Large-eddy simulation: Achievements and challenges," *Progress in Aerospace Sciences*, vol. 35, pp. 335–362, 1999.

[91] Piomelli, U., "Wall-layer models for large-eddy simulations," *Progress in Aerospace Sciences*, vol. 44, pp. 437–446, 2008.

[92] Piomelli, U. and Balaras, E., "Wall layer models for large eddy simulation," *Annual Review of Fluid Mechanics*, vol. 34, pp. 349–374, 2002.

[93] Piomelli, U., Balaras, E., Pasinato, H., Squires, K., and Spalart, P., "The inner-outer layer interface in large-eddy simulations with wall-layer models," *International Journal of Heat and Fluid Flows*, vol. 24, pp. 538–550, 2003.

[94] Piomelli, U., Moin, P., Ferziger, J., and Kim, J., "New approximate boundary conditions for large-eddy simulations of wall-bounded flows," *Physics of Fluids A*, vol. 1, pp. 1061–1068, 1989.

[95] Pope, S. B. Cambridge U. Press, 2000.

[96] Prasad, A. and Koseff, J., "Reynolds number and end-wall effects on a lid-driven cavity flow," *Physics of Fluids*, vol. 1, no. 2, pp. 206–218, 1969.

[97] Radhakrishnan, S., Piomelli, U., Keating, A., and Silva Lopes, A., "Reynolds-averaged and large-eddy simulations of turbulent non-equilibrium flows," *Journal of Turbulence*, vol. 7, no. 63, pp. 1–30, 2006.

[98] Rai, M. M. and Moin, P., "Direct simulations of turbulent flow using finite difference schemes," *Journal of Computational Physics*, vol. 96, pp. 15–53, 1991.

[99] Rhie, C. and Chow, W., "Numerical study of the turbulent flow past an aerofoil with trailing edge separation," *AIAA J.*, vol. 21, pp. 1525–1532, 1983.

[100] Robinson, S. K., "Coherent motions in the turbulent boundary layer," *Annual Review of Fluid Mechanics*, vol. 23, pp. 601–639, 1991.

[101] Rogers, S. E. and Kwak, D., "Steady and unsteady solutions of the incompressible navier-stokes equations," *AIAA Journal*, vol. 29, no. 4, pp. 603–610, 1991.

[102] Sagaut, P. Springer, 2006.

[103] Sanchez-Rocha, M. and Menon, S., "The compressible hybrid rans/les formulation using an additive operator," *to appear in Journal of Computational Physics*, 2008.

[104] Schluter, J., Wu, X., and Pitsch, H., "Large-eddy simulation of a separated plane diffuser," *AIAA Paper 05–0672*, 2005.

[105] Schmidt, R., Kerstein, A., Wunsch, S., and Nilsen, V., "Near-wall LES closure based on One-Dimensional Turbulence modeling," *Journal of Computational Physics*, vol. 186, pp. 317–355, 2003.

[106] Schumann, U., "Subgrid scale model for finite difference simulations of turbulent flows in plane channels and annuli.," *Journal of Computational Physics*, vol. 18, pp. 376–404, 1975.

[107] Schumann, U., "Realizability of reynolds-stress turbulence models," *Physics of Fluids*, vol. 20, no. 5, pp. 721–725, 1977.

[108] Simpson, R. L., "Turbulent boundary-layer separation," *Annual Review of Fluid Mechanics*, vol. 21, pp. 205–234, 1989.

[109] Smagorinsky, J., "General circulation experiments with the primitive equations," *Monthly Weather Review*, vol. 91, no. 3, pp. 99–164, 1993.

[110] Spalart, P. R. and Allmaras, S. R., "A one-equation turbulence model for aerodynamic flows," *AIAA Paper 92–0439*, 1992.

[111] Spalart, P. R., Jou, W.-H., Stretlets, M., and Allmaras, S. R., "Comments on the feasibility of les for wings and on the hybrid rans/les approach," 1997.

[112] Temmerman, L., Hadziabdic, M., Leschziner, M., and Hanjalic, K., "A hybrid two-layer urans-les approach for large eddy simulation at high reynolds numbers," *International Journal of Heat and Fluid Flow*, vol. 26, pp. 173–190, 2005.

[113] Tennekes, H. and J.L., L. MIT Pres, 1972.

[114] Vasilyev, O., "High order finite difference schemes on non-uniform meshes with good conservation properties," *Journal of Computational Physics*, vol. 157, pp. 746–761, 2000.

[115] Vasilyev, O., Lund, T., and Moin, P., "A general class of commutative filters for les in complex geometries," *Journal of Computational Physics*, vol. 146, pp. 105–123, 1998.

[116] Vreman, B., Geurts, B., and Kuerten, H., "Large-eddy simulation of the turbulent mixing layers," *Journal of Fluid Mechanics*, vol. 339, pp. 357–390, 1997.

[117] Wang, M. and Moin, P., "Dynamical wall modeling for large-eddy simulation of complex turbulent flows," *Physics of Fluids*, vol. 14, pp. 2043–2051, 2002.

[118] Webster, D., DeGraff, D., and Eaton, J., "Turbulence characteristics of a boundary layer over a two dimensional bump," *Journal of Fluid Mechanics*, vol. 320, pp. 53–69, 1996.

[119] Werner, H. and Wengle, H., "Large-eddy simulation of turbulent flow around a cube in a plane channel," in *Selected Papers from the 8th Symposium on Turbulent Shear Flows*, pp. 155–168, 1993.

[120] Wu, X., Schluter, J., Moin, P., Pitsch, H., Iaccarino, G., and Ham, F., "Computational study on the internal layer in a diffuser," *Journal of Fluid Mechanics*, vol. 550, pp. 391–412, 2006.

[121] Wu, X. and Squires, K. D., "Numerical investigation of the turbulent boundary layer over a bump," *Journal of Fluid Mechanics*, vol. 362, pp. 229–271, 1998.

[122] Yoshizawa, A. and K., H., "A statistically-derived subgrid-scale kinetic energy model for the large eddy simulation of turbulent flows," *Journal of Phys. Soc. Japan*, vol. 54, pp. 2834–2839, 1985.

[123] Zang, Y., Street, R., and Koseff, J., "A dynamic mixed subgrid-scale model and its application to turbulent recirculating flows," *Physics of Fluids A*, vol. 5, pp. 3186–3193, 1993.

VITA

Ayse Gul Gungor was born on April 12th, 1977 in Giresun, Turkey. She received her double-major B.S degrees in aeropsace and mechanical engineering and her M.S degree in aerospace engineering from Istanbul Technical University in Turkey in 2000, 2001, and 2004, repectively. She joined Computational Combustion Lab at School of Aerospace Engineering, Georgia Institute of Technology in 2003 for her graduate studies where she completed her M.S and Ph.D in 2007 and 2009, respectively. Her areas of research interest include turbulent flows and its modeling, computational fluid dynamics, numerical methods and lattice boltzmann approach.